EXCLUSIVELY AVAILABLE VIA IEEE Xplore® DIGITAL LIBRARY

ISSN 2475-742X (Print)
ISSN 3066-2427 (Online)

CPSS Transactions on Power Electronics and Applications

VOLUME 10 NUMBER 3 SEPTEMBER 2025

REGULAR PAPERS

A New Active Clamp Zero-Voltage-Transition Cell for Non-Isolated DC-DC Converter With Low Current Stress.....*J. Zhang, Y. Li, J. Wan, B. Zhao, Y. Zhang, and F. Liu* 231

Power Management With Event-Triggered Predictive Function Control for DC Microgrid Clusters.....*S. Liu, T. Zhou, T. Hong, Q. Zhang, W. Fang, and X. Liu* 241

Quality Management of Energy Storage VSG Based on Odd-Order Repetitive Control.....*Y. Sun, J. Zhou, S. Chen, and T. Lan* 257

Continuous-Control-Set Predictive Control and Noise Tolerance Strategy for Phase-Shift Modulation DAB Topological Clusters.....*T. Hao, J. Huang, Z. Dong, Z. Zhang, and Q. Chen* 270

Design and Optimization of High Misalignment Edge-Enhanced Stepped Coil Structure for Dynamic Wireless Power Transfer System.....*C. Zhang, Z. Li, J. Wang, and C. Hu* 282

Power Quality Enhancement Using AZQLMS and Fractional Order PID Based Control Through Dynamic Voltage Restorer.....*G. K. Budumuru, P. Ray, P. Kumar, and S. R. Arya* 296

A Family of Single-Phase Back-to-Back Three-Level Power Factor Correction Rectifiers.....*H. Ma, G. Chen, K. Xiang, L. Fan, L. Xi, and Y. Huang* 304

Dual-Layer Control Strategy for Wind-Storage Combined Frequency Regulation Based on Hybrid Energy Storage Lifetime Loss Optimization.....*Y. Li, G. Song, J. Huang, and Z. Liu* 317

Electromechanical Coupling Resonance Analysis and Compensation Strategy of IPMSM Drive System Considering Current Measurement Offset Error.....*X. Ge, Y. Liu, Y. Zuo, and H. Wang* 328

State and Disturbance Estimator Based Feedback Controller Synthesis for Hybrid Electric Vehicle.....*S. Singh and B. Pratap* 340

A PUBLICATION OF THE CHINA POWER SUPPLY SOCIETY

A New Active Clamp Zero-Voltage-Transition Cell for Non-Isolated DC-DC Converter with Low Current Stress

Jie ZHANG, Yong LI, Jianghu WAN, Bing ZHAO, Yuhang ZHANG, and Fang LIU

***Abstract*—In this paper, a novel low voltage and current stress zero voltage transition (ZVT) cell is proposed for a family of non-isolated DC-DC converters. By adding a current transfer circuit composed of an auxiliary switch, a diode, two capacitors, and two inductors to the traditional DC-DC converters, the proposed converters achieve zero voltage switching (ZVS) condition for active switches, and alleviates the reverse recovery problem for two diodes. Moreover, with the proper design of the auxiliary circuit, the voltage spikes during the switching process are significantly reduced. And the proposed ZVT cell only introduces low voltage stress but avoiding any additional current stress on the power semiconductor device. The operating principle and performance analysis of the proposed Boost converter are given in detail. The experiment from a 2-kW laboratory prototype at 100 kHz switching frequency has been carried out to validate the theoretical principles. The experimental results show that the proposed Boost converter has the advantage of simple structure and the peak efficiency is found to be 98.76%.**

***Index Terms*—Boost converter, active clamped, soft-switching, zero voltage switching (ZVS).**

I. Introduction

RECENTLY the rapidly diminishing nonrenewable energy sources and the growing environmental concerns, developing renewable energy is key to addressing these problems. Power converters play a crucial role in integrating renewable energy generation integration into microgrid. The step-up converters are widely utilized in order to manage power between sources and loads of systems with energy storage elements [1]−[2]. In many applications, such as photovoltaic (PV) power generation system and fuel cell power system, automotive electronics and power factor correction (PFC), non-isolated pulse-width modulation DC-DC converters (NPDCs) are popular due to their simple structure and small volume. In the numerous no-isolated topologies, the traditional Boost structure which is the simplest topology makes it popular in widely range applications of power electronics systems [3]−[4]. However, the reverse recovery of the rectifier diodes and elevated switch loss are significant issues, especially at high switching frequency [5]−[7]. In response to these challenges, the concept of soft switching technology was presented [8]−[9]. Some researchers have proposed using control algorithms to make the inductor current a triangular wave with periodic zero crossings to achieve zero voltage switching (ZVS) in converters. However, the control of discontinuous conduction mode (DCM) is relatively complex and all power components are subjected to high peak currents. Hence, some soft switching technologies achieving by adding passive or active auxiliary circuits to the traditional NPDCs is proposed. These converters are comprised of zero voltage transition (ZVT) converters [10]−[22], zero current transition (ZCT) converters [23]−[26]. Several key features are crucial to ensuring the proper performance of these soft switching converters. First, achieving a soft switching condition for active switches is essential when operating at high frequencies to eliminate switching loss and electromagnetic interface (EMI). Second, zero current switching (ZCS) turn OFF for these diodes is essential to remove the reverse recovery problem. Third, the auxiliary circuit or additional elements used to provide a soft switching condition in power flow directions should not adversely impact component count or weight of the Boost converter. Finally, minimizing voltage stress and current stress on the switch and diode is crucial in achieving high efficiency and reliability of the converter.

For high-speed switching applications in power conversion systems, the MOSFET is widely utilized due to its inherent characteristics. Notably, the MOSFET's relatively low turn-OFF loss makes ZVT is preferred over ZCT, as it eliminates the capacitive turn-ON loss. Moreover, ZCT cells incorporate passive components such as inductors and capacitors into a circuit to form a resonant circuit, which is prone to generating higher voltage and current stresses. And ZCT cells require more precise control when implementing zero current switching, which pose challenges to the reliability and stability. Therefore, this paper mainly focuses on the ZVT cells. In the ZVT converters,

Manuscript received July 24, 2024; revised September 14, 2024; accepted June 01, 2025. Date of publication September 30, 2025; date of current version June 20, 2025. This work was supported in part by National Nature Science Foundation of China under the grant U22B200134 and the 111 Project of China under the grant B17016. (*Corresponding author: Yong Li.*)

J. Zhang, Y. Li, B. Zhao, and Y. Zhang are with the College of Electrical and Information Engineering, Hunan University, Changsha 410082, China (e-mail: yongli@hnu.edu.cn; zj0711@hnu.edu.cn; bingzhao@hnu.edu.cn; yuhangzhang@hnu.edu.cn).

J. Wan and F. Liu are with the School of Automation, Central South University, Changsha 410083, China (e-mail: wanjianghu@csu.edu.cn; csuliufang@csu.edu.cn).

Digital Object Identifier 10.24295/CPSSTPEA.2025.00022

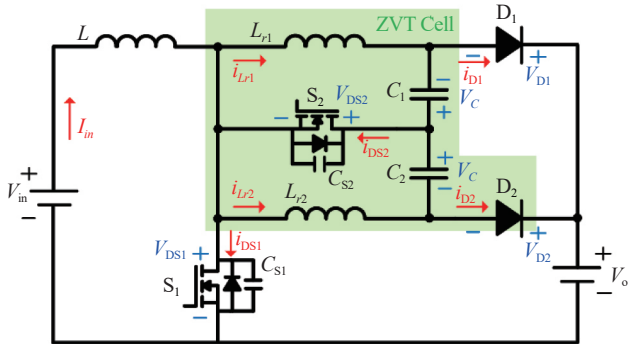

Fig. 1. Boost converter with the Proposed ZVT cell.

the auxiliary circuit consists of active switches and passive elements. The converter proposed in [10] achieves complete ZVS turn ON of the main switch and ZCS turn OFF of the main diode. However, a major drawback is that soft switching is realized with resonant technique, which requires additional resonant component. Besides, the auxiliary circuit will suffer high conduction losses and the auxiliary switch still suffers switching loss even it is turned ON under ZCS condition, which reduces the overall converter efficiency. To solve this problem, some researchers proposed increasing the resonant capacitance as a clamping capacitor to reduce the voltage stress and provide better control flexibility of the ZVS converter. The topology in [11] shows the traditional Boost converter with a compound active clamping circuit connected in series with the Boost switch, which provides fully soft switching operation for both main and auxiliary switches. The problem is the auxiliary circuit causes the main switch to operate with a higher peak current stress, which results in the need for a higher current-rated device for the main switch, and an increase in conduction losses. The converter presented in [12] can provide soft switching operation by adding a single auxiliary switch in the step-up operating mode. However, the voltage and current stress of the main switches are higher than the basic bidirectional DC-DC converter. Due to the high voltage and current stress of active clamp converters, its application in high-power situation is limited. The novel approaches have emerged to address these constraints. In [16], the traditional active clamped soft switching topology with a current transfer circuit composed of a diode and an auxiliary inductor is proposed to decrease the current stress, clamping voltage and duty loss. It contributes to high efficiency and reliability of the converter. But the main diode suffers a higher peak voltage stress. In addition, increasing capacitors of parallel switches can reduce the turn-OFF loss, but it increases the circulation energy during the resonant process. Several ZVT cells introduced in [20]–[21], provide fully soft switching operation for all of the semiconductor devices of the proposed ZVT Boost converter. However, the peak voltage of the auxiliary diode is twice of the output voltage due to the ringing cause by the resonance between the auxiliary inductor and the junction capacitor of the auxiliary diodes, which results in higher cost and conduction losses, and makes the converter unrealizable in high output voltage application.

From the brief overview mentioned above, it can be seen that the previously presented ZVT cells have at least one of the following drawbacks.

1) Extra voltage and current stresses on either the main switch or the auxiliary switch aggravated as well as the losses the auxiliary component.

2) An auxiliary switch operating at ZCS turn ON condition, which will lead to the nonnegligible switching loss.

3) Auxiliary circuit has a high component count.

4) Online calculation is required to achieve ZVS turn ON.

According to the reliability design considerations, some other design considerations such as the number of components, voltage and current stresses, and soft switching conditions must be considered to select the proper ZVT cell. The aim of this paper is to present a single switch auxiliary circuit, which can be applied to all of the basic NPDCs, including Buck/Boost, Buck-Boost, SEPIC, and Cuk to provide fully soft switching operation while the continuous current at input voltage is maintained. The proposed Boost converter with current transfer circuit effectively addresses the previously mentioned issues: It provides the soft switching condition for all the semiconductor devices, maintains an acceptable component count in the proposed ZVT cell, allows control of the main switch and auxiliary switch using a pair of completely pulse width modulation signals with appropriate deadtime, and only introduces low voltage stress without increasing current stress on semiconductor devices. By reducing the voltage and current stress on the main switch, the proposed ZVT cell contributes to extending the life of the power switch, which is significant advantage in reliability-critical applications. Furthermore, the heat is distributed among the main components and the auxiliary components, which relieves the thermal stress of the switching devices. The operation of the proposed Boost converter is discussed in detail at section II and general guidelines for the design is given at section III. The feasibility of the proposed converter is confirmed by experimental results.

II. Circuit Theoretical Operation of Proposed Converter

The proposed Boost converter is illustrated in Fig. 1 and is comprised of a main switch S_1 and an auxiliary switch S_2, auxiliary capacitors C_1 and C_2, filter inductor L and two auxiliary inductors L_{r1} and L_{r2}. C_{S1} and C_{S2} represent the parasitic capacitors of the main switch S_1 and auxiliary switch S_2, respectively. Before the main switch is turned ON, the auxiliary switch is ON-state to ensure the auxiliary capacitor voltage causes current through the auxiliary inductor to reverse. The reverse current is transferred by the auxiliary diode. It will not increase the current stress on the main diode. When the auxiliary switch S_2 is turned off, the parasitic capacitor C_{S1} resonates with the auxiliary inductor L_{r1} and L_{r2} until the body diode of the main switch turns ON, which contributes to achieving ZVS turn ON condition of the main switch. While the auxiliary inductor ensures ZCS operation of the main and auxiliary diode by limiting di/dt at the transition the parasitic capacitor reduces turn-

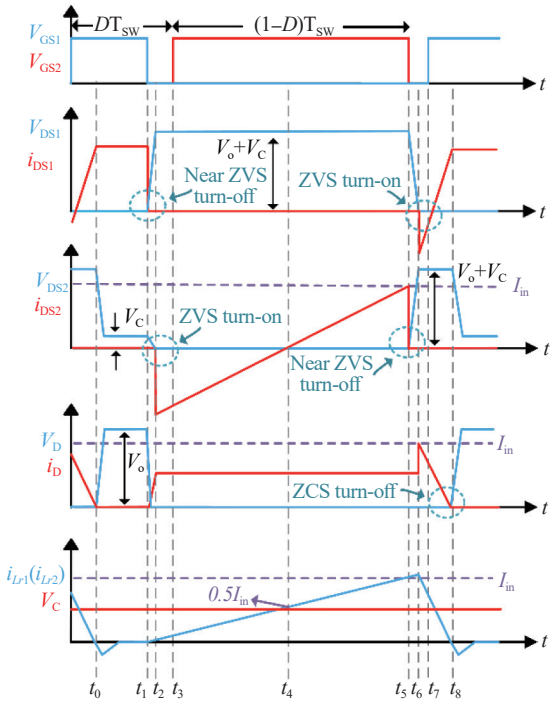

Fig. 2. Theoretical waveforms of the proposed converter.

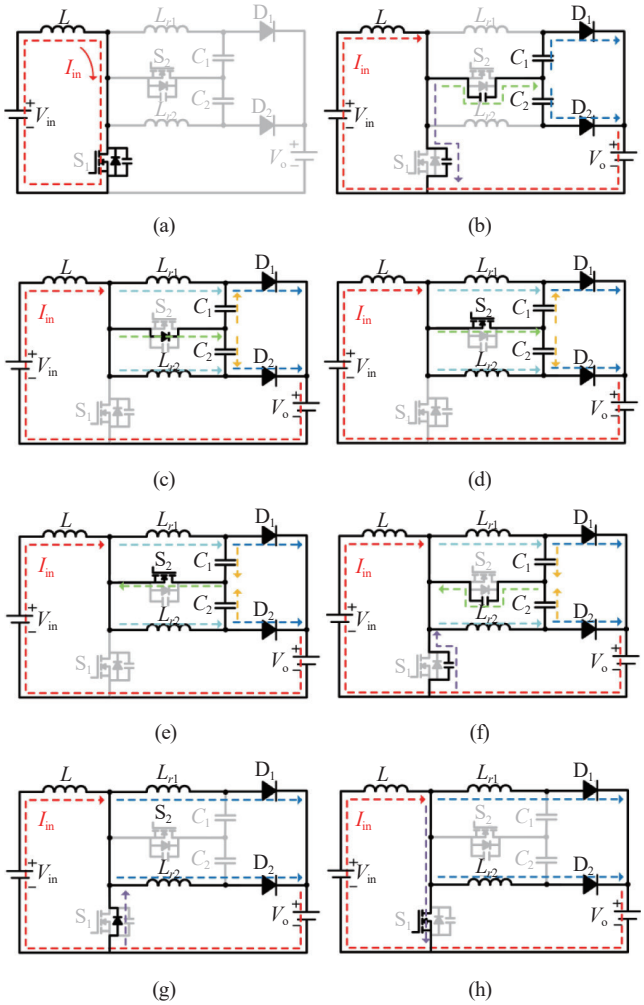

Fig. 3. Equivalent circuits of the operating modes (a) Mode 0. (b) Mode 1. (c) Mode 2. (d) Mode 3. (e) Mode 4. (f) Mode 5. (g) Mode 6. (h) Mode 7.

OFF losses of the switches.

For the sake of simplicity of the operation analysis of the converter, the following assumption are made: the input inductor L, the auxiliary capacitors C_1 and C_2 are large enough to maintain the constant input current and voltage in a switching period. Furthermore, the converter is assumed to be operating under steady-state condition and all semiconductor elements are considered ideal. There are 8 operating modes in one switching cycle, the key waveforms and the equivalent circuits for each mode are shown in Figs. 2 and 3, respectively. The explanation for each operating mode is given as follows:

Mode 0 (t_0-t_1) [see Fig. 3(a)]: In this mode, the main switch S_1 is conducting the input current, and other semiconductor devices are in the OFF-state. Thus, the input inductor L is being linearly charged by V_{in}. The converter is operating as normal ON-state of the traditional Boost converter. This mode ends when the main switch S_1 is turned off at time $t = t_1$.The current through input inductor can be expressed as

$$i_L(t) = i_L(t_0) + V_{in}t / L \tag{1}$$

$$i_L(t_0) = I_{in} - (DV_{in} / 2Lf_s) \tag{2}$$

Mode 1 (t_1-t_2) [see Fig. 3(b)]: At t_1, the main switch S_1 is turned OFF, two diodes D_1 and D_2 are turned ON under ZVS condition. Then, the parasitic capacitors C_{S1}, C_1, and C_2 are charged, while the parasitic capacitors C_{S2} is discharged by the input current I_{in}. Because the parasitic capacitors C_{S1} and C_{S2} have charging process, turn-off losses are minimal in this converter. If additional auxiliary capacitors are used, C_{S1} and C_{S2} will minimize the slope of the capacitor voltage to further reduce the turn-OFF losses. This mode ends when C_{S2} voltage drops to zero. The current through two diodes and the time duration of this mode can be obtained by

$$i_{D1}(t) = i_{D2}(t) = 0.5I_{in} \tag{3}$$

$$t_2 - t_1 = V_C C_{S2} / I_{in} \tag{4}$$

where V_C is the voltage of the auxiliary capacitor C_1 and C_2.

Mode 2 (t_2-t_3) [see Fig. 3(c)]: This mode begins when the body diode of the auxiliary switch S_2 begins to conduct and the main switch S_1 voltage is clamped at V_o+V_C. Then, the L_{r1} and C_1, L_{r2} and C_2 start to resonate. And the auxiliary inductor L_{r1} and L_{r2} voltage is equal to the clamp capacitor voltage (V_C). Therefore, the current through L_{r1} and L_{r2} increases, which leads the current through S_2 (i_{DS2}) to decrease according to Kirchoff's laws. Power is being transferred from V_{in} to V_o. In this mode, the current through two diodes is still $0.5I_{in}$. The voltage C_1, C_2 (V_C), and S_1 (V_{DS1}), the current through L_{r1}, L_{r2} (i_{Lr1}), and S_2 (i_{DS2}) can be expressed, respectively, as follows:

$$i_{Lr1}(t) = i_{Lr2}(t) = V_C(t - t_2) / L_{r1} \quad (5)$$

$$i_{DS2}(t) = I_{in} - i_{Lr1}(t) - i_{Lr2}(t) \quad (6)$$

$$V_C(t) = L_{r1} i_{Lr1}(t) / (t - t_2) \quad (7)$$

$$V_{DS1}(t) = V_o + V_C(t) \quad (8)$$

Mode 3 (t_3-t_4) [see Fig. 3(d)]: At t_3, S_2 is turned ON under ZVS due to the conduction of body diode D_{S2}. The current through D_{S2} continues to decrease as (6). This mode ends when the current through D_{S2} drops to zero. This time duration can be obtained by

$$t_4 - t_3 = (0.5I_{in} - i_{Lr1}(t_3))L_{r1} / V_C \quad (9)$$

Mode 4 (t_4-t_5) [see Fig. 3(e)]: In this mode, the current through auxiliary inductor L_{r1} and L_{r2} increase with the same slope as (5). In order to have sufficient energy to completely discharge the parasitic capacitors C_{S1} and achieve ZVS condition for S_1, the current through S_2 increases in the reverse direction. This reverse current loop consists of the auxiliary switch S_2, the auxiliary inductor L_{r1} (L_{r2}) and the auxiliary capacitor C_1 (C_2). The current through two diodes is still $0.5I_{in}$. And the power is transferred from the input source to the output load continues in a similar manner as in the previous mode. This mode ends when the S_2 is turned OFF. The current $i_{Lr1}(t)$, $i_{Lr2}(t)$ and $i_{DS2}(t)$ can be expressed as

$$i_{Lr1}(t_4) + i_{Lr2}(t_4) = I_{in} \quad (10)$$

$$i_{Lr1}(t_5) + i_{Lr2}(t_5) = I_{in} \quad (11)$$

$$i_{DS2}(t) = i_{Lr1}(t) + i_{Lr2}(t) - I_{in} \quad (12)$$

Mode 5 (t_5-t_6) [see Fig. 3(f)]: At the beginning of this mode, S_2 is turned OFF and turn-OFF losses are minimal in this converter. The parasitic capacitors C_{S1} is discharged through a resonance with the auxiliary inductor L_{r1} and L_{r2}, C_{S2} is charged until the auxiliary switch S_2 voltage is clamped at $V_o + V_C$. When the parasitic capacitor C_{S1} voltage becomes zero, this mode ends. The current through L_{r1} and L_{r2} experience an increase, the duration of this time interval is relatively short, so the increase in current can be disregarded. From (5), the peak current through L_{r1} and two diodes can be obtained at time $t = t_6$ by

$$i_{Lr1}(t_6) = V_C(t_6 - t_2) / L_{r1} \quad (13)$$

$$i_{D1}(t_6) = i_{D2}(t_6) / I_{in} \quad (14)$$

Mode 6 (t_6 - t_7) [see Fig. 3(g)]: At t_6, the body diode of S_1 (D_{S1}) begins to conduct. Thus, S_1 can be turned ON under ZVS condition. Then, the current through L_{r1} and L_{r2} linearly decreases in the reverse direction, which leads the current through D_{S1}, D_1, and D_2 to decrease. In this mode, the current through L_{r1} and L_{r2} behaves as follows:

$$i_{Lr1}(t) = i_{Lr2}(t) = - V_o(t - t_6) / L_{r1} \quad (15)$$

$$i_{DS1}(t) = I_{in} - i_{Lr1}(t) - i_{Lr2}(t) \quad (16)$$

The time duration of the current through S_1 reaches to zero can be calculated by

$$t - t_6 = (i_{Lr1}(t_6) - 0.5I_{in})L_{r1} / V_o \quad (17)$$

In this time duration, S_1 can be turned-ON under ZVS.

Mode 7 (t_7-t_8) [see Fig. 3(h)]: At t_7, the main switch S_1 is turned on under ZVS condition. The current through L_{r1} and L_{r2} decrease with the same slope as (15), which causes the current through S_1 to increase and the current through D_1 and D_2 to decrease. When the S_1 current reaches I_{in}, D_1 and D_2 are turned OFF under ZCS and this mode ends. The current through D_1 and D_2 are obtained as follows:

$$i_{D1}(t) = i_{Lr1}(t) \quad (18)$$

The time duration of this mode can be calculated approximately as

$$t_8 - t_7 = i_{Lr1}(t_7)L_{r1} / V_o \quad (19)$$

After this mode, a next switching cycle begins and the main switch S_1 conducts current like the normal ON-state of the traditional Boost converter.

From the above analysis of the Boost converter with the proposed ZVT cell, all switches can be turned on under ZVS condition and all diodes are turned off under ZCS condition which alleviate the reverse recovery problem. The auxiliary diode and the main diode operate in the same state, they can effectively distribute and share the current stress, thereby leading to a decrease in heat generation and temperature rise of each device. According to (8) and (14), the maximum voltage stress and current stress of switches is V_o+V_C and input current I_{in}, respectively.

III. Design Considerations

A. Auxiliary Circuit Design

The proposed ZVT cell is designed to achieve soft switching operation of the main and auxiliary switch, which also results in soft switching operation of all diodes. According to the operating mode of the proposed Boost converter, these two diode branches are in same operational states. If there is a disparity in the values of L_{r1} and L_{r2}, it results in unequal partitioning of energy storage among the two inductors, potentially causing uneven current distribution across the two diode branches. Similarly, if C_1 and C_2 are not equal, there will be an imbalance in the energy storage and release dynamics of the resonant network. Although this situation will not affect the soft switching conditions of the switch, only the voltage and current stress of the power device. Considering the stability and reliability of

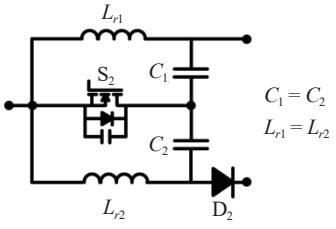

Fig. 4. Simplified equivalent of proposed ZVS cell.

the device, the auxiliary inductors L_{r1} and L_{r2} are designed to be of equal values, while the auxiliary capacitors C_1 and C_2 are also matched. The equivalent circuits of the proposed ZVT cell according these conditions is shown in Fig. 4. Due to simple structure of the auxiliary circuit, only auxiliary inductors L_{r1} and auxiliary capacitor C_1 need to be designed.

B. Soft Switching Condition

In the operating modes, before the main switch S_1 is turned on, the current through L_{r1} and L_{r2} discharge the parasitic capacitor C_{S1} until the body diode conducts. Hence, the main switch can be turned ON under ZVS condition. To guarantee soft switching condition for the main switch, the auxiliary inductance energy has to be greater than the parasitic capacitor energy. The soft switching condition is as follows:

$$L_{r1}i_{Lr1}^2(t_6) + L_{r2}i_{Lr2}^2(t_6) > C_{S1}(V_o + V_C)^2 \tag{20}$$

where V_C is the C_1 and C_2 voltage in each operating mode. When the main switch S_1 voltage drops to zero, S_1 achieves ZVS turned-ON condition. Before the current through S_1 decreases to zero, the main switch S_1 is in a ZVS state. Based on the Kirchoff's law, when the current through S_1 drops to zero means the current through auxiliary inductor drops to $0.5I_{in}$. At t_5, the auxiliary switch S_2 is turned OFF, and the time interval of S_1 ZVS turned-ON condition can be followed by

$$t - t_5 = (i_{Lr1}(t_5) - 0.5I_{in})\, L_{r1} / V_C \tag{21}$$

After the main switch S_1 is turned OFF, the body diode of the auxiliary switch S_2 is conducting. The time interval when the current through D_{S2} drops to zero can be calculated as

$$t_4 - t_2 = L_{r1}I_{in} / V_C \tag{22}$$

In this time interval, the auxiliary switch S_2 can be turned ON under ZVS condition. While the main switch and the auxiliary switch are turned OFF under nearly ZVS due to their parasitic capacitor. Furthermore, due to the addition of two auxiliary inductors, all diodes are turned OFF under ZCS with no limitation which alleviate the reverse recovery problem, which effectively suppressed the switching losses in the proposed converter.

C. Auxiliary Capacitor Design

Based on the Ampere-second balance of the auxiliary capacitor C_1 and C_2, the positive and negative areas under the current waveform is exactly equal. Also, the current through C_1 and C_2 slope in the charging and discharging states is the same. Hence, the negative and positive peak current through the auxiliary capacitor is equal. As a result, the C_1 and C_2 voltage is obtained as follows:

$$V_C = L_{r1}I_{in} / (1 - D)T_{sw} \tag{23}$$

where $I_{in} = P_{in} / V_{in}$, T_{sw} and P_{in} are the switching period and the input power, respectively. During the operation of the converter, the voltage fluctuation on the auxiliary capacitor C_1 which is caused by the periodic charging and discharging of S_2 current (i_{DS2}) should be minimized. The voltage fluctuation can be represented as follows:

$$\Delta V_C = (1 - D)T_{sw}I_{in} / 4C_1 \tag{24}$$

Assuming that $\Delta V_C \leqslant \alpha V_C$, then the lower limit of C_1 can be calculated as

$$C_1 \geqslant (1 - D)^2 T_{sw}^2 / 4\alpha L_{r1} \tag{25}$$

Thus, the auxiliary capacitor C_1 and C_2 can be selected based on the restriction of (25).

D. Auxiliary Inductor Design

From the previous analysis, the value of auxiliary inductor L_{r1} is desired for soft-switching range of the main switches at turn ON condition based on (20), while the larger value of L_{r1} would increase the auxiliary capacitor voltage according to (23), which will increase the active switches voltage stress. Moreover, after the main switch is turned ON, for significant reduction of the reverse recovery loss of two diodes, decay time of the auxiliary inductor current should be greater than three times the reverse recovery time t_{rr} of the diode D_1 (D_2) [10]–[22]. Consequently, the value of L_{r1} is also restricted by

$$L_{r1} > 3t_{rr}V_o / i_{Lr1}(t_6) \tag{26}$$

Thus, there is a tradeoff between soft switching range and the switches voltage stress when selecting the auxiliary inductor L_{r1}.

E. Design Example

In this section, a design example of the proposed ZVT cell used in the traditional Boost converter is given. The specifications of the proposed Boost converter are shown in Table I.

TABLE I
DESIGN SPECIFICATION OF THE PROPOSED CONVERTER

Symbol	Parameter	Value
V_{in}	Input voltage	250 V
V_o	Output voltage	360 V
P	Rated power	2 kW
f_s	Switching frequency	100 kHz

TABLE II
COMPONENT RATINGS AND SELECTED DEVICES

Components		Ratings	Selected devices
Main switch		380 V, 8 A	Infineon: IPW60R037P7
Aux. switch			650 V, 76 A, $C_{oss(er)}$=156 pF, $R_{ds(on)}$= 30 mΩ
main diode		380 V, 4 A	SMC: SDURK2060
Aux. diode			600 V, 20 A, V_F = 1.5 V, t_{rr} = 28 ns
Input inductor		I_{ave} = 8 A I_{peak} = 8.8 A	L = 700 μH, I_{sat} = 15 A
Aux. inductor	L_{r1} L_{r2}	I_{ave} = 8 A I_{peak} = 8.8 A	L_{r1} = L_{r2} =10 μH, I_{sat} = 15 A
Aux. capacitor	C_1 C_2	380 V, 8 A	C_1 = C_2 = 10 μF, V_{rat} = 1000 V

Input current and output voltage are assumed to be constant current source and voltage source, respectively; for this reason, the design of input inductor and output capacitor is not taken into consideration. Therefore, a detailed introduction was provided to the selection of components used in the proposed ZVT cell as follows.

1) *Turn-OFF time of the auxiliary switch t_{off}*: The turn-off time is the sum of the turn-off delay time and fall time. In general, high frequency switches need to have a short turn off time to achieve efficient conversion and stable operation. Based on the selected switching frequency and (19), $t_{off} < 200$ ns is determined. If t_{off} is too long, this makes the ZVS turn-ON of the main switch fail at light load and the conduction loss on the ZVT cell will be high. For this reason, the sum of turn-off delay time and turn-off time of the selected switching device is t_{off} = 94 ns in this paper.

2) *Dead time of the main and auxiliary switch*: The dead time of the main switch should be less than this time interval that the soft switch condition meets, while being greater than the power switch turn off time (t_{off} = 94 ns). If the dead time is too long, it will lead to a loss of duty cycle. Considering the above factors, a dead time of 150 ns was ultimately selected.

3) *Auxiliary inductor*: Based on the selection of the main switch and diode, the minimum value of the auxiliary inductor is determined from (20) and (26) as $L_{r1} > 3.8$ μH. As a result, $L_{r1} = L_{r2} = 10$ μH is selected in this paper. According to the decided value of the auxiliary inductance, the real value of V_C can be calculated approximately from (23) as V_C =11.5 V.

4) *Auxiliary capacitor*: In order to calculate the auxiliary capacitance, ΔV_C is selected to be less than 15% of the auxiliary capacitor voltage. Based on the (25), the auxiliary capacitance is selected as $C_1 > 8.2$ μF. Therefore, $C_1 = C_2 = 10$ μF is decided in this paper. According to the selected value of the auxiliary capacitance, the real value of ΔV_C can be calculated from (24) as ΔV_C = 1.4 V.

5) *Voltage and current stresses*: according to the current paths of eight operation modes in Fig. 3, the voltage stress of S_1/S_2, D_1/D_2 can be obtained as V_o+V_C. When the input voltage is changed and the output voltage is fixed. Moreover, the current stress is presented below. When the charge conversion law is applied on the auxiliary capacitor $C_1(C_2)$, the relationship can obtain

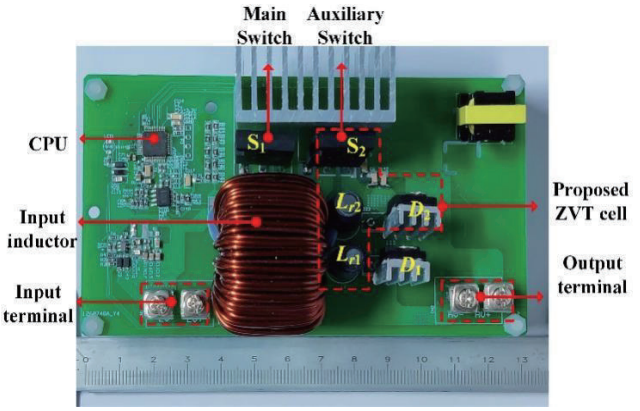

Fig. 5. Photograph of the 2-kW laboratory prototype.

$$\int_{t_1}^{t_4}[\frac{V_o}{2R_o}-i_{Lr1}(t)]\,dt=\int_{t_4}^{t_8}[i_{Lr1}(t)-\frac{V_o}{2R_o}]\,dt \tag{27}$$

where R_o is the load resistor.

Hence, the peak value I_p of $i_{Lr1}(t)$ can be calculated as

$$I_p=\frac{V_o}{R_o(1-D)}=I_{in} \tag{28}$$

From that, it is known that the current stress on the two switches and two diodes is I_{in}. Finally, based on the calculations mentioned above, the current ratings and selected devices for the 2-kW prototype of the proposed converter are listed in Table II.

IV. EXPERIMENTAL VERIFICATION

Based on the selected components listed in Table II, a 2-kW laboratory prototype of the traditional Boost converter with the proposed ZVT cell, controlled by STM32F303, has been built and tested. A photograph of the laboratory prototype is shown in the Fig. 5. The experimental results of the proposed soft switching Boost converter are shown in Figs. 6 and 7.

As can be seen from Fig. 6(a), before the main switch and auxiliary switch are fully turned ON in each operating mode, their body diode is conducting and consequently ZVS operation at turn ON is achieved. Moreover, due to the parasitic capacitors, the switches can be turned OFF under nearly ZVS condition, which mitigate the switching loss. As shown from the Fig. 6(b), when the current through the diodes D_1 and D_2 reduce to zero, the reverse recovery process is completed rapidly. The presence of parasitic capacitance in the diode can store a small amount of energy, which will cause the resonance between parasitic capacitor and the auxiliary inductor, there is still a small reverse recovery current value. Due to the auxiliary inductor L_{r1} and L_{r2}, the main switch is not affected by the reverse recovery process of the diode. When the main switch

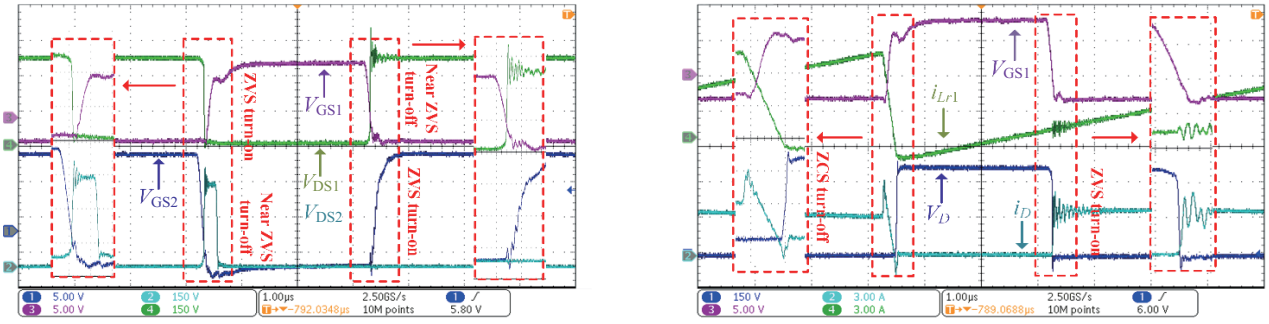

(a) (b)

Fig. 6. Experimental waveforms (a) V_{GS1}, V_{DS1}, V_{GS2}, V_{DS2}. (b) V_{GS1}, i_{Lr1}, V_D, i_D.

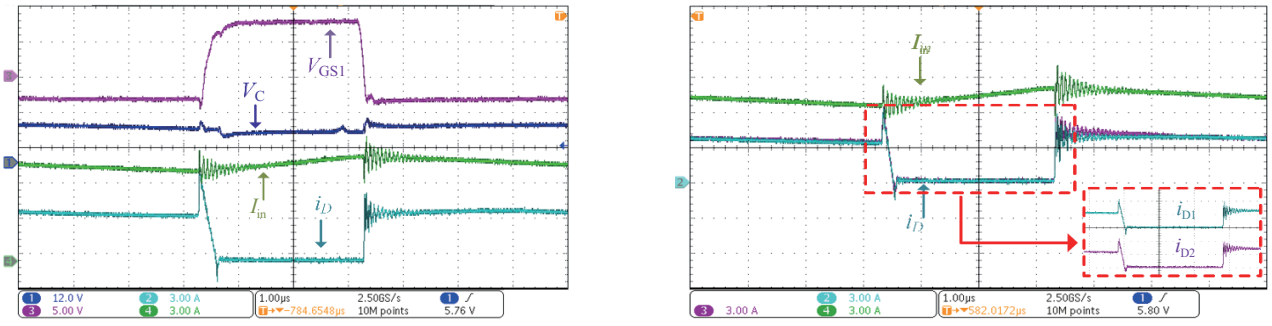

(a) (b)

Fig. 7. Experimental waveforms (a) V_{GS1}, V_C, I_{in}, i_D. (b) I_{in}, i_{D1}, i_{D2}.

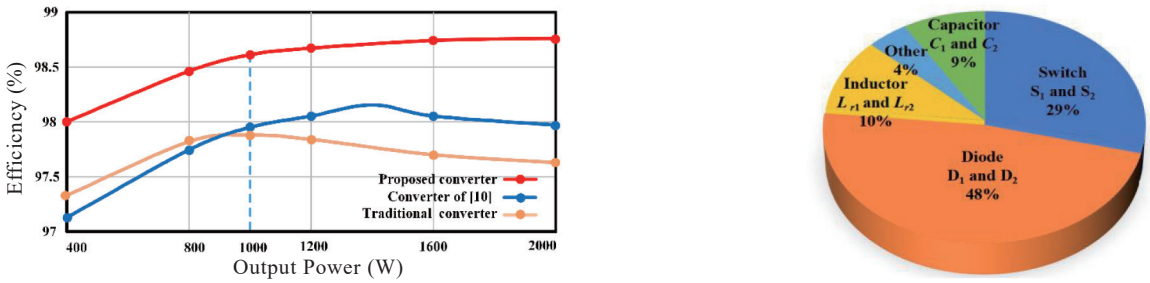

(a) (b)

Fig. 8. (a) Efficiency comparison between the proposed converter, [10], and traditional Boost converter. (b) Power loss breakdown of the protype at full load.

S_1 is turned off, the diodes D_1 and D_2 naturally conducts when V_D decreases to zero, avoiding the voltage resonant peak and the commutation loss during switching. According to the experimental findings, the current through the auxiliary inductor $i_{Lr1}(t)$ continues to increase when the main switches S_1 is turned on. The reason is that the parasitic capacitors of the auxiliary switch S_2 cannot be overlooked in the operation the proposed converter. According to the characteristics of its parasitic capacitance, the terminal voltage ratio is inversely proportional to the parasitic capacitance value. When its terminal voltage approaches zero, the value of parasitic capacitance is large, which will resonate process, the with the auxiliary inductor L_{r1} and L_{r2}. Then, the auxiliary inductor resonates with the auxiliary capacitor.

In Fig. 7(a), the measured value of the auxiliary capacitor voltage is about 12 V and during the charging and discharging voltage fluctuation on the auxiliary capacitor is about 1 V, which corresponds with the theoretical values. From Fig. 7(b), it can be seen that the maximum current through diode D_1 and D_2 are I_{in}. From the experiment results, it can be observed that there is minimal extra voltage stress and no extra current stress imposed on the main and auxiliary components. Moreover, the experimental results verified the theoretical analysis.

Fig. 8(a) shows the efficiencies curve of the proposed Boost converter, the counterpart converter in [10] and the traditional hard-switching Boost converter, from which it can be seen that the efficiency of the proposed converter has been improved significantly compared to the hard-switching Boost converter. And the peak efficiency of the proposed converter can reach 98.76% under full-load condition. And the power loss break-

TABLE III
PERFORMANCE COMPARISON OF PROPOSED BOOST CONVERTER AND OTHER SOFT-SWITCHED BOOST CONVERTER

Topology	S*	L	C	Voltage stress*	Current stress*	Soft switching condition(on/off)		Switch Frequency	Power Rating	Power Efficiency
						Main switch	Auxiliary switch			
[11]	1	1	3	V_o+V_C	I_{in}	ZVS/ZVS	ZVS/ZVS	100 kHz	100 W	97.8%
[12]	2	2	1	V_o+V_C	$I_{in}+V_C/Z_C$	ZVS/ZCS	ZCS/ZCS	100 kHz	250 W	98%
[13]	2	2	1	$DV_o/3$	$3I_{in}$	ZVS/ZVS	ZCS/ZCS	100 kHz	250 W	97.9%
[14]	1	2	2	V_o	I_{in}	ZVS/ZVS	ZCS/ZCS	100 kHz	300 W	98.1%
[15]	5	2	1	V_o	I_{in}	ZVS/ZCS	ZCS/ZVS	100 kHz	300 W	98.7%
[16]	2	2	3	V_o+V_C	I_{in}	ZVS/ZVS	ZVS/ZVS	40 kHz	1.2 kW	97.5%
[21]	5	2	2	V_o	I_{in}	ZVS/ZVS	ZCS/ZVS	100 kHz	2 kW	97.4%
[10]	4	1	1	V_o	$I_{in}+V_C(C_{S1}/L_{r1})^{1/2}$	ZVS/near ZVS	ZCS/near ZVS	100 kHz	2 kW	98.2%
Proposed	2	2	2	V_o+V_c	I_{in}	ZVS/near ZVS	ZVS/near ZVS	100 kHz	2 kW	98.76%

S*: With additional diode Voltage stress*, Current stress*: The voltage and current stress on S_1/S_2, D_1/D_2.

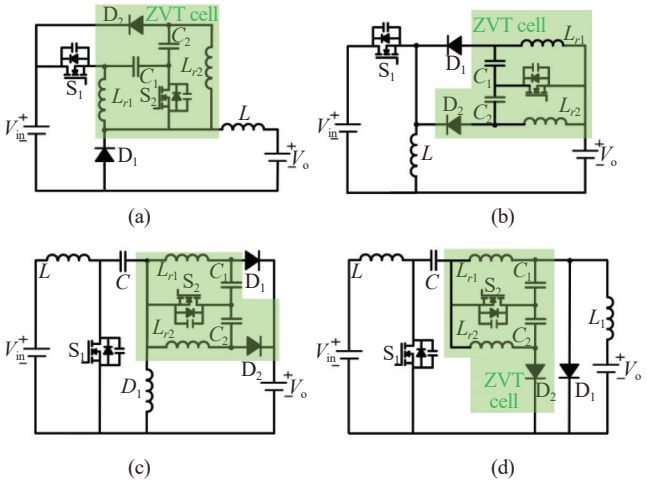

Fig. 9. Other DC-DC converters with the proposed ZVT cell. (a) Buck. (b) Buck-Boost. (c) SEPIC. (d) Cuk.

down is show in Fig. 8(b). It is observed that the power loss due to switches, diodes, inductors and capacitors are 29%, 48%, 10%, and 9%, respectively.

A performance comparison of the proposed Boost converter and some of the well-known ZVT Boost converter is summarized in Table III. As observed, the proposed converter can provide ZVS condition for all active switches and ZCS condition for all diodes. In comparison, it is noted that the converters referenced in [10], [12]−[15], [21] are unable to achieve ZVS condition for the auxiliary switch, which still suffers switching losses. Therefore, the proposed converter can achieve enhanced efficiency when compared to these referenced converters. The converter of [11] can achieve ZVS condition for the main and auxiliary switches. However, the maximum current stress is twice the input current, which results in the need for a higher current-rated device for the main switch, and an increase in conduction losses. The converter of [16] also can achieve ZVS condition for the main and auxiliary switches, but the main diode experiences a peak voltage that is twice the output voltage due to ringing caused by the resonance between the auxiliary inductor and the junction capacitor of the main diode.

V. FAMILY OF THE PROPOSED ZVT CONVERTER

The proposed ZVT cell can be applied to the other family members of NPDCs to provide fully soft switching operation for the switches, which can increase the converters efficiency. The integration of the proposed ZVT cell in the Buck, Buck-Boost, Cuk, and SEPIC converters are shown in Fig. 9, in this family of NPDCs, all active switches and diodes operate under ZVS turn-ON and ZCS turn-OFF, respectively. The design of the auxiliary components and the operational behavior in the other NPDCs remains identical as described in Section III of this paper.

VI. CONCLUSION

A family of non-isolated ZVT DC-DC converter with current transfer circuit was presented in this paper. The family was comprised of Buck/Boost, Buck-Boost, SEPIC, and Cuk. The proposed active clamp ZVT cell provides ZVS turn-ON/near ZVS turn-OFF for all switches and ZCS turn-OFF for all diodes. It effectively alleviates the reverse recovery problem and improves the overall efficiency of the Boost converter. Moreover, the proposed ZVT cell introduces low voltage stress while avoiding additional current stress on the main or auxiliary components. The operation principles and designed producers of the traditional Boost converter with the proposed ZVT cell are presented and verified by the 2-kW laboratory prototype operating at 100 kHz, which was consistent with the theoretical analysis. The peak efficiency of the proposed converter is measured at 98.76% in the experimental results. The simplified implementations of the ZVT cell will be explored that reduces the circuit complexity while retaining the key advantages of ZVS operation in the future work.

References

[1] C. -M. Lai, Y. -H. Cheng, M. -H. Hsieh, and Y. -C. Lin, "Development of a bidirectional DC/DC converter with dual-battery energy storage for hybrid electric vehicle system," in *IEEE Transactions on Vehicular Technology*, vol. 67, no. 2, pp. 1036–1052, Feb. 2018.

[2] L. F. Costa and M. Liserre, "Failure analysis of the dc-dc converter: a comprehensive survey of faults and solutions for improving reliability," in *IEEE Power Electronics Magazine*, vol. 5, no. 4, pp. 42–51, Dec. 2018.

[3] Y. Chen and D. Xu, "Review of soft-switching topologies for single-phase photovoltaic inverters," in *IEEE Transactions on Power Electronics*, vol. 37, no. 2, pp. 1926–1944, Feb. 2022.

[4] R. R. Khorasani, H. M. Jazi, A. K. -Sadigh, N. R. Chaushuri, M. Shaneh, N. Nourieh, E. Adib, and P. Wheeler, "ZVT high step-up Boost converter with wide input voltage and wide output power for renewable energy spplications," in *IEEE Journal of Emerging and Selected Topics in Power Electronics*, vol. 10, no. 5, pp. 6057–6069, Oct. 2022.

[5] T. Shao, P. Zheng, H. Li, Y. Xue, J. Wang, and T. Q. Zheng, "A low-stress zero-current switching technique for power converters," in *IEEE Transactions on Power Electronics*, vol. 33, no. 6, pp. 5087–5096, Jun. 2018.

[6] S. Kulasekaran and R. Ayyanar, "A 500-kHz, 3.3-kW power factor correction circuit with low-loss auxiliary ZVT circuit," in *IEEE Transactions on Power Electronics*, vol. 33, no. 6, pp. 4783–4795, Jun. 2018.

[7] C. Nan, R. Ayyanar, and Y. Xi, "A 2.2-MHz active-clamp Buck converter for automotive applications," in *IEEE Transactions on Power Electronics*, vol. 33, no. 1, pp. 460–472, Jan. 2018.

[8] J. Wan, F. Liu, K. -Z. Liu, and Y. Li, "An efficient soft-switching Buck converter with parasitic resonance suppression in auxiliary circuit," in *IEEE Transactions on Industrial Electronics*, vol. 70, no. 2, pp. 1367–1377, Feb. 2023.

[9] F. Liu, J. Wan, L. Jiang, Y. Li, and K. -Z. Liu, "A new soft-switching AC–DC converter based on coupled inductors for onboard charging applications," in *IEEE Transactions on Power Electronics*, vol. 38, no. 3, pp. 3433–3443, Mar. 2023.

[10] H. N. Tran and S. Choi, "A family of ZVT DC–DC converters with low-voltage ringing," in *IEEE Transactions on Power Electronics*, vol. 35, no. 1, pp. 59–69, Jan. 2020.

[11] M. Packnezhad and H. Farzanehfard, "Family of nonisolated fully soft switched bidirectional converters with single switch auxiliary circuit," in *IEEE Transactions on Industrial Electronics*, vol. 69, no. 12, pp. 12720–12727, Dec. 2022.

[12] S. Rahimi, M. Rezvanyvardom, and A. Mirzaei, "A fully soft-switched bidirectional DC–DC converter with only one auxiliary switch," in *IEEE Transactions on Industrial Electronics*, vol. 66, no. 8, pp. 5939–5947, Aug. 2019.

[13] M. R. Mohammadi and H. Farzanehfard, "A new family of zero-voltage-transition nonisolated bidirectional converters with simple auxiliary circuit," in *IEEE Transactions on Industrial Electronics*, vol. 63, no. 3, pp. 1519–1527, Mar. 2016.

[14] M. Packnezhad and H. Farzanehfard, "Fully soft switched bidirectional Buck–Boost converter with improved voltage conversion ratio and single auxiliary switch," in *IEEE Transactions on Industrial Electronics*, vol. 71, no. 1, pp. 380–387, Jan. 2024.

[15] B. Akin, "An improved ZVT–ZCT PWM DC–DC Boost converter with increased efficiency," in *IEEE Transactions on Power Electronics*, vol. 29, no. 4, pp. 1919–1926, Apr. 2014.

[16] S. Fan, B. Gong, J. You, L. Sun, and J. Duan "Active clamped ZVS soft switching technology with low voltage and current stress." in *Proceedings of the CSEE*, vol. 41, no. 13, pp. 4616–4627, Jul. 2021.

[17] R. Faraji, L. Ding, T. Rahimi, and M. Kheshti, "Application of soft-switching cell with inherent redundancy properties for enhancing the reliability of Boost-based DC–DC converters," in *IEEE Transactions on Power Electronics*, vol. 36, no. 11, pp. 12342–12354, Nov. 2021.

[18] A. V. J. S. Praneeth and S. S. Williamson, "A zero-voltage, zero-current transition Boost cascaded-by-Buck PFC converter for universal E-transportation charging applications," in *IEEE Journal of Emerging and Selected Topics in Power Electronics*, vol. 10, no. 3, pp. 3273–3283, Jun. 2022.

[19] B. Feng and D. Xu, "1-kW PFC converter with compound active-clamping," in *IEEE Transactions on Power Electronics*, vol. 20, no. 2, pp. 324–331, Mar. 2005.

[20] I. Aksoy, H. Bodur, and A. F. Bakan, "A new ZVT-ZCT-PWM DC–DC converter," in *IEEE Transactions on Power Electronics*, vol. 25, no. 8, pp. 2093–2105, Aug. 2010.

[21] H. Bodur and S. Yildirmaz, "A New ZVT snubber cell for PWM-PFC Boost converter," in *IEEE Transactions on Industrial Electronics*, vol. 64, no. 1, pp. 300–309, Jan. 2017.

[22] W. Huang and G. Moschopoulos, "A new family of zero-voltage-transition PWM converters with dual active auxiliary circuits," in *IEEE Transactions on Power Electronics*, vol. 21, no. 2, pp. 370–379, Mar. 2006.

[23] L. Qin, L. Zhou, W. Hassan, J. L. Soon, M. Tian, and J. Shen, "A family of transformer-less single-switch dual-inductor high voltage gain Boost converters with reduced voltage and current stresses," in *IEEE Transactions on Power Electronics*, vol. 36, no. 5, pp. 5674–5685, May 2021.

[24] X. Yu, J. Su, S. Guo, S. Zhong, Y. Shi, and J. Lai, "Properties and synthesis of lossless snubbers and passive soft-switching PWM converters," in *IEEE Transactions on Power Electronics*, vol. 35, no. 4, pp. 3807–3827, Apr. 2020.

[25] M. R. Mohammadi, H. Farzanehfard, and E. Adib, "Soft-switching bidirectional Buck/Boost converter with a lossless passive snubber," in *IEEE Transactions on Industrial Electronics*, vol. 67, no. 10, pp. 8363–8370, Oct. 2020.

[26] T. Shamsi, M. Delshad, E. Adib, and M. R. Yazdani, "A new simple-structure passive lossless snubber for DC–DC Boost converters," in *IEEE Transactions on Industrial Electronics*, vol. 68, no. 3, pp. 2207–2214, Mar. 2021.

Jie Zhang was born in Chongqing, China, in 1999. He received B.S. degree from the College of Electrical and Information Engineering, Hunan University, Changsha, China, in 2022. He is currently working the M.S. degree in Hunan University, Changsha, China. His research interests include active power decoupling control and bidirectional DC/DC converters.

Yong Li was born in Henan, China, in 1982. He received the B.Sc. and Ph.D. degrees from the College of Electrical and Information Engineering, Hunan University, Changsha, China, in 2004 and 2011, respectively, and the Ph.D. degree from the TU Dortmund University, Dortmund, Germany, in 2012. Since 2009, he has been a Research Associate with the Institute of Energy Systems, Energy Efficiency, and Energy Economics, TU Dortmund University. Since 2012, he has been a Research Fellow at the University of Queensland, Australia. Since 2014, he has been a Full Professor with the electrical engineering, HNU. His current research interests include AC/DC energy conversion systems, analysis and control of power quality, and HVDC and FACTS technologies.

Jianghu Wan was born in Sichuan, China, in 1991. He received B.S. degree and M.S. degree in control science and engineering in Central South University, Changsha, China, in 2014 and 2017, respectively. He is currently working toward the Ph.D. degree in control science and engineering in Central South University, Changsha, China. His current research interests include bidirectional DC/DC converters, control of three-phrase PWM rectifiers, and soft-switching technology.

Bing Zhao was born in Henan, China, in 1999. He received the B.S. degree from Hunan University, Changsha, China, in 2021. He is currently working toward the M. Sc. degree in the electrical engineering in College of Electrical and Information Engineering, Hunan University, Changsha, China. His research interests include on-board electrical systems in the new energy vehicles, and the control and design of power electronic systems.

Yuhang Zhang was born in Hebei, China, in 1998. He received B.S. degree from the College of Electrical and Information Engineering, Hunan University, Changsha, China, in 2022. He is currently working the M.S. degree in Hunan University, Changsha, China. His research interests include modeling and digital control for bidirectional DC-DC converters.

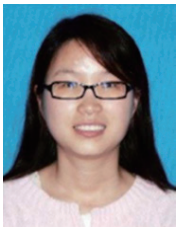

Fang Liu was born in Jiangxi, China, in 1982. She received the B.S. degree from the College of Electric and Information Engineering, Zhengzhou University of Light Industry, Zhengzhou, China, in 2005, and the Ph.D. degree from Waseda University, Tokyo, Japan, in 2011. She has been a Professor with the School of Automation, Central South University, Changsha, China, since 2017. Her main research interests include stability analysis of time-delay system and power system, and robust control of FACTS with wide-area signals.

Power Management With Event-Triggered Predictive Function Control for DC Microgrid Clusters

Sucheng LIU, Taohu ZHOU, Tao HONG, Qianjin ZHANG, Wei FANG, and Xiaodong LIU

***Abstract*—A DC microgrid cluster (DCMGC) is a networked power grid that consists of multiple small-scale DC microgrids (DCMGs), and every single DCMG (sub-grid) can be composed of multiple heterogeneous units, e.g., distributed energy resources like photovoltaic (PV) and wind turbine (WT), energy storage systems (ESS), and local loads. The DCMGC is such a complex network with multiple control objectives that requires control at both system-level and sub-grid level, which suits well with model predictive control (MPC) algorithms. However, the MPC suffers from the high computation burden, especially dealing with complex control plant models like DCMGCs. In this paper, an event-triggered predictive function control (ET-PFC) is proposed for power management of DCMGCs, maintaining excellent control performance of PFC algorithm while saving computing resources in the control process. Further, a universal low-cost microcontroller (STM32) solution is presented for implementation of the ET-PFC scheme and a low-voltage DCMGC laboratory prototype that consists of three DCMGs (six converters) is built to validate the controller implementation by hardware experiment results.**

***Index Terms*—DC microgrid cluster, event-triggered control, predictive function control, power management, stability guarantee.**

I. Introduction

DC microgrids (DCMGs) are localized small-scale power systems that utilize direct current (DC) for distribution, enhancing energy efficiency and integration of renewable energy sources (RESs), energy storage systems (ESSs), and various local loads [1]−[4]. In recent years, DCMGs have been utilized in residential, commercial, industrial, remote, and off-grid areas, as well as data centers and electric vehicle charging stations, etc [5], [6]. A DC microgrid cluster (DCMGC) is an interconnected network of multiple DCMGs that enhance energy sharing, reliability, and resilience across multiple localized power systems [7], [8].

Manuscript received January 03, 2025; revised May 13, 2025 and June 12, 2025; accepted July 10, 2025. Date of publication September 30, 2025; date of current version August 22, 2025. This work was supported in part by National Natural Science Foundation of China under Grant 52277169. (*Corresponding author: Sucheng Liu.*)

All authors are with the Anhui Provincial Key Laboratory of Power Electronics and Motion Control, Anhui University of Technology, Ma'anshan 243032, China (e-mail: liusucheng@ahut.edu.cn; zhoutaohu@163.com; 2635230705@qq.com; zqj1214@ahut.edu.cn; fwei2k@163.com; liuxiaodong@ahut.edu.cn).

Digital Object Identifier 10.24295/CPSSTPEA.2025.00023

Due to the high adoption of power electronic converters for interfacing multiple heterogeneous units including RESs, ESSs, and local loads, DCMGCs are in fact complex networks of higher-order and nonlinear dynamics [9], [10]. Moreover, the control design of DCMGCs usually deals with multiple control objectives across multiple time-scales, e.g., current sharing, voltage restoration, power quality control, and power management, and so forth [11]−[16]. Thus, hierarchical control has been introduced to greatly simplify the control design with multiple objectives for DCMGCs [17]. The hierarchical control in general consists of the local and global control, and assigns the control objectives to each corresponding level with decoupled and elegantly designed fashion. Specifically, the local control consists of primary and secondary controls that is concerned with current sharing and power quality control within each DCMG, while the global control addresses power management of DCMGCs at system-level [18]−[20]. In most cases, the local control for a single DCMG has been well recognized [21], [22], but the power management at global level remains a challenging open problem due to more complex nature of the DCMGCs.

Nowadays, the power management at the global level mainly uses proportional-integral (PI)-based algorithms for different application scenarios of DCMGCs [19]. However, the PI-based algorithms suffer from shortcomings of modeling complexity, parameter tuning, limited optimization, and stability guarantee, and so forth. It is therefore desired to deploy advanced control algorithms like model predictive control (MPC) and intelligent control methods for addressing the shortcomings of linear PI algorithms [23]−[28]. Particularly, the MPC uniquely handles multivariable systems with explicit constraint management, future behavior prediction, and optimal control, offering robustness, flexibility, and adaptability for improved performance in microgrids and complex microgrid clusters [29], [30]. Obviously, MPC need to solve optimization problems in real time to generate control inputs. However, in DCMGCs, the coupled dynamics of multiple microgrids makes the system state change rapidly, which puts severe demands on computational speed and resources [31]. For highly scalable DCMGCs, the computation time of the optimization problem may exceed the allowable control period, resulting in delayed control response, which affects the stability and performance of the system. At this time, how to reduce the computation amount of MPC is particularly important. Among various MPC algorithms, the predictive function control (PFC) is distinguished by its simple control structure, direct set-point tracking, reduced computa-

TABLE I
OVERVIEW OF DIFFERENT CONTROL SCHEMES IN MICROGRIDS

Schemes	Characteristics
PI Control [19]	Simple structure but the control effect of high order nonlinear system is not ideal
MPC [25]	Strong multi-variable processing ability and constraint processing ability but the amount of calculation is huge
PFC [32], [33]	Direct set-point tracking, simple control structure but the computational burden is heavy
ET-MPC [38], [39]	Less computational burden while ensuring performance
Proposed ET-PFC	Simple control structure and low computation resource requirement

tional burden, explicit disturbance rejection, and ease of implementation, making it efficient and robust for real-time control of complex processes like DCMGCs [32]–[34]. Nevertheless, it still costs high computation resources due to online rolling out the optimal command in the implementation of the PFC algorithms for power management of DCMGCs [35]. In fact, it is unnecessary to compute the optimal control sequence during every single control horizon in the MPC when the DCMGCs works in steady-state conditions since the control sequence in the next cycle will remain as before [36], [37]. With this regard, the event-triggered (ET) mechanism is introduced in the MPC control algorithms to substantially reduce the computation burden [31], [38], [39]. In [38], ET-MPC method for power converters is presented and the experiments show that the ET-MPC method can reduce the computational burden and switching actions based on the traditional finite control set MPC (FCS-MPC) while maintaining excellent regulation performance, thereby reducing switching losses. In [39], an integral-type ET mechanism is proposed by incorporating the integral of errors between the actual and predicted state sequences, leading to reduction of average sampling frequency. Similarly, ET control is also used to regulate the bus voltage of hybrid energy storage system (HESS) in microgrids efficiently [31]. In our earlier work [40], the ET-PFC algorithm has been preliminarily verified by MATLAB/Simulink simulations and controller-hardware-in-the-loop results, whereas detailed controller design, stability guarantee, and power hardware-based implementation have yet to be explored.

Table I summarizes the different schemes and their characteristics in microgrids. Followed by previous success of the ET-MPC paradigm, this work attempts to introduce an ET condition to the PFC controller, thereby proposing the ET-PFC of low computation resource requirement for power management of DCMGCs. To this end, a low-cost microcontroller-based implementation of the proposed idea for DCMGCs is presented, and hardware experimental results are given as well for the validation. The main contributions of the work are summarized as follows:

(1) Based on the original PFC scheme, an ET-PFC controller for the power management of DCMGCs is proposed to substantially save the computation resources.

(2) The implementation of the proposed ET-PFC method is achieved with a universal low-cost microcontroller solution.

(3) Unlike most existing validations by simulations or hardware-in-the-loop (HIL) results, a low-voltage DCMGC hardware prototype consisting of three DCMGs (including six DC/DC converters) is built to verify the control implementation by experimental results.

The rest of this paper is organized as follows: First, the principle of hierarchical control and the ET-PFC for DCMGCs is described in Section II. Then, the design of ET-PFC for the DCMGCs is presented in Section III, and exclusion of the Zeno behavior is also discussed. Further, the stability guarantee for the proposed control method of the DCMGC is given in Section IV. The 48 V low-voltage DCMGCs hardware experiment platform that is composed of three DCMGs is presented to verify the control performance of the proposed method in Section V. Conclusions of the work are finally drawn in Section VI.

II. HIERARCHICAL CONTROL FOR DCMGCS

Fig. 1 illustrates a general DCMGC topology which consists of N DCMGs interconnected by tie-lines, and every single DCMG can be composed of RESs including photovoltaic (PV) and wind turbine (WT), battery energy storage systems (BESSs) and a variety of electronic loads acting as constant power load (CPL). In addition, the communication network for the control of the DCMGC is depicted at the top, and both local network and global network use distributed communications and they are connected via the pinning links [41].

According to the structure of the DCMGC, the hierarchical control can be separated into two layers, viz., local control layer that is for a single DCMG, and global control layer for system-level power management of the overall system, which is shown as the block diagram in Fig. 2. In this section, we first discuss the local control, and then propose global control improvements for DCMGC.

A. Local Control for a Single DCMG

The main functions of the local control for a single DCMG cover output voltage regulation for every single DC/DC converter, current sharing among the converters in parallel, and bus voltage restoration, and these are achieved by coordination between the primary control and the secondary control.

Specifically, in primary control, the inner voltage and current loops form the dual-loop control for the output voltage regulation of every single DC/DC converter, and the outer droop control loop performs autonomous current sharing among the converters in parallel. By the output voltage of the converters, the droop control can be expressed as

$$V_{\text{bus}}^{M} = V_{\text{ref}}^{M,i} - i_{\text{o}}^{M,i} \bullet R_{\text{d}}^{M,i} \tag{1}$$

where V_{bus}^{M} is the DC bus voltage, $V_{\text{ref}}^{M,i}$ and $i_{\text{o}}^{M,i}$ denotes the reference output voltage and the output current from converter#i in DCMG#M (M = 1, 2, …, N), and $R_{\text{d}}^{M,i}$ represents the droop

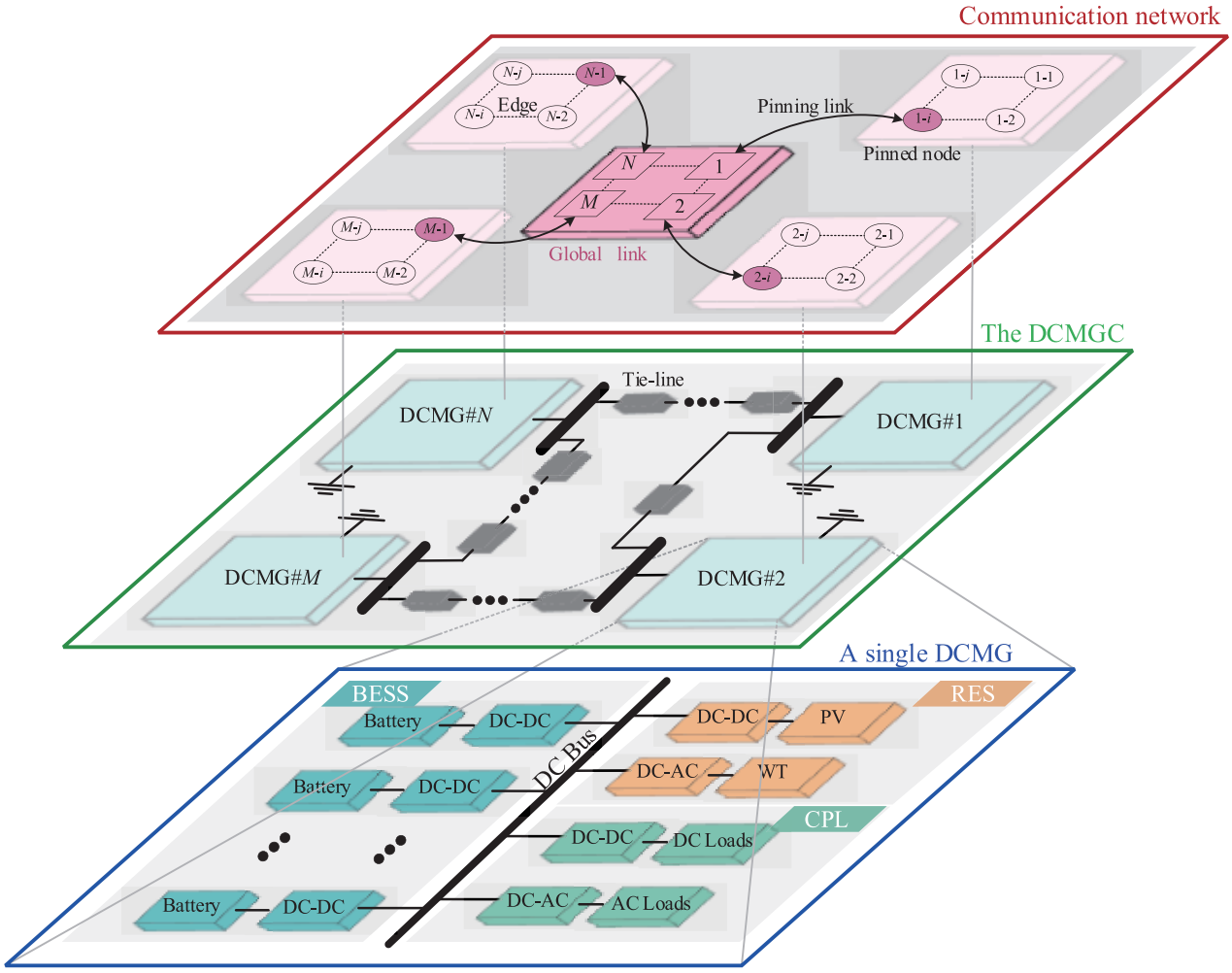

Fig. 1. A general DCMGC topology.

coefficient which can be regarded as a virtual impedance, respectively.

Although the droop control achieves autonomous current sharing without any communication, it equivalently adds the virtual impedance at the output of the converters in parallel, and thus causes bus voltage deviation from its nominal reference, especially in the heavy-load conditions.

To restore the DC bus voltage to its nominal reference, secondary control will be executed. Usually, secondary control is implemented with distributed communications, which means that there is only information shared directly between the neighboring converters. Thus, the consensus algorithm will be required to ensure all the converters in distributed control are with the same averaged output voltage, which can be given by

$$\bar{V}_{\text{avg}}^{M,i} = \sum_{j=1}^{S_{M,j\neq i}} a_{j,i}(V_{\text{avg}}^{M,j} - V_{\text{avg}}^{M,i}) + V_{M,i} \tag{2}$$

where $\bar{V}_{\text{avg}}^{M,i}$ and $V_{\text{avg}}^{M,j}$ stand for the estimated value of the average voltage, the actual average voltage of the converter#*j* in DCMG#*M*, $a_{j,i}$ is the communication weights between converter#*j* and converter#*i*, and $V_{M,i}$ is the sensed voltage of the converter#*i*, S_M denotes the total number of converters in DCMG#*M*, respectively.

Once the estimation of the average voltage is obtained, the deviation of the DC bus voltage can be compensated by integral function of secondary control. Therefore, the bus voltage after secondary control can be written as

$$V_{\text{bus}}^{M} = V_{\text{ref}}^{M,i} - i_{\text{o}}^{M,i} \bullet R_{\text{d}}^{M,i} + \delta V_{\text{sec}}^{M,i} \tag{3}$$

where $\delta V_{\text{sec}}^{M,i}$ denotes the voltage compensation term out from the secondary controller.

B. Global Control for the DCMGC

As mentioned above, the local control only deals with the operation of a single DCMG or the DCMG in standalone operation mode. When multiple DCMGs operate together as the DCMGC, the global control will be employed to handle the power flow among the interconnected DCMGs.

Like the distributed control of the secondary control, the global control also adopts distributed communication network but with more complicated nature. As shown in Fig. 1, in the communication network for global control, the square node

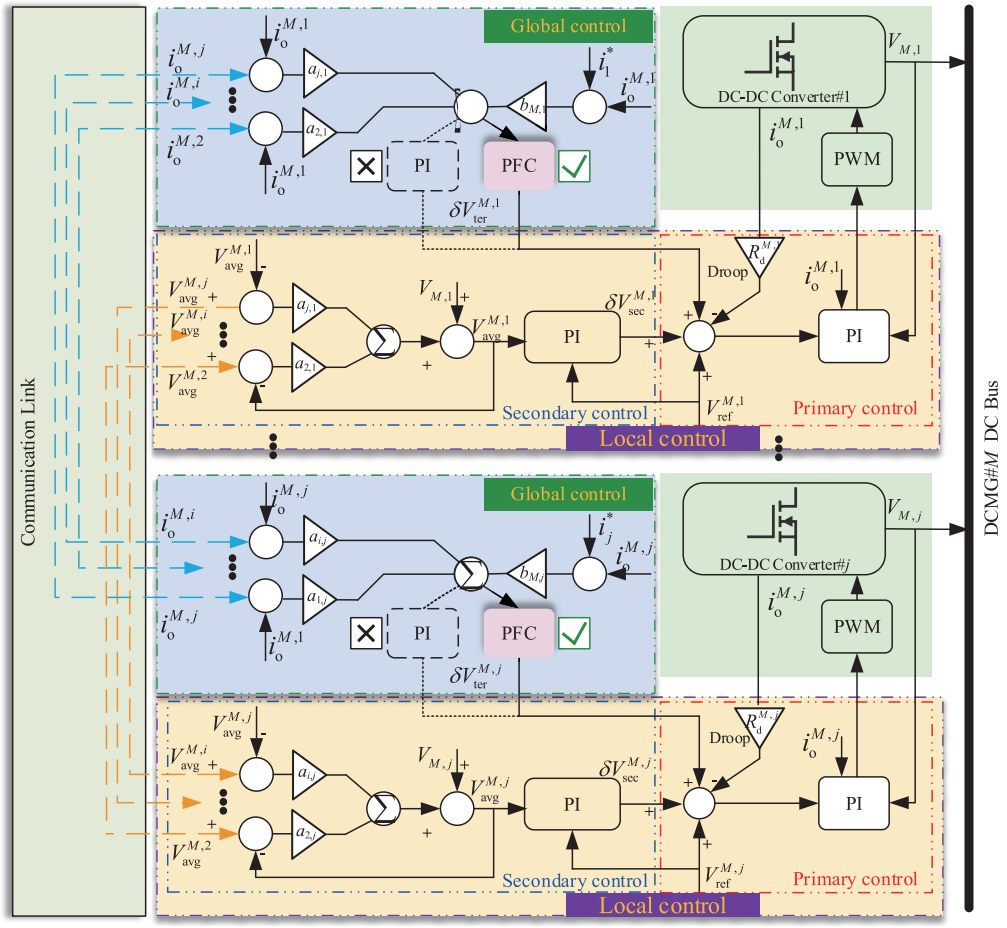

Fig. 2. Hierarchical control block diagram of the DCMGC.

represents control agents for a single DCMG, while the circle node represents control agent for a single converter within each DCMG. The information between the square nodes and the circular nodes is transmitted through the pinning link. Furthermore, the circle node link can be shared with the secondary control to save communication resources.

The voltage and current information of the single converter are obtained through the converter control agents and then transmitted to the DCMG control agent to realize global control, which can be written as

$$e_{M,i} = \sum_{j=1}^{S_{M,j\neq i}} a_{j,i}(i_{\mathrm{o}}^{M,j} - i_{\mathrm{o}}^{M,i}) + b_i(i_i^* - i_{\mathrm{o}}^{M,i}) \tag{4}$$

where $e_{M,i}$ denotes the difference between the local current of the converter and both of the current of its neighboring converters and the set global current i_i^*, b_i represents communication weights for the DCMG control agent and converter#i, respectively.

In the traditional global control, the voltage deviation that is generated by the global PI controller to facilitate the system-level power flow can be expressed as

$$\delta V_{\mathrm{ter}}^{M,i} = K_{\mathrm{P}}^{M,i} \cdot e_{M,i} + \int (K_{\mathrm{I}}^{M,i} \cdot e_{N,i})\,\mathrm{d}t \tag{5}$$

Therefore, the bus voltage of the DCMG will be attained as

$$V_{\mathrm{bus}}^{M} = V_{\mathrm{ref}}^{M,i} - i_{\mathrm{o}}^{M,i} \cdot R_{\mathrm{d}}^{M,i} + \delta V_{\mathrm{sec}}^{M,i} + \delta V_{\mathrm{ter}} \tag{6}$$

Different from the traditional methods, the global control in this work will replace the PI algorithms by the ET-PFC algorithm for the DCMGC. The design of the PFC controller and the ET mechanism in the global control will be detailed in the next section, respectively

III. The ET-PFC Controller Design for System-Level Power Management of the DCMGC

Fig. 3 shows the block diagram of the proposed ET-PFC scheme that is composed of two main parts, i.e., the PFC and the ET mechanism, and design of the ET-PFC controller will take two steps according to the mentioned two parts.

A. Design of the PFC Controller

With the PFC scheme, future control effect can be expressed as a linear combination of a specific family of functions causes rapid deviations in the bus voltages of neighboring DCMG, and the general form of the global control can be given by

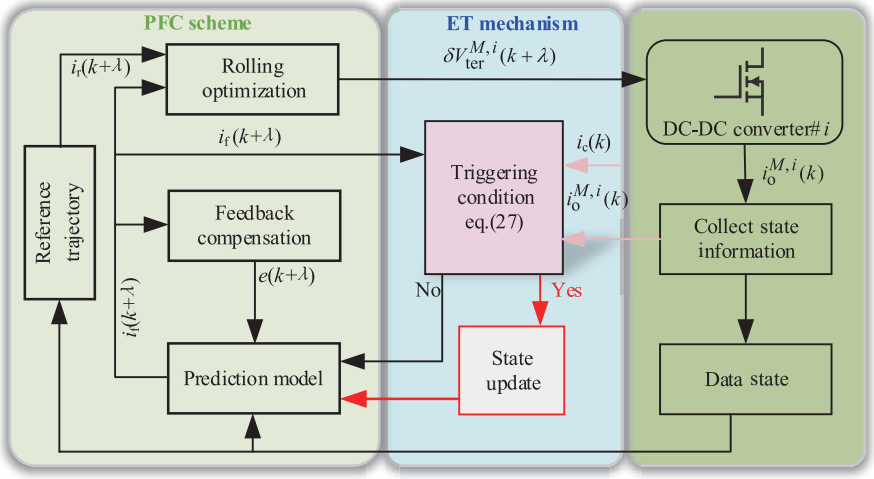

Fig. 3. Block diagram of the proposed ET-PFC scheme.

$$\delta V_{\text{ter}}^{M,i}(k+\lambda|k)=\sum_{q=1}^{\gamma}\mu_q(k)\bullet g_q(\lambda),\lambda=0,1,...,P-1 \quad (7)$$

where $\delta V_{\text{ter}}^{M,i}(k+\lambda|k)$ represents the global control voltage deviations at instant $k+\lambda$ predicting instant k; $g_q(\lambda)$ represents the output response value of the qth basis function; $\mu_q(k)$ represents the coefficient; γ represents the number of basis functions (a step function is selected as the basis function); P represents the predicted horizon, respectively.

1) Prediction Model

The prediction model of the plant is supposed to be established first for predicting the dynamic behavior of the DC-MGC. At the heart of the DCMGC, the DC/DC converters will be modeled by the state-space averaging method to capture the dominant slow-scale dynamics while neglecting the switching frequency component [42], and this can be expressed as

$$\begin{cases}x_{\text{m}}(k+1)=\boldsymbol{A}_{\text{m}}x_{\text{m}}(k)+\boldsymbol{B}_{\text{m}}\delta V_{\text{ter}}^{M,i}(k|k)\\ i_{\text{m}}(k)=\boldsymbol{C}_{\text{m}}x_{\text{m}}(k)\end{cases}(k=1,2,...,P) \quad (8)$$

where x_{m} and i_{m} represent the state vector and the output vector of the prediction model, respectively; $\boldsymbol{A}_{\text{m}}$, $\boldsymbol{B}_{\text{m}}$ and $\boldsymbol{C}$m represent the coefficient matrices of the corresponding vector in the prediction model, respectively.

After continuous iteration, the state space expression of the system at time constant $k+\lambda$ is given by

$$\begin{cases}x_{\text{m}}(k+\lambda|k)=\boldsymbol{A}_{\text{m}}^{\lambda}x_{\text{m}}(k)+\boldsymbol{A}_{\text{m}}^{\lambda-1}\boldsymbol{B}_{\text{m}}\delta V_{\text{ter}}^{M,i}(k|k)\\ \qquad\qquad +...+\boldsymbol{B}_{\text{m}}\delta V_{\text{ter}}^{M,i}(k+\lambda-1|k)\\ i_{\text{m}}(k+\lambda|k)=\boldsymbol{C}_{\text{m}}\left[\begin{matrix}\boldsymbol{A}_{\text{m}}^{\lambda}x_{\text{m}}(k)+\boldsymbol{A}_{\text{m}}^{\lambda-1}\boldsymbol{B}_{\text{m}}\delta V_{\text{ter}}^{M,i}(k|k)\\ +...+\boldsymbol{B}_{\text{m}}\delta V_{\text{ter}}^{M,i}(k+\lambda-1|k)\end{matrix}\right]\end{cases} \quad (9)$$

Then, substituting (7) into (9) yields

$$\begin{aligned}&i_{\text{m}}(k+\lambda|k)\\&=\boldsymbol{C}_{\text{m}}\left[\begin{matrix}\boldsymbol{A}_{\text{m}}^{\lambda}x_{\text{m}}(k)+\boldsymbol{A}_{\text{m}}^{\lambda-1}\boldsymbol{B}_{\text{m}}\sum_{q=1}^{\gamma}\mu_q(k)\bullet g_q(0)\\ +...+\boldsymbol{B}_{\text{m}}\delta\sum_{q=1}^{\gamma}\mu_q(k)\bullet g_q(\lambda-1)\end{matrix}\right]\\&=i_{\text{m}}(k+\lambda|k)=\boldsymbol{C}_{\text{m}}\boldsymbol{A}_{\text{m}}^{\lambda}x_{\text{m}}(k)+\boldsymbol{\mu}(k)^T\boldsymbol{G}_k(\lambda)\\&\quad(\lambda=0,1,...,P-1)\end{aligned} \quad (10)$$

where $\boldsymbol{\mu}(k)=[\mu_1(k),\mu_2(k),\ldots,\mu_q(k)]^T$, $\boldsymbol{G}_k(\lambda)=[g_{1k}(\lambda),g_{2k}(\lambda),\ldots,g_{qk}(\lambda)]$, $\boldsymbol{G}_k(\lambda)=[\boldsymbol{C}_{\text{m}}\boldsymbol{A}_{\text{m}}^{\lambda-1}\boldsymbol{B}_{\text{m}}\boldsymbol{G}_{1k}(0),\boldsymbol{C}_{\text{m}}\boldsymbol{A}_{\text{m}}^{\lambda-2}\boldsymbol{B}_{\text{m}}\boldsymbol{G}_{2k}(1),\ldots,\boldsymbol{C}_{\text{m}}\boldsymbol{B}_{\text{m}}\boldsymbol{G}_{\lambda k}(\lambda-1)]$, respectively.

2) Reference Trajectory

To avoid large fluctuations in the output of each DCMG in the DCMGC, we set a reference trajectory as

$$i_{\text{r}}(k+\lambda|k)=F(i(k),i_{\text{set}}(k+\lambda)) \quad (11)$$

where $i(k)$ represents the actual output current, and $i_{\text{set}}(k+\lambda)$ is the current set at instant $k+\lambda$, and $F(i(k),i_{\text{set}}(k+\lambda))$ denotes the functional relationship between these two variables, respectively.

To ensure that the system output transitions smoothly to the target value, a typical form of the reference trajectory can be represented by

$$i_{\text{r}}(k+\lambda|k)=i_{\text{set}}(k+\lambda)-\exp\left(-\frac{T_{\text{s}}}{T_{\text{r}}}\lambda\right)\bullet[i_{\text{set}}(k)-i(k)] \quad (12)$$

where T_{s} and T_{r} denote sampling period and time constant of the reference trajectory of the system, respectively.

The selection of T_{s} influences the convergence rate of the reference trajectory towards the setpoint. As shown in Fig. 4, these subfigures demonstrate the overshoot and transient time of reference trajectory tracking errors under varying $T_{\text{s}}/T_{\text{r}}$ ratios in (12) through simulations. The selection of $T_{\text{s}}/T_{\text{r}}=0.5$ in this work aims to achieve an optimal trade-off between transient

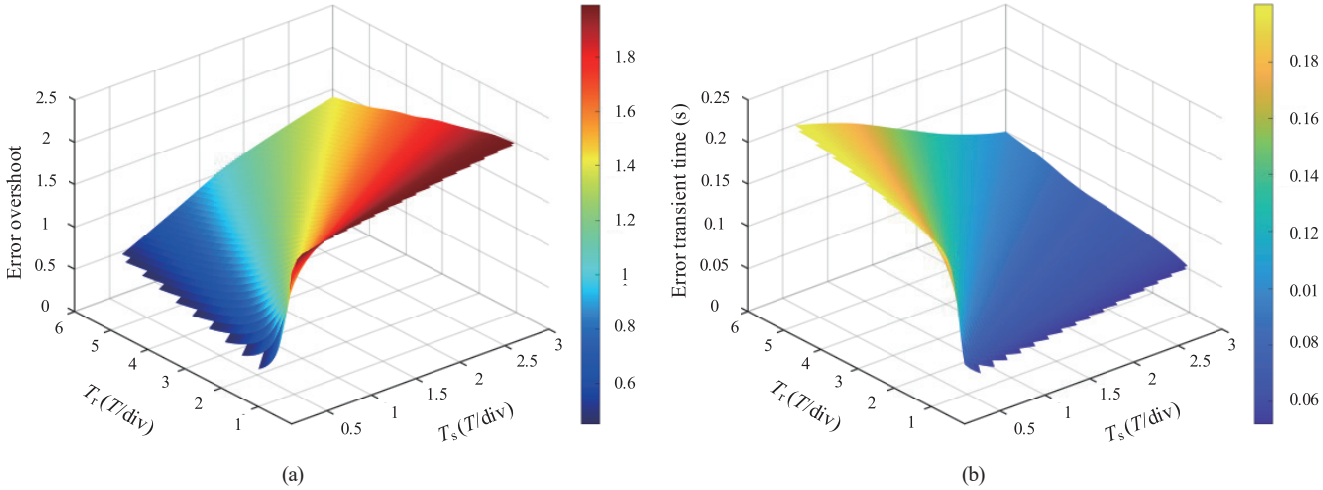

(a) (b)

Fig. 4. The reference trajectory tracking setpoint. (a) error overshoot; (b) transient time.

response time and overshoot suppression.

Further, the set value is expressed as polynomial sums by

$$i_{\text{set}}(k+\lambda) = c_0(k) + \sum c_j(k) i^j(k) \tag{13}$$

where $c_0(k)$, $c_j(k)$, and j stand for the partial current reference at a given instant, coefficients for each term, and the order of the corresponding current, respectively.

Combining (12) and (13), the reference trajectory is obtained as

$$\begin{aligned} & i_{\text{r}}(k+\lambda \mid k) \\ & = c_0(k) + \sum c_j(k) i^j(k) - \exp\left(-\frac{T_{\text{s}}}{T_{\text{r}}}\lambda\right) \cdot \left[i_{\text{set}}(k) - i(k)\right] \end{aligned} \tag{14}$$

3) Feedback Correction

In practical applications, the predicted values may deviate from the actual values due to the influence of uncertainties such as model mismatch and external disturbances. The deviation will increase over time if real-time voltage and current information cannot be transmitted in time for correction and optimization. Hence, the compensation of the deviation is realized by the feedback correction.

The deviation or error between the actual and predicted values can be expressed as

$$e(k) = i(k) - i_{\text{m}}(k \mid k-1) \tag{15}$$

Then, the error value of instant k is given by

$$e(k+\lambda) = h \cdot e(k) \tag{16}$$

where h is the correction coefficient that corrects the mismatch between the model and the actual values.

The correction coefficient h, serving as a critical parameter in the feedback correction module of predictive function control, embodies the mechanism by which current tracking errors are propagated through coefficient h to future predictions at the λ-step prediction horizon terminal, thereby achieving exponential convergence of closed-loop error dynamics.

(1) Stability constraint: constructing an energy function $V(k) = \|e(k)\|^2$, the stability requirement $\Delta V = (h^2-1)\|e(k)\|^2 \leqslant 0$, necessitates $h < 1$.

(2) Error attenuation requirement: to achieve an error decay ratio of Φ, the correction coefficient h must satisfy: $h = \Phi^{\lambda}$.

The predicted value of the model with the feedback correction is derived as

$$\begin{aligned} & i_{\text{f}}(k+\lambda \mid k) \\ & = i_{\text{m}}(k+\lambda) + e(k+\lambda) \\ & = \boldsymbol{C}_{\text{m}} \boldsymbol{A}_{\text{m}}^{\lambda} x_{\text{m}}(k) + \boldsymbol{\mu}(k)^T \boldsymbol{G}_k(\lambda) + h\left[i(k) - i_{\text{m}}(k \mid k-1)\right] \end{aligned} \tag{17}$$

4) Rolling Optimization

The PFC algorithm needs to determine the next step control action based on solving optimal solution based on the cost function in a finite horizon. Since the PFC algorithm does not use a global optimization performance measure, it suggests that this solving process is performed iteratively on-line as the prediction horizon changes, viz., the rolling optimization.

The optimization performance measure at instant k is expressed as

$$\min J(k) = \sum_{i=1}^{s} \sigma_i \left[i_{\text{f}}(k+t_i \mid k) - i_{\text{r}}(k+t_i \mid k)\right]^2 \tag{18}$$

where $i_{\text{r}}(k+t_i|k)$ denotes the desired output at instant k; s is the number of fitting points and t_i is the specific instant of the fitting point; σ_i represents weight coefficient which indicates the degree of suppression of the tracking error; respectively.

The weight σ_i is used to differentially regulate the tracking error priority at different time steps (e.g., the proximal error penalty is stronger than the distal). There exists s independent weight coefficients σ_1, σ_2, …, σ_s, corresponding to the error penalty weights for s time steps. Furthermore, in the hierarchical control architecture of DCMGC, the global control adopts the output current as the controlled variable to achieve energy management objectives. Therefore, the cost function incorporates only current-related variables to derive optimal control sequences.

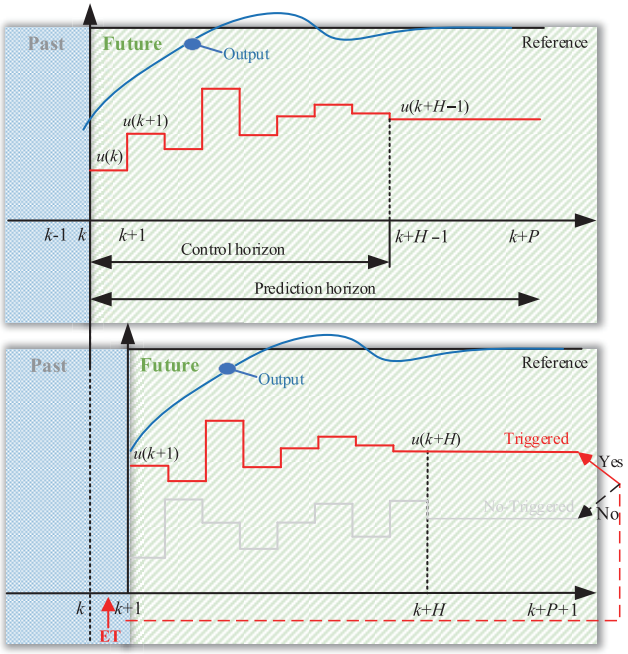

Fig. 5. Principle of event triggering (ET) in PFC.

Based on (14) and (17), we derive

$$\begin{aligned} & i_{\mathrm{f}}(k+t_i \mid k)-i_{\mathrm{r}}(k+t_i \mid k) \\ & \quad=\left[1-\exp\left(-\frac{T_{\mathrm{s}}}{T_{\mathrm{r}}}t_i\right)\right]\left[c_0(k)-i(k)\right] \\ & \quad\quad+\sum c_j(k)t_i^j-\left[\boldsymbol{C}_{\mathrm{m}}\boldsymbol{A}_{\mathrm{m}}^{t_i}x_{\mathrm{m}}(k)+\boldsymbol{\mu}(k)^T\boldsymbol{G}_k(t_i)\right] \end{aligned} \tag{19}$$

Now, (18) can be simplified as

$$J(k)=\min\left\{\sum_{i=1}^{s}\left[l(k+t_i)-\boldsymbol{\mu}(k)^T\boldsymbol{G}_k(t_i)\right]^2\right\} \tag{20}$$

where

$$l(k+t_i)=\left[1-\exp(-\frac{T_{\mathrm{s}}}{T_{\mathrm{r}}}t_i)\right]\left[i_{\mathrm{set}}(k)-i(k)\right]+\sum c_j(k)h_i^j-\boldsymbol{C}_{\mathrm{m}}\boldsymbol{A}_{\mathrm{m}}^{t_i}x_{\mathrm{m}}(k)\,.$$

(20) can be written as the compact form in the following

$$J(k)=\min\left\{\|\boldsymbol{L}(k)-\boldsymbol{G}(k)\boldsymbol{\mu}(k)\|^2\right\} \tag{21}$$

To obtain the minimum value of $J(k)$, the partial derivative of $J(k)$ with respect to $\boldsymbol{\mu}(k)$ can be obtained as

$$\frac{\partial J(k)}{\partial\boldsymbol{\mu}(k)}=2\boldsymbol{G}_k^T\boldsymbol{G}_k\boldsymbol{\mu}(k)-2\boldsymbol{G}_k^T\boldsymbol{L}(k)=0 \tag{22}$$

Hence, the solution is found as

$$\boldsymbol{\mu}(k)=(\boldsymbol{G}_k^T\boldsymbol{G}_k)^{-1}\boldsymbol{G}_k^T\boldsymbol{L}(k) \tag{23}$$

In the predictive control, the first control variable is applied to the system with the rolling optimization, and that is given by

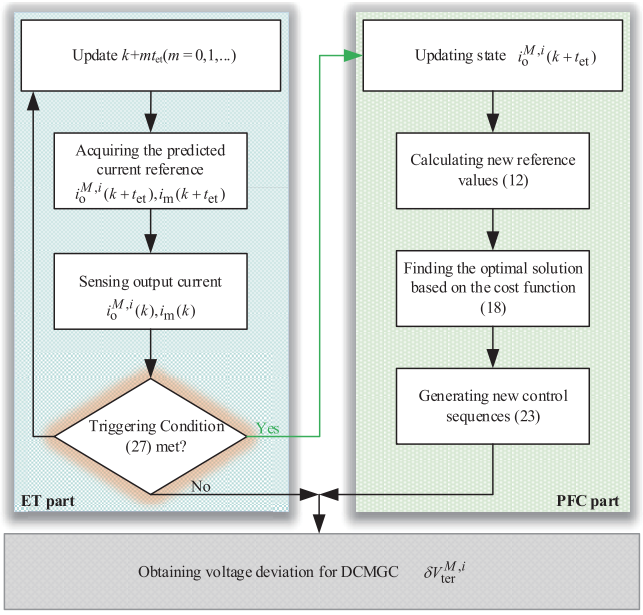

Fig. 6. Flowchart of ET-PFC for the DCMGC.

$$\delta V_{\mathrm{ter}}^{M,i}(k)=\boldsymbol{\mu}(k)g_q(0)=(\boldsymbol{G}_k^T\boldsymbol{G}_k)^{-1}\boldsymbol{G}_k^T\boldsymbol{L}(k)g_q(0) \tag{24}$$

B. Design of the Event-Triggering (ET) Condition

To eliminate redundant operations of the PFC during the rolling optimization process, an ET condition is incorporated into the PFC for the global control, which is illustrated by Fig. 5. In accordance with [38], the derivation of ET-PFC proceeds as follows:

(1) The state variable $x_{\mathrm{m}}(k)$ in the converters within every single DCMG is measured.

(2) The error value $e(k)$ and $e(k+t_{\mathrm{et}})$ are calculated, respectively.

(3) The ET condition is designed.

(4) The error $e(k+t_{\mathrm{et}})$ and $e(k)$ are compared to determine whether to activate PFC, and PFC controller will update the control sequence once the ET condition is met; otherwise, PFC is suspended and the control sequence remained, thus eliminating the redundant operation, and reducing the computational burden.

Where t_{et} denotes the sample time of the ET, and it is equal to the switching cycle of the converter in this paper.

Based on (15), the error with the ET can be expressed as

$$e(k+t_{\mathrm{et}})=i(k+t_{\mathrm{et}})-i_{\mathrm{m}}(k+t_{\mathrm{et}}\mid k) \tag{25}$$

The two neighboring trigger instants are denoted as $k+t_{\mathrm{E}}$ and k, and the relationship between t_{et} and t_{E} is expressed as

$$t_{\mathrm{E}}=m\bullet t_{\mathrm{et}} \tag{26}$$

where m denotes the number of sampling cycles after the trigger condition is satisfied again.

It should be noted that the error is squared before the comparison to prevent false triggering and missed triggering caused

by negative numbers in the solving of the difference. Therefore, the ET condition can be designed as

$$\begin{cases}\left[i(k+t_{\mathrm{et}})-i_{\mathrm{m}}(k+t_{\mathrm{et}})\right]^2<\eta\left[i(k)-i_{\mathrm{m}}(k)\right]^2\\ k+t_{\mathrm{E}}=k+m\cdot t_{\mathrm{et}}\end{cases}\tag{27}$$

where η denotes the contraction or expansion of the triggering condition.

The flowchart in Fig. 6 shows the process of ET-PFC for the DCMGC. The controller obtains the predicted current value and the reference at the instant $k+t_{\mathrm{et}}$, and detects the real-time current value and reference. Comparing them by utilizing the triggering condition, the state variables will be updated to generate a new control sequence acting on the DCMGC if the triggering conditions are satisfied.

On the other hand, the ET-PFC controller may suffer from infinite triggering phenomenon which is known as Zeno behavior [43]. Its underlying mechanism can be rigorously formalized through the convergence analysis of the inter-event time sequence. Assume the qth triggering instant is $k+t_{\mathrm{q}}$. If there exists a finite time $k+t_{\infty}$ such that

$$\begin{cases}\lim\limits_{q\to\infty}(k+t_q)=k+t_{\infty}\\ \sum\limits_{q=1}^{\infty}(t_{q+1}-t_q)=t_{\infty}-t_1<\infty\end{cases}\tag{28}$$

In order to avoid Zeno behavior, regarding the event-triggering condition proposed in this work, a positive time interval is required between any two consecutive trigger instants k and $k+t_{\mathrm{E}}$. The second equation in (27) indicates that the minimum time interval is

$$\tau_{\min}=m\bullet t_{\mathrm{et}}>0\rightarrow\inf_{q}(t_{q+1}-t_q)\geqslant t_{\mathrm{et}}\tag{29}$$

IV. Stability Guarantee With the Proposed Control Scheme

In this section, the closed-loop stability with the proposed ET-PFC control scheme will be tackled based on the Takagi-Sugeno (T-S) fuzzy modeling, Lyapunov function theory, and Gerschgorin's theorem.

Regarding the hierarchical control block diagram of Fig. 2 for the DCMGC, it has been recognized that the inner control loops Fig. 7. Simplified model of the DCMGC.

are always faster than outer ones, which lays foundation on the reduced modeling of the system by separating lower dynamics from faster dynamics. Based on the sufficiently fast response of the inner current loop, the inductor current can rapidly track the current reference generated by the outer voltage loop [44]. Thus, the DC/DC converters with dual-loop control in the primary level for every single DCMG can be approximated by controlled current sources since the inner current loops have much higher bandwidth than the outer voltage loops. As such, the simplified dynamic model of the DCMGC can be derived as in Fig. 7 where each DCMG model consists

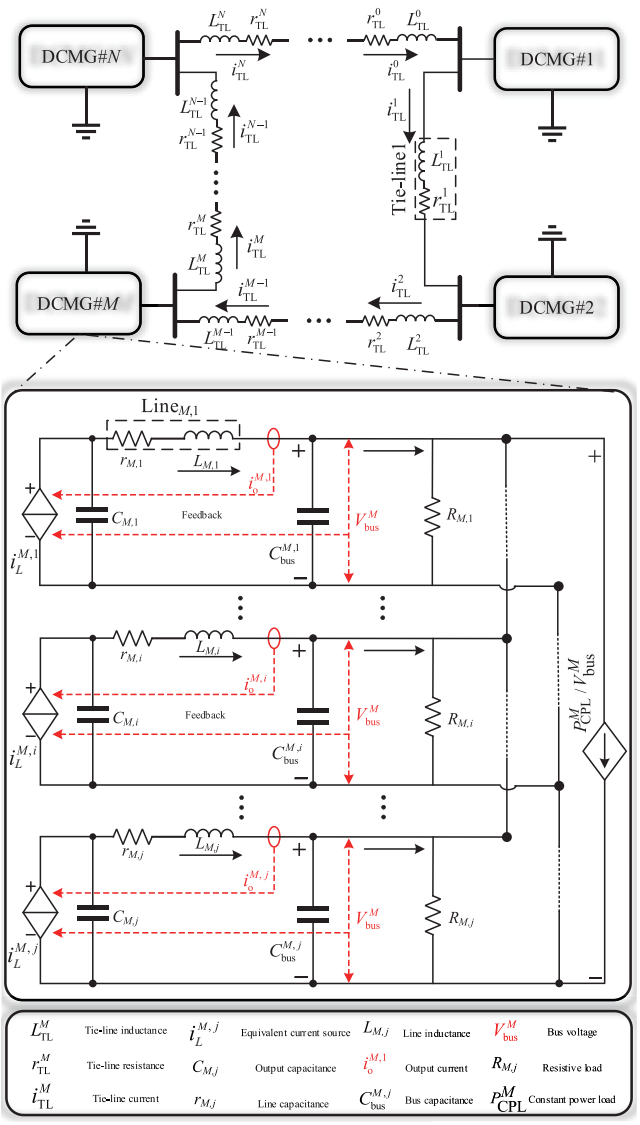

Fig. 7. Simplified model of the DCMGC.

of multiple controlled current sources in parallel and a lumped CPL. Combined with the control block diagram of Fig. 2, the model of the local control can be described as

$$\begin{cases}i_{L\mathrm{ref}}^{M,i}=K_{\mathrm{P}}^{M,i}\left(V_{\mathrm{ref}}^{M,i}+\delta V_{\mathrm{ter}}^{M,i}-i_{\mathrm{o}}^{M,i}R_{\mathrm{d}}^{M,i}-V_{M,i}\right)\\ \qquad\quad+K_{\mathrm{I}}^{M,i}\int\left(V_{\mathrm{ref}}^{M,i}+\delta V_{\mathrm{ter}}^{M,i}-i_{\mathrm{o}}^{M,i}R_{\mathrm{d}}^{M,i}-V_{M,i}\right)\mathrm{d}t\\ \mathrm{d}_{M,i}=k_{\mathrm{P}}^{M,i}\left(i_{L\mathrm{ref}}^{M,i}-i_{L}^{M,i}\right)+k_{\mathrm{I}}^{M,i}\int\left(i_{L\mathrm{ref}}^{M,i}-i_{L}^{M,i}\right)\mathrm{d}t\end{cases}\tag{30}$$

where K_{P}, K_{I} and k_{P}, k_{I} denote the PI parameters of the voltage and current loops, respectively.

On the other hand, the model of global control can be derived as

$$\begin{aligned}&\delta V_{\mathrm{ter}}^{M,i}(k)\\ &=a_1\left[i_{\mathrm{avg}}^{M,i}(k)-i_{\mathrm{o}}^{M,i}(k)\right]+a_2\left[i_{\mathrm{o}}^{M,i}(k-1)+\delta V_{\mathrm{ter}}^{M,i}(k-1)\right]\end{aligned}\tag{31}$$

By the analogy of the consensus algorithm, the variables at instant k in (31) can be represented by those at instant k–1 as follows:

$$\begin{cases} \delta V_{\text{ter}}^{M,i}(k) = \delta V_{\text{ter}}^{M,i}(k-1) + \int \sum B_{j,i}\left[i_{\text{avg}}^{M,j}(k-1) - i_{\text{avg}}^{M,i}(k-1) \right] \mathrm{d}t \\ i_{\text{avg}}^{M,i}(k) = i_{\text{avg}}^{M,i}(k-1) + \int \sum B_{j,i}\left[i_{\text{avg}}^{M,j}(k-1) - i_{\text{avg}}^{M,i}(k-1) \right] \mathrm{d}t \\ i_{\text{o}}^{M,i}(k) = i_{\text{o}}^{M,i}(k-1) + \int \sum b_{i}\left[i_{\text{avg}}^{M,i}(k-1) - i_{\text{o}}^{M,i}(k-1) \right] \mathrm{d}t \end{cases} \tag{32}$$

where a_1, a_2, $B_{j,i}$ and b_i represents relevant communication weights, respectively.

Bringing (32) into (31) yields

$$\begin{aligned} &\delta V_{\text{ter}}^{M,i}(k-1) + \int \sum B_{j,i}\left[i_{\text{avg}}^{M,j}(k-1) - i_{\text{avg}}^{M,i}(k-1) \right] \mathrm{d}t \\ &\quad = a_1 (i_{\text{avg}}^{M,i}(k-1) + \int \sum B_{j,i}\left[i_{\text{avg}}^{M,j}(k-1) - i_{\text{avg}}^{M,i}(k-1) \right] \mathrm{d}t \\ &\qquad - i_{\text{o}}^{M,i}(k-1) + \int \sum b_{j,i}\left[i_{\text{avg}}^{M,i}(k-1) - i_{\text{o}}^{M,i}(k-1) \right] \mathrm{d}t \\ &\qquad + a_2 \left[i_{\text{o}}^{M,i}(k-1) + \delta V_{\text{ter}}^{M,i}(k-1) \right] \end{aligned} \tag{33}$$

Then, we rewrite (33) in a simplified form as

$$\delta V_{\text{ter}}^{M,i} = B_1 \int \sum (i_{\text{avg}}^{M,j} - i_{\text{avg}}^{M,i}) \mathrm{d}t + B_2 i_{\text{o}}^{M,i} + B_3 i_{\text{avg}}^{M,i} \tag{34}$$

where

$$B_1 = \frac{(a_1 B_{j,i} - B_{j,i} - a_1 b_i)}{(1-a_2)}, B_2 = \frac{(a_2 - a_1)}{(1-a_2)}, B_3 = \frac{a_1}{(1-a_2)}.$$

Adding the ET conditions to the global control derives

$$\begin{aligned} \delta V_{\text{ter}}^{M,i} = &\frac{G}{1-a_2}\left[B_1 \int \sum (i_{\text{avg}}^{M,j} - i_{\text{avg}}^{M,i}) \mathrm{d}t + B_2 i_{\text{o}}^{M,i} + B_3 i_{\text{avg}}^{M,i} \right] \\ &+ \frac{1-G}{1-a_2}\left[B_1 \int \sum (i_{\text{avg}}^{M,j} - i_{\text{avg}}^{M,i}) \mathrm{d}t + B_2 i_{\text{o}}^{M,i} + B_3 i_{\text{avg}}^{M,i} \right] \end{aligned} \tag{35}$$

where G = 0 or 1 represents whether the trigger condition is met or not, respectively.

Meanwhile, the circuit model is given by

$$\begin{aligned} i_L^{M,i} = &K_{\text{pv}}^{M,i}\left(V_{\text{ref}}^{M,i} + \delta V_{\text{ter}}^{M,i} - i_{\text{o}}^{M,i} R_{\text{d}}^{M,i} - V_{M,i} \right) \\ &+ K_{\text{iv}}^{M,i} \int \left(V_{\text{ref}}^{M,i} + \delta V_{\text{ter}}^{M,i} - i_{\text{o}}^{M,i} R_{\text{d}}^{M,i} - V_{M,i} \right) \mathrm{d}t \end{aligned} \tag{36}$$

where $i_L^{M,i}$, $K_{\text{pv}}^{M,i}$ and $K_{\text{iv}}^{M,i}$, represent the inductor current, PI parameters of the converter#i in DCMG#M, respectively.

Set the state variables as

$$\begin{cases} \omega_{\text{ter}}^{M,i} = \int \sum (i_{\text{avg}}^{M,j} - i_{\text{avg}}^{M,i}) \mathrm{d}t \\ \omega_{\text{loc}}^{M,i} = \int \left(V_{\text{ref}}^{M,i} + \delta V_{\text{ter}}^{M,i} - i_{\text{o}}^{M,i} R_{\text{d}}^{M,i} - V_{M,i} \right) \mathrm{d}t \end{cases} \tag{37}$$

Then, the general model of the DCMGC including both the main circuit and the control loops is written as

$$\sum_{M=3}^{N(N\geqslant 3)} \text{DCMG\#}M:$$

$$\begin{cases} \dfrac{\mathrm{d}\omega_{\text{ter}}^{M,i}}{\mathrm{d}t} = \sum (i_{\text{avg}}^{j} - i_{\text{avg}}^{i}) \\ \dfrac{\mathrm{d}\omega_{\text{loc}}^{M,i}}{\mathrm{d}t} = V_{\text{ref}}^{M,i} + B_1 \omega_{\text{ter}}^{M,i} + B_2 i_{\text{o}}^{M,i} + B_3 i_{\text{avg}}^{i} - i_{\text{o}}^{M,i} R_{\text{d}}^{M,i} - V_{M,i} \\ C_{M,i} \dfrac{\mathrm{d}V_{M,i}}{\mathrm{d}t} = K_{\text{pv}}^{M,i}(V_{\text{ref}}^{M,i} + B_1 \omega_{\text{ter}}^{M,i} + B_2 i_{\text{o}}^{M,i} + B_3 i_{\text{avg}}^{i} \\ \qquad\qquad - i_{\text{o}}^{M,i} R^{M,i} - V_{M,i}) + K_{\text{iv}}^{M,i} \omega_{\text{loc}}^{M,i} \\ L_{M,i} \dfrac{\mathrm{d}i_{\text{o}}^{M,i}}{\mathrm{d}t} = V_{M,i} - r_{M,i} \cdot i_{\text{o}}^{M,i} - V_{\text{bus}}^{M} \\ C_{\text{bus}}^{M,i} \dfrac{\mathrm{d}V_{\text{bus}}^{M}}{\mathrm{d}t} = i_{\text{o}}^{M,i} - i_{\text{TL}}^{M} - \dfrac{P_{\text{CPL}}^{M}}{V_{\text{bus}}^{M}} - \dfrac{V_{\text{bus}}^{M}}{R_{M,i}} \\ L_{\text{TL}}^{M} \dfrac{\mathrm{d}i_{\text{TL}}^{M}}{\mathrm{d}t} = V_{\text{bus}}^{M} - r_{\text{TL}}^{M} \cdot i_{\text{TL}}^{M} - V_{\text{bus}}^{(M+1)} \end{cases} \tag{38}$$

For simplicity, the model in (38) can be rewritten in the compact form as

$$\dot{\boldsymbol{x}}(t) = f\left(\boldsymbol{x}(t), \boldsymbol{u}(t) \right) \tag{39}$$

where $\boldsymbol{x}(t)$ =[$\omega_{\text{ter}}^{M,i}$, $\omega_{\text{loc}}^{M,i}$, $V_{1,1}$, $i_{\text{o}}^{1,1}$, V_{bus}^{1}, i_{TL}^{1},…, $\omega_{\text{ter}}^{N,i}$, $\omega_{\text{loc}}^{N,i}$, $V_{N,j}$, $i_{\text{o}}^{N,j}$, V_{bus}^{N}, i_{TL}^{N}]$^{\text{T}}$, and $\boldsymbol{u}(t)$ = [0, $V_{\text{ref}}^{1,1}$, 0, 0, 0, 0,…,0, $V_{\text{ref}}^{N,i}$, 0, 0, 0, 0]$^{\text{T}}$, and $\boldsymbol{u}(t)$ $\mathbb{R}^{12\times 1}$ stand for the input vector, respectively.

Subsequently, we use the T-S fuzzy modeling, Lyapunov function theory, and Gerschgorin's theorem to obtain the following stability criterion for the system (39), the details of the proof are given in the Appendix.

$$\sum_{M=3}^{N(N\geqslant 3)} \text{DCMG\#}M:$$

$$\begin{cases} B_1 + B_2 + B_3 - R_{\text{d}}^{M,i} < 0, \dfrac{2 - r_{M,i}}{L_{M,i}} < 0, \dfrac{2 - r_{\text{TL}}^{M}}{L_{\text{TL}}^{M}} < 0 \\ \dfrac{K_{\text{pv}}^{M,i}(B_2 + B_3 - R_{diq}) + B_1 + K_{\text{iv}}^{M,i}}{C_{M,i}} - \dfrac{1}{C_{M,i}} < 0 \\ \dfrac{2}{C_{\text{bus}}^{M,i}} - \dfrac{1}{R_{M,i} C_{\text{bus}}^{M,i}} - \dfrac{P_{\text{CPL}}^{M}}{C_{\text{bus}}^{M,i}(V_{\text{bus}}^{0} + x_M) V_{\text{bus}}^{0}} < 0 \end{cases} \tag{40}$$

The inequalities of (40) implies that stability can be guaranteed by properly designing the prediction horizon P, the sample time of the ET t_{et}, main circuit parameters and the PI parameters for local control.

V. Experimental Verification

To validate the proposed ET-PFC design scheme, the full physical hardware-based laboratory setup of the DCMGC in Fig. 7 has been built. The layout of the setup is shown in Fig. 8 (a) where the DCMGC is comprised by interconnection of three DCMGs with tie-lines and circuit breakers, and each DCMG consists of two DC/DC boost converters in parallel

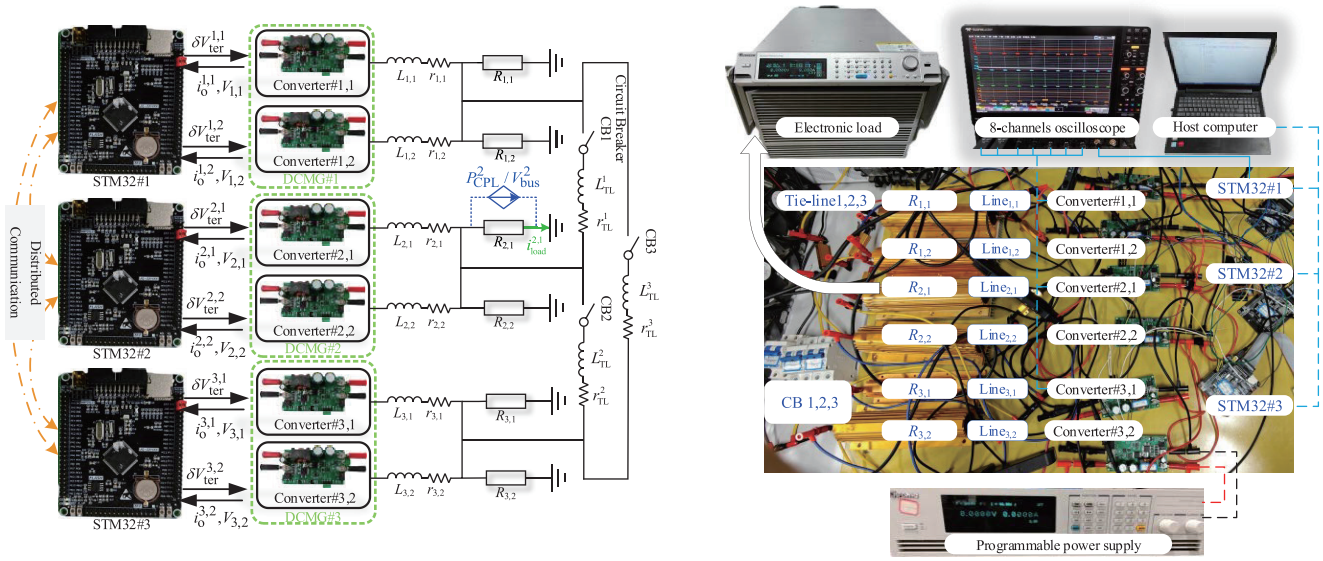

(a) (b)

Fig. 8. Hardware-based laboratory setup. (a) Layout of the DCMGC. (b) Photo of the experimental setup.

TABLE II
PARAMETERS OF THE HARDWARE SETUP. (M = 1, 2, 3; i = 1, 2)

Parameter	Symbol	Value
Input voltage of boost converters (V)	$V_{\text{in}}^{M,i}$	20
Bus voltage in DCMG#M (V)	V_{bus}^{M}	48
Switching frequency of boost converters (kHz)	f_s	100
Output capacitance (μF)	$C_{M,i}$	950
Line$_{M,1}$ resistance (Ω)	$r_{M,1}$	0.2, 0.5, 0.8
Line$_{M,1}$ inductance (mH)	$L_{M,1}$	2.28, 2.35, 2.39
Line$_{M,2}$ resistance (Ω)	$r_{M,2}$	0.2, 0.5, 0.8
Line$_{M,2}$ inductance (mH)	$L_{M,2}$	2.32, 2.38, 2.42
Tie-line M resistance (Ω)	r_{TL}^{M}	1, 1, 1
Tie-line M inductance (mH)	L_{TL}^{M}	2.45, 2.48, 2.55
Converter#M,1 load (Ω)	$R_{M,1}$	12, 48, 60
Converter#M,2 load (Ω)	$R_{M,2}$	96, 24, 16

and two local loads. The ET-PFC scheme for every single DCMG is implemented with a low-cost universal microcontroller (STM32), so that there are three STM32 controllers with distributed communication for the DCMGC. The signal acquisition is realized by using the analog to digital converter (ADC) module that comes with STM32, and the efficient control algorithm operation and PWM signal generation are completed by combining direct memory access (DMA) and timer. Compared to digital signal processor (DSP) controller that require complex peripheral circuits, the STM32 solution significantly reduces hardware design complexity and overall cost, while providing a high degree of realizability in code development and hardware debugging. The main parameters of the experimental setup are listed in Table II. Based on the layout, the experimental test setup is shown Fig. 8(b) where the

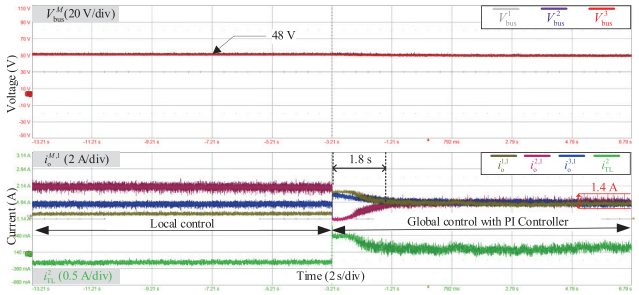

Fig. 9. Power flow management with PI controller.

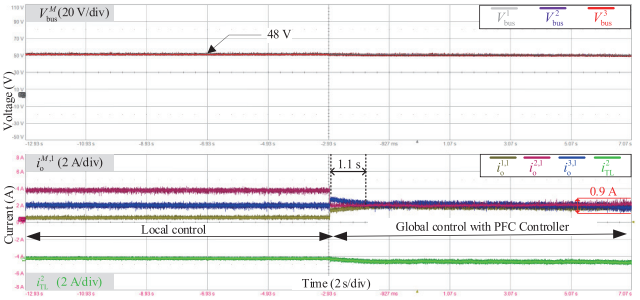

Fig. 10. Power flow management with PFC controller.

8-channels oscilloscope, the programmable power supply and the host computer are included as well as the layout of power stage of the DCMGC.

A. Power Flow Management

Three sets of experiments corresponding to three control schemes, i.e., PI, PFC, and the proposed ET-PFC have been performed, and the results of power flow management with the three control schemes are shown in Figs. 9−11, respectively. As soon as the global control of the DCMGC is engaged, the power

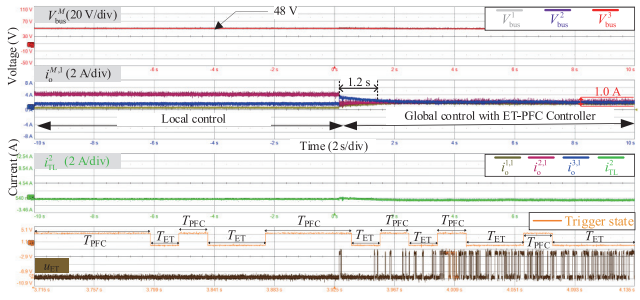

Fig. 11. Power flow management with ET-PFC ($\eta = 1$).

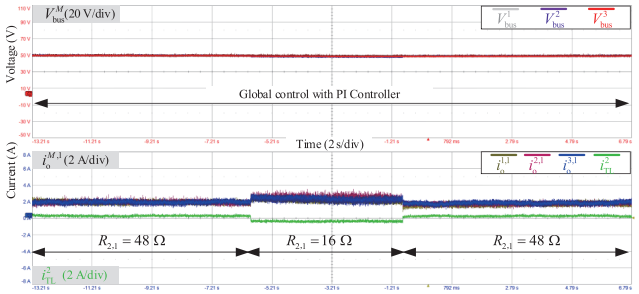

Fig. 12. Load step change with PI controller.

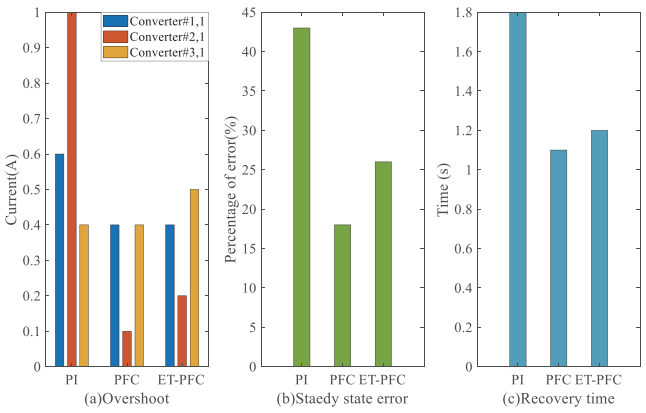

Fig. 13. Comparison of PI, PFC and ET-PFC performance. (a) Overshoot. (b) Steady state error. (c) Recovery time.

flow experiences the transient process, and the regulation time and overshoot of every control scheme differs from each other. Furthermore, the triggering signal denoted by u_{ET} for the controller and implemented by the microprocessor is shown at the bottom of Fig. 11, as well, which indicates the updated time of the ET-PFC controller. Once the ET-PFC controller updates the control sequence due to the trigger condition is satisfied, u_{ET} will generate a high-level signal, and the time required by this process is denoted as T_{PFC}. Otherwise, the time consumed by the unsatisfied trigger condition is defined as T_{ET}. Obviously, the updating frequency of the ET-PFC controller is much lower than that of the controller with the high switching frequency f_s of the DC/DC converter.

Given the results in Figs. 9−11, the performance of the three control schemes in terms of overshoot, steady state error and recovery time, are summarized and compared in Fig. 13. The

TABLE III
PERFORMANCE COMPARISON DIAGRAM OF THREE CONTROL METHODS

Performance index control methods	Overshoot /A	Steady-state error percentages /%	Recovery time/s
PI	0.66	42	1.8
PFC	0.30	18	1.1
ET-PFC	0.33	25	1.2

TABLE IV
EVALUATION OF THE CALCULATION CYCLE OF THE PROPOSED CONTROL ALGORITHM

Modules	Time-consuming /μs	Explanation
ADC sampling	2.57	Call function, floating point conversion
Conditional logic	0.06	GPIO input detection
Matrix calculation	1.36	Multivariate assignment and operation
State update and intermediate variables	0.86	Depend on the previous step results
DAC output	0.36	DAC data conversion and writing
Total	6.31	

quantitative description of the core performance metrics is listed in Table III, where the ET-PFC is similar to traditional PFC in dynamic performance, and ET-PFC is 38 %, 46 % and 33 % better than those of PI control in terms of overshoot, steady-state error and recovery time, respectively, and the comprehensive performance of the proposed control method improves by 40 %.

In PI controller, steady-state errors in control systems predominantly originate from persistent disturbances or the lack of low-frequency gain. As shown in Fig. 12, under load step conditions corresponding current tracking errors progressively amplify.

The microcontroller unit employed in this paper is STM-32F407VET6 operating a clock frequency of 168 MHz, and the switching frequency of DC/DC converter is 100 kHz. The architecture of ET-PFC algorithm architecture incorporates functional modules including ADC sampling, mathematical computation, conditional logic and DAC output. The execution times of individual modules in the proposed algorithm, measured via hardware-based debugging, are presented in Table IV. It is concluded that the execution duration of a single ET-PFC control cycle remains below the switching period of the power converter, satisfying real-time operational requirements.

As shown in Fig.11, the temporal occupation ratios of T_{PFC} (traditional PFC computation) and T_{ET} (event-triggered computation) during complex control operations are quantified as 53% and 47% respectively, demonstrating a 47% computational load reduction through the event-triggered framework. Meanwhile, the ET reduces the online computational burden caused by the prediction mechanism, which is a conciliation between performance and computation.

In addition, to show the constraint of η on the trigger condi-

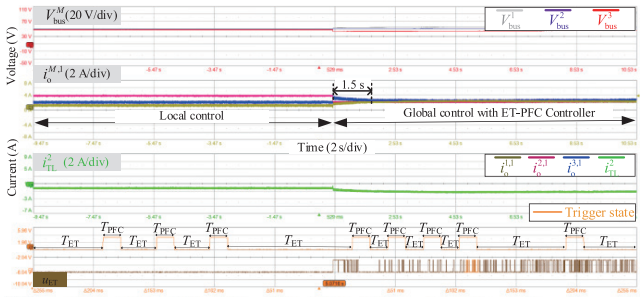

Fig. 14. Power flow management with ET-PFC ($\eta = 1.2$).

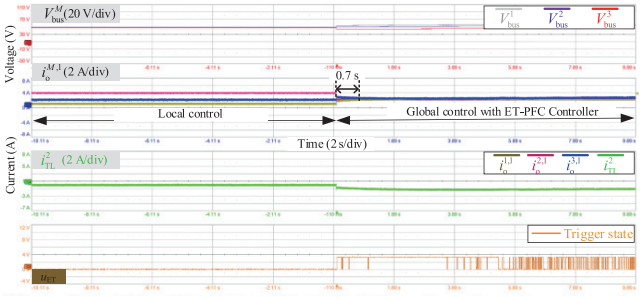

Fig. 15. Power flow management with ET-PFC ($\eta = 0.8$).

TABLE V
THE PROPORTIONAL OF TPFC AND TET UNDER VARYING η

Conditions	T_{PFC} / %	T_{ET} / %
$\eta = 0.8$	62	38
$\eta = 1$	53	47
$\eta = 1.2$	35	65

tion, Figs.14 and 15 show the experimental results of ET-PFC control when η is 1.2 and 0.8, respectively. It can be seen that when the trigger condition is contracted, the trigger condition is more easily satisfied when the global control is started, which increases the time for the system to achieve current sharing; on the contrary, when the trigger condition expands, the PFC controller frequently updates the control sequence in the transient process of the system to speed up the system current sharing. Table V presents the time proportions of T_{ET} and T_{PFC} within 10 seconds after global control activation events in Figs. 11, 14, and 15. These quantitative variations confirm that adjustment of triggering thresholds regulates optimization burden of the PFC controller, achieving computation-resource reallocation without compromising dynamic performance.

Furthermore, since the proposed global controller for the DCMGC employs a distributed communication-based design, it is imperative to investigate the impact of communication delays on system performance. As shown in Fig. 16, experimental results of the global control implementation with intentionally introduced communication delays (30, 80 and 100 ms) reveal a progressive deterioration in system stability as the communication delay increases. This demonstrates the proposed strategy has certain robustness to communication delay.

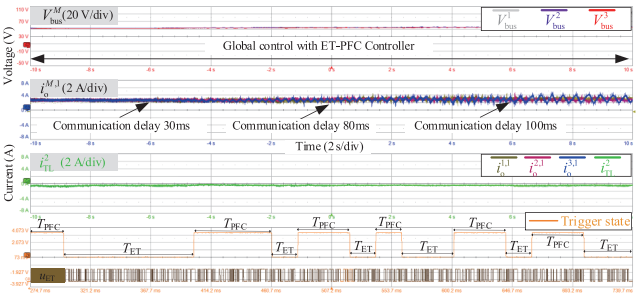

Fig. 16. Experimental result on communication delay in global control with ET-PFC.

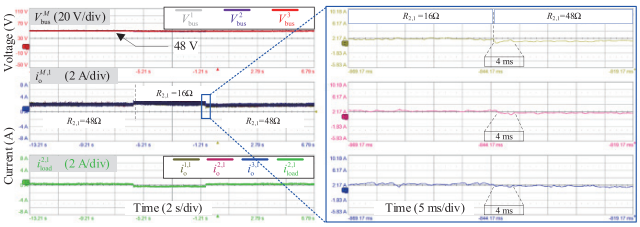

Fig. 17. Transient response to the resistive load step change with PI controller.

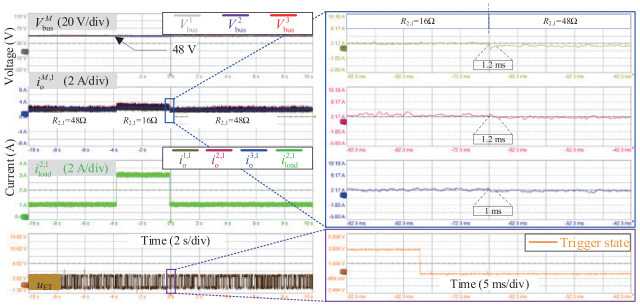

Fig. 18. Transient response to the resistive load step change with ET-PFC.

B. Transient Responses to Load Step Change

To demonstrate the performance of the ET-PFC scheme, the transient response to resistive load step change for the PI control and the ET-PFC are shown in Figs. 17 and 18, respectively. When the load in DCMG#2 $R_{2,1}$ undergoes step changes from 48 Ω to 16 Ω and back to 48 Ω, one can observe that the recovery time with the ET-PFC scheme is around 1−1.2 ms, whereas the PI control takes 4 ms. In other words, the transient response of the ET-PFC scheme is approximately 3−4 times faster than that of the PI control. Furthermore, zoom-in view of u_{ET} in Fig. 18 also indicates that the frequency of u_{ET} is significantly lower than the switching frequency of the DC/DC converter, implying reduction of online computation burden with ET-PFC.

Last, the transient responses to the CPL step changes in Converter#2, 1 with the proposed ET-PFC scheme implementation are given in Fig. 19, and the stable transitions to different magnitudes of CPL load changes demonstrate well stability of

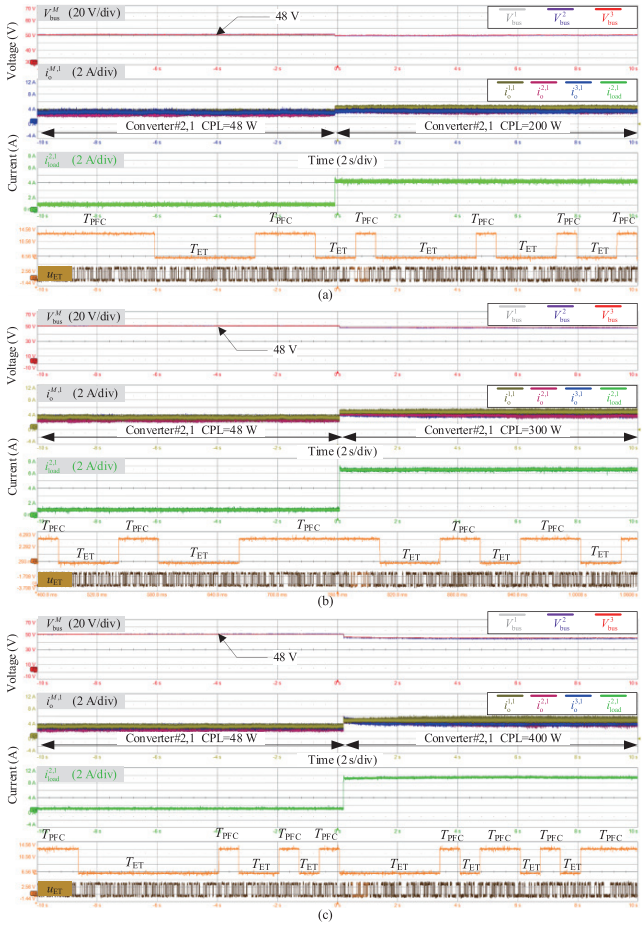

Fig. 19. Transient response to the CPL step change with the ET-PFC. (a) P^2_{CPL} from 48 W to 200 W. (b) P^2_{CPL} from 48 W to 300 W. (c) P^2_{CPL} from 48 W to 400 W.

the system.

VI. Conclusions and Discussions

In this work, power management for the DCMGC with the microcontroller-based implementation of ET-PFC scheme is proposed. Dynamic modeling, controller design and stability guarantee with the proposed control scheme are presented. The hardware-based experimental results have verified superior performance of the proposed scheme. Conclusions can be drawn as follows:

(1) By introducing the ET condition, the ET-PFC has successfully reduced the computation burden of the predictive control in the power management for DCMGCs while preserving the control performance. With this, reduction of the communication resources is another benefit with the ET-PFC.

(2) The steady-state error and dynamic performance of the ET-PFC algorithm outperforms the PI controller. Compared with the PFC algorithm, the computation burden is significantly reduced while the performance remains.

(3) The stability of the proposed control scheme is guaranteed based on the T-S fuzzy modeling approach and Gershgorin circle theorem, which has been corroborated by experimental verification.

(4) The universal low-cost microcontroller (STM32)-based implementation offers a promising solution for practical applications of the proposed scheme in DCMGCs and could be potentially applicable to other similar applications like DC and AC active distribution power systems.

(5) The experimental results show that the ET-PFC scheme has a satisfactory performance in terms of scalability of DCMGCs and integration with renewable energy sources.

While the ET achieves benefits as above, it has several limitations:

(1) Designing event-triggering conditions in the predictive control requires careful tuning to balance performance and resource usage.

(2) Applying ET to large-scale systems remains a grand challenge due to the communication latency and synchronization issues

In future work, evaluations of adaptive ET design and more effective communication means will be conducted.

Appendix
Derivation of the Stability Criterion

Now, to facilitate the simplified analysis of the derived nonlinear model of the DCMGC, the T-S fuzzy modelling method represents the original nonlinear system in (39) by a convex combination of a set of linear subsystem models.

Rule R^k: If z_1 is F_1^k, …, and z_{u} is F_{u}^k, the subsystem can be described as

$$\dot{\boldsymbol{x}}(t)=\boldsymbol{A}_k\cdot\boldsymbol{x}(t)+\boldsymbol{B}_k\cdot\boldsymbol{u}(t) \tag{41}$$

where z_1, …, z_{u} are functions of state variables; F_{u}^k denotes a fuzzy set of z_{u} or so-called membership function and 2^N is the number of fuzzy rules, respectively; $\boldsymbol{A}_k\in\mathbb{R}^{N\times 6N}$, $\boldsymbol{B}_k\in\mathbb{R}^{6N\times 1}$ stand for system matrix the kth fuzzy subsystem, respectively.

The nonlinear system of (39) has N nonlinear terms and each of them requires two linear terms to be constantly approximated, so that 2^N matrix are required for the linearization. Then the matrix $\boldsymbol{A}_k$ can be expressed as

$$\begin{cases}\boldsymbol{A}_k=\begin{bmatrix}\boldsymbol{A}_{k\mathrm{sub}1} & \ddots & \cdots & \cdots & \cdots & \cdots\\ \vdots & \boldsymbol{A}_{k\mathrm{sub}2} & \ddots & \cdots & \cdots & \vdots\\ \vdots & \ddots & \ddots & \ddots & \cdots & \vdots\\ \vdots & \cdots & \ddots & \boldsymbol{A}_{k\mathrm{sub}M} & \ddots & \vdots\\ \vdots & \cdots & \cdots & \ddots & \ddots & \vdots\\ \vdots & \cdots & \cdots & \cdots & \cdots & \boldsymbol{A}_{k\mathrm{sub}N}\end{bmatrix}\\ \boldsymbol{A}_{k\mathrm{sub}M}=\begin{bmatrix}\boldsymbol{A}_{k\mathrm{sub}M11} & \boldsymbol{A}_{k\mathrm{sub}M12} & \boldsymbol{A}_{k\mathrm{sub}M13}\\ \boldsymbol{A}_{k\mathrm{sub}M21} & \boldsymbol{A}_{k\mathrm{sub}M22} & \boldsymbol{A}_{k\mathrm{sub}M23}\\ \boldsymbol{A}_{k\mathrm{sub}M31} & \boldsymbol{A}_{k\mathrm{sub}M32} & \boldsymbol{A}_{k\mathrm{sub}M33}\end{bmatrix},\boldsymbol{A}_k[6M,5(M+1)]=-\dfrac{1}{L_{\mathrm{TL}}^M}\end{cases} \tag{42}$$

The value of $-1/L_{\mathrm{TL}}^N$ in the off-diagonal term implies the coupling between the sub-grids in the DCMGC. Hence, the sub-matrix of DCMG#M $\boldsymbol{A}_{k\mathrm{sub}M}$ containing the nonlinear term can be expressed as (43).

Meanwhile, the nonlinear terms in DCMG#M are approximated by the linear terms of $\boldsymbol{A}_{k\mathrm{sub}M33}$ in (43), choosing x_M to be $x_{\mathrm{min}M}$ or $x_{\mathrm{max}M}$, respectively.

$$\boldsymbol{A}_{k\mathrm{sub}M}=\left[\begin{array}{cccc|cc} 0 & 0 & 0 & -1 & 0 & 0 \\ B_1 & 0 & -1 & B_2+B_3-R_{\mathrm{d}}^{M,i} & 0 & 0 \\ \dfrac{B_1}{C_{M,i}} & \dfrac{K_{\mathrm{iv}}^{M,i}}{C_{M,i}} & -\dfrac{1}{C_{M,i}} & \dfrac{K_{\mathrm{pv}}^{M,i}(B_2+B_3-R_{\mathrm{d}}^{M,i})}{C_{M,i}} & 0 & 0 \\ 0 & 0 & \dfrac{1}{L_{M,i}} & -\dfrac{r_{M,i}}{L_{M,i}} & -\dfrac{1}{L_{M,i}} & 0 \\ 0 & 0 & 0 & \dfrac{1}{C_{\mathrm{bus}}^{M,i}} & -\dfrac{1}{R_{M,i}C_{\mathrm{bus}}^{M,i}}-\dfrac{P_{\mathrm{CPL}}^{M}}{C_{\mathrm{bus}}^{M,i}(V_{\mathrm{bus}}^{0}+x_M)V_{\mathrm{bus}}^{0}} & -\dfrac{1}{C_{\mathrm{bus}}^{M,i}} \\ 0 & 0 & 0 & 0 & -\dfrac{1}{L_{\mathrm{TL}}^{M}} & -\dfrac{r_{\mathrm{TL}}^{M}}{L_{\mathrm{TL}}^{M}} \end{array}\right] \tag{43}$$

By single point fuzzification, multiplicative reasoning and weighted average defuzzification, the T-S fuzzy model is expressed as

$$\dot{\boldsymbol{x}}(t)=\sum_{k=1}^{r=2^N}h_k\left(z_{\mathrm{u}}\right)\cdot\left[\boldsymbol{A}_k\cdot\boldsymbol{x}(t)+\boldsymbol{B}_k\cdot\boldsymbol{u}(t)\right] \tag{44}$$

where $h_k(z_{\mathrm{u}})=\omega_{\mathrm{k}}(z_u)/\sum_{k=1}^{r}\omega_{\mathrm{k}}(z_u)$, and $\omega_k(z_{\mathrm{u}})=\prod_{q=1}^{u}F_{\mathrm{u}}^{k}(z_{\mathrm{u}})$.

The stability of T-S fuzzy model is studied by Lyapunov direct method, and the Lyapunov function candidate is defined as

$$V(\boldsymbol{x},t)=\boldsymbol{x}(t)^{\mathrm{T}}\boldsymbol{P}\boldsymbol{x}(t) \tag{45}$$

Therefore, the stability of the system is guaranteed if exist a $\boldsymbol{P}$ satisfying

$$\begin{cases}\boldsymbol{P}=\boldsymbol{P}^{\mathrm{T}}>0\\ \sum_{k=1}^{2^N}\boldsymbol{A}_k^{\mathrm{T}}\boldsymbol{P}+\boldsymbol{P}\boldsymbol{A}_k<0\end{cases} \tag{46}$$

Bring the linearized matrix $\boldsymbol{A}_k$ into (46) and then determine whether the system is asymptotically stable based on the solvability of the set of linear matrix inequalities (LMIs) (i.e., the existence of $\boldsymbol{P}$). In other words, all the real parts of the eigenvalues of the matrix $\boldsymbol{A}_k$ in (46) are negative, then the system is asymptotically stable. It is difficult to find the eigenvalues directly from the eigenequations when the order of the matrix is high, here we need use the following Gershgorin circle theorem to estimate the range of the eigenvalues.

Theorem 1 [45]: Let matrix $\boldsymbol{A}=(a_{ij})\in C^{n\times n}$, make n circles in the complex plane (called Gale circles, first introduced by Gerschgorin)

$$C_i:\ |Z-a_{ii}|\leqslant R_i,\text{which } R_i=\sum_{j=1,i\neq 1}^{n}|a_{ij}|\quad(i=1,2,\cdots,n) \tag{47}$$

then the set of eigenvalues of $\boldsymbol{A}$ is $\lambda(\boldsymbol{A})\subset\bigcup_{i=1}^{n}C_i=\boldsymbol{G}$($\boldsymbol{G}$ is the Gale circle system of $\boldsymbol{A}$).

Thus, the Gale circle system of $2N$ linear matrices $\boldsymbol{A}_k$ for (44) is described as

$$\sum_{M=3}^{N(N\geqslant 3)}\mathrm{DCMG}\#M:$$

$$\begin{cases}C_{1M}: & |Z-0|\leqslant 1\\ C_{2M}: & |Z-0|\leqslant B_1+B_2+B_3-R_{\mathrm{d}}^{M,i}\\ C_{3M}: & |Z+\dfrac{1}{C_{M,i}}|\leqslant\dfrac{K_{\mathrm{pv}}^{M,i}(B_2+B_3-R_{\mathrm{d}}^{M,i})+B_1+K_{\mathrm{iv}}^{M,i}}{C_{M,i}}\\ C_{4M}: & |Z+\dfrac{r_{M,i}}{L_{M,i}}|\leqslant\dfrac{2}{L_{M,i}}\\ C_{5M}: & |Z+\dfrac{1}{R_{M,i}C_{\mathrm{bus}}^{M,i}}+\dfrac{P_{\mathrm{CPL}}^{M}}{C_{\mathrm{bus}}^{M,i}(V_{\mathrm{bus}}^{0}+x_M)V_{\mathrm{bus}}^{0}}|\leqslant\dfrac{2}{C_{\mathrm{bus}}^{M,i}}\\ C_{6M}: & |Z+\dfrac{r_{\mathrm{TL}}^{M}}{L_{\mathrm{TL}}^{M}}|\leqslant\dfrac{2}{L_{\mathrm{TL}}^{M}}\end{cases} \tag{48}$$

Finally, the eigenvalues need to be satisfied in the left half plane as (40), with this, the derivation is completed.

References

[1] M. Datta, T. Senjyu, A. Yona, T. Funabashi, and K. Chul-Hwan, "A frequency-control approach by photovoltaic generator in a PV– diesel hybrid power system," in *IEEE Transactions on Energy Conversion*, vol. 26, no. 2, pp. 559–571, Jun. 2011.

[2] L. Meng, Q. Shafiee, G. F. Trecate, H. Karimi, D. Fulwani, X. Lu, and J. M. Guerrero, "Review on control of DC microgrids and multiple microgrid clusters," in *IEEE Journal of Emerging and Selected Topics in Power Electronics*, vol. 5, no. 3, pp. 928–948, Sept. 2017,

[3] D. Tan and D. Novosel, "Energy challenge, power electronics & systems (PEAS) technology and grid modernization," in *CPSS Transactions on Power Electronics and Applications*, vol. 2, no. 1, pp. 3–11, 2017.

[4] M. Mao, C. Qian, and Y. Ding, "Decentralized coordination power control for islanding microgrid based on PV/BES-VSG," in *CPSS Transactions on Power Electronics and Applications*, vol. 3, no. 1, pp. 14–24, Mar. 2018.

[5] W. Qi, J. Li, Y. Liu, and C. Liu, "Planning of distributed internet data center microgrids," in *IEEE Transactions on Smart Grid*, vol. 10, no. 1, pp. 762–771, Jan. 2019.

[6] H. Arya and M. Das, "Fast charging station for electric vehicles based on DC microgrid," in *IEEE Journal of Emerging and Selected Topics in Industrial Electronics*, vol. 4, no. 4, pp. 1204–1212, Oct. 2023.

[7] R. Babazadeh-Dizaji, M. Hamzeh, and K. Sheshyekani, "A consensus-based cooperative control for DC microgrids interlinked via multiple converters," in *IEEE Systems Journal*, vol. 15, no. 4, pp. 491–4926, Dec. 2021.

[8] H. Zhang, Y. Wang, H. Yu, and Z. Chen, "A novel flexible multiport interlinking converter for DC microgrid clusters," in *IEEE Transactions on Industry Applications*, vol. 60, no. 2, pp. 2901–2913, Mar.-Apr. 2024.

[9] J. Yang, C. K. Tse, and D. Liu, "Nonlinear behavior and reduced-order models of islanded microgrid," in *IEEE Transactions on Power Electronics*, vol. 37, no. 8, pp. 9212–9225, Aug. 2022.

[10] S. Liu, C. Fang, X. Huang, Q. Zhang, W. Fang, and X. Liu, "A cyber-physical system perspective on large signal stability of DC microgrid clusters," in *CPSS Transactions on Power Electronics and Applications*, vol. 9, no. 1, pp. 112–125, Mar. 2024.

[11] T. Dragičević, X. Lu, J. Vasquez, and J. Guerrero, "DC microgrids–part I: A review of control strategies and stabilization techniques," in *IEEE Transactions on Power Electronics*, vol. 31, no. 7, pp. 4876–4891, Jul. 2015.

[12] A. Iovine, T. Rigaut, G. Damm, E. De Santis, and M. D. Di Benedetto, "Power management for a DC microgrid integrating renewables and storages," in *Control Engineering Practice*, vol. 85, pp. 59–79, Apr. 2019.

[13] J. Peng, B. Fan, Q. Yang, and W. Liu, "Fully distributed discrete-time control of DC microgrids with ZIP loads," in *IEEE Systems Journal*, vol. 16, no. 1, pp. 155–165, Mar. 2022.

[14] U. Vuyyuru, S. Maiti, and C. Chakraborty, "Active power flow Control between DC microgrids," in *IEEE Transactions on Smart Grid*, vol. 10, no. 5, pp. 5712–5723, Sept. 2019.

[15] T. Simon, J.-F. Trégouët, X. Lin-Shi, and H. Morel, "Robust nonlinear control of a power flow controller for meshed DC grids," in *Control Engineering Practice*, vol. 131, pp.105389, 2023.

[16] M. Zaery, P. Wang, W. Wang, and D. Xu, "Distributed global economical load sharing for a cluster of DC microgrids," in *IEEE Transactions on Power Systems*, vol. 35, no. 5, pp. 3410–3420, Sept. 2020.

[17] A. Bidram and A. Davoudi, "Hierarchical structure of microgrids control system," in *IEEE Transactions on Smart Grid*, vol. 3, no. 4, pp. 1963–1976, Dec. 2012.

[18] J. M. Guerrero, M. Chandorkar, T.-L. Lee, and P. C. Loh, "Advanced control architectures for intelligent microgrids—Part I: Decentralized and hierarchical control," in *IEEE Transactions on Industrial Electronics*, vol. 60, no. 4, pp. 1254–1262, Apr. 2013.

[19] Q. Shafiee, T. Dragicevic, J. C. Vasquez, and J. M. Guerrero, "Hierarchical control for multiple DC-microgrids clusters," in *IEEE Transactions on Energy Conversion*, vol. 29, no. 4, pp. 922–933, Dec. 2014.

[20] J. Ma, L. Yuan, Z. Zhao, and F. He,"Transmission loss optimization-based optimal power flow strategy by hierarchical control for DC microgrids," in *IEEE Transactions on Power Electronics*, vol. 32, no. 3, pp. 1952–1963, Mar. 2017.

[21] V. Nasirian, A. Davoudi, F. L. Lewis, and J. M. Guerrero, "Distributed adaptive droop control for DC distribution systems," in *IEEE Transactions on Energy Conversion*, vol. 29, no. 4, pp. 944–956, Dec. 2014.

[22] Q. Li, C. Peng, M. Wang, M. Chen, J. M. Guerrero, and D. Abbott, "Distributed secondary control and management of islanded microgrids via dynamic weights," in *IEEE Transactions on Smart Grid*, vol. 10, no. 2, pp. 2196–2207, Mar. 2019.

[23] M. Badar, I. Ahmad, A. A. Mir, S. Ahmed, and A. Waqas, "An autonomous hybrid DC microgrid with ANN-fuzzy and adaptive terminal sliding mode multi-level control structure," in *Control Engineering Practice*, vol. 121, 2022.

[24] S. Chaturvedi, V.-H. Bui, W. Su, and M. Wang, "Reinforcement learning-based integrated control to Improve the efficiency of DC microgrids," in *IEEE Transactions on Smart Grid*, vol. 15, no. 1, pp. 149–159, Jan. 2024.

[25] Q. Guo, I. Bahri, D. Diallo, and E. Berthelot, "Model predictive control and linear control of DC–DC boost converter in low voltage DC microgrid: An experimental comparative study," in *Control Engineering Practice*, vol. 131, 2023.

[26] J. Hu, Y. Shan, J. M. Guerrero, A. Ioinovici, K. W. Chan, and J. Rodriguez, "Model predictive control of microgrids – An overview," in *Renewable and Sustainable Energy Reviews*, vol. 136, p. 110422, 2021.

[27] T. Wang, H. Kamath, and S. Willard, "Control and optimization of grid-tied photovoltaic storage systems using model predictive control," in *IEEE Transactions on Smart Grid*, vol. 5, no. 2, pp. 1010–1017, Mar. 2014.

[28] Q. Qin, S. Liu, and W. Fu, "Tertiary control based on non-parametric model prediction for DC microgrid cluster," in *Proceedings of 2021 IEEE International Conference on Predictive Control of Electrical Drives and Power Electronics (PRECEDE)*, Jinan, China, 2021, pp. 798–803.

[29] J. Hu, J. Zhu, and J. M. Guerrero, "Model predictive control of smart microgrids," in *Proceedings of 2014 17th International Conference on Electrical Machines and Systems (ICEMS)*, Hangzhou, China, 2014, pp. 2815–2820.

[30] A. Parisio, C. Wiezorek, T. Kyntäjä, J. Elo, K. Strunz, and K. H. Johansson, "Cooperative MPC-based energy management for networked microgrids," in *IEEE Transactions on Smart Grid*, vol. 8, no. 6, pp. 3066–3074, Nov. 2017.

[31] W. Peng, Q. Chen, U. Manandhar, B. Wang, and J. Rodriguez, "Event-triggered model predictive control for the inverter of a grid-connected microgrid with a battery-supercapacitor HESS," in *IEEE Journal of Emerging and Selected Topics in Power Electronics*, vol. 11, no. 6, pp. 5540–5552, Dec. 2023.

[32] R. Liu, S. Liu, J. Zheng, W. Fang and X. Liu, "Function controller design in tertiary level for DC microgrid clusters," in *Proceedings of 2020 IEEE 9th International Power Electronics and Motion Control Conference (IPEMC2020-ECCE Asia)*, Nanjing, China, 2020, pp. 1199–1204.

[33] S. Liu, R. Liu, J. Zheng, and X. Liu,"Predictive function control in tertiary level for power flow management of DC microgrid clusters," in *Electronics Letters*, vol. 56, no. 13, pp. 675–676, Jun. 2020.

[34] J. Ma, R. Liu, Q. Qin, S. Liu, and X. Liu, "Distributed predictive tertiary control for DC microgrid clusters," in *Proceedings of 2021 IEEE International Conference on Predictive Control of Electrical Drives and Power Electronics (PRECEDE)*, Jinan, China, 2021, pp. 804–809.

[35] Y.-G. Xi, D.-W. Li, and S. Lin, "Model predictive control-status and challenges," in *Acta Automatica Sinica*, vol. 39, no. 3, pp. 222–236, 2014.

[36] X. Dong, J. Gan, H. Wu, C. Deng, S. Liu, and C. Song, "Self-triggered model predictive control of AC microgrids with physical and communication state constraints," in *Energies*, vol. 15, no. 3, 2022.

[37] P. Ge, B. Chen, F. J. I. J. o. R. Teng, and N. Control, "Event-triggered distributed model predictive control for resilient voltage control of an islanded microgrid, " in *International Journal of Robust and Nonlinear Control*, vol. 31, no. 6, pp. 1979–2000, 2021.

[38] B. Wang, J. Huang, C. Wen, J. Rodriguez, C. Garcia, H. B. Gooi, and Z. Zeng, "Event-triggered model predictive control for power converters," in *IEEE Transactions on Industrial Electronics*, vol. 68, no. 1, pp. 715–720, Jan. 2021.

[39] Q. Sun, J. Chen, and Y. Shi, "Integral-type event-triggered model predictive control of nonlinear systems with additive disturbance," in *IEEE Transactions on Cybernetics*, vol. 51, no. 12, pp. 5921–5929, Dec. 2021.

[40] T. Zhou, S. Liu, J. Diao, Q. Zhang, W. Fang, and X. Liu, "Event-triggered predictive function control of DC microgrid clusters," in *Proceedings of 2023 IEEE International Conference on Predictive Control of Electrical Drives and Power Electronics (PRECEDE)*, Wuhan, China, 2023, pp. 1–6.

[41] S. Liu, G. Hu, M. Xia, Q. Zhang, W. Fang, and X. Liu,"Detection and mitigation via alternative data for false data injection attacks in DC microgrid cluster," in *CPSS Transactions on Power Electronics and Applications*, vol. 9, no. 1, pp. 27–34, Mar. 2024.

[42] R. W. Erickson and D. Maksimovic, in *Fundamentals of Power Electronics*, Switzerland: Springer Cham, 2020.

[43] P. Tabuada, "Event-triggered real-time scheduling of stabilizing control tasks," in *IEEE Transactions on Automatic Control*, vol. 52, no. 9, pp. 1680–1685, Sept. 2007.

[44] D. Peng, M. Huang, J. Li, J. Sun, X. Zha, and C. Wang, "Large-signal stability criterion for parallel-connected DC-DC converters with current source equivalence," in *IEEE Transactions on Circuits and Systems II: Express Briefs*, vol. 66, no. 12, pp. 2037–2041, Dec. 2019.

[45] S. A. Gershgorin, "Uber die abgrenzung der eigenwerte einer matrix," *Известия Российской академии наук. Серия математическая*, no. 6, pp. 749–754, 1931.

Sucheng Liu received Ph. D. degree in electrical engineering from Chongqing University, Chongqing, China, in 2013. He has been with the School of Electrical and Information Engineering, Anhui University of Technology, where he is currently a Full Professor. He was a Visiting Research Associate with Queen's University, Kingston, Ontario, Canada, where he conducted two research projects sponsored by GE and NSERC, from Feb. 2015 to Feb. 2016, and a Visiting Research Fellow with Nanyang Technological University, Singapore, from Sept. 2024 to Feb. 2025. His research interests include modeling and control of DC microgrids and clusters and switching power converters. He has published more than 60 refereed journal and conference papers and holds 16 patents and has 4 patents pending.

Dr. Liu is an IEEE Member, a CPSS Member, and a Member of IEEE Power Electronics Society. He also serves as an active reviewer for a dozen of international journals and conferences, such as *IEEE Transactions on Power Electronics, IEEE JESTPE, IEEE Open Journal of Power Electronics, IEEE Transactions on Industrial Electronics*, etc. He served as TPC members and Session Chairs for multiple conferences. He received Best Paper Awards at the IEEE International Conference on Predictive Control of Electrical Drives and Power Electronics (PRECEDE), Jinan, China, in 2021, IEEE International Conference on DC Microgrids (ICDCM), Matsue, Japan, in 2019, and The China Power Supply Society Conference (CPSSC), Shanghai, China, in 2017, respectively.

Taohu Zhou was born in Anhui, China, in 1998. He received the B.S. degree in electrical engineering from Anhui University of Technology, Ma'anshan, China, in 2021, where he is currently pursuing the M.S. degree in electrical engineering. His research interests include the predictive control and event-triggered control of DC microgrid cluster systems.

Tao Hong was born in Anhui, China, in 1999. He received the B.S. degree in electrical engineering from Anhui University of Technology, Ma'anshan, China, in 2022, where he is currently pursuing the M.S. degree in electrical engineering. His research interests include the modeling and small signal stability analysis of DC microgrid cluster system

Qianjin Zhang received his Ph.D. degree in power electronics from Chongqing University, Chongqing, China, in 2020.

He was a Visiting Scholar in the University of Exeter, Penryn, U.K., from May 2018 to May 2019. He is presently a Lecture with Anhui University of Technology, Anhui, China. His research interests include PV power generation, the modeling, control, and stability analysis of power electronics system.

Wei Fang was born in Anhui Province, China, in 1977. He received the B.S. degree from Anhui university of Technology, Anhui, China, in 1998, and M.S. and Ph.D. degrees from Nanjing University of Aeronautics and Astronautics, Nanjing, China, in 2004 and 2008, respectively. He has been with Anhui university of Technology, since 2008 and is currently a professor in the School of Electrical and Information Engineering, Anhui university of Technology. He was a visiting scholar at Queen's University, Kinston, Ontario, Canada, from Sept. 2010 to Feb. 2011. His research interests are in the areas of switching power converters, and renewable energy.

Xiaodong Liu was born in Jilin, China, in 1971. He received the Ph.D. degree in electric machines and electric apparatus from Zhejiang University, Hangzhou, China, in 1999. Since 2003, he has been with School of Electrical and Information Engineering, Anhui University of Technology, Ma'anshan, China, where he is now a full professor. He was a visiting scholar at Queen's University, Kinston, Ontario, Canada, from July 2007 to Oct. 2007. His major fields of interest include the dc-dc switching converter, power factor correction techniques, and motor design and driving control.

Quality Management of Energy Storage VSG Based on Odd-Order Repetitive Control

Yifei SUN, Jinghua ZHOU, Shasha CHEN, and Tianfeng LAN

***Abstract*—As renewable energy integration reduces grid strength, energy storage virtual synchronous generator (VSG) control becomes critical for grid support. However, power quality challenges arise from nonlinear loads and background harmonics in distribution networks. This study addresses energy storage VSG's power quality limitations by proposing a sensor-free selective control strategy to optimize point of common coupling (PCC) voltage or grid current without altering existing VSG structures. An odd-order repetitive control technique reshapes harmonic impedance, supported by a grid-VSG harmonic impedance model. Two supplementary loops selectively suppress voltage/current harmonics, enhancing power quality management without external sensors or harmonic extraction modules. The method eliminates hardware additions while resolving VSG harmonic issues in micro-grids and large grids. Results demonstrate significant improvements in harmonic mitigation, enabling energy storage VSG systems to partially replace active power filters (APFs). This approach offers a cost-effective solution for harmonizing renewable integration with grid stability, broadening VSG applicability. Key innovations include dual-loop adaptive harmonic suppression and impedance reshaping through modified repetitive control, advancing sensor-less power quality enhancement in modern power systems. The strategy effectively balances grid support functionality with harmonic management, facilitating scalable renewable energy adoption.**

***Index Terms*—Harmonic impedance reshaping, odd-order repetitive control, power conversion system, power quality, virtual synchronous generator.**

Nomenclature

VSG	Virtual synchronous generator.
PCC	Point of common coupling.
APF	Active power filter.
ORC	Odd-order repetitive control.
RC	Repetitive control.
PCS	Power conversion system.
VI	Virtual impedance.
THD	Total harmonic distortion.
V2G	Vehicle-to-grid.
PMR	Proportional multi-resonant.
VPI	Vector proportional-integral.
PLL	Phase-locked loop.
PI	Proportional-integral.
PWM	Pulse width modulation.
$v_{ga,b,c}(v_g)$	Grid voltage.
$v_{oa,b,c}(v_o)$	PCS voltage.
$i_{ga,b,c}(i_g)$	Grid current.
$i_{oa,b,c}(i_o)$	VSG current.
L_g	Grid impedance.
IGBT	Insulate-gate bipolar transistor.
R_L	Linear load.
LC	Nonlinear load filter.
L_fC_f	PCS filter.
$i_{La,b,c}(i_L)$	Inductor currents of PCS.
v_{dc}	DC voltage.
i_{dc}	DC current.
$v_{a,b,c}$	Voltage of C_f.
θ_{PLL}	Grid angle.
P_e	Average active power.
Q_e	Average reactive· power.
ω_c	Power filter cutoff frequency.
P_m	Mechanical power of VSG.
P_{ref}	Reference active power.
J	Rotational inertia.
D	Damping of the governor.
K_f	Active power droop coefficient.
ω_n	Rated angular frequency.
ω	Angular frequency of VSG.
θ	Output angular of VSG.
Q_m	Total reactive power reference.
Q_{ref}	Reactive power reference.
K_V	Reactive power droop coefficient.
K_Q	Excitation regulation coefficient.
V_{ref}	Reference voltage (peak).
V	Grid voltage (peak).
E_p	VSG internal electromotive force (peak).

Manuscript received January 13, 2025; revised February 23, 2025 and March 20, 2025; accepted April 19, 2025. Date of publication September 30, 2025; date of current version May 12, 2025. This work was supported in part by Beijing Municipal Natural Science Foundation under Grant L242007. (*Corresponding author: Jinghua Zhou.*)

Y. Sun and S. Chen are with School of Electrical and Control Engineering, North China University of Technology, Beijing 100043, China (e-mail: sunyifei@mail.ncut.edu.cn; chenshasha77@126.com).

J. Zhou is with Beijing Laboratory of New Energy Storage Technology, Beijing Municipal Education Commission and North China University of Technology, Beijing 100043, China (e-mail: zjh@ncut.edu.cn).

T. Lan is with Shanghai Electrical Apparatus Research Institute(Group) Co., Ltd., Shanghai 200333, China (e-mail: lantf@seari.com.cn).

Digital Object Identifier 10.24295/CPSSTPEA.2025.00019

e_{VSG}	VSG internal electromotive force.
m_{abc}	Modulation wave signals.
$G_u(s)$	Voltage PI regulator.
$Z_v(s)$	VI-component.
k_c	Current proportional coefficient.
$G_i(s)$	Closed-loop transfer functions.
$Z_o(s)$	Output impedance of VSG.
$Z_g(s)$	Grid impedance.
Z_o^h	VSG h-th harmonic impedance.
Z_g^h	Grid h-th harmonic impedance.
$M_{rc}(s)$	RC internal model.
$M_{orc}(s)$	ORC internal model.
$G_{orc}(z)$	ORC discrete implementation.
T_s	Discretization time.
$P_{non\text{-}load}$	Nonlinear load power.
L_v, R_v	VI parameters.

I. Introduction

With the rapid development of modern power systems, the integration of power electronic converters into microgrids and the main grid has introduced challenges such as reduced damping, weak inertia, and insufficient transient voltage support, which affect grid stability. The power conversion system (PCS), serving as the interface between energy storage devices and the grid/load, is a key component in energy storage systems. Among various control strategies, the energy storage virtual synchronous generator (VSG) is a promising solution to address these challenges[1], [2]. Moreover, the integration of nonlinear loads into distribution networks has worsened harmonic pollution, leading to significant power quality issues. These include increased line losses, transformer overheating, and mechanical vibrations, which threaten the stable operation of the grid. Therefore, further research on power quality management for energy storage VSGs is urgently needed.

Fig. 1 illustrates the harmonic suppression strategies for different types of inverters, which will be discussed separately. Research on power quality harmonic suppression methods for converters has predominantly focused on grid-following converters. Since these converters are current-controlled sources, suppressing internal harmonics (self-generated harmonic currents) is relatively straightforward. Techniques from [3]–[5] can effectively mitigate the harmonic currents they produce. [6] proposed a direct adaptive control strategy, achieving effective harmonic suppression of grid-connected converter output currents. External harmonic currents can be compensated for by installing passive filters or centralized active power filters (APFs) [7]. However, these solutions may introduce resonance problems and require additional inductive/capacitive components, which increase both system costs and maintenance complexity. To independently suppress external harmonic currents caused by nonlinear loads, a harmonic current compensation based on frequency-domain repetitive control was proposed in [8], aiming to counteract the harmonic currents generated by nonlinear loads. Additionally, by applying appropriate PCC

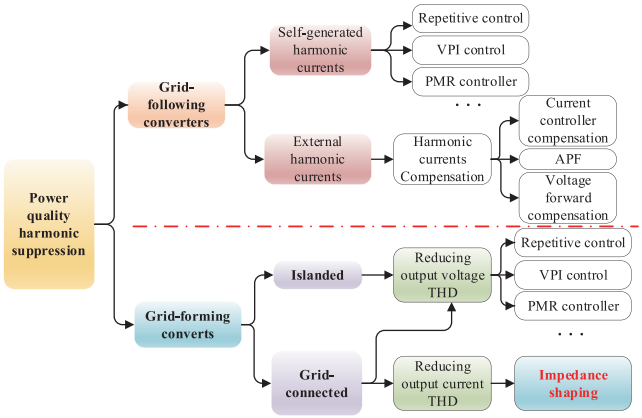

Fig. 1. Different harmonic suppression methods.

voltage feedforward control, the harmonic impedance of the inverter can be driven to infinity [9], significantly improving the power quality at the PCC point and providing some of the effects of an APF.

However, grid-forming energy storage converters exhibit voltage control characteristics, which differ from the current control characteristics of grid-following converters. As a result, traditional harmonic suppression methods designed for grid-following converters cannot be directly applied to energy storage VSG. Current research on power quality management for energy storage VSGs can be categorized into two main scenarios: islanded and grid-connected.

In islanded mode, VSGs act as voltage sources and should maintain the highest possible output voltage quality. The control objectives for energy storage VSG in islanded operation are clear. [10] proposed using third-order general integrator strategies to separate harmonic currents, which are then combined with variable virtual impedance to provide voltage harmonic compensation fed forward into the modulation wave, thereby reducing output voltage THD. However, this strategy alters the VSG's virtual impedance (VI), which is generally undesirable in practical applications, as VI also serves critical functions such as current limiting and grid strength adaptation, should not be easily changed. [11] proposed a control strategy involving adaptive VI to address this issue during fault conditions, thereby enhancing the VSG's output voltage quality. [12] introduced a method based on impedance angle estimation, enabling optimized VI adjustments to improve the output voltage quality when multiple VSGs operate in parallel under islanded conditions. [13] proposed a VSG quasi-harmonic voltage feedforward control method based on the rated and sampled voltages, which significantly reduces the harmonic impedance of the VSG, bringing it closer to an ideal voltage source. This improvement enhances the output voltage quality; however, it does not provide the capability to optimize the output current quality. [14] utilized repetitive control and a voltage-current harmonic extraction module to obtain harmonic information. This information is then multiplied by a variable coefficient to reshape the VSG's harmonic impedance, addressing the voltage harmonic suppression issue in islanded microgrids. However, this strategy does not account for hardware real-time

constraints. Repetitive control itself is already resource-intensive for digital processing controllers, and with the addition of the complex harmonic extraction module, there is a risk that the algorithm may not complete within the required time under high switching frequency conditions. [15] eliminated the voltage-current harmonic extraction and adopted PMR in the inner loop of the VSG. By setting different controller coefficients, voltage and current harmonics are compensated separately. This strategy involves more parameters, compared to [14], it significantly improves software running speed and enhances practical applicability. The strategy has been successfully applied in V2G interconnected systems. [16] proposed an optimization control strategy for off-grid energy storage converters based on the internal model principle of repetitive control. This strategy is simple to design and does not require harmonic current extraction; however, it has not been thoroughly tested on grid-forming energy storage converters and is limited to voltage harmonic suppression. Additionally, [17] compared the performance of model predictive control in suppressing VSG output harmonics under resistive load conditions, demonstrating lower harmonic distortion compared to conventional control.

In grid-connected, the situation becomes more complex, the power quality optimization objective can be divided into two aspects:

- Optimizing the converter's output current;
- Optimizing the converter's output voltage.

The issue then becomes whether the harmonic current flows to the grid or to the grid-forming energy storage converter. If the optimization goal is to optimize the converter's output current, the majority of the harmonic current flows to the grid. However, if the goal is to optimize the converter's output voltage, the majority of the harmonic current flows into the converter, which then acts as an APF to supply harmonic current to the nonlinear loads. Based on this concept, [18]–[21] have established a harmonic impedance model for grid-forming energy storage converters and proposed a harmonic current distortion suppression method based on impedance shaping, which optimizes the grid current. These studies propose adding reactors at the PCC point to reduce the harmonic impedance between the PCC and the converter, thereby adapting to a wide range of grid impedance variations and optimizing the grid current. However, this strategy is challenging to implement in practice and requires additional hardware costs, such as low-latency data communication for relevant data acquisition. If the goal is to optimize the PCC voltage, research on this subject is limited, the relevant strategies can refer to the control of grid-forming energy storage VSGs in islanded operation[10]–[16]. [22] proposed adding harmonic voltage and current feedback control loops into modulation wave based on the existing VSG control framework to suppress converter output voltage harmonics. This strategy requires external load current sampling to obtain current and voltage harmonics, and the design of harmonic feedback control loop parameters is complex, involving numerous control parameters.

Existing research primarily concentrates on harmonic extraction and impedance reshaping strategies, which incur additional hardware costs and require the integration of multiple harmonic extraction and calculation modules. This paper proposes a harmonic suppression controller for grid-forming energy storage converters, utilizing the internal model principle and harmonic impedance reshaping. The innovations of this paper are as follows:

1) It respects the existing hardware design of energy storage converters and achieves PCC voltage optimization or output current optimization without adding extra voltage or current sensors.

2) Most previous studies have separated PCC voltage optimization and output current optimization, requiring harmonic extraction modules[18]–[21]. The proposed control strategy in this paper does not require harmonic extraction modules. Users can flexibly choose to suppress current or voltage harmonics, and the controller parameter design is simple.

The structure of this paper is organized as follows: Section II formulates the system model under investigation and introduces the impedance equivalent model of the energy storage VSG. Section III proposes a novel control, developed based on the impedance equivalent model, utilizing odd-order repetitive control. Section IV presents experimental validation of the proposed control strategy, demonstrating its accuracy and practical feasibility. Finally, Section V concludes the paper, summarizing the key findings and implications of the study.

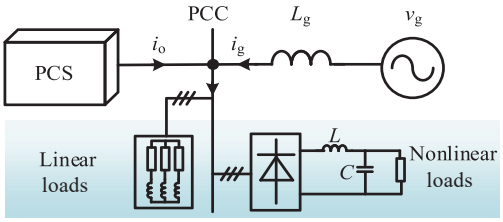

Fig. 2. System diagram of the energy storage converter.

II. System Structure and Equivalent Impedance Model

A. System Structure Under Study

The system configuration of the energy storage converter is depicted in Fig. 2. This simplified schematic outlines the connection between the PCS and the grid. The left represents the PCS device, with its output side connected to the grid through the PCC. Positioned to the right of the PCC, the inductor L_g symbolizes the grid impedance.

B. Energy Storage VSG Control

Fig. 3(a) illustrates the main circuit diagram of the PCS. The circuit topology employs a three-phase six-switch structure, where S1 to S6 represent IGBTs, and L_f and C_f denote the filter inductance and filter capacitance, respectively. The system samples the DC voltage v_{dc}, DC current i_{dc}, inductor currents i_{La}, i_{Lb}, and i_{Lc}, as well as the output currents i_a, i_b, and i_c. The voltages on both sides of the AC switch are v_a, v_b, v_c, v_{ga}, v_{gb},

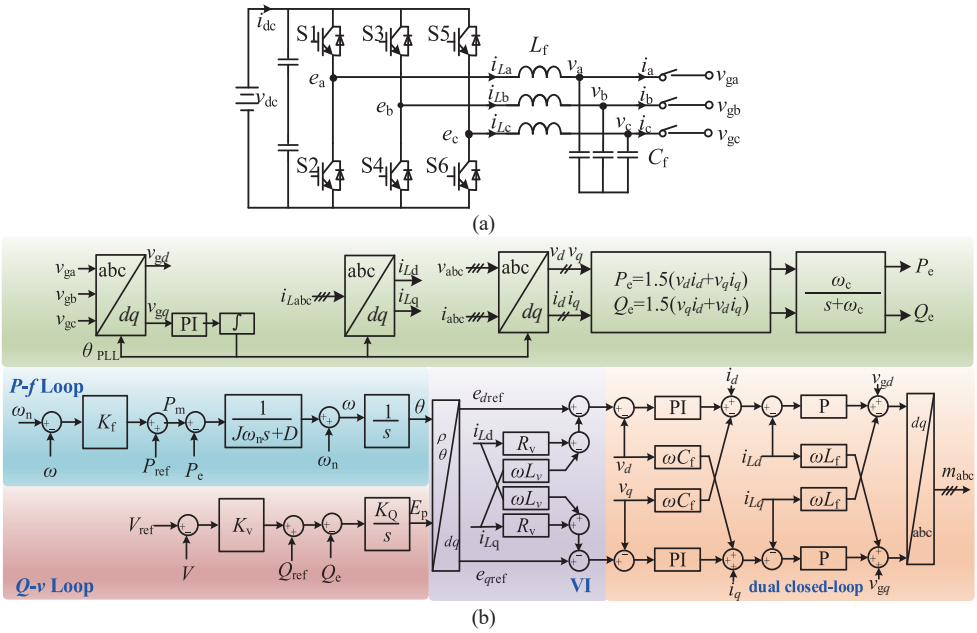

Fig. 3. Main circuit of PCS and VSG control block diagram. (a) Main circuit, (b) Control structure of VSG.

and v_{gc}.

Fig. 3(b) illustrates the control strategy of the VSG. The energy storage VSG control algorithm consists several modules, including the phase-locked loop (PLL), power calculation and filtering, *P-f* loop, *Q-v* loop, VI, and dual closed-loop control.

The instantaneous electromagnetic power output from the VSG is calculated using the three-phase instantaneous power theory as shown in Fig. 3(b). The average electromagnetic power P_e and reactive power Q_e of the VSG are derived by passing through a first-order low-pass filter with a cutoff frequency ω_c.

In the *P-f* loop, the primary frequency regulation function is achieved by simulating the behavior of a synchronous generator governor. *J* and *D* represent the rotational inertia and damping of the governor, respectively. The mathematical expressions for these are:

$$P_m = P_{ref} + K_f(\omega_n - \omega) \tag{1}$$

P_m represents the mechanical power of VSG, while P_{ref} is the reference active power. K_f denotes the active power-frequency droop coefficient. ω_n represent the rated angular frequency. In the *P-f* loop, the functions of inertia and damping are modeled by the rotor dynamics equation of a synchronous generator [1]. The mathematical expression for the first-order transfer function is:

$$P_m - P_e - D(\omega - \omega_n) = J\omega\frac{d\omega}{dt} \approx J\omega_n\frac{d\omega}{dt} \tag{2}$$

In the *P-f* loop, the expression for the VSG output angular velocity and angle is given by:

$$d\theta = dt = \omega \tag{3}$$

In the *Q-v* loop, the primary voltage regulation function is achieved by simulating the reactive power voltage droop characteristic of a synchronous generator. Q_m represents the total reactive power reference of the VSG, and its mathematical expression is:

$$Q_m = Q_{ref} + K_V(V_{ref} - V) \tag{4}$$

In the *Q-v* loop, the output voltage control is realized by simulating the excitation regulator of a synchronous generator. The mathematical expression is:

$$E_p = K_Q\int(Q_m - Q_e)dt \tag{5}$$

Within the *Q-v* loop, the reference voltage amplitude E_p is generated based on the output angle θ from the *P-f* loop. Through a coordinate transformation, the internal reference voltage for the VSG is derived. This reference voltage is then processed through VI and a dual closed-loop control to generate the modulation wave signals m_{abc}. These modulation signals are compared with carrier signals, which ultimately producing pulse signals that control the switches S1 to S6.

C. VSG Equivalent Impedance Model

The equivalent voltage-current control diagram of the VSG in the *abc* coordinate system is depicted in Fig. 4. The internal electromotive force of the VSG, denoted as e_{VSG}, is synthesized using e_o and angle θ, as shown in Fig. 3(b). The voltage proportional-integral (PI) regulator is represented by $G_u(s)$, whose expression is provided in (6). Additionally, k_e denotes the proportional gain of current inner-loop. The k_{pwm} represents the equivalent gain of the inverter bridge and can be considered a constant value of 1. $Z_v(s)$ is the VI component, and its expression is given in (7).

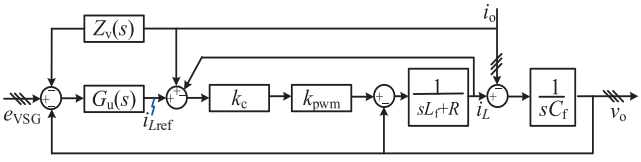

Fig. 4. Traditional VSG control equivalent voltage-current dual-loop control block diagram.

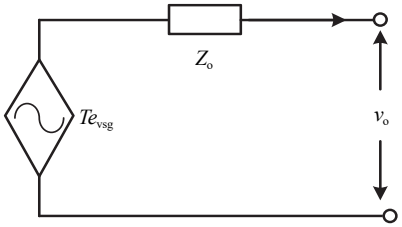

Fig. 5. VSG equivalent voltage source diagram.

$$G_u(s) = k_p + \frac{k_i}{s} \tag{6}$$

$$Z_v(s) = L_v(s) + R_v \tag{7}$$

The closed-loop transfer functions of the current loop and voltage loop can be derived from Fig. 4 as follows:

$$G_i(s) = \frac{i_L}{i_{Lref}} = \frac{k_c k_{pwm} \dfrac{1}{sL_f + R}}{1 + k_c k_{pwm} \dfrac{1}{sL_f + R}} \tag{8}$$

$$v_o(s) = \frac{G_u(s)G_i(s)}{Cs + G_u(s)G_i(s)}[e_{VSG}(s) - i_o(s)Z_v(s)] - \frac{1}{Cs + G_u(s)G_i(s)} i_o(s) \tag{9}$$

From (8) and (9), the voltage and current control loops of the traditional VSG can be equivalently modeled as a controllable voltage source with an external impedance, as shown in Fig. 5. Here, T and Z_o are defined by (10).

$$\begin{cases} T(s) = \dfrac{G_u(s)G_i(s)}{Cs + G_u(s)G_i(s)} \\ Z_o(s) = \dfrac{G_u(s)G_i(s)Z_v(s) + 1}{Cs + G_u(s)G_i(s)} \end{cases} \tag{10}$$

As illustrated in Fig. 5, the harmonic equivalent circuit of the VSG, load, and grid is further depicted in Fig. 6. The nonlinear load is modeled as a harmonic current source. In the absence of any special control, the harmonic impedance of the VSG, $Z_o^h(s)$, is equal to the grid impedance, $Z_o(s)$. The harmonic impedance of the grid is denoted as $Z_g^h(s) = Z_g(s)$.

Based on (10), the bode plot of the output impedance of the VSG and the grid is shown in Fig. 7. In Zone 1, where the VSG output impedance is greater than the grid output impedance, the grid absorbs a larger portion of the harmonic currents introduced by the nonlinear load. Conversely, in Zone 2, where the VSG output impedance is smaller than the grid output impedance, the VSG absorbs a larger portion of the harmonic currents from the nonlinear load.

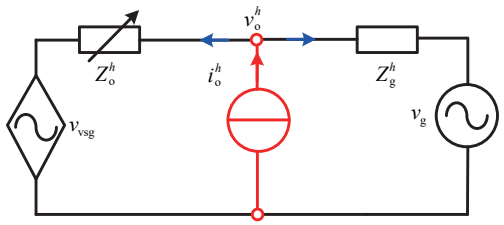

Fig. 6. Harmonic equivalent circuit diagram of VSG, load and grid connection.

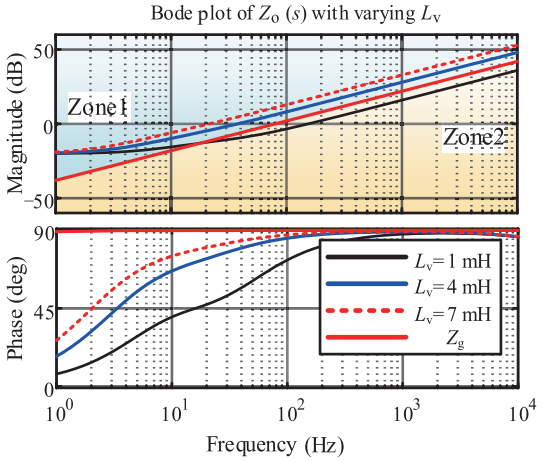

Fig. 7. Bode plot of VSG output impedance and grid impedance.

If the harmonic impedance of the VSG can be adjusted across different harmonic frequency bands, it would enable effective harmonic suppression and allow targeted control of harmonic current flow. This capability would facilitate the achievement of various control objectives by optimizing the distribution of harmonic current, offering an adaptable solution for different operational conditions.

III. Harmonic Impedance Reshaping Strategy Based on Odd-Order Repetitive Control

A. Principle of Odd-Order Repetitive Control

The basic principle of odd-order repetitive control is derived from the internal model principle, which introduces poles corresponding to targeted harmonic frequencies into the feedback loop. This internal model matches the dynamic characteristics of external periodic disturbance signals, enabling the control system to achieve near-zero steady-state error tracking for periodic reference signals and effectively suppress harmonic disturbances.

Fig. 8 presents a comparative illustration of the internal model structures used in traditional repetitive control (RC) and odd-order repetitive control (ORC). Here, u denotes the

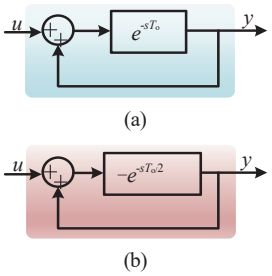

Fig. 8. Internal models of repetitive control. (a) RC internal model, (b) ORC internal model.

reference input signal, y is the output of the controller's internal model, T_o denotes the fundamental period of reference signal, and s denotes the differential operator.

The transfer functions of the internal models for the RC and ORC are given as follows:

$$M_{rc}(s)=\frac{e^{-sT_o}}{1-e^{-sT_o}}=\frac{1}{e^{sT_o}-1} \tag{11}$$

$$M_{orc}(s)=\frac{-e^{-sT_o/2}}{1+e^{-sT_o/2}}=\frac{-1}{e^{sT_o/2}+1} \tag{12}$$

As demonstrated in (11) and (12), the ORC utilizes $T_o/2$ storage units per cycle, representing a 50% reduction compared to the RC implementation. This structural advantage significantly lowers computational complexity while reducing hardware processor load. To extend the analysis of $M_{orc}(s)$, the following derivation is presented:

$$M_{orc}(s)=-\frac{1}{2}+\frac{4}{T}\sum_{k=1,3,5,7,\cdots}^{2n-1}\frac{s}{s^2+(k\omega_o)^2} \tag{13}$$

According to (13), M_{orc} is equivalent to multiple parallel PR controllers, and its internal model characteristics cover the fundamental frequency and its odd-order harmonic frequency bands of sine signals. This feature provides a theoretical basis for optimizing and shaping the impedance characteristics of the VSG [23].

Fig. 9 illustrates a comparison of the amplitude-frequency responses of the RC and ORC. The results demonstrate that at odd harmonic frequencies, the bandwidth of ORC (ω_{orc}) is twice that of RC (ω_{rc}) [24]. This implies that when the frequency fluctuates, the controller based on ORC internal model has stronger adaptability than the controller based on the RC internal model.

As shown in Fig. 2, the harmonic components are predominantly odd-order. The ORC not only requires fewer hardware resources, but also delivers superior performance in harmonic suppression. Based on this observation, this paper proposes a harmonic impedance reshaping strategy based on odd-order repetitive control, to exploit its advantages in power quality management.

Since the controller design is implemented in the discrete domain, the ORC controller is implemented as shown in Fig. 10. The transfer function expression is provided in (14).

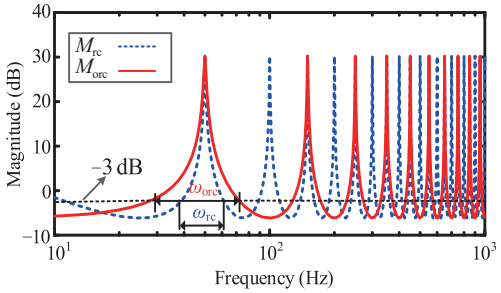

Fig. 9. Comparison of amplitude-frequency characteristics between RC and ORC.

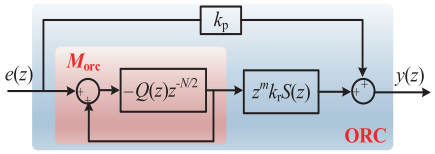

Fig. 10. Odd-order repetitive control discrete domain implementation.

$$G_{ORC}(z)=\frac{-Q(z)z^{-N/2}}{1+Q(z)z^{-N/2}}z^m k_r S(z)+k_p \tag{14}$$

The functions of each component in (14) are explained as follows:

- $e(z)$: Error signal;
- $y(z)$: Controller output;
- k_p: Proportional controller in parallel with the odd-order repetitive control;
- k_r: Internal gain coefficient of the odd-order repetitive control;
- $Q(z)$: Internal constant of the odd-order repetitive controller, or a zero-phase low-pass filter;
- $S(z)$: Low-pass filter;
- z^m: Phase lead compensation;
- N: Represents the sampling point period, where $N=f_s/f_g$, with f_s being the switching frequency and f_g being the grid frequency.

The proportional controller k_p effectively improves the dynamic response performance of the system, while the internal gain coefficient k_r adjusts the amplitude of the output signal, to ensure stability. The internal constant $Q(z)$ plays a crucial role in maintaining the stability of the system. The low-pass filter $S(z)$ further enhances the system's stability by attenuating high-frequency gains. Furthermore, the phase lead compensation z^m compensates for the phase delay introduced by $S(z)$ and the controlled system, ensuring that the system's phase characteristics in the frequency domain meet the design requirements.

B. The Proposed Controller Design

The power quality management control strategy based on ORC is illustrated in Fig. 11.

Compared with Fig. 3(b), the proposed control strategy achieves both voltage and current harmonic mitigation by adding only two simple loops and a three-way switch. When the

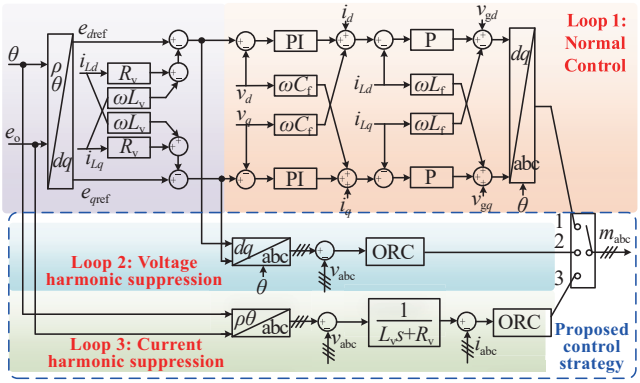

Fig. 11. The proposed control strategy.

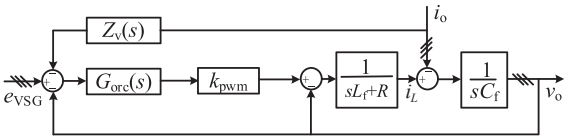

Fig. 12. VSG voltage harmonic suppression control block diagram.

switch is in position 1, the energy storage converter operates in the traditional grid-connected mode; when in position 2, the converter activates the voltage harmonic suppression; and in position 3, the converter performs current harmonic suppression. The proposed strategy significantly simplifies the software structure, enabling multifunctional harmonic mitigation while enhancing system flexibility and adaptability. For the ORC parameter design, readers can refer to [25], [26].

C. Analysis of the Proposed Controller's Capabilities

1) Voltage Harmonic Suppression Loop

The control block diagram of the voltage harmonic suppression loop, based on ORC control strategy is shown in Fig. 12. This loop is designed primarily as a voltage control loop, utilizing the ORC method. While the structure also allows for the addition of a current control loop in the subsequent stage, the focus of this paper is specifically on the design of the voltage loop. Thus, the current control loop is not discussed further in this study. This streamlined focus on the voltage loop ensures that the core functionality of the proposed strategy is fully explored, while the current loop remains a secondary consideration for future research.

The output impedance of the voltage harmonic suppression loop is given by:

$$Z_{out}(s)=\frac{v_o}{i_o}=\frac{\dfrac{1}{sC_f}+\dfrac{sL+R}{s^2LC_f+sRC_f}}{1+G_{orc}(s)k_{pwm}Z_v(s)} \tag{15}$$

Fig. 13 illustrates the magnitude-frequency characteristics of the output impedance Z_o of the grid-forming power conversion system and the grid output impedance Z_g in the frequency domain. The blue curve represents Z_o, which displays a notch filter characteristic at odd harmonic frequencies (e.g., 1st, 3rd,

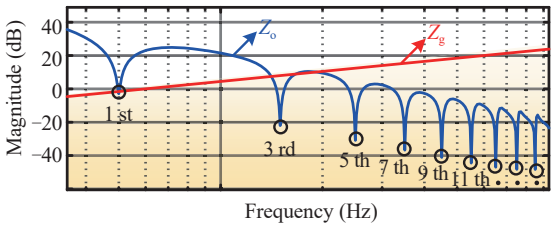

Fig. 13. The Magnitude-frequency characteristic curve of the VSG voltage harmonic suppression.

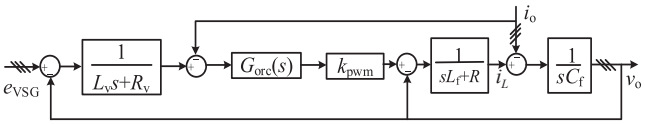

Fig. 14. VSG current harmonic suppression control block diagram.

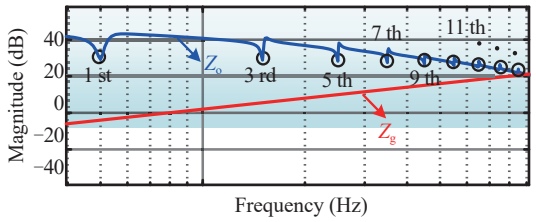

Fig. 15. The magnitude-frequency characteristics curve of the VSG current harmonic suppression.

5th, etc.). In contrast, the red straight line represents Z_g, which increases linearly with frequency.

At those odd harmonic frequencies, the significant reduction in Z_o and the relatively high Z_g cause harmonic currents to flow primarily into the PCS for absorption and suppression. This behavior indicates that the PCS can effectively absorb harmonic currents at these frequencies by optimizing its output impedance characteristics. Consequently, the proposed strategy improves power quality and reduce harmonic pollution at the PCC.

2) Current Harmonic Suppression Loop

The control block diagram of the current harmonic suppression loop, based on the ORC strategy, is shown in Fig. 14.

The output impedance of the current harmonic suppression loop is as follows:

$$Z_{out}(s)=\frac{v_o}{i_o}=\frac{sL_f+R+\dfrac{1}{sC_f}}{1+G_{orc}(s)k_{pwm}\dfrac{1}{L_vs+R_v}} \tag{16}$$

Fig. 15 shows the magnitude-frequency characteristics of the output impedance Z_o and the grid output impedance Z_g when using loop 3. At odd harmonic frequencies, Z_o is significantly higher than Z_g, causing the harmonic current to primarily flow into the grid rather than the PCS. This behavior indicates that by optimizing its output impedance characteristics, the PCS can effectively reject harmonic currents at odd harmonic frequen-

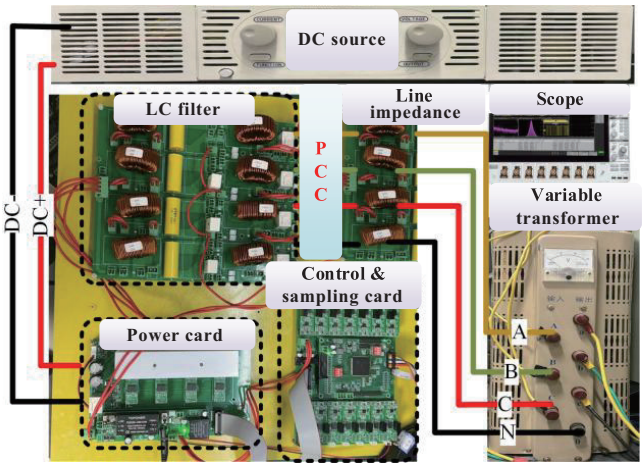

Fig. 16. Hardware platform.

TABLE I
POWER CIRCUIT PARAMETERS

Parameter	Value
DC voltage v_{dc}	75 V
AC voltage RMS v_g	38 V
Rated power P_n	300 VA
Line impedance L_g	3 mH
Linear load R_L	4.8 Ω
Nonlinear load R_{non}	12 Ω
Nonlinear load filter L	0.01 H
Nonlinear load filter C	0.001 F
Energy storage inverter L_f	1 mH
Energy storage inverter C_f	10 e−6 F
Filter damping resistor R_d	1 Ω
IGBT switching frequency	10 kHz

cies, thereby improving the output current quality of the PCS.

IV. EXPERIMENTAL VERIFICATION

To evaluate the efficacy of the proposed control strategy, a DC/AC experimental platform was developed, as depicted in Fig. 16. The platform consists of essential components such as the power module, control and sampling cards, LC filter, line impedance module, voltage regulator, and oscilloscope. The power circuit parameters are listed in Table I, and the control parameters are provided in Tables II and III.

A. Harmonic Suppression Capability of the Proposed Control Strategy

Fig. 17 presents the waveforms of the PCC point voltage, grid current, and VSG output current under various control strategies. The tested strategies include:

(a) Operation with a nonlinear load connected without any optimization;

TABLE II
VSG CONTROL PARAMETERS

Parameter	Value
Discretization time T_s	1/10 k
Rated angular frequency ω_n	314 rad
Active power frequency droop coefficient K_f	47.7 W/rad·s^{-1}
Inertia J	0.01*T_s kg·m^2
Damping coefficient D	0.5 Nm·s·rad^{-1}
Reactive power voltage droop coefficient K_v	300 Var/V
Excitation regulator coefficient K_Q	0.1*T_s
Virtual impedance R_v	0.1 Ω
Virtual impedance L_v	1 mH
Current loop proportional coefficient P	3
Voltage loop proportional coefficient PI	0.02 0.1*T_s

TABLE III
PROPOSED CONTROLLER PARAMETERS

Parameter	Value
Voltage harmonic suppression controller	
k_p	0.02
$Q(z)$	0.98
N	200
m	8
k_r	0.01
Current harmonic suppression controller	
k_p	0.05
$Q(z)$	0.98
N	200
m	200
k_r	0.08
$S(z)$	$\frac{0.002z^4+0.009z^3+0.013z^2+0.009z+0.0022}{z^4-2.69z^3+2.87z^2-1.4z+0.26}$

(b) Application of loop 2 for PCC voltage optimization using ORC as the inner model;

(c) Application of loop 3 for VSG current optimization using ORC as the inner model;

(d) Application of loop 2 for PCC voltage optimization using RC as the inner model;

(e) Application of loop 3 for VSG current optimization using RC as the inner model.

Fig. 18 illustrates the THD analysis of the PCC voltage, grid current, and VSG output current under various conditions. The results are as follows:

(a) THD when a nonlinear load is connected without any optimization;

(b) THD after implementing loop 2 for PCC voltage optimization using ORC as the inner model;

(c) THD after implementing loop 3 for VSG current optimization using ORC as the inner model;

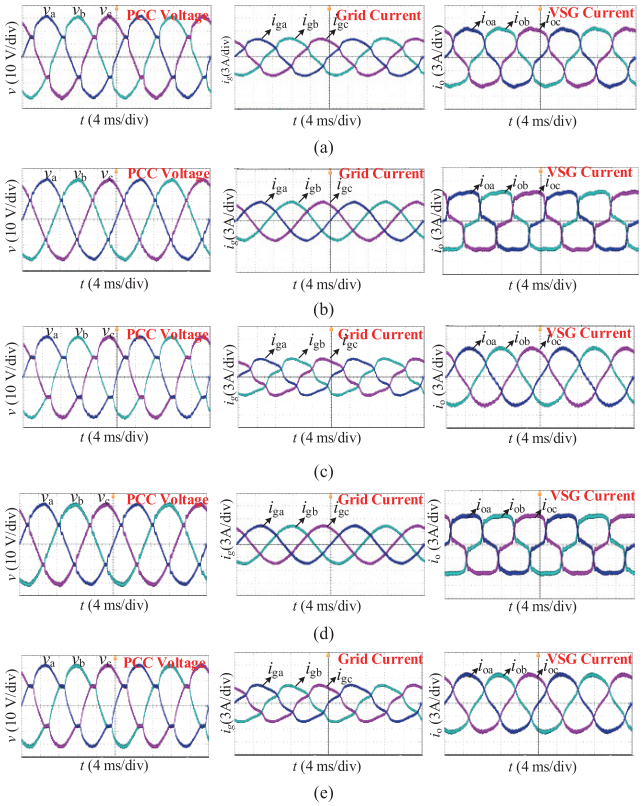

Fig. 17. Waveforms of PCC voltage, grid current, and VSG output current. (a) Loop 1, (b) Loop 2-ORC, (c) Loop 3-ORC, (d) Loop 2-RC, (e) Loop 3-RC.

(d) THD after implementing loop 2 for PCC voltage optimization using RC as the inner model;

(e) THD after implementing loop 3 for VSG current optimization using RC as the inner model.

Under linear load conditions, where no nonlinear loads are present, the PCC voltage, grid current, and VSG output current can maintain sinusoidal waveforms. However, when the system is connected to a nonlinear load without any optimization, the THD of the PCC voltage increases to 6.32% (Fig. 18(a)), and both the grid current and VSG output current exhibit significant distortion, with THD values of 6.38% and 13.29%, respectively. Furthermore, the distribution of harmonic currents is largely influenced by the output impedance of the VSG and the grid impedance. Without a control strategy, the harmonic current distribution remains unchanged, making it challenging to improve power quality.

When loop 2 (PCC voltage optimization using ORC as the inner model) is applied, the quality of the PCC voltage and grid current improves. The PCC voltage THD reduces from 6.32% (Fig. 18(a)) to 3.02% (Fig. 18(b)), and the grid current THD decreases from 6.38% (Fig. 18(a)) to 4.63% (Fig. 18(b)). However, this optimization strategy results in a higher THD for the VSG output current, which increases from 13.29% (Fig. 18(a)) to 18.71% (Fig. 18(b)), as more harmonic current is allocated to the VSG.

Switching to loop 3 (VSG current optimization) significantly improves the VSG output current quality, with the THD decreasing from 13.29% (Fig. 18(a)) to 5.97% (Fig. 18(b)). However, this leads to an increase in the grid current THD,

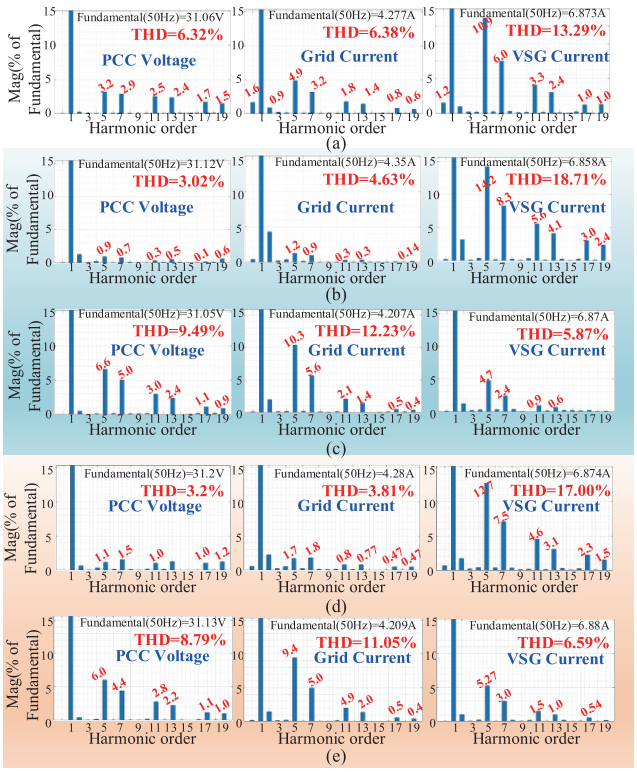

Fig. 18. THD analysis of PCC voltage, grid current, VSG output current. (a) Loop 1, (b) Loop 2-ORC, (c) Loop 3-ORC, (d) Loop 2-RC, (e) Loop 3-RC.

from 6.38% (Fig. 18(a)) to 12.23% (Fig. 18(b)), and the PCC voltage quality deteriorates, with the THD rising from 6.32% to 9.49%.

Additionally, the performance of the ORC and RC inner models is compared (Fig. 18(d) and (e)). Although the RC model offers similar performance in terms of THD reduction, it does not provide significant improvements over ORC, espe cially in terms of optimization. The THD values for the PCC voltage and VSG output current using RC (3.2% and 6.59%, respectively) are only marginally different from those achieved with ORC (3.02% and 5.89%). Moreover, the use of RC significantly impacts processor speed, making it a less desirable choice for this application.

In conclusion, the proposed control strategy demonstrates a trade-off between different optimization objectives: Loop 2 focuses on optimizing the PCC voltage and grid current, while loop 3 prioritizes optimizing the VSG output current. The optimal choice depends on the system's operational requirements and the specific power quality goals.

B. Subharmonics and Interharmonics Analysis

For power systems operating at a fundamental frequency of 50 Hz, the instantaneous voltage and current waveforms analyzed by discrete fourier transform typically consist of various frequency components. Components at integer multiples of the fundamental frequency are defined as harmonics, while those at non-integer multiples of the fundamental frequency are termed interharmonics. Additionally, frequency components below the fundamental frequency are known as subharmonics,

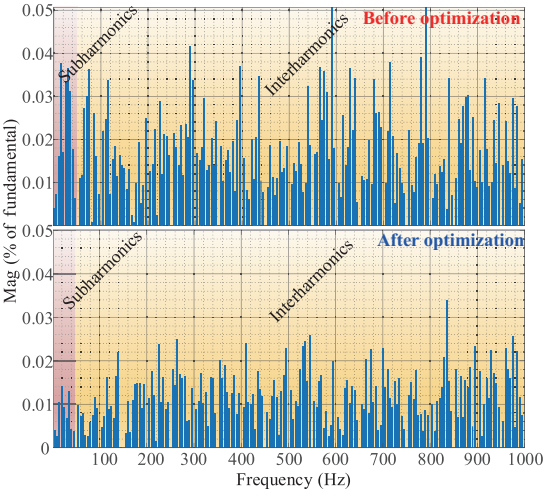

Fig. 19. Analysis of interharmonics and subharmonics in the PCC voltage.

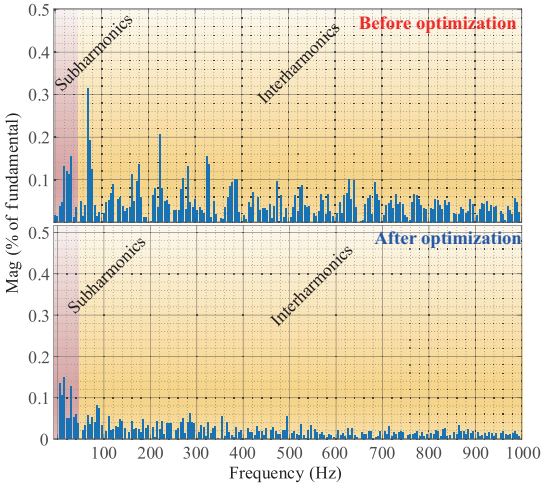

Fig. 20. Analysis of interharmonics and subharmonics in the VSG current.

which can also be considered as interharmonics existing between DC and the fundamental frequency. In this study, experimental data were recorded using an oscilloscope with a sampling depth of 1 m. To meet the required frequency resolution for interharmonic measurement (5 Hz), continuous sampling over 10 fundamental periods (0.2 s for a 50 Hz fundamental) was performed. The sampled data were subsequently imported into MATLAB/Simulink for fast Fourier transform analysis.

Fig. 19 shows the analysis of interharmonics and subharmonics in the PCC voltage before and after PCC voltage optimization. Before optimization, the maximum magnitude of subharmonics reaches approximately 0.35% of the fundamental component, while interharmonics reach around 0.4%. After optimization, the magnitudes of subharmonics and interharmonics decrease, both dropping below approximately 0.2%. This demonstrates that the proposed optimization strategy effectively mitigates both interharmonic and subharmonic distortion, significantly enhancing PCC voltage quality. Fig. 20 illustrates the interharmonics and subharmonics in the VSG

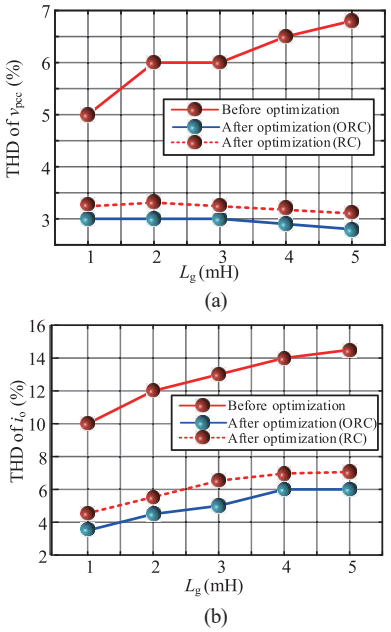

Fig. 21. Comparison of optimization effects under grid impedance variations. (a) Loop 1 vs loop 2, (b) Loop 1 vs loop 3.

output current before and after optimization. Initially, the subharmonic and interharmonic components in the current reach as high as approximately 0.5% and 0.4% of the fundamental component, respectively. After the proposed optimization, these magnitudes are significantly reduced, with the highest values of subharmonics and interharmonics falling below about 0.1%. This indicates that the proposed control method also effectively improves the VSG output current waveform, substantially reducing harmonic distortion.

The proposed method employs ORC, which provides a relatively wide bandwidth as illustrated in Fig. 9. As a result, this approach exhibits low sensitivity to subharmonics and interharmonics caused by frequency fluctuations and achieves effective suppression.

C. Robustness of the Proposed Control Strategy

To assess the robustness of the proposed control strategy, we evaluated its optimization effects on the PCC voltage and VSG output current under varying grid impedance and nonlinear load power conditions.

1) Grid Impedance Variation

Fig. 21(a) illustrates the optimization results for the PCC voltage as the grid impedance changes from 1 mH to 5 mH. Before optimization, the PCC voltage THD fluctuates significantly with changes in grid impedance. However, after optimization (using ORC), the PCC voltage THD is consistently maintained below 3%.

Fig. 21(b) presents the optimization results for the VSG output current under the same grid impedance variations. Prior to optimization, the minimum value of output current THD is 10%, but after optimization (ORC), the maximum output current THD remains below 6%.

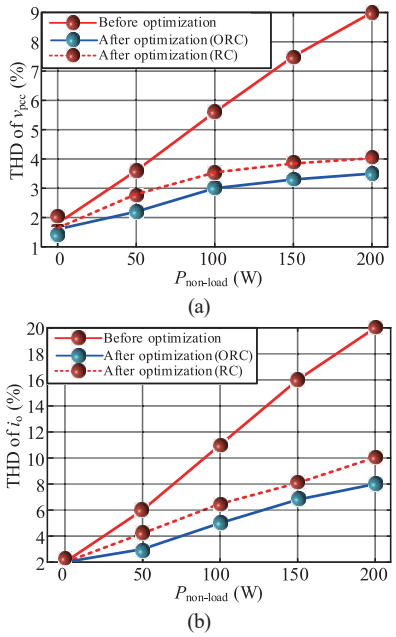

Fig. 22. Comparison of optimization effects of the proposed control strategy under variations in nonlinear load power. (a) Loop 1 vs loop 2, (b) Loop 1 vs loop 3.

2) Nonlinear Load Power Variation

Fig. 22(a) shows the optimization results for the PCC voltage as the nonlinear load power varies from 0 to 200 W. Before optimization, the PCC voltage THD increases approximately linearly with the nonlinear load power, reaching a maximum of 9%. After applying ORC optimization, the PCC voltage THD is consistently kept below 3.5%.

Similarly, Fig. 22(b) shows the optimization results for the VSG output current under the same load power variations. Before optimization, the output current THD increases nearly linearly with the load power, peaking at 20%. After optimization, the output current THD does not exceed 8%.

The results obtained with RC optimization are similar to those from ORC; however, the optimization performance with RC is slightly inferior. These results clearly demonstrate that the proposed power quality management strategy exhibits robust performance. Despite parameter variations in the system, it effectively suppresses harmonics and maintains output power quality.

D. Dynamic Performance of the Proposed Control Strategy

To evaluate the dynamic performance of the proposed control strategy, the active power reference of the VSG is stepped from 100 W to 300 W. The following figures present the PCC voltage, VSG output current, and grid current under different control strategies: Fig. 23 shows the results for loop 1 (without optimization); Fig. 23(a) presents the results for loop 2 using ORC as the inner model (PCC voltage optimization); Fig. 22(b) shows the results for loop 3 using ORC as the inner model (VSG output current optimization); Fig. 24(c) demonstrates the results for loop 2 using RC as the inner model (PCC voltage optimization); Fig. 24(d) illustrates the results for loop 3 using RC as the inner model (VSG output current optimization).

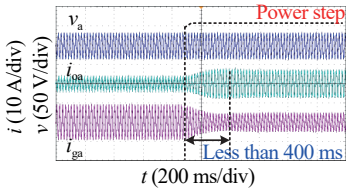

Fig. 23. Dynamic response of traditional control under power step change.

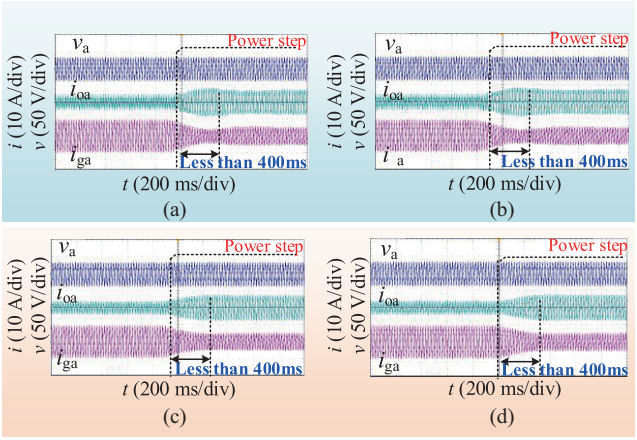

Fig. 24. Dynamic response of the proposed control strategy under power step change. (a) Loop 2-ORC, (b) Loop 3-ORC, (c) Loop 2-RC, (e) Loop 3-RC.

As observed in Figs. 22 and 23, the dynamic response time of the energy storage VSG remains consistently below 400 ms, regardless of the control method employed. This is consistent with the analysis presented in [27], which emphasizes that the dynamic response of VSG control is primarily influenced by the outer loop control. The proposed strategy modifies the inner loop, and thus does not affect the system's dynamic performance.

V. Conclusion

This paper proposes an odd-order repetitive controller based on the internal model principle, which reshapes the harmonic impedance of the VSG while preserving its fundamental functions. This approach enhances the power quality management capability of the energy storage VSG. The proposed method allows for selective control of either voltage optimization or output current optimization, enabling the energy storage VSG to operate similarly to an APF without the need for additional external sensors, thus achieving “one machine with multiple uses”. Consequently, this technology can not only complement traditional APFs in power quality management but also offers great flexibility.

References

[1] Z. Qing-Chang and G. Weiss, “Synchronverters: Inverters that mimic synchronous generators,” in *IEEE Transactions on Industrial Electronics*, vol. 58, no. 4, pp. 1259–1267, Apr. 2011.

[2] O. Babayomi, Z. Li, and Z. Zhang, “Distributed secondary frequency and voltage control of parallel-connected VSCs in microgrids: A predictive VSG-based solution,” in *CPSS Transactions on Power Electronics and Applications*, vol. 5, no. 4, pp. 342–351, Dec. 2020.

[3] G. Zhang, Q. Zhao, Y. Ye, A. Wang, S. Wen, and Y. Wang, "Feedforward repetitive control for grid-tied inverters in microgrids: Analysis, design, and verification," in *IEEE Transactions on Industrial Electronics*, vol. 71, no. 9, pp. 11239–11249, Sept. 2024.

[4] Q.-N. Trinh and H.-H. Lee, "An advanced current control strategy for three-phase shunt active power filters," in *IEEE Transactions on Industrial Electronics*, vol. 60, no. 12, pp. 5400–5410, Dec. 2013.

[5] Z. Wu, X. Guo, and B. Wang, "Coordinated control strategy for cascaded current-source converter under unbalanced grid voltage," in *IEEE Transactions on Power Electronics*, vol. 39, no. 5, pp. 5439–5448, May 2024.

[6] G. V. Hollweg, P. J. D. de O. Evald, E. Mattos. L. C. Borin, R. V. Tambara, and H. A. Gründling, and W. Su, "A direct adaptive controller with harmonic compensation for grid-connected converters," in *IEEE Transactions on Industrial Electronics*, vol. 71, no. 3, pp. 2978–2989, Mar. 2024.

[7] X. Jiang, H. Yi, F. Zhuo, and Y. Li, "A stabilization strategy based on grid current feedforward for the harmonic oscillation of APF system," in *IEEE Journal of Emerging and Selected Topics in Power Electronics*, vol. 12, no. 2, pp. 2116–2129, Apr. 2024.

[8] Q.-N. Trinh and H.-H. Lee, "An enhanced grid current compensator for grid-connected distributed generation under nonlinear loads and grid voltage distortions," in *IEEE Transactions on Industrial Electronics*, vol. 61, no. 12, pp. 6528–6537, Dec. 2014.

[9] Q. Yan, X. Wu, X. Yuan, and Y. Geng, "An improved grid-voltage feedforward strategy for high-power three-phase grid-connected inverters based on the simplified repetitive predictor," in *IEEE Transactions on Power Electronics*, vol. 31, no. 5, pp. 3880–3897, May 2016.

[10] J. M. Alcala, M. Castilla, L. G. de Vicuña, J. Miret, and J. C. Vasquez, "Virtual impedance loop for droop-controlled single-phase parallel inverters using a second-order general-integrator scheme," in *IEEE Transactions on Power Electronics*, vol. 25, no. 12, pp. 2993–3002, Dec. 2010.

[11] A. H. Jafariazad, S. A. Taher, Z. D. Arani, M. H. Karimi, and J. M. Guerrero, "Adaptive supplementary control of VSG based on virtual impedance for current limiting in grid-connected and islanded microgrids," in *IEEE Transactions on Smart Grid*, vol. 15, no. 1, pp. 89–98, Jan. 2024.

[12] M. Aquib, A. S. Vijay, S. Doolla, and M. C. Chandorkar, "Model reference adaptive system based apparent power sharing in inverter based microgrids," in *IEEE Transactions on Energy Conversion*, vol. 37, no. 3, pp. 1987–1997, Sept. 2022.

[13] G. Li, W. Song, and X. Liu, "A quasi-harmonic voltage feedforward control for improving power quality in VSG-based islanded microgrid," in *IEEE Journal of Emerging and Selected Topics in Power Electronics*, vol. 12, no. 3, pp. 2994–3004, Jun. 2024.

[14] Q. Chen, "A Control Strategy of Islanded Microgrid With Nonlinear Load for Harmonic Suppression," in *IEEE Access*, vol. 9, pp. 39171–39181, 2021.

[15] D. Elik and M. E. Meral, "A coordinated virtual impedance control scheme for three phase four leg inverters of electric vehicle to grid (V2G)," in *Energy*, vol. 246, p. 123354, May 2022.

[16] J. Zhou, Y. Sun, S. Chen, and T. Lan, "A fast repetitive control strategy for a power conversion system," in *Electronics*, vol. 13, no. 7, p. 1186, 2024.

[17] C. Zheng, T. Dragičević, and F. Blaabjerg, "Model predictive control-based virtual inertia emulator for an islanded alternating current microgrid," in *IEEE Transactions on Industrial Electronics*, vol. 68, no. 8, pp. 7167–7177, Aug. 2021.

[18] L. Zhou, Z. Shuai, Y. Chen, W. Wu, X. Zhou, K. Yan, and A. Luo, "Impedance-based harmonic current suppression method for VSG connected to distorted grid," in *IEEE Transactions on Industrial Electronics*, vol. 67, no. 7, pp. 5490–5502, Jul. 2020.

[19] W. Yang, M. Wang, S. Aziz, and A. Y. Kharal, "Magnitude-reshaping strategy for harmonic suppression of VSG-based inverter under weak grid," in *IEEE Access*, vol. 8, pp. 184399–184413, 2020.

[20] S. Li, J. Wu, G. D. Agundis-Tinajero, S. K. Chaudhary, J. C. Vasquez, and J. M. Guerrero, "A decomposed harmonic current suppression method for VSG-based microgrids connected to distorted grids," in *IEEE Transactions on Industrial Electronics*, vol. 71, no. 9, pp. 10669–10680, Sept. 2024.

[21] L. Zhou, S. Liu, Y. Chen, W. Yi, S. Wang, X. Zhou, W. Wu, J. Zhou, C. Xiao, and A. Liu, "Harmonic current and inrush fault current coordinated suppression method for VSG under non-ideal grid condition," in *IEEE Transactions on Power Electronics*, vol. 36, no. 1, pp. 1030–1042, Jan. 2021.

[22] G. Lou, Q. Yang, W. Gu, X. Quan, J. M. Guerrero, and S. Li, "Analysis and design of hybrid harmonic suppression scheme for VSG considering nonlinear loads and distorted grid," in *IEEE Transactions on Energy Conversion*, vol. 36, no. 4, pp. 3096–3107, Dec. 2021.

[23] Q. Zhao, H. Zhang, Y. Xia, Q. Chen, and Y. Ye, "Equivalence relation analysis and design of repetitive controllers and multiple quasi-resonant controllers for single-phase inverters," in *IEEE Journal of Emerging and Selected Topics in Power Electronics*, vol. 13, no. 3, pp. 3338–3349, Jun. 2025.

[24] S. Chen, Q. Zhao, S. Chen, and Y. Ye, "Modified PIMR-type ORC for odd harmonic current suppression in a single-phase grid-tied inverter," in *Proceedings of 2019 IEEE 8th Data Driven Control and Learning Systems Conference (DDCLS)*, Dali, China, 2019, pp. 1044–1048,

[25] J. Zhou, D. Fan, and Y. Sun, "Inertia-active power filter design based on repetitive control," in *Electronics*, vol. 13, no. 13, p. 2615, 2024.

[26] Y. Sun and J. Zhou, "Grid-tied inverter fractional-order phase compensation via odd repetition control," in *Proceedings of 2023 6th International Conference on Electrical Engineering and Green Energy (CEEGE)*, 2023, pp. 62–68.

[27] H. Wu, X. Ruan, D. Yang, X. Chen, W. Zhao, Z. Lv, and Q. Zhong, "Small-signal modeling and parameters design for virtual synchronous generators," in *IEEE Transactions on Industrial Electronics*, vol. 63, no. 7, pp. 4292–4303, Jul. 2016.

Yifei Sun was born in 1997 in China. He received his Bachelor's degree in electrical engineering from Zhongyuan University of Technology in 2019, and continued his studies at North China University of Technology, where he is currently a Ph.D. candidate in electrical engineering since 2022. His research focuses on power electronic converters and their applications.

From 2019 to 2022, he studied at Zhongyuan University of Technology, and since 2022, he has been working as a Ph.D. student at North China University of Technology. His current research interests include the design, control, and application of power electronic converters in various energy systems, with particular attention to grid-connected systems, renewable energy integration, and advanced control strategies.

His academic work has led to several published papers and conference presentations in the field of power electronics. He is dedicated to advancing the application of power electronics technologies for improving energy efficiency and power quality in modern electrical systems.

Zhou Jinghua is a professor and Ph.D. supervisor. He is a Senior Member of CPSS. His research interests include high-power power electronic conversion technology and grid-connected energy storage inverters.

Shasha Chen is a Ph.D. student whose research focuses on high-power power electronic conversion technology and power quality management.

Tianfeng Lan received the B.Eng. degree in electrical engineering and automation from Shanghai University, China, in 2013, and the M.Eng. degree in electrical engineering from the University of Sydney, Australia, in 2017. Since 2019, he has been serving as a Testing and Certification Manager at Shanghai Electrical Apparatus Research Institute (SEARI) Co., Ltd., where he leads technical evaluations and compliance assessments for power electronics systems. His research focuses on high-power energy storage converters, including topology optimization, grid-connected control strategies, and reliability enhancement for industrial-scale applications. He has contributed to multiple national-level certification standards for energy storage systems in China. Mr. Lan actively collaborates with industry partners to bridge advanced theoretical research with practical engineering solutions.

Continuous-Control-Set Predictive Control and Noise Tolerance Strategy for Phase-Shift Modulation DAB Topological Clusters

Tianqu HAO, Jiazheng HUANG, Zheng DONG, Zhenbin ZHANG, and Qian CHEN

***Abstract*—A continuous-control-set predictive control strategy is proposed for the phase-shift-modulation dual-active-bridge topological cluster. This strategy addresses two critical issues: high sensitivity to model parameters and sampling noise in traditional model predictive control. The steady-state error is analyzed in detail, considering model parameters and modeling methods. We establish a unified and simplified predictive model that is suitable for different dual-active-bridge topologies, reducing dependence on model parameters and computational burden. To mitigate sensitivity to sampling noise, we design a noise tolerance enhancement strategy by redefining a coefficient in the simplified model. This strategy expands the noise tolerance range while maintaining excellent dynamic performance, low system cost, and computational burden. The proposed control strategy is verified by using an experimental platform with TMS320F28379D as the core controller. Results show that our strategy effectively reduces sensitivity to model and noise while ensuring excellent dynamic performance compared to traditional model predictive control. The strategy is universal and significantly reduces the computational burden.**

***Index Terms*—Dual-active-bridge topological cluster, model predictive control, noise tolerance, simplified model.**

I. Introduction

RECENTLY, with the increasing integration of distributed power sources and energy storage devices into the grid, bidirectional isolated DC/DC converters have gained widespread use in DC microgrids, electric vehicles, and photovoltaic power generation [1]–[6]. These converters, such as dual-active-bridge (DAB) converters, dual-bridge-series-resonant converters (DBSRC), CLLC converters, and others, serve as interface devices for bidirectional power flow and have been extensively studied [7]. Among the various modulation strategies for these topologies, phase-shift modulation stands out due to its advantages of a high degree of freedom, fixed switching frequency, and fast dynamic response. These advantages simplify the design of magnetic components and enable multi-dimensional performance optimization, making it particularly suitable for high-power applications [8]–[10].

In modern power systems, energy storage devices operate under uncertain conditions due to the randomness and variability of load operating conditions. To achieve better dynamic performance, DC/DC converters need to be equipped with effective control strategies. Model predictive control (MPC), a nonlinear control strategy, offers advantages such as fast dynamic response, multi-objective control, and easy integration of constraints. Consequently, MPC has found increasing use in power electronics control [11]–[12]. Extensive research has been conducted on the application of MPC in various topologies, including DAB converters [13]–[14], DBSRCs [15]–[16], and CLLC converters [17]. Research results indicate that the steady-state performance under MPC is highly influenced by the accuracy of the predictive model parameters [18]. Additionally, even small sampling noise disturbances can lead to significant fluctuations in control variables [19]. Consequently, the extreme sensitivity to model parameters and sampling noise have emerged as two critical factors limiting the practical application of MPC in engineering.

Parameter identification and predictive model reconstruction are two key approaches to address the issue of high sensitivity to predictive model parameters in MPC strategies. For a multi-DAB-module system, the impact of parameter mismatch on steady-state performance has been analyzed, then an online parameter identification method based on recursive least squares has been proposed [20]. This method successfully eliminates steady-state error in the output voltage caused by parameter mismatch. However, it is limited to specific DAB converters and lacks universality. Also, a model predictive power control (MPPC) strategy has been introduced [21], which relates the control variable solely to the input and output voltage. However, this strategy requires an integrator to correct the output voltage, resulting in a potential degradation of system dynamics. For the three-phase DAB converter, a model-free discrete-control-set predictive control (MFPC) strategy has been proposed [22]. It uses the adaptive forgetting factor recursive least squares method to rectify the predictive model, achieving fast and unbiased control of the output voltage. However, precise

Manuscript received March 04, 2025; revised April 23, 2025; accepted May 26, 2025. Date of publication September 30, 2025; date of current version June 20, 2025. This work was supported in part by the Key Program of Joint Fund for Regional Innovative Development of the National Natural Science Foundation of China under the grant U23A20654. (*Corresponding author: Zheng Dong*.)

All authors are with Shandong University, Jinan 250061, China (email: haotianqu@sdu.edu.cn; 202334704@mail.sdu.edu.cn; z.dong@connect.polyu.hk; zbz@sdu.edu.cn; qian.chen@mail.sdu.edu.cn).

Digital Object Identifier 10.24295/CPSSTPEA.2025.00021

model is still needed to acquire the output current on the secondary side, and the calculation process is complex, imposing a heavy computational burden on the controller.

To mitigate the challenge of high sensitivity to sampling noise in model predictive control, current research focuses on improving processor performance, incorporating peripheral hardware filters, employing software filters, and reconstructing state space models. Yang [23] analyzed the impact of switching noise, quantization noise, and measurement noise on the control performance of DAB converters. They propose noise suppression methods such as increasing sampling frequency, reducing signal transmission delay, and raising the controller's basic frequency. However, these solutions increase system costs and are not practical for engineering applications. The Kalman Filter algorithm [19] was introduced to enhance the robustness of continuous-control-set model predictive control by utilizing optimal estimated values of state variables instead of measurements, effectively addressing the influence of measurement noise. However, this system still relies on the Kalman Filter for steady-state state variable estimation, requiring significant storage space and computing power. Babayomi [24] combined a hybrid cascaded extended state observer with model-free predictive control to improve interference and noise suppression capability. Nonetheless, compared to the control strategy proposed previously [19], this approach incurs higher computational costs.

In summary, existing work has limitations in addressing the challenges of high sensitivity to model parameters and sampling noise in model predictive control. These shortcomings are as follows:

(i) Traditional parameter identification strategies result in complex predictive models, leading to a significant computational burden.

(ii) Current noise tolerance range improvement strategies struggle to strike a balance between dynamic performance, system cost, and computational burden.

(iii) The predictive models lack the ability to facilitate algorithm transplantation across different topologies.

To address the challenges posed by model parameters and sampling noise in MPC schemes, this article presents a novel continuous-control-set predictive control strategy based on a simplified model. This approach effectively mitigates the control target deviation caused by model parameter mismatch and approximation errors in modeling methods. Moreover, it significantly reduces the computational burden on the controller. Furthermore, the Kalman Filter algorithm is employed to correct the simplified model parameters instead of relying on real-time optimal estimation of sampling values. This integration enhances the accuracy of the model and contributes to improved control performance. In addition, a simple yet efficient noise tolerance range improvement strategy is proposed to reduce the sensitivity to sampling noise in traditional model predictive control. This strategy achieves a balance between a fast dynamic response and a wide noise tolerance range. The proposed control strategy is versatile and applicable to various dual-active-bridge topological clusters.

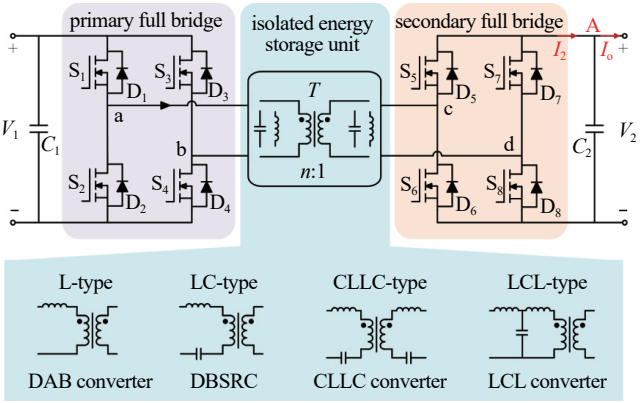

Fig. 1. Variation of cumulative index for islanding detection.

The structure of this paper is as follows. In Section II, the working process of the isolated phase-shift modulation DC/DC converter is analyzed. By considering the DBSRC as an example, the steady-state error of the system is quantified from two perspectives: model parameters and modeling methods. A unified simplified predictive model based on the Kalman Filter algorithm is then established. In Section III, the two-step continuous control set predictive control is employed to obtain the optimal control quantity. Additionally, a noise tolerance range improvement strategy is proposed by redefining the simplified model parameters, ensuring fast dynamic response and reduced computational burden. Section IV presents the experimental results. Finally, Section V concludes the paper.

II. Phase-Shift-Modulation Converters

A. Operating Process

The common phase-shift modulation control technique is utilized in various converters such as DAB converters, DBSRC, CLLC converters, among others. These converters adjust the phase-shift angle of the drive signals between the primary and secondary switches to regulate the phase difference between voltage and current in the energy storage components. This enables bidirectional power flow across a wide voltage gain range. Fig. 1 illustrates the topology cluster of phase-shift modulation converters, comprising two full bridge modules and an isolated energy storage unit. Each full-bridge module consists of four switches (S_1–S_4 and S_5–S_8) and four freewheeling diodes (D_1–D_4 and D_5–D_8). The isolated energy storage unit incorporates a high-frequency transformer with a ratio of n:1 and energy storage elements of different structures. It is important to note that different combinations of energy storage elements form different types of converters. The input-side and output-side filter capacitances are represented by C_1 and C_2, respectively. i_2 denotes the current of the secondary full bridge module, while i_o represents the output current. I_2 and I_o is the average current of the secondary full bridge module and load, respectively, and the equation $I_2 = I_o$ is hold.

Fig. 2 illustrates the operation waveforms of a DBSRC

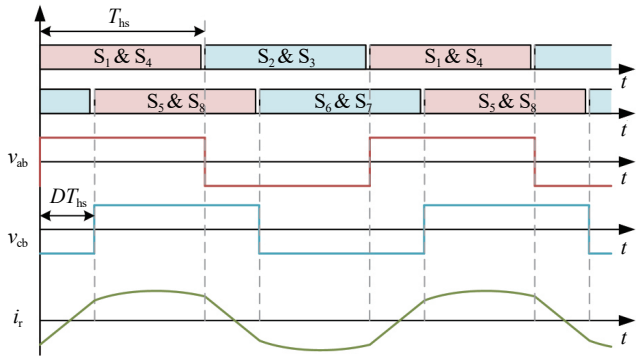

Fig. 2. Operating waveforms of DBSRC.

under single phase-shift modulation. In this analysis, we consider the grouping of switches on the primary or secondary side full bridge, where a group consists of switches such as S_1 and S_4. During the dead time preceding the switch conduction, the paralleled parasitic capacitors of the switches within the corresponding group undergo a charging process. Meanwhile, the complementary switches on the same side undergo a discharging process resulting in the switch terminal voltage reaching zero before opening. This achieves a zero voltage switching (ZVS) condition. In Fig. 2, T_{hs} represents half the switching cycle time, and i_r denotes the current flowing through the resonant inductor. By adjusting the phase-shift duty cycle, denoted as D, the magnitude and direction of power flow can be freely switched, offering flexibility in the operation of the converter.

Applying Kirchhoff's current law to node A shown in Fig. 1, the differentiation of output voltage can be discretized by the forward Euler method as

$$C_2\frac{\mathrm{d}V_2}{\mathrm{d}t}=C_2\frac{V_o(k+1)-V_o(k)}{T_c}=i_2(k)-i_o(k) \tag{1}$$

where T_c denotes the control cycle, which is usually set a few times higher than the switching cycle to reduce the computational burden in fixed-frequency phase-shift modulation converters. Assuming zero loss of the converter, the value of I_2 can be calculated using the ratio of transmitted power to the output voltage.

Using the transmitted power of DBSRC calculated previously [25], the deviation between the actual value and the reference value of output voltage in the k-th moment can be expressed as

$$\Delta V_2(k)=\frac{1}{C_2 f_c}\frac{8nV_1\sin(\pi D_{opt})}{\pi^2 X_{LC}}-\frac{1}{C_2 f_c}I_o \tag{2}$$

where D_{opt} represents the optimal phase-shift duty in the k-th moment under MPC strategy, and X_{LC} represents the impedance of the LC resonant tank.

Substituting the above analysis process into other phase-shift modulation converters, we can obtain the output voltage deviation of different topologies, as shown in Table I. Parameter L, $X_{LC.all}$, and X_{LCL} denote the impedance of the energy storage unit for the DAB converter, the CLLC converter and the LCL converter, respectively. It is worth noticing that the above parameters are the equivalent impedances reflected to the primary side from the secondary side.

TABLE I
OUTPUT VOLTAGE DEVIATION OF DIFFERENT TOPOLOGIES

Topology	Output voltage deviation
DBSRC	$\Delta V_2(k)=\frac{1}{f_c C_2}\frac{8nV_1\sin(\pi D_{opt})}{\pi^2 X_{LC}}-\frac{1}{f_c C_2}I_o$
DAB converter	$\Delta V_2(k)=\frac{1}{f_c C_2}\frac{nV_1 D_{opt}\lvert 1-D_{opt}\rvert}{2f_s L}-\frac{1}{f_c C_2}I_o$
CLLC converter	$\Delta V_2(k)=\frac{1}{f_c C_2}\frac{8nV_1\sin(\pi D_{opt})}{\pi^2 X_{LC.all}}-\frac{1}{f_c C_2}I_o$
LCL Converter	$\Delta V_2(k)=\frac{1}{f_c C_2}\frac{8nV_1\sin(\pi D_{opt})}{\pi^2 X_{LCL}}-\frac{1}{f_c C_2}I_o$

B. Steady-State Error Analysis

In the design process of magnetic components for isolated DC/DC converters, the initial values of the inductance of the transformer and inductors are measured in the specific environment (test frequency: 1 kHz; test current: 0.5 mA; ambient temperature: 25 °C). Due to the long-term operation and the frequent load switching during the converter operation, problems such as high coil current, uncertain switching frequency, and heating of the magnetic core may occur, resulting in a significant difference between the inductance coefficient A_L of the magnetic core and the design reference value. This can cause the magnetic components of the converter to deviate from the initial measurement value during the actual operation, making it difficult to operate stably at the pre-designed working point. Meanwhile, due to factors such as modeling methods, switch losses, and dead time of complementary switch driving signals, the model accuracy can be affected and the transmission power of the converter under model predictive control cannot accurately track the given value, even if there is no measurement bias in magnetic components.

Taking DBSRC as an example, we assume that the actual value of the resonant tank impedence and the output filter capacitor are X_{LC} and C_2, while the substitution values of both in the predictive model are X_{LC}' and C_2'. Ignoring modeling error temporarily, the output voltage reaches V_2 in the steady state, i.e.,

$$V_2(k+1)=\frac{8n\sin(\pi D)}{\pi^2 C_2 f_c X_{LC}}V_1-\frac{I_o}{C_2 f_c}+V_2(k)=V_2 \tag{3}$$

Parameters X_{LC}' and C_2' are introduced into the predictive model when the MPC algorithm operates in a digital signal processor. The optimal phase-shift duty cycle in the next moment should be set to keep the predicted output voltage equal to the given voltage V_2*. Thus, we get

$$\frac{8n\sin(\pi D)}{\pi^2 C_2' f_c X_{LC}'}V_1-\frac{I_o}{C_2' f_c}+V_2(k)=V_2^* \tag{4}$$

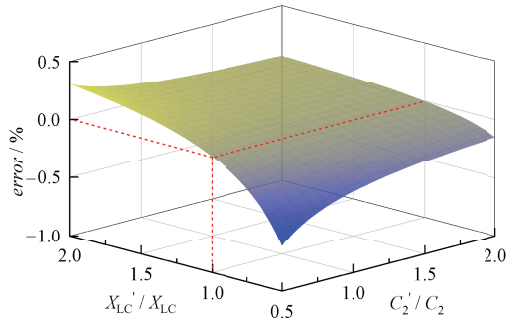

Fig. 3. Output voltage deviation caused by model parameter variations.

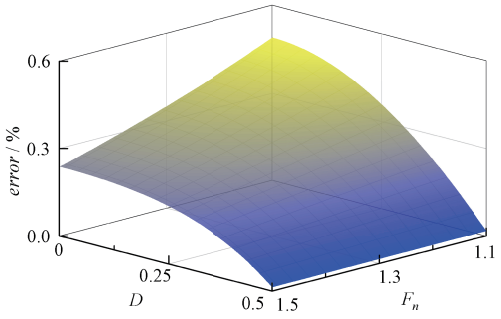

Fig. 4. Output voltage deviation caused by modeling method.

The output voltage remains unchanged in the steady state, which means that $V_2(k+1)$ is equal to $V_2(k)$. Combining (3) and (4) gives

$$\frac{V_2}{V_2^*}=\frac{1}{2}\left(\sqrt{1-\frac{X_{LC}-X_{LC}'}{X_{LC}}\frac{4P}{V_2^{*2}C_2'f_c}}+1\right) \tag{5}$$

where P is the transmitted power of DBSRC. It can be seen from (5) that the output voltage deviation increases as the transmitted power rises gradually.

In order to further explore the impact of model parameters, a surface graph is presented to show the influence of the resonant tank impedance and output side capacitance on the output voltage under the same transmitted power, which is shown in Fig. 3 with the output voltage error expressed as $error = (V_2 - V_2^*) / V_2^* \times 100\%$.

It can be concluded from Fig. 3 that: (i) the deviation of the output voltage is always zero as long as the resonant tank impedance is accurate (see the red dotted line in Fig. 3); (ii) the inductance mismatch affects the voltage deviation regardless of the accuracy of the capacitance value; (iii) as the capacitance ratio of the model value to the actual value increases, the voltage deviation shows lower sensitivity to the inductance mismatch.

Besides the impact of mismatch of the model parameters on the output voltage, the transmitted power deviation caused by modeling methods also makes it hard for the output voltage to track its given value. Ignoring parameter error temporarily, the output current I_2 from time-domain analysis (TDA) can be expressed as [26]

$$\begin{cases} I_2=\dfrac{2n\left(F_n^{\,2}-1\right)V_1}{\pi X_{LC}}g(D) \\ g(D)=\dfrac{\cos\left(\pi D/F_n-\pi/2F_n\right)-\cos\left(\pi/2F_n\right)}{\cos\left(\pi/2F_n\right)} \end{cases} \tag{6}$$

where F_n is the resonant ratio given by f_s / f_r. The resonant frequency f_r can be obtained from the resonant inductance L_r and capacitance C_r.

We assume that the inductance and capacitance are accurate to neglect the influence of model parameters mismatch. The predicted phase-shift duty cycle satisfies that the voltage in the next moment is equal to the given voltage V_2^* under fundamental harmonic analysis (FHA) while the actual voltage is V_2, then we can obtain

$$\frac{8n\sin(\pi D)}{\pi^2 C_2 f_c X_{LC}}V_1-\frac{I_o}{C_2 f_c}+V_2=V_2^* \tag{7}$$

Combining (7) and (8) yields

$$\begin{cases} \dfrac{V_2}{V_2^*}=1-h\left[\dfrac{4n\sin(\pi D)}{\pi^2}-(F_n^{\,2}-1)g(D)\right] \\ h=\dfrac{2nV_1}{V_2^* C_2 f_c X_{LC}} \end{cases} \tag{8}$$

Fig. 4 shows the influence of the FHA method on the output voltage. Compared to the precise modeling based on power balance using the TDA method, it can be concluded that: (i) as the phase-shift duty cycle decreases, the voltage deviation is more susceptible to the resonant ratio; (ii) as the resonant ratio decreases, the voltage deviation is more susceptible to the phase-shift duty cycle; (iii) the output voltage steady-state error caused by FHA modeling method always exists.

According to the above analysis, we observe that: (i) the voltage deviation caused by the modeling method can be eliminated by utilizing the TDA method based on a precise power balance equation; (ii) the voltage deviation caused by both model parameters and modeling methods can be eliminated simultaneously by parameter identification. However, the computational burden is relatively high due to the predictive model.

Apart from DBSRC, other types of converters also suffer from transmitted power deviation caused by the mismatch of model parameters and modeling methods, and the above conclusions still hold.

C. Simplified Model

For the various dual-active-bridge topologies, as shown in Fig. 1, the relationship between transmitted power and control quantity is different. Therefore, a unified predictive model cannot be constructed to meet the engineering requirements in various scenarios. Based on the analysis of the factors affecting the voltage deviation given in Section II.*B*, we propose here a unified simplified model that is suitable for the phase-shift modulation topology cluster, and the Kalman Filter algorithm

is introduced to solve the correlation coefficients of the simplified model iteratively to achieve fast and unbiased control.

The deviation between the actual output voltage and the given value depends on the phase-shift duty cycle D and the output current I_o. When the average current on the secondary side I_2 determined by D is equal to the output current I_o, the output voltage reaches the given value, i.e., ΔV_2 is zero. According to Table I, it can be seen that in the output voltage deviation models of different topologies, only the relevant term of D are distinct, while the coefficients of I_o are the same, all of which are $1 / C_2 f_c$. Considering the simplicity of calculation and the universality of the predictive model, the relevant term of D in the output voltage deviation can be simplified as a linear term. Therefore, in Table I, the output voltage deviation in discrete time can be simplified as

$$\begin{cases} \Delta V_2(k) = G(k) \cdot D(k) - \dfrac{1}{C_2 f_c} I_o \\ \Delta V_2(k) = V_2(k+1) - V_2(k) \end{cases} \tag{9}$$

where $I_o(k)$ is the sampling value of the output current at the k-th moment, and $D(k)$ is the calculated value of the phase-shift duty cycle at the k-th moment. Parameter $G(k)$ represents the control gain, which is related to the actual operating condition of the converter at the current moment.

Generally, the voltage deviation of the resonant DC/DC converter topology is affected by many factors and has significant nonlinear effects. If a linear simplified model with a fixed control gain is used to replace the complex nonlinear model which ignores the circuit parasitic parameters, the output voltage is difficult to track the reference value quickly and accurately due to parasitic parameters, model accuracy, operating power, and other factors under a fixed control gain. The magnitude of $G(k)$ has a crucial impact on the control accuracy of the converter. Therefore, to eliminate the output voltage steady-state error, it is necessary to choose an appropriate $G(k)$ according to specific operating conditions.

The parameter identification algorithm can eliminate the steady-state errors caused by circuit parameter variations and modeling methods simultaneously. Therefore, in order to correct the control gain in real time when ΔV_2 is equal to zero under different loads, we introduce the Kalman filtering algorithm to estimate $G(k)$ accurately. Expressing (9) in matrix form, the state predictive equation of the linear discrete system can be obtained as

$$y(k) = X(k)^T H(k) \tag{10}$$

where

$$\begin{cases} y(k) = \Delta V_2(k) \\ X(k) = \left[G(k) \; -1 / C_2 f_c \right]^T \\ H(k) = \left[D(k) \; i_o(k) \right]^T \end{cases} \tag{11}$$

According to (9)–(11), the linear simplified model based on the Kalman Filter is established as

$$\begin{cases} X(k) = X(k-1) + K(k)\left[y(k) - X(k-1)^T H(k) \right] \\ K(k) = \dfrac{P(k-1)H(k)}{R + H(k)^T P(k-1) H(k)} \\ P(k) = \left[I - K(k) H(k)^T \right] \cdot P(k-1) + Q \end{cases} \tag{12}$$

where $P(k)$ is the covariance matrix of the estimation error at the k-th moment and K is the Kalman gain. R and Q represent the covariance matrices of measurement noise and process noise, respectively. It is worth mentioning that the convergence rate of the Kalman Filter is affected by the Kalman gain, in the range of 0 to $1 / H$. When K is close to 0, the optimal state estimation relies more on the state estimation at the last moment. When K is close to $1 / H$, the optimal state estimation relies more on the measurement value at this moment.

In (12), the parameter $y(k)$, which is equal to ΔV_2, can be measured directly. $H(k)$, $X(k-1)$, and $P(k-1)$ can be obtained from the values at the last moment. $X(k)$, $P(k)$, and $K(k)$ are the variables to be solved later, which can be obtained from (12). The offset-free model predictive control will be achieved by iterative correction of the control gain $G(k)$. Due to the fact that only the variable $G(k)$ in the first line of $X(k)$ is unknown, the process of optimization estimation of $X(k)$ can be simplified, thus alleviating the computational burden in the controller.

III. Continuous-Control-Set Predictive Control Using Simplified Model

A. Solution to Predicted Phase-Shift Duty Cycle

The model predictive control algorithm generally includes three segments: predictive model, rolling optimization, and feedback correction. The control sequence is continuously optimized to achieve fast dynamic response through updating the system state in real-time, solving the open-loop optimization issue online, and repeating the above processes at the next moment. The state-space averaging model of the converter can be used in the predictive model. According to (9), the discretized output voltage of the phase-shift modulation converter can be obtained as

$$V_2(k+1) = G(k) \cdot D(k) - \frac{i_o(k)}{C_2 f_c} + V_2(k) \tag{13}$$

In single-step model predictive control, the controller aims to ensure that the output voltage at the next moment reaches its given value as soon as possible and solves the optimal phase-shift duty cycle within this control cycle. The system's operating process is shown in Fig. 5(a). The output voltage before the k-th moment deviates significantly from the given value, and the converter operates at maximum power with the phase-shift duty cycle being 0.5. The sampling value of the output voltage at the k-th moment is $V_{2.cal}(k)$. In order to achieve the output voltage of V_2* at the $(k+1)$-th moment, the controller calculates the optimal operating trajectory and obtains the predicted

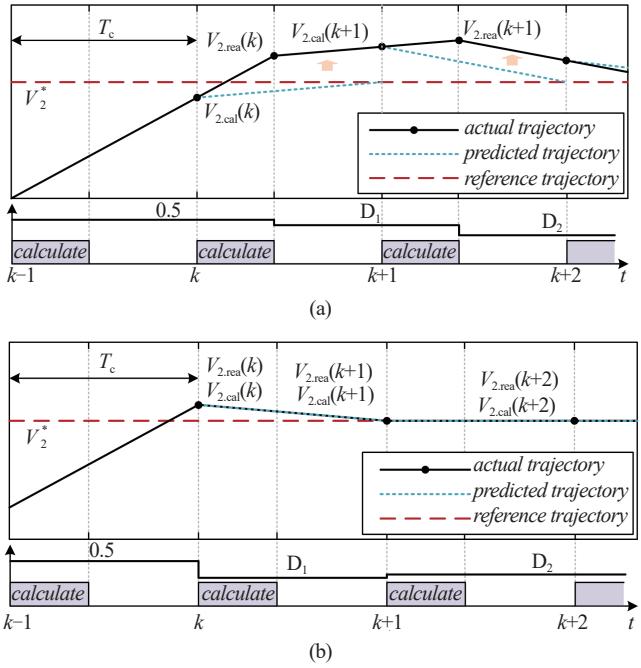

Fig. 5. Schematic diagram of system operation process under different MPC strategies. (a) Single-step model predictive control. (b) Two-step model predictive control.

phase-shift duty cycle of D_1. Considering the calculation time of the controller, the output voltage has risen to $V_{2.rea}(k)$ at the time of updating the phase-shift duty cycle. Thus, the output voltage cannot reach V_2* at the (k+1)-th moment. Similarly, the optimal phase-shift duty cycle D_2 calculated by $V_{2.cal}(k+1)$ at the (k+1)-th moment is updated when the output voltage is $V_{2.rea}(k+1)$. Thus, it still cannot satisfy the condition that $V_{2.cal}(k+2) = V_2$*. Under the single-step model predictive control, the actual output voltage gradually approaches its given value over time. However, the calculation speed is limited due to the cost of the controller. Since the controller's calculation time is non-negligible, the output voltage cannot move along the predicted trajectory, and the dynamic performance of the system deteriorates.

To solve the problem of calculation delay, we adopt a two-step model predictive control to compute the optimal phase-shift duty cycle. According to (9), the output voltage deviation at the (k+1)-th moment can be obtained as:

$$\Delta V_2(k+1) = G(k+1)\cdot D(k+1) - \frac{1}{C_2 f_c} i_o(k+1) \tag{14}$$

Combining (13) and (14), the predicted output voltage value at the (k+2)-th moment is

$$\begin{aligned} V_2(k+2) = {} & G(k+1)\cdot D(k+1) - \frac{1}{C_2 f_c} i_o(k+1) + \\ & G(k)\cdot D(k) - \frac{1}{C_2 f_c} I_o(k) + V_2(k) \end{aligned} \tag{15}$$

The implementation process of the predictive control with a simplified model (SMPC) proposed in this paper is as follows:

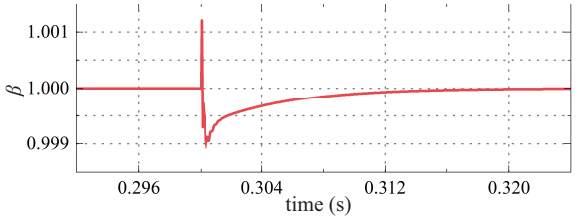

Fig. 6. Simulation of β when the load changes.

The controller calculates the optimal phase-shift duty cycle D_1 at the k-th moment, and updates it at the (k+1)-th moment. At the same time, the optimal phase-shift duty cycle D_2 at the (k+2)-th moment is calculated. The calculation process is shown in Fig. 5(b). This two-step predictive control algorithm predicts the optimal phase-shift duty cycle for the next time step at the current moment and updates it at the beginning of the next control cycle to ensure that the output voltage at the next step reaches the reference value as quickly as possible.

In (15), V_2 and I_o can be measured. $D(k)$ is the optimal phase-shift duty cycle obtained at the last step, and $G(k)$ can be obtained from (12). The change of load current is small within one control cycle, i.e., $I_o(k+1) = I_o(k)$. The variable $G(k+1)$ cannot be measured directly, but its magnitude can be obtained by fitting the historical data. To reduce the computational burden, we only consider the term related to the control gain at the last moment, i.e.,

$$G(k+1) = \beta(k)\cdot G(k) \tag{16}$$

where $\beta(k)$ is the fitting coefficient. Regarding (16) as the state predictive equation for discrete systems, the one-dimensional data-driven model based on Kalman Filter is established as

$$\begin{cases} \beta(k) = \beta(k-1) + K_\beta(k)\left[G(k) - \beta(k-1)G(k-1)\right] \\ K_\beta(k) = \dfrac{P_\beta(k-1)G(k-1)}{R_\beta + G(k-1)^2 P_\beta(k-1)} \\ P(k) = \left[1 - K_\beta(k)G(k-1)\right]\cdot P_\beta(k-1) + Q_\beta \end{cases} \tag{17}$$

By solving the optimal estimation of the Kalman gain K_β, the prediction of $G(k+1)$ can be achieved.

When the converter reaches the steady state, the control gain G no longer changes, at the operating point of $G(k+1) = G(k)$. When a sudden change in load from 50% to 100% causes the system to break away from the steady state, the simulation of the change process of the fitting coefficient β is shown in Fig. 6. It can be seen that the change of β is extremely small during the harsh transient process. As the estimation process of β will increase the computational burden of the controller, $G(k)$ can be approximated as $G(k+1)$ in practice, which further simplifies the predictive model while ensuring dynamic performance.

B. Improvement of Noise Tolerance

When the measurement value of output voltage fluctuates due to sampling noise or low bit count of the controller's A/

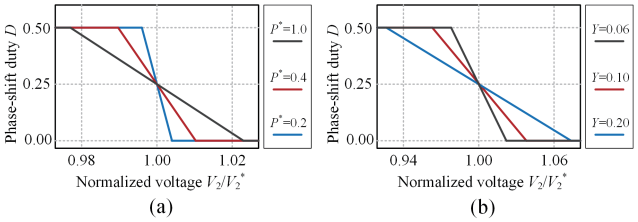

Fig. 7. Relation between phase-shift duty cycle and normalized output voltage. (a) Under different power levels. (b) Under different values of noise tolerance coefficient.

D converter, the measurement noise will be fed back to the predictive model, resulting in the change of the phase-shift duty cycle accordingly. When the system operates in the steady state, the measurement noise of the output voltage is δV_2, and the resulting phase-shift duty cycle change is δD. According to (9), it can be obtained as

$$D+\delta D=\frac{1}{GC_2f_c}\left(I_o+C_2f_c\delta V_2\right) \tag{18}$$

In practical circuit, the output filter capacitor C_2 is designed as hundreds of microfarad and the control frequency f_c is usually set in tens of kilohertz. According to (18), a tiny voltage fluctuation can cause D to jump between 0 and 0.5. When D jumps to a larger value, the device current of the switches increases significantly, resulting in increased switching loss. The energy storage unit needs to withstand higher voltage and current stresses and it accelerates device aging. When D jumps to a smaller value, the primary and secondary side switches cannot all achieve ZVS under non-unit voltage gain, resulting in reduced system efficiency. When the phase-shift duty cycle fluctuates between 0 and 0.5, the output voltage noise increases, which is not conducive to the stable operation of the voltage-sensitive loads.

Assuming that the steady-state phase-shift duty cycle of the converter is 0.25, the relationship between normalized output voltage V_2 / V_2* and phase-shift duty cycle D can be plotted according to (18), as shown in Fig. 7. When the output voltage deviates from the reference voltage, the converter will transmit power at its maximum capacity (D = 0.5 or 0) to achieve fast response. When the output voltage approaches the reference value, the phase-shift duty cycle will vary linearly with the output voltage deviation. However, due to the extremely small linear region, a slight fluctuation in the output voltage sampling value can lead to a significant change in the phase-shift duty cycle. Meanwhile, the linear region gradually becomes narrow as the transmitted power of the converter decreases. Therefore, the key to achieving stable operation of the converter is to reduce the sensitivity of D to high-frequency noise.

We define the noise tolerance coefficient as Y, i.e.,

$$Y=\frac{1}{C_2f_c} \tag{19}$$

Substituting (19) into (9), the output voltage deviation can be expressed as

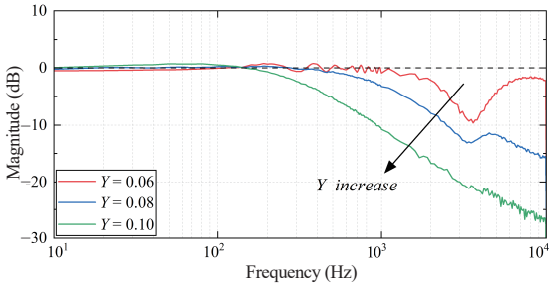

Fig. 8. Amplitude-frequency curves under different values of noise tolerance coefficient.

$$\Delta V_2=G\cdot D-Y\cdot I_o \tag{20}$$

When the system reaches the steady state, the phase-shift duty cycle is

$$D=\frac{Y}{G}\cdot I_o \tag{21}$$

The correction of the control gain G ensures that the output voltage deviation is zero. Thus, the Kalman Filter algorithm can always obtain an optimal estimation of G to satisfy $V_2(k+2) = V_2^*$ for different Y values. The operating condition of the system remains unchanged under the same transmitted power and different values of the noise tolerance coefficient. Hence, the value of G increases or decreases proportionally with the change in the noise tolerance coefficient. According to (18), the phase-shift duty cycle can tolerate larger output voltage fluctuations in the linear region as the increment of G. Fig. 7(b) shows the relationship between the normalized output voltage and the phase-shift duty cycle for different values of noise tolerance coefficient when the normalized transmitted power is 1. It can be observed that the linear region becomes wide as the value of Y increases, which means that the sensitivity of D to δV_2 decreases, and a higher tolerance of the system for high-frequency sampling noise is achieved.

AC sweepings based on PLECS are carried out for the steady-state point V_1 = 100 V, V_2 = 100 V, and R_L = 20 Ω. Perturbations from 10 Hz to 10 kHz with amplitude of 0.01 V are superposed on the output voltage steady-state value V_2 = 100 V. The closed-loop transfer function for DBSRC can be defined as

$$G_v(f)=\frac{V_2(f)}{v_2^*(f)} \tag{22}$$

where v_2* is the injected perturbation of the reference output voltage. The sweeping results are presented in Fig. 8, showing the closed-loop transfer function in the frequency domain with different values of Y. The noise tolerance coefficient has a negative impact on the system bandwidth. As the value of Y increases, it moves the pole to a lower frequency and the theoretical dynamic response time of the system slows down. Thus, it is not advisable to take a too large value of Y.

The selection process of Y is as follows: Firstly, we should estimate the noise level. The content of quantization noise and measurement noise is higher, so we use the sum of them to ap-

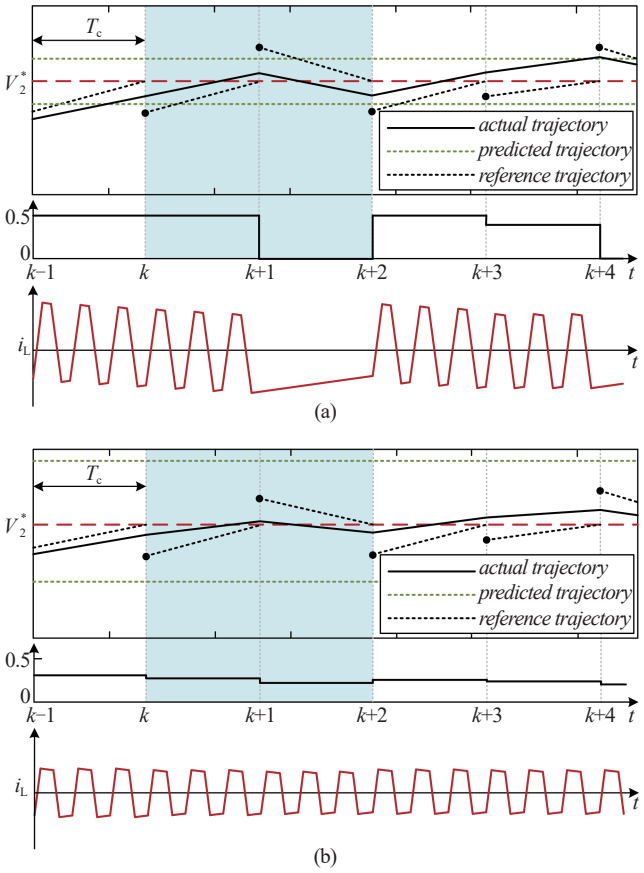

Fig. 9. Schematic diagram of system operation process under different *Y*. (a) Without noise tolerance strategy. (b)With noise tolerance strategy.

proximate the sampling noise:

$$\Delta = \Delta_{\max}^{q} + \Delta_{\max}^{m} = \frac{V_{\mathrm{REF}} \cdot V_{\max}}{2^{n+1}} + V_{\mathrm{OS}} \times \frac{V_{\max}}{V_{\mathrm{REF}}} \tag{23}$$

where the bit of ADC is n, with the maximum input voltage V_{REF}, and $V_{\max}$ is the full scale. V_{OS} is the input offset voltage.

Then, we need to set a suitable Y to ensure δD fluctuates in a small range. According to (18) and (21) :

$$Y_{\min} = \frac{D \cdot \Delta}{I_o \cdot \delta D} \tag{24}$$

where D is the steady-state phase-shift duty cycle, and I_o is the steady-state output current. Obviously, the larger the Y is, the smaller degree the δD fluctuates in. We limit the value of δD to 0.1 generally.

Besides, when the converter output power at maximum capacity (D = 0.5), $\Delta V_{2.\mathrm{m}}$ should be small enough to ensure the fast response in one control cycle

$$Y_{\max} = \frac{D}{0.5 \cdot I_o} \Delta V_{2.\mathrm{m}} \tag{25}$$

where $\Delta V_{2.\mathrm{m}}$ is the minimum value of the voltage error which makes D reach 0.5. The boundary of $\Delta V_{2.\mathrm{m}}$ can be set to 5 V.

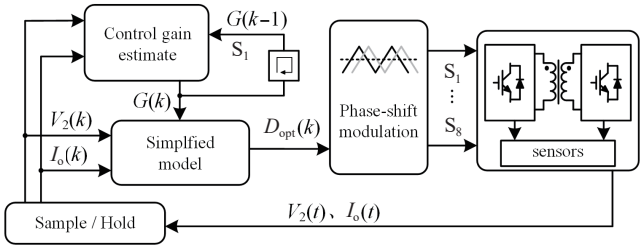

Fig. 10. Block diagram of SMPC.

Finally, we get the range of Y. It is noted that the value of Y should be as close as possible to its maximum value to ensure the priority of noise tolerance.

Fig. 9 is the schematic diagrams of system operation process under different Y, which can further explain the simulation results. It is noted that the switching frequency is three times more than the control frequency. Fig. 9(a) shows the system operation process under $Y = 1 / C_2 f_c$, without the noise tolerance strategy, and Fig. 9(b) means that the converter operates under a higher coefficient Y. The black dots are the measurement values which are affected by the sampling noise. The area between green dashed lines represents the maximum voltage range. When the sampling point exceeds the maximum voltage range, the converter will transfer power at its maximum capacity and the phase-shift duty cycle will reach its boundary value. As the increase of Y, the maximum voltage range become larger, and the phase-shift duty cycle is more difficult to reach its boundary value. Taking the blue area as an example, the control variable with noise tolerance strategy is smoother than that which satisfies $Y = 1 / C_2 f_c$. In addition, the inductor current is not symmetric in Fig. 9(a), which indicates that the transformer is faced with DC bias and saturate easily. However, the introduction of Y means that the actual voltage trajectory can not follow the predicted trajectory, and the dynamic response become slower. Therefore, the coefficient Y can be regarded as a weight coefficient to balance the dynamic response and robustness of the converter.

Fig. 10 shows the block diagram of the continuous-control-set predictive control based on the simplified model proposed in this article. Firstly, the output voltage V_2 and output current I_o are sampled, and the control gain $G(k)$ can be calculated by the optimal phase-shift duty cycle $D_{\mathrm{opt}}(k)$ at the current moment, as shown in (12). Then, $G(k)$ is substituted into the simplified model shown in (15), and the optimal phase-shift duty cycle $D_{\mathrm{opt}}(k+1)$ at the next moment is obtained. It is worth noting that $D(k+1)$ in (15) can be replaced by $D_{\mathrm{opt}}(k+1)$. Finally, the phase-shift duty cycle is updated at the beginning of the next control cycle, and the corresponding triggering signals are generated by the phase-shift modulator to regulate the switches.

IV. Experimental Validation

To verify the effectiveness of the proposed continuous-control-set predictive control strategy based on a simplified model, an experimental prototype is constructed, as shown in Fig. 11.

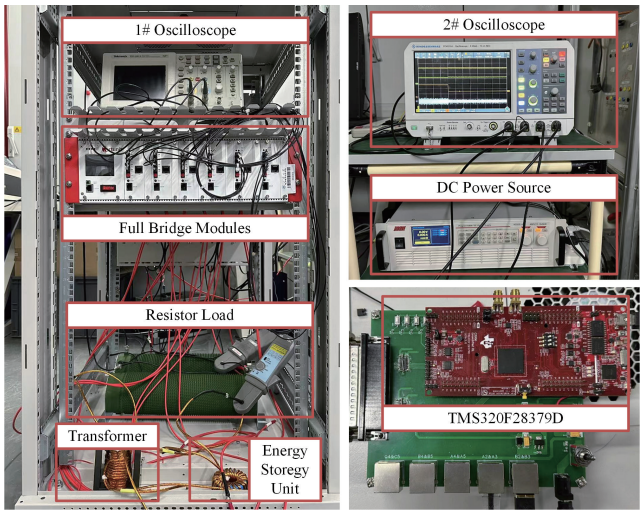

Fig. 11. Experimental prototype.

TABLE II
PARAMETERS OF EXPERIMENTAL PROTOTYPE

Topology	Parameter	Values
General parameter	Input DC voltage (V_1)	100 V
	Output DC voltage (V_2)	100 V
	Transformer turn ratio (n)	1:1
	Output filter capacitor (C_2)	1640 μF
	Load resistor (R_L)	20/40 Ω
DBSRC	Switching frequency ($f_{s,1}$)	40 kHz
	Resonant capacitor (C_r)	1.037 μF
	Resonant inductor (L_r)	44.29 μH
DAB converter	Switching frequency ($f_{s,2}$)	25 kHz
	Series inductor (L_s)	44.29 μH

The experimental platform contains several RT-Unit full-bridge modules with TMS320F28379D controller. By changing the structure of the energy storage unit and the switching frequency, the universality of the proposed control strategy is verified for two topologies of DAB converter and DBSRC. The parameters of the experimental prototype are shown in Table II.

A. Dynamic Performance Comparison

With the load abruptly changing from 40 Ω to 20 Ω, Figs. 12 (a)(c)(e) are the operation waveforms of the DAB converter under PI control, TMPC, and SMPC, respectively. Figs. 12(b) (d)(f) are the operating waveforms of DBSRC under PI control, TMPC and SMPC, respectively. The results show that the recovery time and the voltage overshoot are the worst under PI control regardless of DAB converter (about 66 ms) or DBSRC (about 75 ms) among above three control schemes. However, for TMPC and SMPC schemes, both of them show excellent dynamic performance and the output voltage almost remains

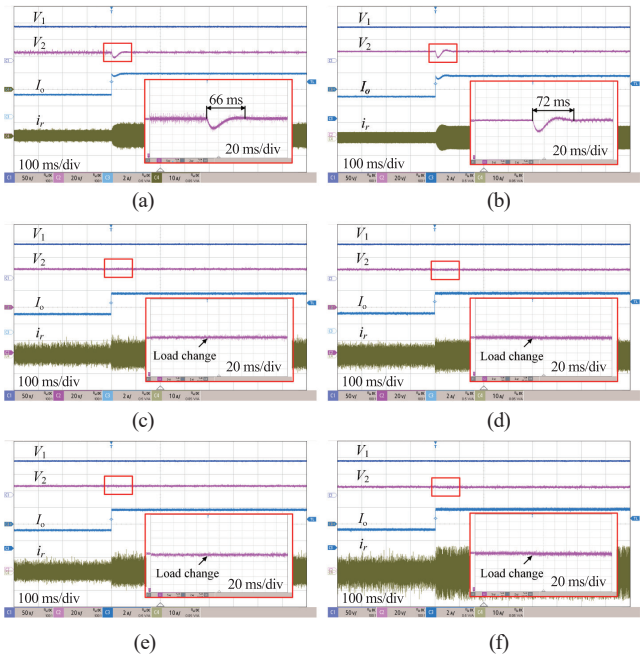

Fig. 12. Dynamic performance comparison when load increases suddenly. (a) DAB converter, PI control. (b) DBSRC, PI control. (c) DAB converter, TMPC. (d) DBSRC, TMPC. (e) DAB converter, SMPC. (f) DBSRC, SMPC. (V_1: 50 V/div; V_2: 20 V/div; I_o: 2 A/div; i_r: 10 A/div; time: 100 ms/div).

unchanged regardless of DAB converter or DBSRC. It can be observed that with the introduction of Kalman filter, the proposed SMPC scheme still maintains excellent dynamic performance as the TMPC scheme does. All two MPC schemes demonstrate faster response than the PI control scheme.

B. Parameter Sensitivity Suppression

The reference voltage is set to 100 V and the load resistance has a constant value of 20 Ω. Fig. 3 and Fig. 4 indicate that both the mismatch of model parameters and modeling method affect the accuracy of the control target. We set an operation condition of 50% mismatch both on the energy storage components impedance and the output side capacitance under the TMPC scheme, while the predictive model of the SMPC scheme is estimated by the Kalman Filter algorithm. The voltage sensors are calibrated under PI control to eliminate the output voltage deviation caused by measurement errors.

Figs. 13(a) and (b) are the operating waveforms under the TMPC scheme, while Figs. 13(c) and (d) are the operating waveforms under the SMPC scheme. The glitches of the output voltage is caused by the switching action, and we avoid setting he sampling points at the switching moment to reduce the interference of switching noise. It can be seen that the voltage deviation always exists under the TMPC scheme regardless of the DAB converter (about 0.75 V) or DBSRC (about 0.92 V). By comparison, the proposed SMPC scheme demonstrates extremely high control accuracy for both topologies. The experiment results prove that the proposed control strategy can effectively reduce the sensitivity of the output voltage to the predictive model.

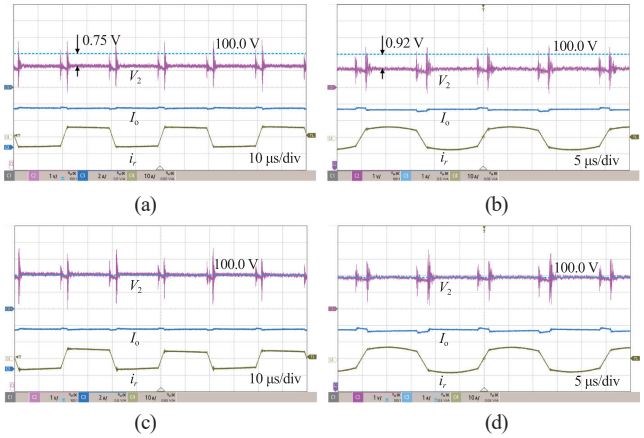

Fig. 13. Steady-state performance comparison under two different MPC strategies. (a) DAB converter, TMPC. (b) DBSRC, TMPC. (c) DAB converter, SMPC. (d) DBSRC, SMPC. (V_2: 1 V/div; I_o: 2 A/div; i_r: 10 A/div).

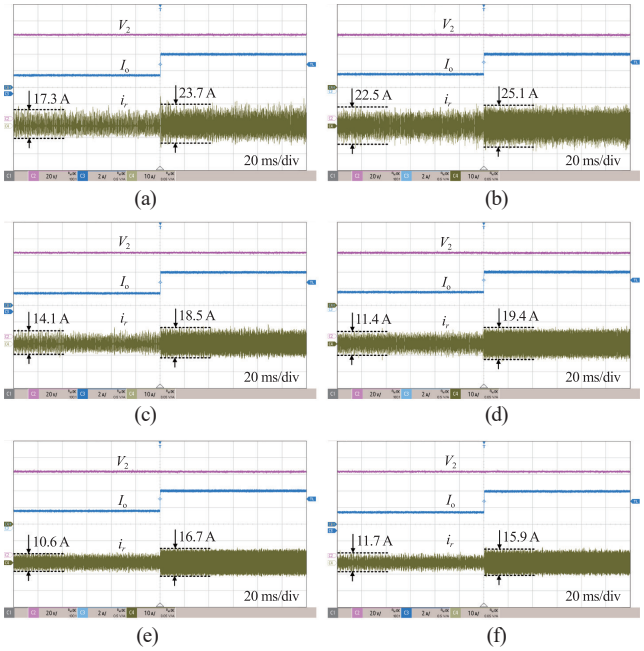

Fig. 14. Current stress comparison under different noise tolerance coefficients. (a) DAB converter, Y = 0.03. (b) DBSRC, Y =0.03. (c) DAB converter, Y = 0.06. (d) DBSRC, Y =0.06. (e) DAB converter, Y = 0.12. (f) DBSRC, Y = 0.12. (V_2: 20 V/div; I_o: 2 A/div; i_r: 10 A/div; time: 20 ms/div).

C. Noise Sensitivity Suppression

According to the above analysis, the narrow noise tolerance range causes the large steady-state phase-shift duty cycle to fluctuate and leads to high current stress on the energy storage unit. Therefore, the magnitude of the current stress can reflect the noise tolerance capability of the system.

In the experiment platform, the controller TMS320F28379D has a 12-bit ADC module and the full scale is 3 V, thus the quantizer's least significant bit is

$$LSB = \frac{3}{2^{12}} = 0.732 \text{ mV} \tag{26}$$

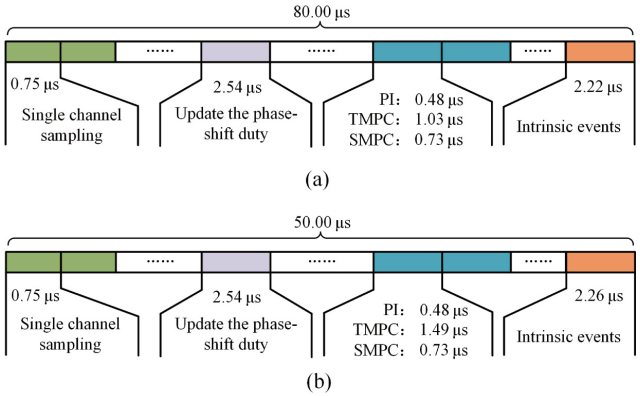

Fig. 15. Running time of different stages in one cycle. (a) DAB converter; (b) DBSRC.

When the rating sampling voltage is 400 V, the maximum quantization noise is

$$\Delta^q_{\max} = \frac{1}{2} \times LSB \times 400 = 0.146 \text{ V} \tag{27}$$

According to the datasheet of the voltage sensor chip AMC1311B, the input offset voltage V_{OS} =1.5 mV, thus the measurement noise can reach

$$\Delta^m_{\max} = 1.5 \text{ mV} \times \frac{400}{3} = 0.2 \text{ V} \tag{28}$$

Besides, the temperature drift of AMC1311 is 20 μV/°C, which is effected by the chip temperature. However, the thermal noise is much smaller than the quantization noise and the measurement noise, so it can be ignored in the experiment.

Setting the load resistance from 40 Ω to 20 Ω, our experiments are conducted under the proposed SMPC scheme for different values of the noise tolerance coefficient. Fig. 14 shows the operating waveforms of the DAB converter (see Figs. 14 (a), (c) and (e)) and DBSRC (see Figs. 14 (b), (d) and (f)) with the noise tolerance coefficient value Y being 0.03, 0.06, and 0.12. It can be seen that the resonant current decreases by 32.4 % when the noise tolerance coefficient increases from 0.03 to 0.12 at the power of 250 W for the DAB converter, and the resonant current decreases by 32.9% at the power of 500 W under the same condition. The inductor current decreases by 52.9% when the noise tolerance coefficient increases from 0.03 to 0.12 at the power of 250 W for DBSRC, and the inductor current decreases by 33.5% at the power of 500 W under the same condition. Obviously, the proposed SMPC scheme can significantly improve the noise tolerance capability and reduce the current stress of energy storage unit without weakening the dynamic performance, which means smaller switching turn off current and higher system efficiency.

D. Comparison of Running Time

Figs. 15(a) and (b) show the running time of different stages in one control cycle for DAB converter and DBSRC. Compared to the TMPC scheme, the computational time of the DAB

converter and DBSRC under SMPC have reduced by 29% and 51%, respectively, and the control target deviation is eliminated completely. Meanwhile, the proposed strategy requires fewer sensors (no input voltage sensor), which implies that the running time can be further reduced. Although the running time under SMPC is longer than PI control, it has much better dynamic performance with the same sensors.

V. Conclusion

This paper proposes a continuous-control-set model predictive control strategy based on a simplified model that is suitable for different dual-active-bridge topologies under phase-shift modulation. The proposed strategy effectively solves the problem of the high sensitivity of the model predictive control to both model parameters and sampling noise with a high level of portability. Compared to the traditional model predictive control, the proposed control strategy does not result in steady-state error caused by model parameter variations and modeling methods. By regulating the noise tolerance coefficient of the simplified model, the system's noise tolerance range is significantly widened, while the converters can still maintain excellent dynamic performance, and the computational burden of the controller is significantly reduced. Experimental results verify the effectiveness of the proposed control strategy.

References

[1] F. Xue, R. Yu, and A. Q. Huang, "A 98.3% efficient GaN isolated bidirectional DC–DC converter for DC microgrid Energy storage system applications," in *IEEE Transactions on Industrial Electronics*, vol. 64, no. 11, pp. 9094–9103, Nov. 2017.

[2] Q. Xu, N. Vafamand, L. Chen, T. Dragičević, L. Xie, and F. Blaabjerg, "Review on advanced control technologies for bidirectional DC/DC converters in DC microgrids," in *IEEE Journal of Emerging and Selected Topics in Power Electronics*, vol. 9, no. 2, pp. 1205–1221, Apr. 2021.

[3] V. Rathore, S. R. P. Reddy, and K. Rajashekara, "An isolated multilevel DC–DC converter topology with hybrid resonant switching for EV fast charging application," in *IEEE Transactions on Industry Applications*, vol. 58, no. 5, pp. 5546–5557, Sept.-Oct. 2022.

[4] S. Sarkar and A. Das, "An isolated single input-multiple output DC–DC modular multilevel converter for fast electric vehicle charging," in *IEEE Journal of Emerging and Selected Topics in Industrial Electronics*, vol. 4, no. 1, pp. 178–187, Jan. 2023.

[5] P. Shan, Y. Sun, Y. Song, F. Zhang, Y. Li, and K. Sun, "Adaptive parameter tuning and virtual impedance injection control for coupled harmonic mitigation of photovoltaic converter," in *IEEE Transactions on Power Electronics*, vol. 40, no. 1, pp. 162–175, Jan. 2025.

[6] S. Inoue and H. Akagi, "A bidirectional DC–DC converter for an energy storage system with galvanic isolation," in *IEEE Transactions on Power Electronics*, vol. 22, no. 6, pp. 2299–2306, Nov. 2007.

[7] L. Li, G. Xu, D. Sha, Y. Liu, Y. Sun, and M. Su, "Review of dual-active-bridge converters with topological modifications," in *IEEE Transactions on Power Electronics*, vol. 38, no. 7, pp. 9046–9076, Jul. 2023.

[8] K. Wu, C. W. de Silva, and W. G. Dunford, "Stability analysis of isolated bidirectional dual active full-bridge DC–DC converter with triple phase-shift control," in *IEEE Transactions on Power Electronics*, vol. 27, no. 4, pp. 2007–2017, Apr. 2012.

[9] Z. Zhou, H. Li, and X. Wu, "A constant frequency ZVS control system for the four-switch Buck–Boost DC–DC converter with reduced inductor current," in *IEEE Transactions on Power Electronics*, vol. 34, no. 7, pp. 5996–6003, Jul. 2019.

[10] C. Yang, J. Wang, C. Wang, X. You, and L. Xu, "Transient DC bias current reducing for bidirectional dual-active-bridge DC–DC converter by modifying modulation," in *IEEE Transactions on Power Electronics*, vol. 36, no. 11, pp. 13149–13161, Nov. 2021.

[11] P. Cortes, M. P. Kazmierkowski, R. M. Kennel, D. E. Quevedo, and J. Rodriguez, "Predictive control in power electronics and drives," in *IEEE Transactions on Industrial Electronics*, vol. 55, no. 12, pp. 4312–4324, Dec. 2008.

[12] B. Wang, J. Huang, C. Wen, J. Rodriguez, C. Garcia, and H. B. Gooi, "Event-triggered model predictive control for power converters," in *IEEE Transactions on Industrial Electronics*, vol. 68, no. 1, pp. 715–720, Jan. 2021.

[13] X. Han, Y. Liao, and D. Yang, "Model predictive control strategy for DAB-LLC hybrid bidirectional converter based on power distribution balance," in *IEEE Transactions on Circuits and Systems II: Express Briefs*, vol. 71, no. 6, pp. 3236–3240, Jun. 2024.

[14] L. Chen, S. Shao, Q. Xiao, L. Tarisciotti, P. W. Wheeler, and T. Dragičević, "Model predictive control for dual-active-bridge converters supplying pulsed power loads in naval DC micro-grids," in *IEEE Transactions on Power Electronics*, vol. 35, no. 2, pp. 1957–1966, Feb. 2020.

[15] W. Song, M. Zhong, Y. Deng, S. Yin, and B. Yu, "Model predictive power control for bidirectional series resonant isolated DC–DC converters with steady-state and dynamic performance optimization," in *IEEE Journal of Emerging and Selected Topics in Industrial Electronics*, vol. 3, no. 3, pp. 604–615, Jul. 2022.

[16] W. Song, M. Zhong, and S. Luo, "Model predictive power control with current stress optimization for bidirectional series resonant DC-DC converter," in *2020 15th IEEE Conference on Industrial Electronics and Applications (ICIEA)*, Kristiansand, Norway, 2020, pp. 31–36.

[17] K. Yu, F. Zhuo, F. Wang, and X. Jiang, "Deep-learning-based steady-state modeling and model predictive control for CLLC DC-DC resonant converter in DC distribution system," in *2022 IEEE Applied Power Electronics Conference and Exposition (APEC)*, TX, USA, 2022, pp. 1–5.

[18] Y. Zhu, Y. Yang, H. Wen, J. Mao, P. Wang, and X. Fan, "Model predictive control with a novel parameter identification scheme for dual-active-bridge converters," in *IEEE Journal of Emerging and Selected Topics in Power Electronics*, vol. 11, no. 5, pp. 4704–4713, Oct. 2023.

[19] M. Han, H. He, X. Wang, Z. Dong, and Z. Zhang, "Current-sensorless model predictive control of dual active bridge converters with Kalman Filter," in *2021 IEEE International Conference on Predictive Control of Electrical Drives and Power Electronics (PRECEDE)*, Jinan, China, 2021, pp. 663–667.

[20] X. Li, Z. Dong, Y. Cao, J. Qin, Z. Zhang, and C. K. Tse, "Model-predictive control with parameter identification for multi-dual-active-bridge converters achieving Accurate power balancing," in *IEEE Transactions on Power Electronics*, vol. 38, no. 9, pp. 10880–10894, Sept. 2023.

[21] W. Song, M. Zhong, S. Luo, and S. Yang, "Model predictive power control for bidirectional series-resonant isolated DC–DC converters with fast dynamic response in locomotive traction system," in *IEEE Transactions on Transportation Electrification*, vol. 6, no. 3, pp. 1326–1337, Sept. 2020.

[22] J. Sun, L. Qiu, X. Liu, J. Ma, J. Rodríguez, and Y. Fang, "Model-free moving-discretized-control-set predictive control for three-phase dual-active-bridge converters," in *IEEE Transactions on Power Electronics*, vol. 39, no. 8, pp. 9160–9173, Aug. 2024.

[23] J. Yang, J. Liu, J. Zhang, N. Zhao, Y. Wang, and T. Q. Zheng, "Multirate digital signal processing and noise suppression for dual active bridge DC–DC converters in a power electronic traction transformer," in *IEEE Transactions on Power Electronics*, vol. 33, no. 12, pp. 10885–10902, Dec. 2018.

[24] O. Babayomi, Z. Zhang, Z. Li, M. L. Heldwein, and J. Rodriguez, "Robust predictive control of grid-connected converters: sensor noise suppression with parallel-cascade extended state observer," in *IEEE Transactions on Industrial Electronics*, vol. 71, no. 4, pp. 3728–3740, Apr. 2024.

[25] X. Li and A. K. S. Bhat, "Analysis and design of high-frequency isolated

dual-bridge series resonant DC/DC converter," in *IEEE Transactions on Power Electronics*, vol. 25, no. 4, pp. 850–862, Apr. 2010.

[26] W. Song, S. Yin, Y. Deng, and M. Zhong, "Steady-state performance optimization of dual-bridge series resonant DC/DC converters," in *IEEE Journal of Emerging and Selected Topics in Power Electronics*, vol. 11, no. 2, pp. 1767–1777, Apr. 2023.

Tianqu Hao received the B.Eng. degree in electronic engineering from the Ocean University of China, Qingdao, China, in 2008, and the M.Sc. and Ph.D. degrees in electrical engineering from Durham University, Durham, U.K., in 2009 and 2017, respectively. In 2017, he joined Shandong University, Jinan, China, as a Lecturer. His current research interests include control of power electronic devices and flexible transmission technologies.

Jiazheng Huang was born in Shandong, China, in 2001. He received the B.S. degree in electrical engineering from the College of New Energy, China University of Petroleum, Qingdao, China, in 2023. He is currently working toward the master's degree in electrical engineering with the School of Electrical Engineering, Shandong University, Jinan, China. His current research interests include multiple-port power supply systems, power electronic transformers, and power electronic devices.

Zheng Dong received the B.Eng. and M.Phil. degrees in electrical engineering from Southwest Jiaotong University, Chengdu, China, in 2011 and 2014, respectively, and the Ph.D. degree in electronic and information engineering from the Hong Kong Polytechnic University, Hong Kong, in 2019. Since 2019, he has been an Associate Professor with Shandong University, Jinan, China. His current research interests include power electronics, energy storage systems, and circuit theory.

Zhenbin Zhang received the Ph.D. degree in electrical and energy engineering from the Technical University of Munich, Munich, Germany, in 2016. Since 2017, he has been a Full Professor with Shandong University, Jinan, China. His research interests include power electronics and electrical drives, sustainable energy systems, smart grids, and microgrids.

Qian Chen was born in Shandong, China, in 1999. She received the B.S. degree in electrical engineering in 2022 from China University of Mining and Technology. Currently, she is working toward the master's degree in electrical engineering at Shandong University with the School of Electrical Engineering. Her current research interests include triple-active-bridge power converters, model predictive control, and fault tolerant control.

Design and Optimization of High Misalignment Edge-Enhanced Stepped Coil Structure for Dynamic Wireless Power Transfer System

Chenxi ZHANG, Zhongqi LI, Jianbin WANG, and Changxuan HU

***Abstract*—In order to address the issue of mutual inductance variation in dynamic wireless power transfer systems for electric vehicles, which leads to significant fluctuations in system output, an edge-enhanced stepped coil structure is proposed to improve the system's anti-offset performance. Firstly, a model of the edge-enhanced stepped coil structure has been constructed, and the characteristics of mutual inductance variation for this structure have been analyzed. Secondly, a method for calculating mutual inductance in a stepped coil structure is proposed based on the Biot-Saval law. Then, based on the proposed method for calculating mutual inductance in stepped coils, the parameters of the edge-enhanced stepped coil structure are optimized according to the principle of minimizing fluctuations in mutual inductance. Additionally, a magnetic core structure that aligns with the coil's characteristics is designed to enhance both mutual inductance and the coil's resistance to offset performance. Finally, a 500 W experimental prototype has been constructed. The experimental results show that the mutual inductance fluctuation rate of the edge-enhanced stepped coil does not exceed 5% when the *Y*-axis direction is offset by 50% (362 mm) of the outer diameter of the transmitter coil. The transmission efficiency of the system is as high as 93.92%, and the fluctuation rate of the output current is less than 5%.**

***Index Terms*—High misalignment tolerance; mutual inductance calculation; stepped coil structure; wireless power transfer.**

I. Introduction

WIRELESS power transfer (WPT) technology enables the non-contact transfer of energy using electromagnetic fields and alternative media, providing an innovative solution to the safety and convenience issues associated with traditional contact charging methods [1]–[3]. WPT technology has attracted considerable attention from researchers both domestically and internationally due to its remarkable flexibility, high safety and reliability, and its ability to function effectively in harsh environmental conditions. Currently, WPT technology has been successfully applied across various domains, including underwater power supply systems for equipment [4]–[6], consumer electronics [7]–[9], and intelligent rail transit systems [10]–[11].

In dynamic WPT, positional shifts of the coupling coil result in variations in mutual inductance between the coils. These fluctuations negatively impact the stable operation of the WPT system, presenting challenges to its reliability and safety [12]–[14]. In response to the aforementioned issues, researchers have conducted extensive studies on the anti-offset performance of coils, with the goal of improving the stability and reliability of the system when the coil position is misaligned. Consequently, investigating coil structures that exhibit quasi-constant mutual inductance is of great significance.

The classification of coils depends on the number of coils present. Coils can be categorized as either single-coil or multi-coil structures. The magnetic field produced by the single-coil structure is unidirectional. Consequently, when the coil is misaligned, the positive area of the coil decreases, leading to a reduction in positive magnetic flux. When the misalignment reaches half the diameter of the transmitting coil, there is not only a decrease in positive magnetic flux but also the emergence of negative magnetic flux, which compromises the anti-offset performance. The offset performance of the single-coil structure is enhanced through the optimization of coil size [15]–[17], turn spacing and core structure [18]–[20].

The multi-coil structure leverages the spatial superposition of multiple coils, employing the principle of magnetic field superposition to enhance effective coupling and improve the coil's resistance to offset performance. A team from the University of Auckland, New Zealand, proposed a double-D (DD) coil, which consists of two unipolar coils connected in series and placed side by side. They also incorporated an orthogonal Q-type coil into the DD coil to create a double-D quadrature (DDQ) coil structure. This design effectively compensates for the induction blindness inherent in the DD coil [21]. In addition, to reduce consumable materials, the team proposed

Manuscript received March 23, 2025; revised July 01, 2025; accepted July 11, 2025. Date of publication September 30, 2025; date of current version August 22, 2025. This work was supported in part by National Key R&D Program Project under the grant 2022YFB3403200, Key Projects of Hunan Provincial Department of Education under the grant 23A0432, Excellent Youth Project of Scientific Research of Hunan Provincial Department of Education under the grant 22B0577, National Natural Science Foundation of China (NSFC) Youth Science Fund Project under the grant 62303178, and A Project Supported by Scientific Research Fund of Hunan Provincial Education Department under the grant 23C0182. (*Corresponding authors: Zhongqi Li.*)

All authors are with the School of Transportation and Electrical Engineering, Hunan University of Technology, Zhuzhou 412007, China (e-mail:17873436232@163.com; lizhongqi@hnu.edu.cn; 1366597990@qq.com; 905436194@qq.com).

Digital Object Identifier 10.24295/CPSSTPEA.2025.00024

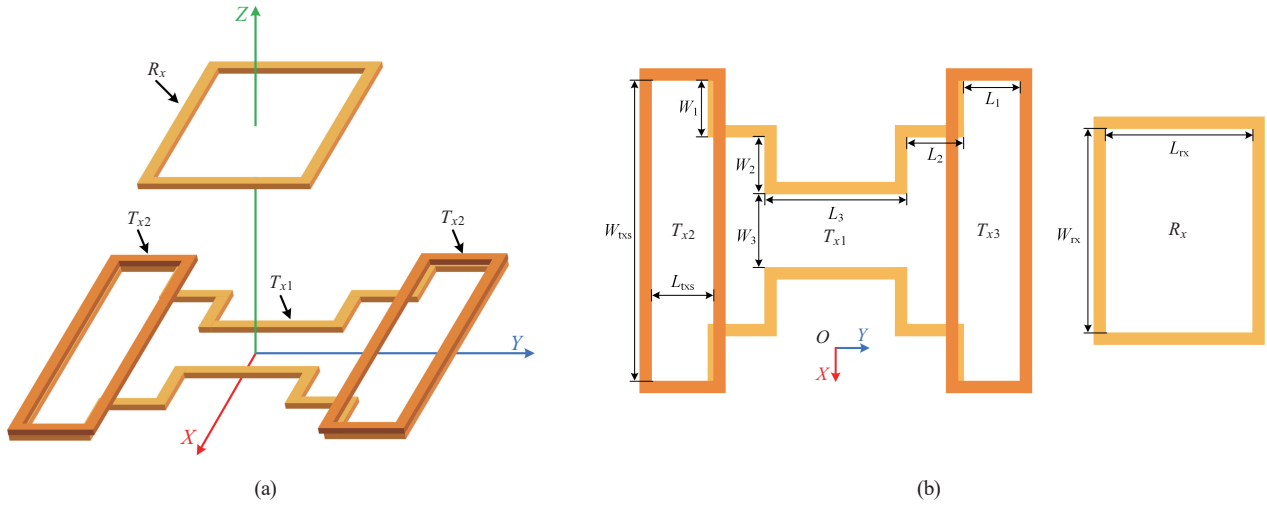

Fig. 1. EESC structure diagram. (a) 3D structural model. (b) Top view of structure.

the bipolar (BP) coil structure in [22] and the tripolar (TP) coil structure in [23], utilizing coil stacking. This approach can enhance the coil offset performance to some extent.

Researchers have investigated more advanced coil structures by employing modular combination strategies. One notable design is the double-layer quadrature double-D(DQDD) structure, which consists of two pairs of DD coils arranged orthogonally in a double-layer configuration. This arrangement facilitates decoupling between the coils and creates a periodic variation in the excited magnetic field. However, the DQDD structure exhibits a coupling coefficient fluctuation of 55% under a horizontal offset of 150 mm, indicating that its anti-offset performance is insufficient to withstand significant positional shifts [24]. In addition to the above magnetic field superposition approach, researchers have exploited the feature that the reverse series coil has the opposite tendency to the forward coil with coil offset to achieve a largely constant mutual inductance during coil offset. A multi-receiver reverse series coil structure has been proposed, and by optimizing the forward and reverse series coils, the mutual inductance fluctuation is only 3.81% when the coil is offset by 34% (225 mm) of the maximum coil outer length [25].

In summary, most current coil structures accommodate a limited offset range during static charging. However, there are issues related to the small maximum allowable offset distance of the coupling coil and the significant fluctuations in mutual inductance that occur during coil offset in dynamic wireless power transfer. The contributions of this paper are as follows:

1) An edge-enhanced stepped coil structure is proposed, an edge-enhanced stepped coil structure model is dissected, and the mutual inductance characteristics of the edge-enhanced stepped coil structure are analyzed.

2) Stepped coils are modelled and a method for calculating the mutual inductance of stepped transmitting coils and rectangular receiving coils based on the Biot-Saval law is proposed.

3) An optimisation strategy based on the principle of minimising mutual inductance fluctuations is proposed, aiming to optimise the coil sizing parameters and core sizing parameters, with the objective of achieving the maximum coil offset distance of 50% of the length of the outer diameter of the transmitting coil and a mutual inductance fluctuation rate of less than 5%.

4) The 500 W experimental prototype is built, and the experiment proves that the proposed coil structure has good anti-offset performance, and the output of the system is smooth.

In this paper, the structural model of the edge-enhanced stepped coil is given and analyzed in Section II. The formula for calculating the mutual inductance of the stepped coil in Section III. The experimental verification in Section IV. Finally, the conclusions are shown in Section V.

II. Edge-Enhanced Stepped Coil Structure

A. Structure Model

In this paper, an edge-enhanced stepped coil structure is proposed in order to achieve a larger limit offset range of the coupling coil in dynamic wireless power transfer system and to keep the mutual inductance quasi-constant within the limit offset range. The EESC structure employs a stepped coil as the main coil and applies the principle of magnetic field superposition to introduce isotropic series compensation coils at the edges of the stepped coil, with the objective of enhancing the mutual inductance at the edges of the main coil. A three-dimensional representation of the EESC structure is presented in Fig. 1(a). The transmitter coil (T_x) consists of a step coil (T_{x1}) and two compensation coils (T_{x2} and T_{x3}),compensation coils are arranged in a stacked configuration along step coil in the *Y*-axis direction. The receiving coil (R_x) is a rectangular coil.

The plan view of the EESC coil structure is illustrated in Fig. 1(b). The coil parameter variables are defined as follows: L_1, L_2, and L_3 will be used to denote the length of the stepped coil T_{x1}. W_1, W_2, and W_3 will be used to denote the width of the same coil. L_{txs} and W_{txs} will be used to denote the length and width of compensation coils T_{x2} and T_{x3}, respectively. L_{rx} and

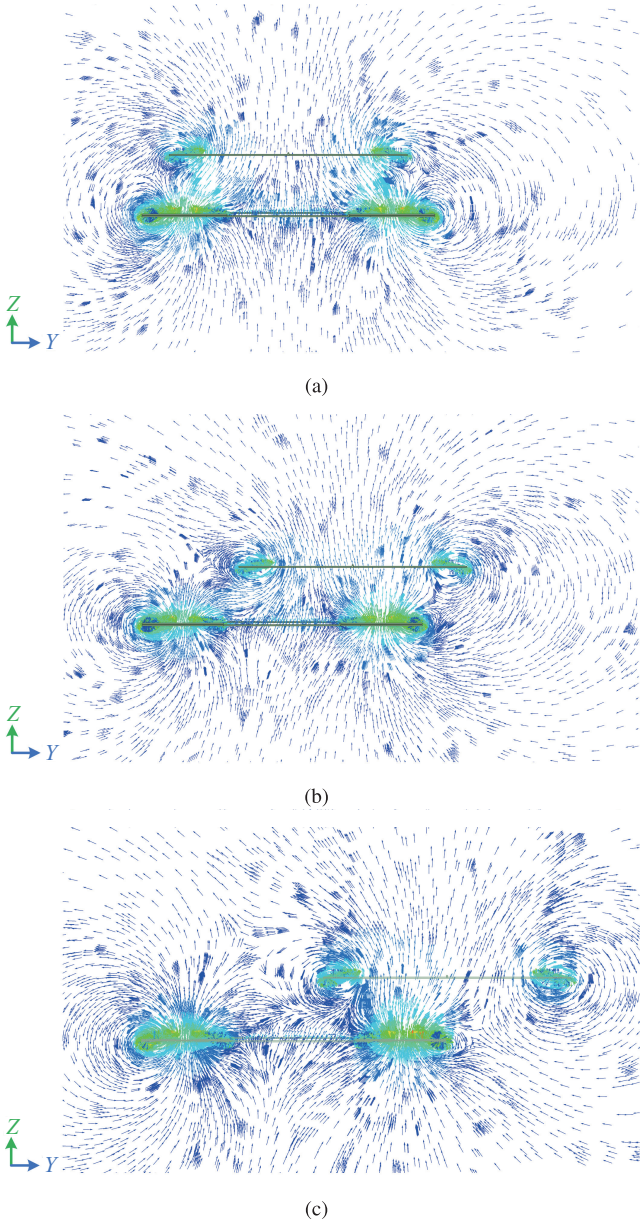

Fig. 2. EESC magnetic field diagrams at offset along the *Y*-axis direction. (a) $\Delta Y = 0$. (b) $\Delta Y = 0.25L_{tx\text{-}o}$. (c) $\Delta Y = 0.5L_{tx\text{-}o}$.

W_{rx} will be used to denote the length and width of the receiver coil R_x, respectively. In order to guarantee optimal anti-offset functionality when the coils are offset, compensation coils are of identical dimensions and arranged in a symmetrical fashion to align the outer edges of the main coils.

The stepped coil is designed with three distinct levels, which progressively extend along the *Y*-axis and result in an increased coil width along the *X*-axis. This design effectively increases the positive overlap area between the transmitting and receiving coils when an offset occurs. Consequently, a larger longitudinal flux passes through the coils, enabling the mutual inductance to be preserved to a significant extent. Compared to conventional rectangular coils, the stepped coil demonstrates enhanced anti-offset performance, making it a more robust option for dynamic wireless power transfer systems.

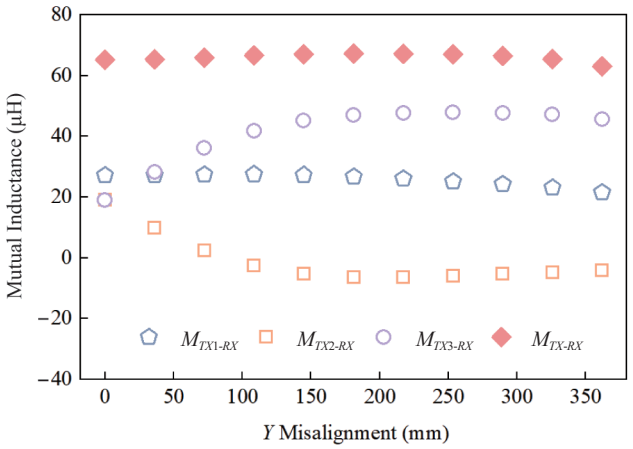

Fig. 3. Variation curves of mutual inductance at offset along the *Y*-axis direction.

B. Mutual Inductance Characterisation of Coil Structures

To evaluate the anti-offset performance of the EESC structure, a simulation model was developed using ANSYS Maxwell software. The magnetic field distribution is simulated in the *Y*-axis, as illustrated in Fig. 2. ΔY denotes the offset distance along the *Y*-axis direction, $L_{tx\text{-}o}$ denotes the outer diameter length of the transmitter coil.

When the transmitting and receiving coils are perfectly aligned ($\Delta Y = 0$) in Fig. 2(a), the transmitting coil generates a longitudinal magnetic flux that passes vertically through the receiving coil, facilitating effective coupling between the coils. As the receiving coil offsets along the positive *Y*-axis ($\Delta Y = 0.25L_{tx\text{-}o}$) in Fig. 2(b), it gradually shifts from the center toward the edge. During this shift, the area directly opposite the receiving coil on compensating coil T_{x2} decreases, while the area directly opposite compensating coil T_{x3} increases. Through the principle of magnetic field superposition, this redistribution enhances the total magnetic flux across the three coils, thereby increasing the mutual inductance. When the offset continues in a positive direction along the *Y*-axis ($\Delta Y = 0.5L_{tx\text{-}o}$) in Fig. 2(c), the longitudinal flux through the receiving coil R_x gradually diminishes. Consequently, the total magnetic flux and the mutual inductance between the coils also decrease.

Fig. 3 shows the mutual inductance variation curves for horizontal offset along the positive direction of *Y*-axis between the receiving coil R_x and the main coil T_{x1}, the compensation coil T_{x2} and the compensation coil T_{x3}, respectively. The mutual inductance expression between the EESC coupling mechanism is shown in (1).

$$M_{TX\text{-}RX} = M_{TX1\text{-}RX} + M_{TX2\text{-}RX} + M_{TX3\text{-}RX} \tag{1}$$

where $M_{TX\text{-}RX}$ is the mutual inductance between T_x and R_x, $M_{TX1\text{-}RX}$ is the mutual inductance between T_{x1} and R_x, $M_{TX2\text{-}RX}$ is the mutual inductance between T_{x2} and R_x, and $M_{TX3\text{-}RX}$ is the mutual inductance between T_{x3} and R_x.

As the offset distance increases, $M_{TX1\text{-}RX}$ and $M_{TX2\text{-}RX}$ gradually decrease, $M_{TX3\text{-}RX}$ exhibits a significant increasing trend. The $M_{TX\text{-}RX}$ remains basically stable in the limit offset range. During

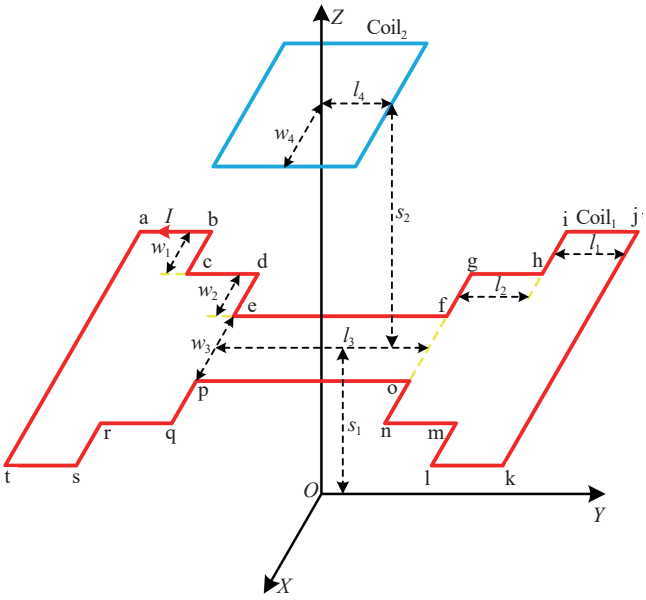

Fig. 4. EESC structure diagrams.

the coil offset process, the magnetic field superposition principle is used to superimpose the magnetic flux through the receiving coil to form a region where the mutual inductance of the coils increases and then decreases. This ensures that the mutual inductance between the coils is quasi-constant.

III. Calculation of Mutual Inductance of Stepped Coils

In order to study the working mechanism of the EESC structure under different offsets and its offset characteristics, it is necessary to create a model of the coil structure. However, there is currently no established methodology for calculating the mutual inductance of stepped coils. Such a model would provide a theoretical foundation for understanding the performance of the EESC structure and optimizing its design for improved anti-offset capabilities.

As shown in Fig. 4, the transmitting coil is a stepped coil, the receiving coil is a rectangular coil. l_1, l_2, and l_3 are the lengths of the different echelons of the stepped coil. w_1, w_2, and w_3 are the widths of the different echelons of the stepped coil. l_4 and w_4 are the lengths and widths of the rectangular receiving coil. s_1 is the vertical distance between the stepped coil O_1 and O. s_2 is the vertical distance between the rectangular coil O_2 and O_1.

Setting any point $P(x, y, z)$ in the plane of the receiving coil, the magnetic flux density generated by the transmitting coil at P inside the receiving coil can be expressed according to the Biot-Saval law:

$$\vec{B}=\frac{\mu_0 I}{4\pi}\oint_C\left(\frac{\mathrm{d}\vec{l}'\times\vec{R}}{R^3}\right) \tag{2}$$

where μ_0 is the magnetic permeability in vacuum, I is the current on the transmitting coil, C' is the curve enclosed by the transmitting coil, $I\mathrm{d}\vec{l}'$ denotes the current element, $\vec{R}$ is the distance vector from any point P to the current element. $I\mathrm{d}\vec{l}'\times\vec{R}$ can be calculated in (3) to (5).

$$\begin{aligned}
&\mathrm{d}\vec{l}'_{\mathrm{ab}}=-\mathrm{d}y'\hat{y},\ \mathrm{d}\vec{l}'_{\mathrm{bc}}=-\mathrm{d}x'\hat{x},\ \mathrm{d}\vec{l}'_{\mathrm{cd}}=-\mathrm{d}y'\hat{y},\ \mathrm{d}\vec{l}'_{\mathrm{de}}=-\mathrm{d}x'\hat{x}\\
&\mathrm{d}\vec{l}'_{\mathrm{ef}}=-\mathrm{d}y'\hat{y},\ \mathrm{d}\vec{l}'_{\mathrm{fg}}=\mathrm{d}x'\hat{x},\ \mathrm{d}\vec{l}'_{\mathrm{gh}}=-\mathrm{d}y'\hat{y},\ \mathrm{d}\vec{l}'_{\mathrm{hi}}=\mathrm{d}x'\hat{x}\\
&\mathrm{d}\vec{l}'_{\mathrm{ij}}=-\mathrm{d}y'\hat{y},\ \mathrm{d}\vec{l}'_{\mathrm{jk}}=-\mathrm{d}x'\hat{x},\ \mathrm{d}\vec{l}'_{\mathrm{kl}}=\mathrm{d}y'\hat{y},\ \mathrm{d}\vec{l}'_{\mathrm{lm}}=\mathrm{d}x'\hat{x}\\
&\mathrm{d}\vec{l}'_{\mathrm{mn}}=\mathrm{d}y'\hat{y},\ \mathrm{d}\vec{l}'_{\mathrm{no}}=\mathrm{d}x'\hat{x},\ \mathrm{d}\vec{l}'_{\mathrm{op}}=\mathrm{d}y'\hat{y},\ \mathrm{d}\vec{l}'_{\mathrm{pq}}=-\mathrm{d}x'\hat{x}\\
&\mathrm{d}\vec{l}'_{\mathrm{pr}}=\mathrm{d}y'\hat{y},\ \mathrm{d}\vec{l}'_{\mathrm{rs}}=-\mathrm{d}x'\hat{x},\ \mathrm{d}\vec{l}'_{\mathrm{st}}=\mathrm{d}y'\hat{y},\ \mathrm{d}\vec{l}'_{\mathrm{ta}}=-\mathrm{d}x'\hat{x}
\end{aligned} \tag{3}$$

$$\begin{aligned}
&\vec{R}_{\mathrm{ab}}=(x+(w_1+w_2+w_3/2))\hat{x}+(y-y')\hat{y}+z\hat{z}\\
&\vec{R}_{\mathrm{bc}}=(x-x')\hat{x}+(y+(l_2+l_3/2))\hat{y}+z\hat{z}\\
&\vec{R}_{\mathrm{cd}}=(x+(w_2+w_3/2))\hat{x}+(y-y')\hat{y}+z\hat{z}\\
&\vec{R}_{\mathrm{de}}=(x-x')\hat{x}+(y+(l_3/2))\hat{y}+z\hat{z}\\
&\vec{R}_{\mathrm{ef}}=(x+(w_3/2))\hat{x}+(y-y')\hat{y}+z\hat{z}\\
&\vec{R}_{\mathrm{fg}}=(x-x')\hat{x}+(y-(l_3/2))\hat{y}+z\hat{z}\\
&\vec{R}_{\mathrm{gh}}=(x+(w_2+w_3/2))\hat{x}+(y-y')\hat{y}+z\hat{z}\\
&\vec{R}_{\mathrm{hi}}=(x-x')\hat{x}+(y-(l_2+l_3/2))\hat{y}+z\hat{z}\\
&\vec{R}_{\mathrm{ij}}=(x+(w_1+w_2+w_3/2))\hat{x}+(y-y')\hat{y}+z\hat{z}\\
&\vec{R}_{\mathrm{jk}}=(x-x')\hat{x}+(y-(l_1+l_2+l_3/2))\hat{y}+z\hat{z}\\
&\vec{R}_{\mathrm{kl}}=(x-(w_1+w_2+w_3/2))\hat{x}+(y-y')\hat{y}+z\hat{z}\\
&\vec{R}_{\mathrm{lm}}=(x-x')\hat{x}+(y-(l_2+l_3/2))\hat{y}+z\hat{z}\\
&\vec{R}_{\mathrm{mn}}=(x-(w_2+w_3/2))\hat{x}+(y-y')\hat{y}+z\hat{z}\\
&\vec{R}_{\mathrm{no}}=(x-x')\hat{x}+(y-(l_3/2))\hat{y}+z\hat{z}\\
&\vec{R}_{\mathrm{op}}=(x-(w_3/2))\hat{x}+(y-y')\hat{y}+z\hat{z}\\
&\vec{R}_{\mathrm{pq}}=(x-x')\hat{x}+(y+(l_3/2))\hat{y}+z\hat{z}\\
&\vec{R}_{\mathrm{qr}}=(x-(w_2+w_3/2))\hat{x}+(y-y')\hat{y}+z\hat{z}\\
&\vec{R}_{\mathrm{rs}}=(x-x')\hat{x}+(y+(l_2+l_3/2))\hat{y}+z\hat{z}\\
&\vec{R}_{\mathrm{st}}=(x-(w_1+w_2+w_3/2))\hat{x}+(y-y')\hat{y}+z\hat{z}\\
&\vec{R}_{\mathrm{ta}}=(x-x')\hat{x}+(y+(l_1+l_2+l_3/2))\hat{y}+z\hat{z}
\end{aligned} \tag{4}$$

$$\begin{aligned}
&\mathrm{d}l'_{\mathrm{ab}}\times\vec{R}_{\mathrm{ab}}=-z\mathrm{d}y'\hat{x}+\mathrm{d}y'(x+(w_1+w_2+w_3/2))\hat{z}\\
&\mathrm{d}l'_{\mathrm{bc}}\times\vec{R}_{\mathrm{bc}}=z\mathrm{d}x'\hat{y}-\mathrm{d}x'(y+(l_2+l_3/2))\hat{z}\\
&\mathrm{d}l'_{\mathrm{cd}}\times\vec{R}_{\mathrm{cd}}=-z\mathrm{d}y'\hat{x}+\mathrm{d}y'(x+(w_2+w_3/2))\hat{z}
\end{aligned} \tag{5}$$

$$\begin{cases}
\mathrm{d}l'_{\mathrm{de}}\times\vec{R}_{\mathrm{de}}=z\mathrm{d}x'\hat{y}-\mathrm{d}x'(y+(l_3/2))\hat{z}\\
\mathrm{d}l'_{\mathrm{ef}}\times\vec{R}_{\mathrm{ef}}=-z\mathrm{d}y'\hat{x}+\mathrm{d}y'(x+(w_3/2))\hat{z}\\
\mathrm{d}l'_{\mathrm{fg}}\times\vec{R}_{\mathrm{fg}}=-z\mathrm{d}x'\hat{y}+\mathrm{d}x'(y-(l_3/2))\hat{z}\\
\mathrm{d}l'_{\mathrm{gh}}\times\vec{R}_{\mathrm{gh}}=-z\mathrm{d}y'\hat{x}+\mathrm{d}y'(x+(w_2+w_3/2))\hat{z}\\
\mathrm{d}l'_{\mathrm{hi}}\times\vec{R}_{\mathrm{hi}}=-z\mathrm{d}x'\hat{y}+\mathrm{d}x'(y-(l_2+l_3/2))\hat{z}\\
\mathrm{d}l'_{\mathrm{ij}}\times\vec{R}_{\mathrm{ij}}=-z\mathrm{d}y'\hat{x}+\mathrm{d}y'(x+(w_1+w_2+w_3/2))\hat{z}\\
\mathrm{d}l'_{\mathrm{jk}}\times\vec{R}_{\mathrm{jk}}=z\mathrm{d}x'\hat{y}-\mathrm{d}x'(y-(l_1+l_2+l_3/2))\hat{z}\\
\mathrm{d}l'_{\mathrm{kl}}\times\vec{R}_{\mathrm{kl}}=z\mathrm{d}y'\hat{x}-\mathrm{d}y'(x-(w_1+w_2+w_3/2))\hat{z}\\
\mathrm{d}l'_{\mathrm{lm}}\times\vec{R}_{\mathrm{lm}}=-z\mathrm{d}x'\hat{y}+\mathrm{d}x'(y-(l_2+l_3/2))\hat{z}\\
\mathrm{d}l'_{\mathrm{mn}}\times\vec{R}_{\mathrm{mn}}=z\mathrm{d}y'\hat{x}-\mathrm{d}y'(x-(w_2+w_3/2))\hat{z}\\
\mathrm{d}l'_{\mathrm{no}}\times\vec{R}_{\mathrm{no}}=-z\mathrm{d}x'\hat{y}+\mathrm{d}x'(y-(l_3/2))\hat{z}\\
\mathrm{d}l'_{\mathrm{op}}\times\vec{R}_{\mathrm{op}}=z\mathrm{d}y'\hat{x}-\mathrm{d}y'(x-(w_3/2))\hat{z}\\
\mathrm{d}l'_{\mathrm{pq}}\times\vec{R}_{\mathrm{pq}}=z\mathrm{d}x'\hat{y}-\mathrm{d}x'(y+(l_3/2))\hat{z}\\
\mathrm{d}l'_{\mathrm{qr}}\times\vec{R}_{\mathrm{qr}}=z\mathrm{d}y'\hat{x}-\mathrm{d}y'(x-(w_2+w_3/2))\hat{z}\\
\mathrm{d}l'_{\mathrm{rs}}\times\vec{R}_{\mathrm{rs}}=z\mathrm{d}x'\hat{y}-\mathrm{d}x'(y+(l_2+l_3/2))\hat{z}\\
\mathrm{d}l'_{\mathrm{st}}\times\vec{R}_{\mathrm{st}}=z\mathrm{d}y'\hat{x}-\mathrm{d}y'(x-(w_1+w_2+w_3/2))\hat{z}\\
\mathrm{d}l'_{\mathrm{ta}}\times\vec{R}_{\mathrm{ta}}=-z\mathrm{d}x'\hat{y}-\mathrm{d}x'(y+(l_1+l_2+l_3/2))\hat{z}
\end{cases}\tag{5}$$

The magnetic flux density generated by each line segment of the stepped coil at any point P can be obtained by substituting (4) into (1). The magnetic flux density at any point P in the Z-axis direction can be expanded according to (1) as follows:

$$B_{\mathrm{ab}}=\frac{\mu_0 N_1 I}{4\pi}\left(\frac{(x+(w_1+w_2+w_3/2))}{(x+(w_1+w_2+w_3/2))^2+z^2}\right)\times\left(\frac{y+(l_1+l_2+l_3/2)}{R_{\mathrm{a}}}-\frac{y+(l_2+l_3/2)}{R_{\mathrm{b}}}\right)\tag{6}$$

$$B_{\mathrm{bc}}=\frac{\mu_0 N_1 I}{4\pi}\left(\frac{-(y+(l_2+l_3/2))}{(y+(l_2+l_3/2))^2+z^2}\right)\times\left(\frac{x+(w_1+w_2+w_3/2)}{R_{\mathrm{b}}}-\frac{x+(w_2+w_3/2)}{R_{\mathrm{c}}}\right)\tag{7}$$

$$B_{\mathrm{cd}}=\frac{\mu_0 N_1 I}{4\pi}\left(\frac{(x+(w_2+w_3/2))}{(x+(w_2+w_3/2))^2+z^2}\right)\times\left(\frac{y+(l_2+l_3/2)}{R_{\mathrm{c}}}-\frac{y+(l_3/2)}{R_{\mathrm{d}}}\right)\tag{8}$$

$$B_{\mathrm{de}}=\frac{\mu_0 N_1 I}{4\pi}\left(\frac{-(y+(l_3/2))}{(y+(l_3/2))^2+z^2}\right)\times\left(\frac{x+(w_2+w_3/2)}{R_{\mathrm{d}}}-\frac{x+(w_3/2)}{R_{\mathrm{e}}}\right)\tag{9}$$

$$B_{\mathrm{ef}}=\frac{\mu_0 N_1 I}{4\pi}\left(\frac{(x+(w_3/2))}{(x+(w_3/2))^2+z^2}\right)\times\left(\frac{y+(l_3/2)}{R_{\mathrm{e}}}-\frac{y-(l_3/2)}{R_{\mathrm{f}}}\right)\tag{10}$$

$$B_{\mathrm{fg}}=\frac{\mu_0 N_1 I}{4\pi}\left(\frac{-(y-(l_3/2))}{(y-(l_3/2))^2+z^2}\right)\times\left(\frac{x+(w_3/2)}{R_{\mathrm{f}}}-\frac{x+(w_2+w_3/2)}{R_{\mathrm{g}}}\right)\tag{11}$$

$$B_{\mathrm{gh}}=\frac{\mu_0 N_1 I}{4\pi}\left(\frac{(x+(w_2+w_3/2))}{(x+(w_2+w_3/2))^2+z^2}\right)\times\left(\frac{y-(l_3/2)}{R_{\mathrm{g}}}-\frac{y-(l_2+l_3/2)}{R_{\mathrm{h}}}\right)\tag{12}$$

$$B_{\mathrm{hi}}=\frac{\mu_0 N_1 I}{4\pi}\left(\frac{-(y-(l_2+l_3/2))}{(y-(l_2+l_3/2))^2+z^2}\right)\times\left(\frac{x+(w_2+w_3/2)}{R_{\mathrm{h}}}-\frac{x+(w_1+w_2+w_3/2)}{R_{\mathrm{i}}}\right)\tag{13}$$

$$B_{\mathrm{ij}}=\frac{\mu_0 N_1 I}{4\pi}\left(\frac{(x+(w_1+w_2+w_3/2))}{(x+(w_1+w_2+w_3/2))^2+z^2}\right)\times\left(\frac{y-(l_2+l_3/2)}{R_{\mathrm{i}}}-\frac{y-(l_1+l_2+l_3/2)}{R_{\mathrm{j}}}\right)\tag{14}$$

$$B_{\mathrm{jk}}=\frac{\mu_0 N_1 I}{4\pi}\left(\frac{-(y-(l_1+l_2+l_3/2))}{(y-(l_1+l_2+l_3/2))^2+z^2}\right)\times\left(\frac{x+(w_1+w_2+w_3/2)}{R_{\mathrm{j}}}-\frac{x-(w_1+w_2+w_3/2)}{R_{\mathrm{k}}}\right)\tag{15}$$

$$B_{\mathrm{kl}}=\frac{\mu_0 N_1 I}{4\pi}\left(\frac{(x-(w_1+w_2+w_3/2))}{(x-(w_1+w_2+w_3/2))^2+z^2}\right)\times\left(\frac{y-(l_1+l_2+l_3/2)}{R_{\mathrm{k}}}-\frac{y-(l_2+l_3/2)}{R_{\mathrm{l}}}\right)\tag{16}$$

$$B_{\mathrm{lm}}=\frac{\mu_0 N_1 I}{4\pi}\left(\frac{-(y-(l_2+l_3/2))}{(y-(l_2+l_3/2))^2+z^2}\right)\times\left(\frac{x-(w_1+w_2+w_3/2)}{R_{\mathrm{l}}}-\frac{x-(w_2+w_3/2)}{R_{\mathrm{m}}}\right)\tag{17}$$

$$B_{mn}=\frac{\mu_0 N_1 I}{4\pi}\left(\frac{(x-(w_2+w_3/2))}{(x-(w_2+w_3/2))^2+z^2}\right)\times\left(\frac{y-(l_2+l_3/2)}{R_m}-\frac{y-(l_3/2)}{R_n}\right) \tag{18}$$

$$B_{no}=\frac{\mu_0 N_1 I}{4\pi}\left(\frac{-(y-(l_3/2))}{(y-(l_3/2))^2+z^2}\right)\times\left(\frac{x-(w_2+w_3/2)}{R_n}-\frac{x-(w_3/2)}{R_o}\right) \tag{19}$$

$$B_{op}=\frac{\mu_0 N_1 I}{4\pi}\left(\frac{(x-(w_3/2))}{(x-(w_3/2))^2+z^2}\right)\times\left(\frac{y-(l_3/2)}{R_o}-\frac{y+(l_3/2)}{R_p}\right) \tag{20}$$

$$B_{pq}=\frac{\mu_0 N_1 I}{4\pi}\left(\frac{-(y+(l_3/2))}{(y+(l_3/2))^2+z^2}\right)\times\left(\frac{x-(w_3/2)}{R_p}-\frac{x-(w_2+w_3/2)}{R_q}\right) \tag{21}$$

$$B_{qr}=\frac{\mu_0 N_1 I}{4\pi}\left(\frac{(x-(w_2+w_3/2))}{(x-(w_2+w_3/2))^2+z^2}\right)\times\left(\frac{y+(l_3/2)}{R_q}-\frac{y+(l_2+l_3/2)}{R_r}\right) \tag{22}$$

$$B_{rs}=\frac{\mu_0 N_1 I}{4\pi}\left(\frac{-(y+(l_2+l_3/2))}{(y+(l_2+l_3/2))^2+z^2}\right)\times\left(\frac{x-(w_2+w_3/2)}{R_r}-\frac{x-(w_1+w_2+w_3/2)}{R_s}\right) \tag{23}$$

$$B_{st}=\frac{\mu_0 N_1 I}{4\pi}\left(\frac{(x-(w_1+w_2+w_3/2))}{(x-(w_1+w_2+w_3/2))^2+z^2}\right)\times\left(\frac{y+(l_2+l_3/2)}{R_s}-\frac{y+(l_1+l_2+l_3/2)}{R_t}\right) \tag{24}$$

$$B_{ta}=\frac{\mu_0 N_1 I}{4\pi}\left(\frac{-(y+(l_1+l_2+l_3/2))}{(y+(l_1+l_2+l_3/2))^2+z^2}\right)\times\left(\frac{x-(w_1+w_2+w_3/2)}{R_t}-\frac{x+(w_1+w_2+w_3/2)}{R_a}\right) \tag{25}$$

where the expressions for R_a, R_b, R_c ⋯ R_s, R_t are as folllws:

$$\begin{aligned}
R_a&=\sqrt{(x+(w_1+w_2+w_3/2))^2+(y+(l_1+l_2+l_3/2))^2+z^2}\\
R_b&=\sqrt{(x+(w_1+w_2+w_3/2))^2+(y+(l_2+l_3/2))^2+z^2}\\
R_c&=\sqrt{(x+(w_2+w_3/2))^2+(y+(l_2+l_3/2))^2+z^2}\\
R_d&=\sqrt{(x+(w_2+w_3/2))^2+(y+l_3/2)^2+z^2}\\
R_e&=\sqrt{(x+w_3/2)^2+(y+l_3/2)^2+z^2}\\
R_f&=\sqrt{(x+w_3/2)^2+(y-l_3/2)^2+z^2}\\
R_g&=\sqrt{(x+(w_2+w_3/2))^2+(y-l_3/2)^2+z^2}\\
R_h&=\sqrt{(x+(w_2+w_3/2))^2+(y-(l_2+l_3/2))^2+z^2}\\
R_i&=\sqrt{(x+(w_1+w_2+w_3/2))^2+(y-(l_2+l_3/2))^2+z^2}\\
R_j&=\sqrt{(x+(w_1+w_2+w_3/2))^2+(y-(l_1+l_2+l_3/2))^2+z^2}\\
R_k&=\sqrt{(x-(w_1+w_2+w_3/2))^2+(y-(l_1+l_2+l_3/2))^2+z^2}\\
R_l&=\sqrt{(x-(w_1+w_2+w_3/2))^2+(y-(l_2+l_3/2))^2+z^2}\\
R_m&=\sqrt{(x-(w_2+w_3/2))^2+(y-(l_2+l_3/2))^2+z^2}\\
R_n&=\sqrt{(x-(w_2+w_3/2))^2+(y-l_3/2)^2+z^2}\\
R_o&=\sqrt{(x-w_3/2)^2+(y-l_3/2)^2+z^2}\\
R_p&=\sqrt{(x-w_3/2)^2+(y+l_3/2)^2+z^2}\\
R_q&=\sqrt{(x-(w_2+w_3/2))^2+(y+l_3/2)^2+z^2}\\
R_r&=\sqrt{(x-(w_2+w_3/2))^2+(y+(l_2+l_3/2))^2+z^2}\\
R_s&=\sqrt{(x-(w_1+w_2+w_3/2))^2+(y+(l_2+l_3/2))^2+z^2}\\
R_t&=\sqrt{(x-(w_1+w_2+w_3/2))^2+(y+(l_1+l_2+l_3/2))^2+z^2}
\end{aligned} \tag{26}$$

In summary, the total flux density B_{total} in the Z-axis direction of the flux density generated by the transmitting coil at any point P is shown in (27).

$$\begin{aligned}
B_{total}=&B_{ab}+B_{bc}+B_{cd}+B_{de}+B_{ef}+\\
&B_{fg}+B_{gh}+B_{hi}+B_{ij}+B_{jk}+\\
&B_{kl}+B_{lm}+B_{mn}+B_{no}+B_{op}+\\
&B_{pq}+B_{qr}+B_{rs}+B_{st}+B_{ta}
\end{aligned} \tag{27}$$

According to the flux density method, the mutual inductance between a single-turn stepped transmitting coil and a single-turn rectangular receiving coil is calculated as follows:

$$M=\frac{\oint\limits_D B\cdot \mathrm{d}s}{I} \tag{28}$$

where s denotes the area where the receiving coil is located, I denotes the current on the transmitting coil.

TABLE I
OPTIMISED RANGE OF EESC STRUCTURAL PARAMETERS

Parameters	Optimisation Scope
L_1	50 ~ 150 mm
L_2	50 ~ 150 mm
L_3	300 ~ 400 mm
W_1	100 ~ 200 mm
W_2	100 ~ 200 mm
W_3	100 ~ 200 mm
L_{rxs}	50 ~ 100 mm
W_{rxs}	500 ~ 600 mm
L_{rx}	400 ~ 500 mm
W_{rx}	500 ~ 700 mm
N_{tx1}	5 ~ 15
N_{txs}	15 ~ 25
N_{rx}	15 ~ 25

In order to facilitate the numerical calculation, the rectangular receiving coil is subdivided, it is assumed that the magnetic flux density at each place in each small rectangle after subdividing is uniformly distributed, which is equal to the magnetic flux density at the centre of the small rectangle. The length l_4 of the receiving coil is subdivided into N_L parts, the width w_4 of the receiving coil is subdivided into N_W parts, and the length and width of the subdivided small rectangle are d_L and d_W, respectively. The mutual inductance between single turn coils is calculated as follows

$$M_{11}=\frac{d_L d_W}{I}\sum_{i=1}^{N_L}\sum_{j=1}^{N_W}B_{ij} \tag{29}$$

When the stepped coil calculates the mutual inductance of the n-th turn to the rectangular receiving coil, in order to ensure that the shape of the stepped coil remains unchanged, the inner diameters of the transmitting coils l_2, w_1, and w_2 remain unchanged, and l_1, l_3, and w_3 satisfy the following rule of law:

$$l_{1\_N}=l_1+2(N-1)R_{line} \tag{30}$$

$$l_{3\_N}=l_3-2(N-1)R_{line} \tag{31}$$

$$w_{3\_N}=w_3+2(N-1)R_{line} \tag{32}$$

where l_{1_N}, l_{3_N}, and w_{3_N} are the lengths of the N-th turn l_1, l_3, and w_3, respectively, and R_{line} is the wire diameter.

According to the superposition theorem, the following for-mula for calculating the mutual inductance between multi-turn rectangular coils can be obtained:

$$M=\sum_{m=1}^{N_T}\sum_{n=1}^{N_R}M_{mn} \tag{33}$$

where N_T denotes the number of turns of the transmitting coil, N_R denotes the number of turns of the receiving coil, and M_{mn} denotes the mutual inductance between the m-th turn of $Coil_1$ and the n-th turn of $Coil_2$.

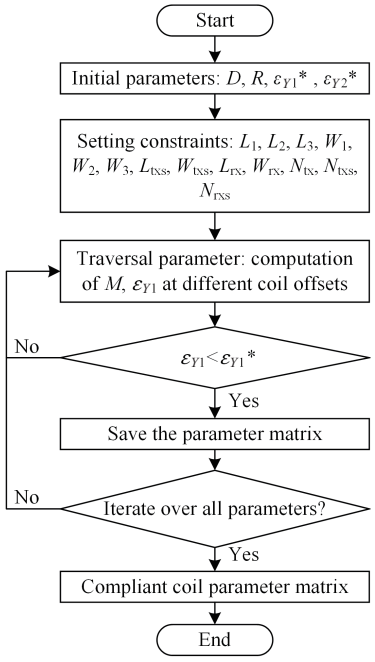

Fig. 5. Flowchart for the coil parameter optimization.

IV. EESC COIL OPTIMISATION

The mutual inductance M is taken as the optimisation objective, the parameters of the EESC structure are optimised based on the principle of minimum mutual inductance fluctuation in order to achieve a strong anti-offset performance. To ensure the mutual inductance and anti-offset performance of the coil structure, the coil structure parameters and core parameters are optimised respectively. Firstly, the coil parameters are optimised to find the coil structure parameter matrix that meets the requirements. Secondly, the core structure is analysed on the basis of the coil parameters and the optimisation of the core size parameters is completed.

A. Optimisation of Coil Parameters

1) Objective function

The key parameters influencing the mutual inductance M of the coil are analyzed and optimized, specifically focusing on the dimensional parameters of the coil structure.

$$M=f(L_1, L_2, L_3, W_1, W_2, W_3, L_{txs}, W_{txs}, L_{rx}, W_{rx}, N_{tx}, N_{txs}, N_{rx}) \tag{34}$$

2) Setting constraints

The mutual inductance M of the coil is dependent on both the inner diameter and the number of turns. The constraints on the coil structure are determined based on the practical application. The range of coil parameters to be optimized is presented in Table I.

3) Coil parameter optimisation process

TABLE II
EESC Structure Dimension Parameter

Parameters	Value
L_1	100 mm
L_2	50 mm
L_3	360 mm
W_1	150 mm
W_2	150 mm
W_3	100 mm
L_{rxs}	50 mm
W_{rxs}	600 mm
L_{rx}	430 mm
W_{rx}	650 mm
N_{tx1}	8
N_{txs}	20
N_{rx}	20

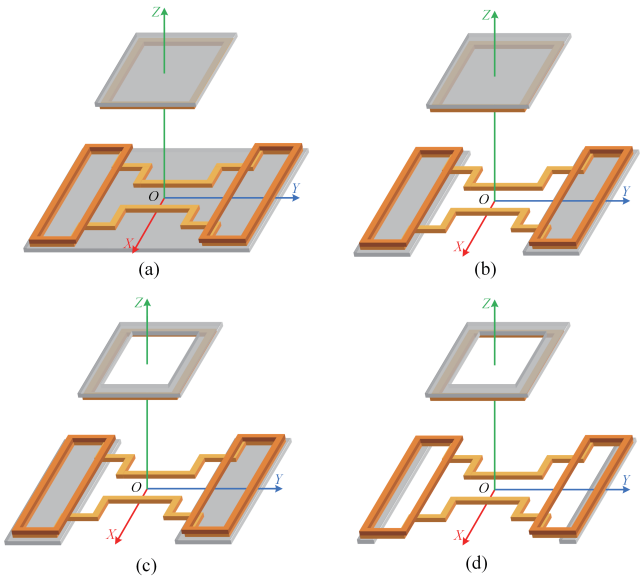

Fig. 6. Schematic diagrams of different magnetic core structures. (a) Conventional non-skeletonised core structure. (b) Separate core structure. (c) Separate skeletonised core structure. (d) Optimised core structure.

The parameter optimization of the EESC structure is conducted based on the principle of minimizing mutual inductance fluctuations. This optimization ensures that the mutual inductance and its fluctuation rate meet the specified requirements when the coil is offset at various positions. The mutual inductance fluctuation rate is defined as the rate of change in mutual inductance when the coil is displaced along the *Y*-axis. The formula for this fluctuation rate is as follows:

$$\varepsilon_{Y1}=\left|\frac{M_{\Delta Y}-M_0}{M_0}\right|\times 100\% \tag{35}$$

where M_0 denotes the mutual inductance between the coils when they are aligned, $M_{\Delta Y}$ denotes the mutual inductance between the coils when the coil are offset in the *Y*-axis.

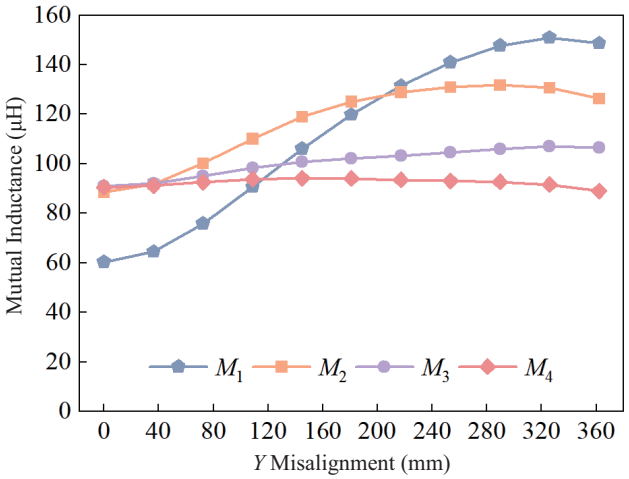

Fig. 7. Trend of mutual inductance of different magnetic core structures.

The optimization flow chart of coil parameters based on the principle of minimum mutual inductance fluctuation is shown in Fig. 5.

The specific steps of the optimization process are as follows: First, the transmission distance *D* between the coils is set to 150 mm, the wire diameter is 4 mm, the mutual inductance fluctuation rates ε_{Y1}^{*} are set to 5%. Second, relevant constraints are established according to the range of coil parameters provided in Table I. Next, the optimized parameters are traversed to calculate the mutual inductance *M* at various positional offsets. The mutual inductance fluctuation rate ε_{Y1} is calculated according to (35). ε_{Y1} is judged whether satisfies $\varepsilon_{Y1}<\varepsilon_{Y1}^{*}$, when it satisfies the above conditions, the corresponding parameter matrix is saved. If the result is not satisfied, the program traverses the next set of parameters.

Finally, after all parameters have been traversed, the output meets the required coil parameter matrix for the subsequent core optimization process. By optimising the parameters of the EESC structure, the dimensional parameters of the transmitter-side coil and receiver-side coil are shown in Table II.

B. Optimisation of Core Parameters

In order to improve the offset resistance of the coil structure and the mutual inductance between the coils, magnetic materials are usually added to the coupling coils. The common magnetic materials are ferrites. In this section, in order to design a core structure that fits the changing characteristics of the mutual inductance of the coils, the influence of different shapes of the core structure on the mutual inductance of the coils is analysed on the basis of the EESC structure, the parameters of the core structure are optimised after the shape is determined. The evolution of the core structure is shown in Fig. 6. Fig. 6(a) shows the traditional non-skeletonised core structure with mutual inductance denoted as M_1; Fig. 6(b) shows the separated core structure with mutual inductance denoted as M_2; Fig. 6(c) shows the separated skeletonised core structure with mutual inductance denoted as M_3; and Fig. 6(d) shows the optimised core

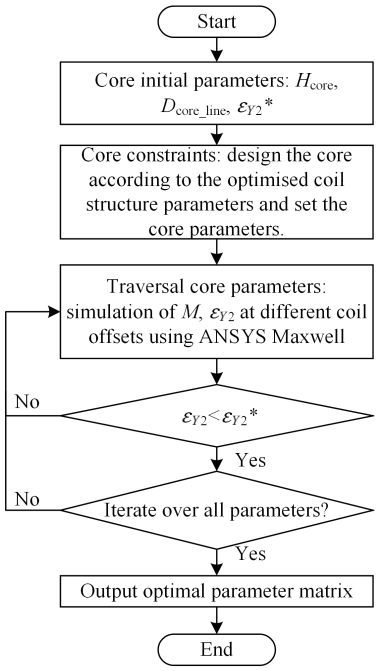

Fig. 8. Flowchart for the magnetic core parameter optimization.

structure of this paper with mutual inductance denoted as M_4.

Fig. 7 shows the trend of mutual inductance of coils with different core structures. When the conventional non-skeletonised core structure is used, the mutual inductance M_1 between the coils increases from 60.27 μH to 148.51 μH as the coil position is shifted, the mutual inductance between the coils decreases instead of increasing when it is positively aligned, and the mutual inductance fluctuation rate is as high as 150%. In order to make the core structure fit the structural characteristics of the coils better, the core on the transmitter side adopts a separated structure using two smaller bar-shaped cores, which are placed in the overlapping part of the main coil and the compensation coil. With the separated core structure, the mutual inductance M_2 between the coils increases from 88.37 μH to 126.21 μH with the coil offset, and the mutual inductance fluctuation rate decreases to 49%. The use of the separated core structure solves the problem of reducing the mutual inductance of the coils when the conventional non-skeletonised core structure is positively aligned, and saves 38.8% of the core material compared to the conventional non-skeletonised core structure. Subsequently, based on the use of the separated core structure on the transmitter side, the core on the receiver side adopts a centre skeleton design, which is designed to provide better magnetic path access to the coil. With the offset of the coils, the mutual inductance M_3 between the coils increases from 90.95 μH to 106.37 μH with a maximum mutual inductance fluctuation of only 16.9%. It can be seen that for the edge-enhanced stepped coil structure proposed in this chapter, the most fitting core structure is a separated core on the transmitter side and a skeletonised core on the receiver side. After determining the approximate shape of the core structure, a core parameter optimisation strategy based on the principle of minimising mutual inductance fluctuation is proposed to optimise the dimensions

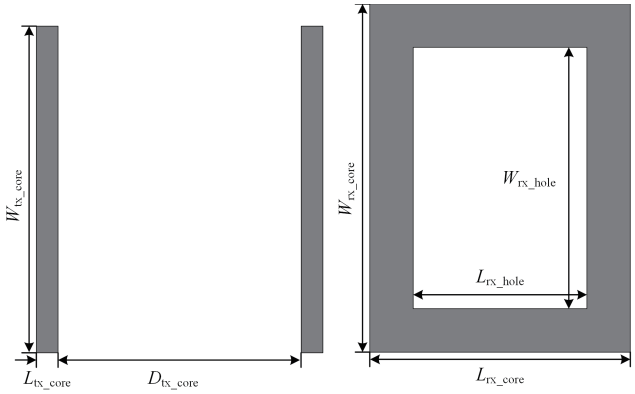

Fig. 9. Magnetic core structure diagram.

of the separated core on the transmitter side and the separation spacing, as well as the dimensions of the skeletonised core on the receiver side and the size of the skeleton, in order to address the problem of mutual inductance fluctuation caused by coil offset.

The flowchart of core parameter optimisation based on the principle of minimum mutual inductance fluctuation is shown in Fig. 8.

1) Core parameter setting

The core of the transmitting coil is located below the transmitting coil, and the core of the receiving coil is located above the receiving coil. The given core thickness H_{core} is 10 mm, the core and the winding line are close to each other, the spacing between the core and the winding line D_{core_line} is nearly 0, and the mutual inductance fluctuation rate ε_{Y2}^* is set to 5%.

2) Setting core constraints

The core structure is designed based on the optimized coil structure dimensions. The coil design is constrained by the actual core structure, which imposes several limitations. These constraints include the transmitting side core dimensions,the receiving side core dimensions and core skeleton dimensions. These constraints ensure that the core structure is appropriately sized and positioned to support the optimized coil configuration and achieve the desired performance.

3) Core parameter optimization

The mutual inductance between the transmitting and receiving coils can be measured by ANSYS Maxwell simulation software, the mutual inductance fluctuation rate ε_{Y2} is calculated according to (36). ε_{Y2} is judged whether satisfies $\varepsilon_{Y2} < \varepsilon_{Y2}^*$, when it satisfies the above conditions, the corresponding parameter matrix is saved. When the result does not satisfy the requirements, the program traverses the next set of parameters. Finally, when all the parameters have

$$\varepsilon_{Y1}=\left|\frac{M_{\Delta Y}^*-M_0^*}{M_0^*}\right|\times 100\% \tag{36}$$

where M_0^* denotes the mutual inductance between the coils when they are aligned, $M_{\Delta Y}^*$ denotes the mutual inductance between the coils when they are offset in the Y-axis.

According to the above optimisation, the transmitting-side

TABLE III
EESC STRUCTURE MAGNETIC CORE DIMENSION PARAMETER

Parameters	Value
L_{tx_core}	50 mm
W_{tx_core}	750 mm
D_{tx_core}	560 mm
L_{rx_core}	600 mm
W_{rx_core}	800 mm
L_{rx_hole}	400 mm
R_{rx_hole}	600 mm
H_{core}	10 mm

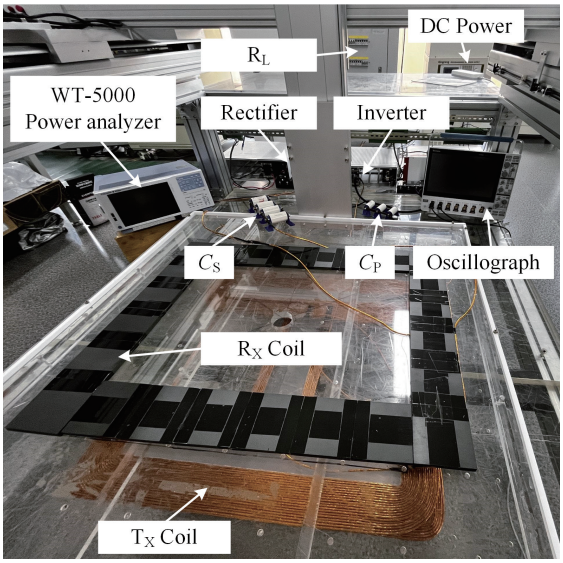

Fig. 10. Prototype of the WPT system.

core adopts a separated structure, which is symmetrically placed on the left and right sides, and the receiving-side core is a hollow structure in the middle, as shown in Fig. 6(d), and the variation curve of the coil mutual inductance is shown in Fig. 7 as M_4, and the mutual inductance fluctuation rate is less than 5%. The core plan view is shown in Fig. 9, and the core size parameters are shown in Table III.

V. EXPERIMENTAL VERIFICATION

A. Prototype

To verify the feasibility and effectiveness of the proposed WPT system, a 500 W experimental prototype of the wireless energy transmission system is constructed. This prototype is used to assess the anti-offset performance of the system, ensuring its reliability under various operating conditions.

Based on the coil size parameters provided in Table II, physical coils were wound, and the experimental prototype was constructed on a 3D motion platform. Fig. 10 displays the experimental prototype of the system, which includes

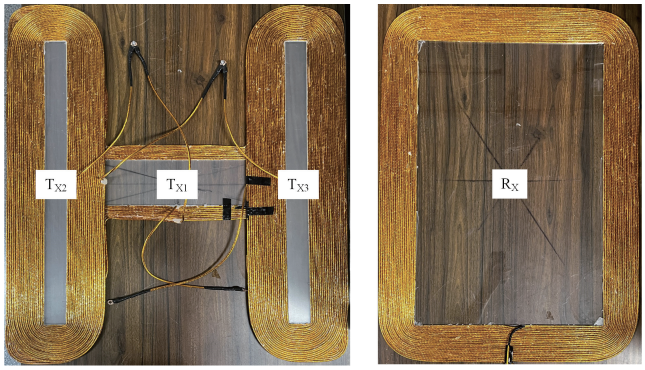

Fig. 11. EESC structure.

TABLE IV
MAIN PARAMETERS OF THE WPT SYSTEM PROTOTYPE

Parameters	Value	Parameter	Value
U_{DC} (V)	170.0	f (kHz)	85
L_P (μH)	898	L_P^* (μH)	1038
C_P (nH)	3.67	C_P^* (nF)	3.16
L_S (μH)	521	L_S^* (μH)	804
C_S (nF)	6.54	C_S^* (nF)	4.18
M (μH)	64.05	M^* (μH)	89.1

the components of the WPT system, such as the DC power supply, inverter module, rectifier module, transmitter coil T_x, transmitter-side compensation capacitor C_P, receiver coil R_x, receiver-side compensation capacitor C_S, and load resistor. Fig. 11 shows the EESC structure. The inverter and rectifier components utilize silicon carbide power devices, specifically the model C3M0075120D. The experimental platform consists of a three-dimensional moving structure, featuring a stationary lower level and a three-dimensionally movable upper level. The transmitting coil is positioned on the lower level, while the receiving coil is located on the upper movable platform. Offset control is achieved through the 3D platform interface controller. The main parameters of the prototype WPT system are summarized in Table IV.

B. Mutual Inductance Analysis

Firstly, MATLAB is used to develop a program for calculating the mutual inductance of the coreless coil, allowing for the determination of the theoretical mutual inductance value M_c for the EESC structure. Secondly, finite element software is employed for modeling and simulation to obtain the simulated coupling coefficient M_s of the EESC structure. Finally, the self-inductance and mutual inductance of the physical coil are measured using an impedance analyzer to obtain the experimental value M_e. The error between the theoretical value and the experimental value is defined as ε_c, and the error between the simulation value and the experimental value is defined as ε_s. These errors are calculated using the following formulas:

TABLE V
MUTUAL INDUCTANCE AND ERROR WITHOUT MAGNETIC CORE AT OFFSET ALONG *Y*-AXIS

ΔY/mm	M_C	M_S	M_e	ε_C	ε_S
0	64.22	65.81	64.05	0.27%	2.75%
36.2	64.54	66.03	64.05	0.77%	3.09%
72.4	65.31	66.58	64.69	0.96%	2.92%
108.6	66.13	67.23	65.33	1.22%	2.91%
144.8	66.68	67.64	65.79	1.35%	2.81%
181.0	66.89	67.73	65.66	1.87%	3.15%
217.2	66.85	67.58	65.56	1.97%	3.08%
253.4	66.62	67.27	65.04	2.43%	3.43%
289.6	66.13	66.71	64.43	2.64%	3.54%
325.8	65.04	65.53	63.05	3.16%	3.93%
362.0	62.72	63.05	60.95	2.90%	3.45%

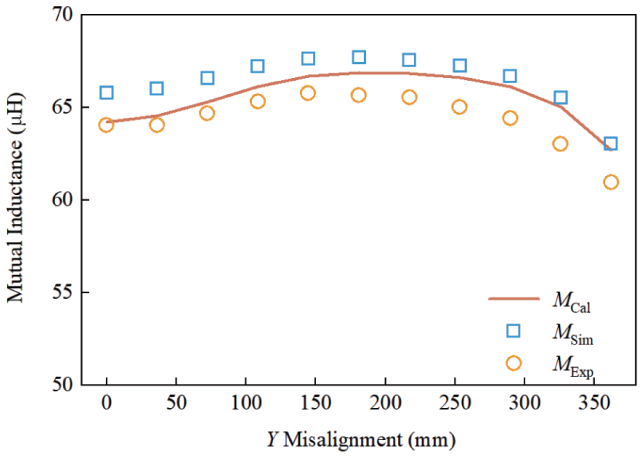

Fig. 12. Variation curves of coil mutual inductance without magnetic core at offset along the *Y*-axis direction.

$$\varepsilon_c = \left| \frac{M_c - M_e}{M_e} \right| \times 100\% \tag{37}$$

$$\varepsilon_s = \left| \frac{M_s - M_e}{M_e} \right| \times 100\% \tag{38}$$

Table V presents the mutual inductance values and associated errors for the coreless coil when offset along the *Y*-axis. From the table, it can be observed that the experimental mutual inductance of the coil is 64.05 μH when it is aligned. When the coil is offset by 50% (362 mm) of the outer diameter length of the launching coil along the *Y*-axis, the experimental mutual inductance decreases to 60.95 μH. The fluctuation rate of the mutual inductance at this offset is 4.84%. The trend of the mutual inductance of the EESC structure with respect to the offset distance along the *Y*-axis shows an initial increase followed by a decrease, which aligns with the theoretical analysis of the magnetic field behavior in the EESC structure. The error ε_c is less than 3.16%, and the error ε_s is less than 3.93%. To provide a more intuitive understanding of the coil's behavior, Fig. 12 shows the change curve of the mutual inductance of the coreless coil when offset along the *Y*-axis. From this curve, it can be seen that the mutual inductance of the coil remains relatively stable around 64 μH.

TABLE VI
MUTUAL INDUCTANCE AND ERROR WITH MAGNETIC CORE AT OFFSET ALONG *Y*-AXIS

ΔY/mm	M_S	M_e	ε_S
0	90.49	89.10	1.56%
36.2	91.14	88.74	2.70%
72.4	92.57	89.72	3.18%
108.6	93.76	90.74	3.33%
144.8	94.18	91.34	3.11%
181.0	93.95	91.34	2.86%
217.2	93.50	91.22	2.50%
253.4	93.12	90.71	2.66%
289.6	92.61	90.36	2.49%
325.8	91.63	89.11	2.83%
362.0	89.01	86.19	3.27%

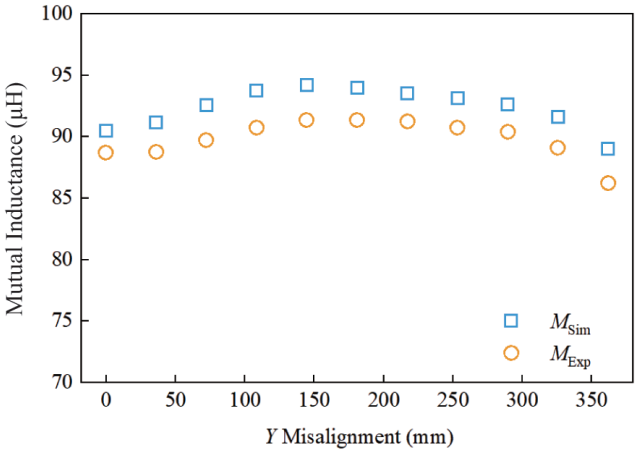

Fig. 13. Variation curves of coil mutual inductance with magnetic core at offset along the *Y*-axis direction.

Table VI presents the mutual inductance values and associated errors for the coil with a magnetic medium when offset along the *Y*-axis. The experimental mutual inductance is 89.10 μH when the coils are aligned. When the coil is offset by 50% (362 mm) of the outer diameter length of the launching coil along the *Y*-axis, the experimental mutual inductance decreases to 86.19 μH, with a fluctuation rate of 3.27%. The error ε_s is less than 3.33%. To provide a more intuitive view of the coil's behavior, Fig. 13 shows the change curve of the mutual inductance for the coil with magnetic core when offset along the *Y*-axis. The mutual inductance of the coil changes smoothly and remains relatively stable at about 89.1 μH.

In summary, both the EESC structures without magnetic core and those with magnetic cores demonstrate strong offset

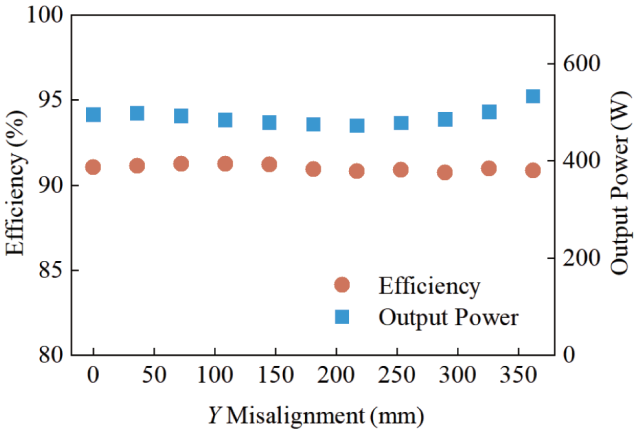

Fig. 14. Variation curves of coil mutual inductance with magnetic core at offset along the *Y*-axis direction.

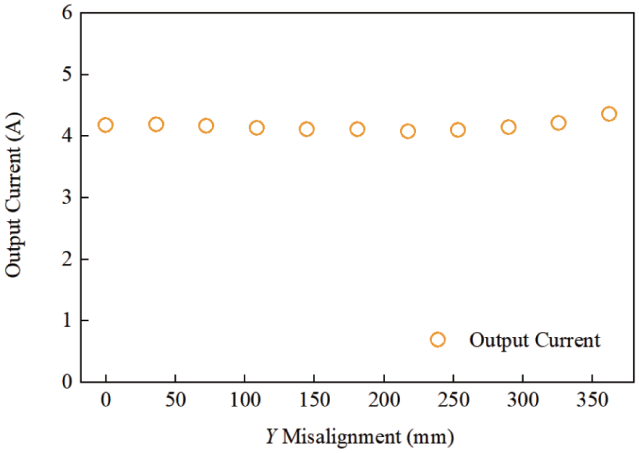

Fig. 15. Variation curves of system output current and without magnetic core at offset along the *Y*-axis direction.

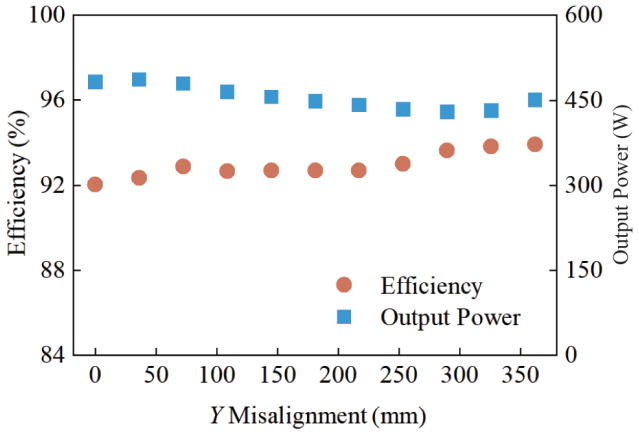

Fig. 16. Variation curves of system output power and transmission efficiency with magnetic core at offset along the *Y*-axis direction.

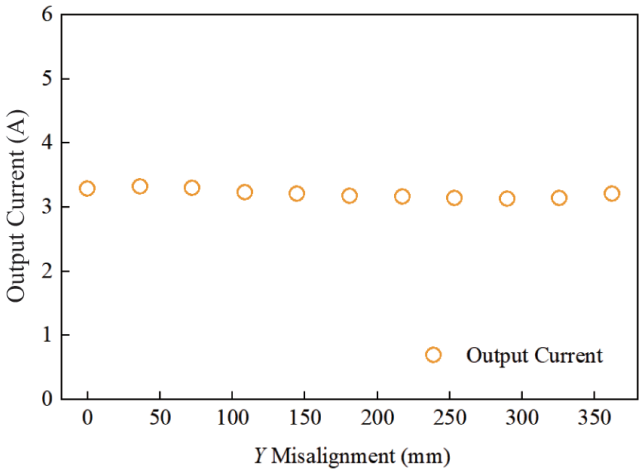

Fig. 17. Variation curves of system output current and with magnetic core at offset along the *Y*-axis direction.

resistance, capable of withstanding 50% (362 mm) offset of the outer diameter of the transmitter coil in the *Y*-axis direction. In all cases, the mutual inductance fluctuation rate remains below 5%, indicating robust performance even under significant displacement.

C. System Performance Analysis

Fig. 14 shows the variation curves of output power and transmission efficiency of the WPT system without magnetic medium with offset distance. From Fig. 11, it can be seen that the output power of the system is 495.44 W when the coil is aligned. When the offset distance is within 362 mm, the maximum output power and minimum output power are 533.9 W and 473.39 W. The transmission efficiency of the system has a tendency to increase and then decrease when offset along the *Y*-axis. This behavior aligns with the mutual inductance fluctuations shown in Fig. 9, where the transmission efficiency peaks at 91.3%. The maximum fluctuations in transmission efficiency and output power are 0.21% and 7.76%, respectively.

Fig. 15 shows the output current variation curve of the coreless system, from which it can be seen that the system output current is 4.18 A when the coil is aligned, and when the coil offset distance is within 50% (362 mm) of the outer diameter length of the transmitter coil, the maximum and minimum output currents of the system are 4.36 A and 4.08 A, respectively, and the output current fluctuation rate is less than 5%.

Fig. 16 shows the relationship between the output power and transmission efficiency of the WPT system with magnetic media and the offset distance. It can be seen that the transmission efficiency and output power are 92.04% and 482.79 W when the coil is aligned. When the offset distance is within 362 mm, the maximum transmission efficiency and minimum measured efficiency are 93.92% and 92.04%, respectively, and the maximum output power and minimum output power are classified as 486.71 W and 429.78 W, the system efficiency and power fluctuations are 0.2% and 10.98%, respectively. When offset along the *Y*-axis direction, the transmission efficiency shows a gradual increasing trend, and the transmission efficiency of the system is as high as 93.92%.

Fig. 17 shows the output current variation curve of the sys-

TABLE VII
MPPT Algorithm Performance for Different PV Array Topologies under Shade Case-III

Ref.	Coil Structure	Transmission Distance / mm	Maximum Offset Distance / mm	Offset Rate / %	Fluctuation Rate / %	Output Power / W
[18]	FSC	170	200	50%	20.2%	500
[19]	Flat Solenoid	170	120	40%	12.3%	500
[24]	DQDD	130	150	38.4%	55%	500
[26]	ISC	150	225	50%	3.81%	108.8
Proposed	EESC	150	362	50%	3.27%	495.6

Note: Offset ratio equals the *X*/*Y* direction coil offset distance / the maximum *X*/*Y* direction coil outer length.

tem with magnetic core. It can be seen that the system output current is 3.29 A when the coil is aligned, and when the coil offset distance is within 50% (362 mm) of the outer diameter length of the transmitter coil, the maximum and minimum output currents of the system are 3.32 A and 3.13 A, respectively, and the fluctuation rate of the output current is less than 5%.

D. Comparison of Anti-Offset Performance

In order to demonstrate the resistance to deflection of the proposed coil structure and the innovativeness of the optimised design method, the WPT system proposed in this paper is compared with the existing literature, as shown in Table VII.

Compared to the solenoidal coupling structure mentioned in [18]−[19], the coil structure proposed in this paper has a larger offset distance and offset rate with a smaller offset resistance. Compared to the literature [24]−[25], the coil structure proposed in this paper has a larger offset distance while the mutual inductance fluctuation rate is only 3.27%, which provides a better anti-offset performance.

VI. Conclusion

In this paper, an edge-enhanced stepped coil (EESC) structure is proposed to improve the anti-offset performance of the system. Firstly, the model of the edge-enhanced stepped coil structure is analyzed, and the mutual inductance characteristics of this structure are examined. Secondly, a new method for calculating the mutual inductance of stepped coils is introduced, based on the Biot-Savart law. Subsequently, an optimization strategy is developed, focusing on minimizing the fluctuation of mutual inductance, to optimize both the coil size and the core size parameters. Finally, to validate the proposed methods, a 500 W experimental prototype is constructed. Simulation and experimental results confirm the accuracy of the coil mutual inductance calculation method and demonstrate the robust offset resistance of the coil structure. The experimental findings show that the mutual inductance fluctuation rate of the EESC, both with and without a magnetic core, remains below 5% when the system is offset along the *Y*-axis by 50% (362 mm) of the outer diameter of the transmitting coil. Additionally, the error between the measured mutual inductance and the theoretical and simulated values does not exceed 5%. The transmission efficiency of the coreless EESC system is 91.3%, with an output current of 4.18 A and a fluctuation rate of the output current less than 5%. The EESC system with magnetic core achieves a transmission efficiency of 93.92%, an output current of 3.29 A, a fluctuation rate of the output current of less than 5%. Therefore, the EESC structure proposed in this study is well-suited for dynamic wireless charging of electric vehicles. Further research will focus on improving the anti-offset performance of the EESC coil in the *X*-axis direction.

References

[1] Y. Zhang, W. Pan, C. Liu, Z. Shen, Y. Wu, Y. Zhuang, and Z. Li, "Interoperability study of electric vehicle wireless charging system based on three decoupled nonoverlapping unipolar transmitting coils," in *IEEE Transactions on Transportation Electrification*, vol. 10, no. 4, pp. 8630–8639, Dec. 2024.

[2] H. Zhou, Z. Shen, Y. Wu, X. Chen, and Y. Zhang, "A stable dynamic electric vehicle wireless charging system based on triple decoupling receiving coils and a novel triple-diode rectifier," in *IEEE Transactions on Industrial Electronics*, vol. 71, no. 10, pp. 12011–12018, Oct. 2024.

[3] Z. Shen, H. Zhou, R. Xie, Y. Zhuang, X. Mao, and Y. Zhang, "A strong offset-resistant electric vehicle wireless charging system based on dual decoupled receiving coils," in *IEEE Transactions on Industrial Electronics*, vol. 71, no. 11, pp. 15216–15219, Nov. 2024.

[4] X. Wu, P. Sun, S. Yang, L. He, and J. Cai, "Review on underwater wireless power transfer technology and its Application," in *Transactions of China Electrotechnical Society*, vol. 34, no. 8, pp. 1559–1568, Apr. 2019.

[5] H. Guo, X. Zhang, Q. Yang, L. Sha, F. Wang, and Z. Zhu, "Review of research and application of spatial omnidirectional wireless power transmission technology," in *Proceedings of the CSEE*, vol. 42, no. 24, pp. 9006–9022, Dec. 2022.

[6] D. Wang, J. Zhang, C. Zhu, Z. Bie, and S. Cui, "Review of progress in the study of marine environment effects on underwater wireless power transfer systems," in *Transactions of China Electrotechnical Society*, vol. 40, no. 3, pp. 653–675, Feb. 2025.

[7] Y. Yang, W. Jia, D. Liang, J. Xue, and Y. Li, "A self-switching wireless power transfer system based on hybrid topology of LCC-LCC/S with constant current and constant voltage," in *Transactions of China Electrotechnical Society*, vol. 38, no. 18, pp. 4823–4837+4852, Sept. 2023.

[8] V. -B. Vu, D. -H. Tran, and W. Choi, "Implementation of the constant current and constant voltage charge of inductive power transfer systems with the double-sided LCC compensation topology for electric vehicle battery charge applications," in *IEEE Transactions on Power Electronics*, vol. 33, no. 9, pp. 7398–7410, Sept. 2018.

[9] L. Ji, M. Zhang, B. Qian, and H. Sun, "A series of hybrid WPT systems with automatic switching between constant-current and constant-voltage modes on the secondary side," in *IEEE Journal of Emerging and Selected Topics in Power Electronics*, vol. 11, no. 1, pp. 361–371, Feb. 2023.

[10] K. Chen, Y. Jiang, T. Tan, Q. Lin, J. Li, and Z. Zhao, "Research on 350kW high power wireless power transfer system for rail transit," in

Transactions of China Electrotechnical Society, vol. 37, no. 10, pp. 2411–2421+2445, May 2022.

[11] L. Wu, G. Li, Z. Zhang, and H. Ma, "A wireless power transfer system topology with automatic switching characteristics of constant current and constant voltage output for electric vehicle charging" in *Transactions of China Electrotechnical Society*, vol. 35, no. 18, pp. 3781–3790, Sept. 2020.

[12] J. Li, C. Zhu, J. Xie, F. Lu, and X. Zhang, "Design and implementation of high-misalignment tolerance WPT system for underwater vehicles based on a variable inductor," in *IEEE Transactions on Power Electronics*, vol. 38, no. 10, pp. 11726–11737, Oct. 2023.

[13] Y. Chen, B. Yang, X. Zhou, Q. Li, Z. He, R. Mai, and J.-S. Lai, "A hybrid inductive power transfer system with misalignment tolerance using quadruple-D quadrature pads," in *IEEE Transactions on Power Electronics*, vol. 35, no. 6, pp. 6039–6049, Jun. 2020.

[14] Y. Zhang, C. Liu, M. Zhou, and X. Mao, "A novel asymmetrical quadrupolar coil for interoperability of Unipolar, Bipolar, and Quadrupolar coils in electric vehicle wireless charging systems," in *IEEE Transactions on Industrial Electronics*, vol. 71, no. 4, pp. 4300–4303, Apr. 2024.

[15] J. Ren, K. Zhou, H. Li, Y. Liu, and R. Mai, "Study of dual coupled LCL topology IPT system based on DDQ coils and its anti-misalignment method," in *Proceedings of the CSEE*, vol. 39, no. 09, pp. 2778–2788, May 2019.

[16] Z. Li, J. Li, S. Li, Y. Yu, and J. Yi, "Design and optimization of asymmetric and reverse series Coil structure for obtaining quasi-constant mutual inductance in dynamic wireless charging system for electric vehicles," in *IEEE Transactions on Vehicular Technology*, vol. 71, no. 3, pp. 2560–2572, Mar. 2022.

[17] Y. Chen, B. Yang, Z. Kou, Z. He, G. Cao, and R. Mai, "Hybrid and reconfigurable IPT systems with high-misalignment tolerance for constant-current and constant-voltage battery charging," in *IEEE Transactions on Power Electronics*, vol. 33, no. 10, pp. 8259–8269, Oct. 2018.

[18] Y. Yao, S. Gao, Y. Wang, X. Liu, X. Zhang, and D. Xu, "Design and optimization of an electric vehicle wireless charging system using interleaved Boost converter and flat solenoid coupler," in *IEEE Transactions on Power Electronics*, vol. 36, no. 4, pp. 3894–3908, Apr. 2021.

[19] Y. Wang, K. Lu, Y. Yao, X. Liu, and D. Xu, "An electric vehicle (EV)-oriented wireless power transfer system featuring high misalignment tolerance," in *Proceedings of the CSEE*, vol. 39, no. 13, pp. 3907–3917, Jul. 2019.

[20] Y. Peng, B. Zhang, B. Yang, S. He, Y. Chen, and R. Mai, "A high misalignment tolerant inductive power transfer system based on double solenoid quadrature pad," in *Proceedings of the CSEE*, vol. 42, no. 20, pp. 7352–7363, Oct. 2022.

[21] M. Budhia, J. T. Boys, G. A. Covic, and C. -Y. Huang, "Development of a single-sided flux magnetic coupler for electric vehicle IPT charging systems," in *IEEE Transactions on Industrial Electronics*, vol. 60, no. 1, pp. 318–328, Jan. 2013.

[22] A. Zaheer, G. A. Covic, and D. Kacprzak, "A Bipolar Pad in a 10-kHz 300-W distributed IPT system for AGV applications," in *IEEE Transactions on Industrial Electronics*, vol. 61, no. 7, pp. 3288–3301, Jul. 2014.

[23] S. Kim, G. A. Covic, and J. T. Boys, "Tripolar Pad for inductive power transfer systems for EV charging," in *IEEE Transactions on Power Electronics*, vol. 32, no. 7, pp. 5045–5057, Jul. 2017.

[24] H. Xiao, Q. Zhou, S. Xiong, Y. Yang, and S. Xie, "Wireless power transfer system based on double-layer quadrature double-D coupling structure with anti-misalignment and anti-deflection," in *Transactions of China Electrotechnical Society*, vol. 37, no. 16, pp. 4004–4018, Aug. 2022.

[25] Z. Li, S. Li, J. Li, R. Zou, and S. Huang, "Mutual inductance calculation and optimization of multi-receiver positive and negative series coil structure in dynamic wireless power transfer systems," in *Transactions of China Electrotechnical Society*, vol. 36, no. 24, pp. 5153–5164, Dec. 2021.

Chenxi Zhang received the bachelor's degree in electrical engineering and automation from Hunan Institute of Technology, Hengyang, China, in 2021 and the master's degree in electronic information from Hunan University of Technology, Zhuzhou, China in the year 2025. His research interests include wireless power transfer systems.

Zhongqi Li received the master's degree from Hunan University of Technology, Zhuzhou, China in 2012, and the Ph.D. degree from the Hunan University in the year 2016. From 2016, he is working associate professor in Hunan University of Technology, China. From 2020, he is now working postdoctoral fellow in Hunan University. His research interests include wireless power transfer systems and softswitching power converters.

Changxuan Hu received a bachelor's degree in Electrical Engineering form Henan Polytechnic University, Jiaozuo, China, in 2021 and the master's degree in control science and engineering from Hunan University of Technology, Zhuzhou, China in 2025. His research interests include wireless power transfer.

Jianbin Wang received the bachelor's degree in electronic information from Shandong Huayu University of Technology, Dezhou, China, in 2022 and the master's degree in electronic information from Hunan University of Technology, Zhuzhou, China in 2025. His research interests include wireless power transfer systems.

Power Quality Enhancement Using AZQLMS and Fractional Order PID Based Control Through Dynamic Voltage Restorer

Ganesh Kumar BUDUMURU, Papia RAY, Prashant KUMAR, and Sabha Raj ARYA

***Abstract*—The rapid growth of nonlinear and unstable load penetration into the grid network has a detrimental impact on the grid system's ability to deliver high-quality power. Moreover, it results in a situation where it becomes difficult to maintain high-quality power in the distribution sectors. As a result, it is exceedingly challenging to maintain a high standard of power quality (PQ) in a distribution system. To improve the quality of grid voltage a series compensating filter called dynamic voltage restorer (DVR) is used in this suggested work. An adaptive zero-attracting quaternion-based least mean square (AZQLMS) approach is suggested to extract the fundamental quantity from the polluted voltage of the grid. An optimization technique, frilled lizard (FL) inspired by nature, is employed to estimate the gains of the fractional order proportional integral derivative (FOPID) controllers used in this control algorithm for DC link voltage stabilization. Compared to the marine predator (MP) optimizer, the proposed Frilled Lizard algorithm demonstrates enhanced capability to escape from local entrapment with quicker convergence and also reduces the complexity of manual tuning effort simultaneously. From the perspectives of DC link time response characteristics under transitory scenario, control technique, and the range of compensated voltage, the enhanced DVR's principle has been examined. By minimizing the voltage issues and the voltage total harmonic distortion (THD) at the connection point below 5%, both controllers were able to restore the voltage magnitude. MATLAB/Simulink with experimentation work is utilized to analyze the efficacy of the suggested approach. It is evident from the information that the AZQLMS and FL-FOPID successfully control the distribution grid's voltage.**

***Index Terms*—Fractional order proportional integral derivative (FOPID), least mean square (LMS), optimization, power quality, unit vector, voltage regulation.**

Manuscript received April 18, 2025; accepted May 20, 2025. Date of publication September 30, 2025; date of current version June 20, 2025. No funding was received to assist with the preparation of this manuscript. (*Corresponding author: Prashant Kumar.*)

G. K. Budumuru and P. Ray are with the Department of Electrical Engineering, Veer Surendra Sai University of Technology, Burla, Odisha 768018, India (e-mail: ganeshbudumuru@gmail.com; papiaray_ee@vssut.ac.in).

P. Kumar is with the School of Sustainability Studies, Symbiosis Skills and Professional University, Pune, Maharashtra 395007, India (email: prashant2685@gmail.com).

S. R. Arya is with the Department of Electrical Engineering, Sardar Vallabhbhai National Institute of Technology, Surat, Gujarat 395007, India (email: sabharaj21@gmail.com).

Digital Object Identifier 10.24295/CPSSTPEA.2025.00020

I. Introduction

DUE to a surge in power consumption, electrical power system infrastructures have become more complicated in recent years. The accuracy of the electric power supply is mainly related to its voltage and current, and is known as power quality (PQ) [1]. Of all the PQ issues, voltage dips and swells, voltage imbalance, and disturbances for loads that are highly susceptible to voltage fluctuations, such as harmonics, occur most frequently [2].

While rectifying the disturbed grid voltage, the suggested DVR-based control approach kept a stabilized voltage profile with low harmonic content. Authors have developed an advanced DQ technique for DVR, and the transient voltage scenarios are considered for their comparative study with a conventional DQ theory [3]. This time domain approaches underperform if the supply voltage deteriorates, however, they operate well when the voltage supply is sinusoidal [4]. A comprehensive analysis of DVR operation, encompassing both with and without energy storage devices, has been provided by Gammal et al. [5]. To compensate for voltage-based PQ problems, the capacitor-supported DVR setup has been researched [6]. In [7] authors have created a control system based on the integration of a generalized neural network estimator and neuro-fuzzy for precisely designing the DVR response to regulate the load voltage when dealing with fluctuating PQ problems. Numerous DVR functioning methods are described by the authors in [8], and it is demonstrated that an energy-saving approach via zero power insertion may be achieved by keeping the DC-bus voltage constant. However, these controllers have certain drawbacks, including low dynamic response, local convergence, and considerable steady-state error when the grid voltage is disturbed. Therefore, to achieve a quicker convergence rate, the appropriate selection of an adaptive algorithm is required for optimal solution.

In the view of PQ improvement, control algorithms based on variable learning rate based least mean square (LMS) have been implemented based on a filter weight updating mechanism at each run of the error signal [9]. Authors have employed the fourth-order LMS/F technique for extracting the fundamental weight for further estimation of the load reference voltage signal. This paper discusses the estimation of active and reactive quantities using hybrid filters like LMS/F [10], TSKARNA

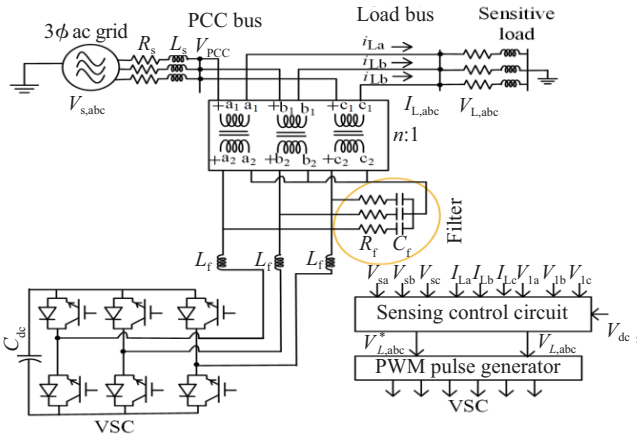

Fig. 1. Power circuit for three phase DVR.

LMS, and mixed-norm constraint-based improved proportionate normalized least mean square fourth (MNC-IPNLMS/F) [11]. These techniques are utilised to lessen the input noises and provide improved performance using error criteria. The zero attractor LMS controller was proposed based on sparsity, where the optimal zero attractor controller minimizes mean square deviation (MSD) error, and extends the LMS approach to the quaternion domain for processing of multidimensional signals. Therefore, speeds the convergence performance for steady-state compared to basic LMS algorithms [12]. Several methods are available are studies in the literature for voltage error stabilization, like optimized PI [13]. Artificial Intelligence methods like ANN, ANFIS [14], and Fuzzy [15] involve expertise to select the data and training of it to extract the forecasted model. The fractional order proportional integral derivative (FOPID)-controller is used to improve error regulation of the internal control circuits and maintain a constant DC link voltage. The gains of FOPID are estimated with frilled lizard optimizer (FLO) [16]. The optimization saves the computational effort required for coefficient tuning and obtains the improved dynamic response of the recommended system. The proposed FOPID is examined with the ITSE function, which offers optimized fast settling time and lessens oscillation [17].

The research work primarily focuses on the implementation of an adaptive quaternion-based least mean square approach for estimating load reference voltage. The major benefit of AZQLMS is quick convergence, reducing noise interference, and unaffected steady state performance. The Fractional Order PID (FOPID) is integrated with the FL tuning approach for stabilizing the voltages of the DC link. The voltage balancing of adaptively regulated DC link plays a crucial role in enhancing the PQ performance, as judged by a comparative study with LMS-PI in terms of smaller oscillations during active weight estimation. The comparative convergence curves of FL are superior over the marine predator (MP) optimizer, confirming the fast-tracking capability of FOPID over the PI controller. The simulation and experimental test results for the proposed topology and control have been conducted under different PQ issues to validate the efficacy of the proposed control scheme.

II. System Configuration and Control Strategy

The detailed diagram of the DVR arrangement is shown in Fig. 1. The capacitor is linked to the inverter for injecting the required amount of voltage via injection transformers. A linear load (RL-load) is taken into consideration and a constant voltage needs to maintain during operation. The energy storage system is replaced by a capacitor (C_{DC}) that stores energy, and the system design is self-supported [5]. Additionally, maintains the supply voltage's (v_s) voltage dynamics, whenever it's needed. "L_f" is the interface inductors utilised to reduce the current's waves waveform of the converter [8].

A. Active and Reactive Quanity Estimation

Fundamental estimation of active and reactive quantity with the support of an injection transformer and the necessary parts listed in the voltage source converter (VSC) functions as a DVR, and the control algorithm monitors its operation. The DVR attached VSC and receives gate pulses from the control algorithm would be accountable for the intended voltage compensatory methods. The error is estimated between the measured (d_{meas}) and targeted signal (d_{est}), i.e., $e_{ra} = d_{meas} - d_{est}$ [11]. The error signal e_{ra} for each phase can be computed as

$$\begin{cases} e_{p,m} = v_{s,m} - W_{p,n} z_{p,m} \\ e_{q,m} = v_{s,m} - W_{q,m} z_{q,m} \end{cases} \tag{1}$$

where 'm' can represent the phases a, b, and c.

The updated fundamental direct component (W_{pa}) for phases a, b and c are evaluated as [12].

$$\begin{cases} W_{pa}(n+1) = W_{pa}(n) + \frac{1}{2}(\alpha_1 - 4\mu_1)\left[e_{pa}(n) z_{pa} - \mu_1 \operatorname{sgn}(W_{pa}(n))\right] \\ W_{pb}(n+1) = W_{pb}(n) + \frac{1}{2}(\alpha_1 - 4\mu_1)\left[e_{pb}(n) z_{pb} - \mu_1 \operatorname{sgn}(W_{pb}(n))\right] \\ W_{pc}(n+1) = W_{pc}(n) + \frac{1}{2}(\alpha_1 - 4\mu_1)\left[e_{pc}(n) z_{pc} - \mu_1 \operatorname{sgn}(W_{pc}(n))\right] \end{cases} \tag{2}$$

The controlling parameter step size μ and α is a constant term that attracts the coefficients of weighted value to zero (varies from 0.1e-5–0.1 and 0.8 is opted value for minimization of error) is used to adjust the errors and estimated the targeted voltage signal. The fundamental averaging weight component (W_{pabc}) for the direct axes can be computed as

$$W_{pabc} = \frac{W_{pa} + W_{pb} + W_{pc}}{3} \tag{3}$$

Reactive weight quantity of each phase a, b and c are evaluated as follows:

$$\begin{cases} W_{qa}(n+1) = W_{qa}(n) + \frac{1}{2}(\alpha_1 - 4\mu_1)\left[e_{qa}(n) z_{qa} - \mu_1 \operatorname{sgn}(W_{qa}(n))\right] \\ W_{qb}(n+1) = W_{qb}(n) + \frac{1}{2}(\alpha_1 - 4\mu_1)\left[e_{qb}(n) z_{qb} - \mu_1 \operatorname{sgn}(W_{qb}(n))\right] \\ W_{qc}(n+1) = W_{qc}(n) + \frac{1}{2}(\alpha_1 - 4\mu_1)\left[e_{qc}(n) z_{qc} - \mu_1 \operatorname{sgn}(W_{qc}(n))\right] \end{cases} \tag{4}$$

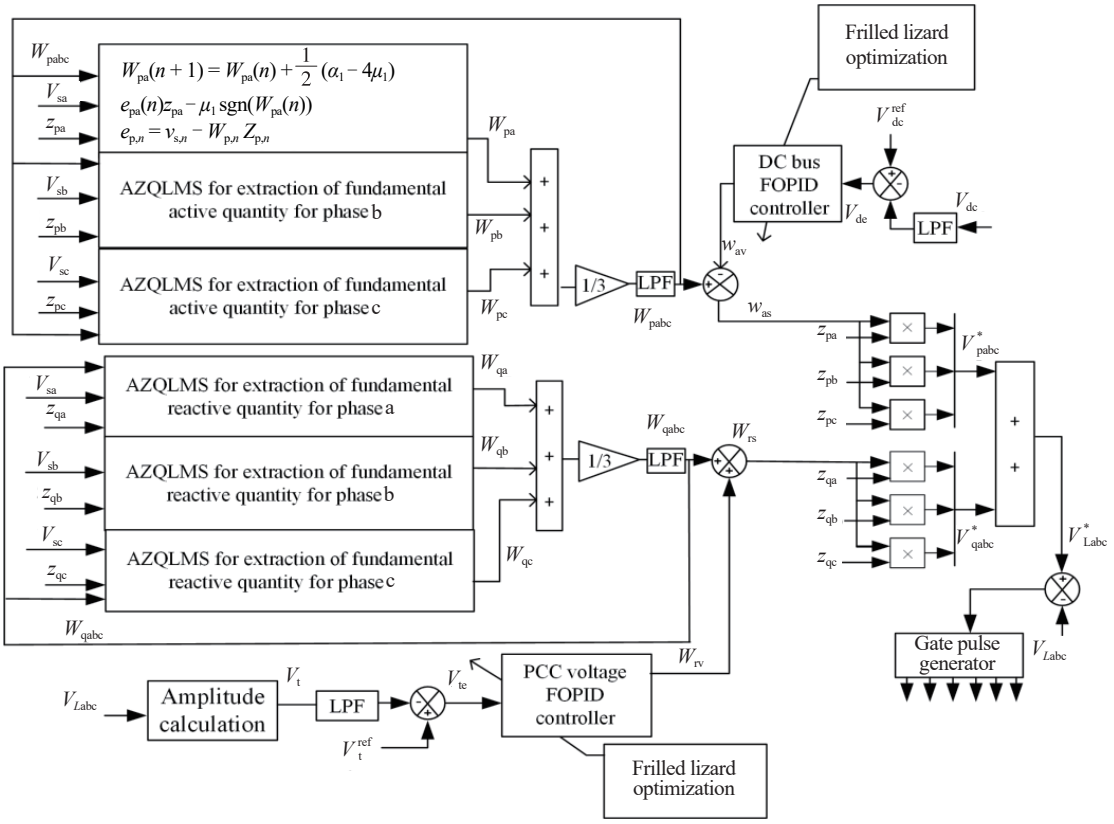

Fig. 2. Control algorithm for three phase DVR.

The fundamental averaging weight component (W_{qabc}) for the direct axes can be computed as

$$W_{qabc} = \frac{W_{qa} + W_{qb} + W_{qc}}{3} \tag{5}$$

B. Tempate Estimation

Estimated direct and quadrature unit vector from measured load currents (i_{Labc}) is evaluated as [6], [8]

$$\begin{cases} z_{pa}(i) = \dfrac{i_{La}}{I_{LA}}; z_{pb}(i) = \dfrac{i_{Lb}}{I_{LA}}; z_{pc}(i) = \dfrac{i_{Lc}}{I_{LA}} \\ z_{qa} = 0.577(z_{pc} - z_{pb}); z_{qb} = 0.577(3z_{pc} + z_{pb} - z_{pc}) \\ z_{qc} = 0.289(-3z_{pc} + z_{pb} - z_{pc}) \end{cases} \tag{6}$$

where $I_{LA} = \sqrt{0.6666(i_{La}^2 + i_{Lb}^2 + i_{Lc}^2)}$.

III. Voltage Regulation Analysis

Since voltage deviations must be restored to the prescribed value using FOPID, the voltage regulation analysis is of utmost importance. When other artificial intelligence-based grid-connected controllers are compared, the proposed FOPID controller exhibits a considerably error-free response [13]. Using the FL approach, optimised FOPID controllers are used stabilizing the voltage deviation. The FOPID variables are fine-tuned with the FLO for the precise estimation of direct and quadrature load components.

A block diagram of control algorithm is displayed in Fig. 2. The proposed controller FLO based FOPID has five variables given in time domain as [17]

$$y(t) = k_p r(t) + k_i d^{-\lambda} r(t) + k_d d^{\gamma} r(t), \quad (\lambda, \gamma > 0) \tag{7}$$

The FL is integrated with the FOPID controller, for achieving the tuneable parameters and assessed with the considered fitness function (ITSE).

$$\text{Fitness function } (J) = ITSE = \int_0^{T_s} t \cdot \left[e^2(t)\right] \cdot \mathrm{d}t \tag{8}$$

In (8), $e(t)$ is the value of error, t is the time period and T_s is simulation run time. The obtained variables of FOPID are employed to estimate the direct and quadrature load voltage. The input to the FOPID controller is the error voltage (V_{de}) of the DC link that needs to minimized the dynamics of voltage and enhance the tracking of FOPID. The error value of DC link is computed as

$$V_{de} = V_{dc}^{ref} - V_{dc} \tag{9}$$

The obtained response of controller is (w_{av}) and subtracting from the mean weighting value of active component (W_{pabc}) to obtain (w_{as}), is computed by (9).

$$W_{as} = W_{pabc} - w_{av} \tag{10}$$

TABLE I
FOPID CONTROLLER GAIN UTILIZED FOR FINE TUNING OF DC AND AC LINK

Methods	Variables									
	Optimum values for DC-FOPID					Optimum values for AC-FOPID				
	K_{p1}	K_{i1}	K_{d1}	λ_1	γ_1	K_{p2}	K_{i2}	K_{d2}	λ_2	γ_2
FOPID(Hit and Error)	8	0.4	0.04	1	1	29.88	0.4	0.01	1	1
FLO-FOPID	20.14	0.01	0.01	0.3979	0.8066	41	2.08	2.08	2	0.1

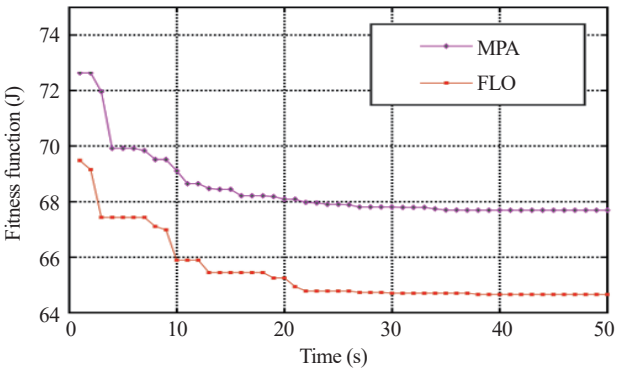

Fig. 3. Converging analysis for fine tuning of FOPID gain.

FOPID is utilized to suppress the oscillations of AC terminal voltage, and the input to FOPID is defined as

$$V_{te} = V_t^{ref} - V_t \tag{11}$$

The load voltage quantity (V_t) computation is expressed in (12).

$$V_t = \sqrt{0.667(V_{LA}^2 + V_{LB}^2 + V_{LC}^2)} \tag{12}$$

The FOPID response (w_{rv}) is taken the mean sum weighting value of the computed fundamental reactive weight (W_{qabc}) to achieve (w_{rs}) shown as

$$W_{rs} = W_{qabc} + W_{rv} \tag{13}$$

The estimated direct and quadrature quantity are achieved by multiply with unit template given as,

$$\begin{cases} V_{pa}^* = W_{as} \times z_{pa}; V_{pb}^* = W_{as} \times z_{pb}; V_{pc}^* = W_{as} \times z_{pc} \\ V_{qa}^* = W_{rs} \times z_{qa}; V_{qb}^* = W_{rs} \times z_{qb}; V_{qc}^* = W_{rs} \times z_{qc} \end{cases} \tag{14}$$

The reference quantity of load voltage v_{Labc}^* is derived with the summation terms of v_{pabc}^* and v_{qabc}^*.

With minimal oscillations and overshoots, the FOPID regulator receives these optimum gain values in order to achieve the perfect balancing voltage control. The ITSE index performance is verified using the FLO chosen parameters. The control parameters taken into account for optimising are number of populations = 30, maximum trials = 50, and variables =10. The constants of FOPID are K_p = [0.01, 30], K_i = [0.01, 4], K_d = [0.011, 1], λ = [0.01, 4] and γ = [0.01, 4]. AC FOPID limits are K_p = [1, 50], K_i = [0.01, 4], K_d = [0.0001, 4], λ = [0.01, 4] and γ = [0.01, 10]. For the purpose of comparing the effectiveness of the FLO with marine predator algorithm (MPA), the established bounds for the gain variables of the DC link and AC terminal. The considered cost function justifying nature of DC-FOPID gain values tuning with FLO, and MPA is depicted in Fig. 3. According to the converging analysis, the FLO optimization surpasses the MPA and converges quickly at the 24th iteration with the optimum cost for DC link is 35.538 and AC link 22.145, respectively. Table I demonstrates the optimum set values for DC and AC FOPID for voltage stabilization. Table I is required to minimize the stated FF in a minimum amount of time and iterations in order to get the optimal dynamic response of the FOPID. Table I depicts the optimal FOPID variables. The proposed controller technique requires moderate control efforts to maintain the desired load voltage. The transient response performance is summarized in Table II, further highlights its effectiveness.

TABLE II
COMPARATIVE STUDY OF VOLTAGE STABILIZATION OF DC LINK

Parameters	LMS-PI[9]−[11]	AZQLM-optimized FOPID
Settling time t_s (s)	0.26	0.18
Peak overshoot M_p (%)	18	5.7
Undershoot (%)	12	3.4
Repones time	Low	Quick
Power quality	Lower	Higher
Oscillation during transient	Higher	Lower
Accuracy	Moderate	Better
Complexity degree	High	Low
Step size	Constant	Variable
Static error	High	Low
Dynamic oscillations	High	Low

IV. RESULT AND DISCUSSION

The simulation work of DVR is simulated based on AZQLMS and FOPID Mtalab environment with a toolbox of sim power system. The performance is demonstrated with AZQLMS and FOPID based control under different grid voltage issues using solver of ode5 and sample time is 20 μs. It includes overall signals which are utilized for the computation of reference generation of load voltage and its compensation capability. The electrical system parameters rating for simulation and hardware are listed in Appendix.

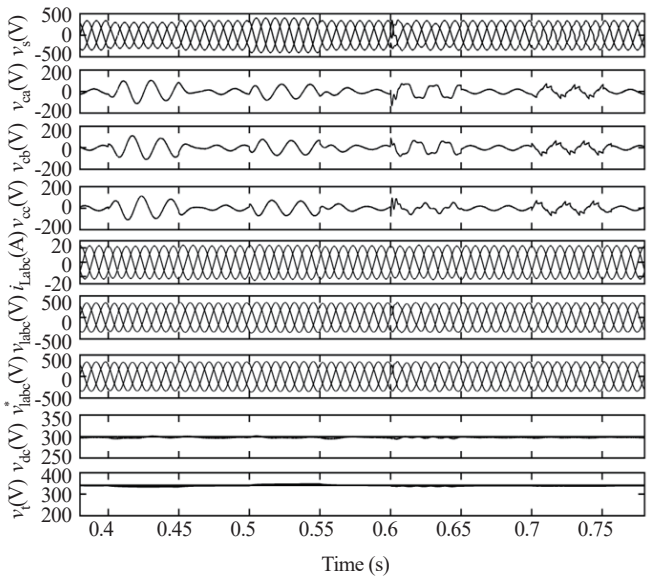

Fig. 4. DVR dynamic performance with AQLAM-FOPID based control algorithm.

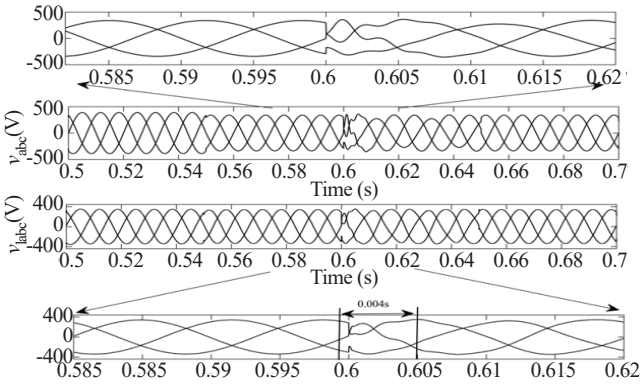

Fig. 5. Compensatory DVR response for unbalanced voltage.

Compensation peromnce of DVR is as follow: The analysis of the recommended algorithm is done during the computation of reference signal of load voltage are illustrated in Fig. 4 for DVR system. The proposed integrated controller AZQLMS and FOPID alleviates the disturbances from grid voltages v_{sa} of 'phase a'. The compensating voltages for 3 phases v_{ca}, v_{sa} and v_{cc} are represented in subplot 3 (b), (c) and (d). The sinusoidal load current of 21.99 A is depicted in subplot 3(e). These quantities help to achieves distortion free reference load voltage of 415 V with expected amplitude and sinusoidal nature of signals. The DC and AC link voltages with minimal deviations confirms the stability of computed load voltage. Fig. 5 demonstrates compensatory time for case of voltage unbalancing is 0.004 s. The designed controller is evaluated through simulation and practical tests, confirming its robustness and effectiveness in case of voltage distortion and DC-link voltage variations. Additionally, the controller demonstrates a rapid dynamic response time under transient state. Supply voltage (v_{sab})

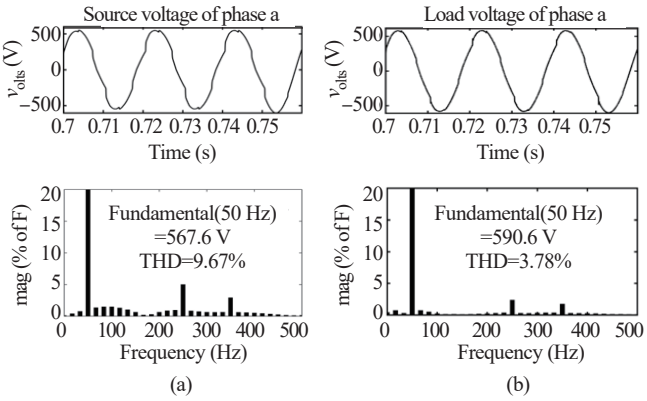

Fig. 6. THD performance in three phase system using DVR.

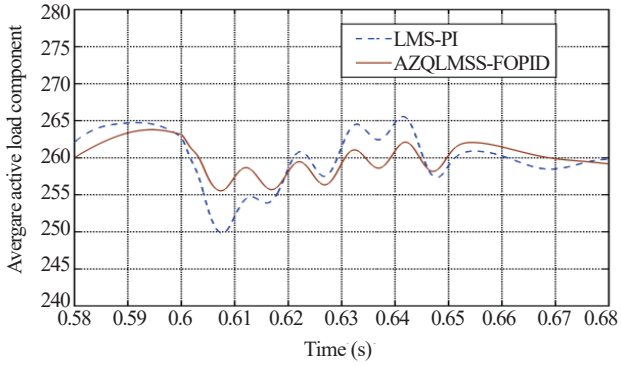

Fig. 7. Comparative in terms of convergence of average active weight component of LMS-PI with proposed method.

has voltage harmonics level of around 10% THD is portrayed in Fig. 6. The compensated corresponding load voltage (v_{lab}) is restored to 415 V and THD level is limited to 3.78% which is below 5%. By using optimised values, the response transitory time of DC link voltages has significantly improved and quick settled to the set level rapidly with lessen peak overshoot shown in Fig. 7. Compared to the basic LMS-PI approach, the DC link voltage has reduced peak overshoot and better setting time.

To further analyze the performance efficiency illustrated in Fig. 7, the estimated mean weight active load components under voltage imbalance conditions are compared across various control strategies, including the proposed AZQLMS and FOPID. This figure highlights that the AZQLMS and FOPID exhibits smaller oscillations compared to the LMS-PI. Consequently, the tracking and convergence capabilities of AZQLMS and FOPID are notably enhanced and faster under dynamic conditions.

The proposed AZQLMS and FOPID-FLO based control method excel in performance and offer greater flexibility in tuning compared to PI controllers as shown in Fig. 8. This deliver notable improvements in time response behavior, achieving a faster settling time of 0.18 s, as well as reduced overshoot of 5.7% and undershoot of 3.4%. Table II shows the comparative study of the AZQLMS technique, which outperforms the basic LMS-PI.

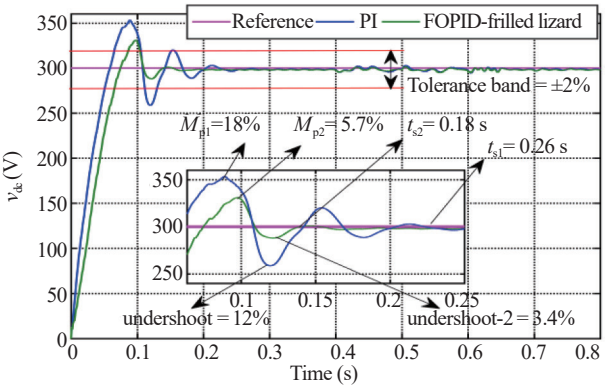

Fig. 8. Voltage stabilization of DC link.

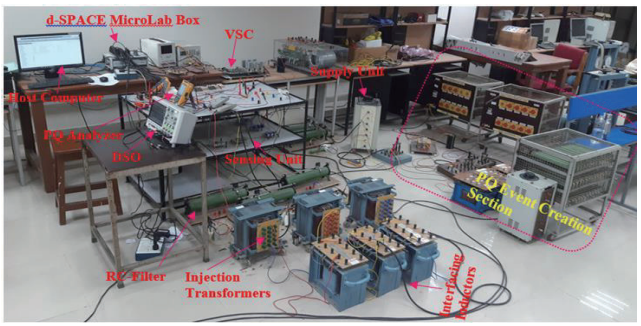

Fig. 9. Prototype of DVR setup.

V. Experimental Performance

The DVR prototype, utilizing AZQLMS and FOPID control techniques as illustrated in Fig. 9, integrates the control hardware with the power circuit. A laboratory-scale prototype is developed to evaluate PQ issues such as voltage sag, swell, imbalance, and distortion. Hall effect-based sensor circuitry (LEM-LA55P and LEM-LV25P) is employed to capture the desired signals of the designed system control. The Micro-LabBox is used to process the sensed signals and generate the required switching sequences for the VSC converter. Simulation outcomes are validated through laboratory experiments, where devices like digital storage oscilloscope (DSO), PQ analyzer, and multimeters are used to monitor voltage waveforms and other DVR performance parameters.

The DVR test results and voltage PQ issues mitigation compensation capacity are discussed and analyzed with DSO captured waveforms. A voltage distortion of 12% is introduced in the grid (v_{sabc}), and the load voltage (v_{Labc}) is restored to 110 V with the incorporation of recommended control and depicted in Fig. 10. The analysis of distortion compensation includes phase a signals like voltages of supply (v_{sa}), injecting voltage (v_{inja}), load side voltage (v_{La}), dc link (V_{dc}), and load side current (i_{La}) during harmonic injection in Fig. 10(a) and (b). The DC link (V_{dc}) errors are stabilized under distortion and showing maintained voltage level with less fluctuation whilst Fig. 10(c) shows the stabilized dc link voltage (V_{dc}) of 70 V with a balanced load voltage (v_{La}) of 110 V and load current (i_{La}) is distortion free during removal of distortion phenomena from supply voltage (v_{sab}).

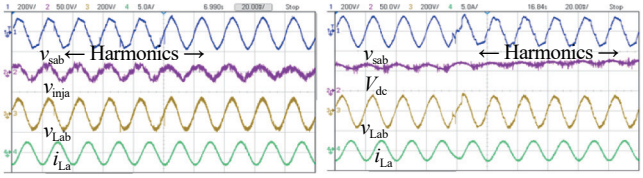

(a) In *y*-axis: CH1, CH3-200 V/div, CH2-50 V/div, CH4-5 A/div; In *x*-axis: 20 ms/div

(b) In *y*-axis: CH1, CH3-200 V/div, CH2-50 V/div, CH4-5 A/div; In *x*-axis: 20 ms/div

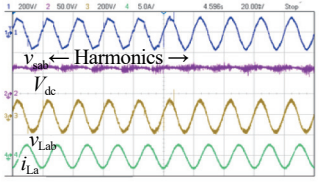

(b) In *y*-axis: CH1-200 V/div, CH2, CH3-50 V/div, CH4-5 A/div; In *x*-axis: 20 ms/div

Fig. 10. Dynamic compensation with developed controlling scheme during distortion (a) v_{sab}, v_{inja}, v_{Lab}, i_{La}. (b) v_{sab}, V_{dc}, v_{Lab}, i_{La}. (c) v_{sab}, V_{dc}, v_{Lab}, i_{La}.

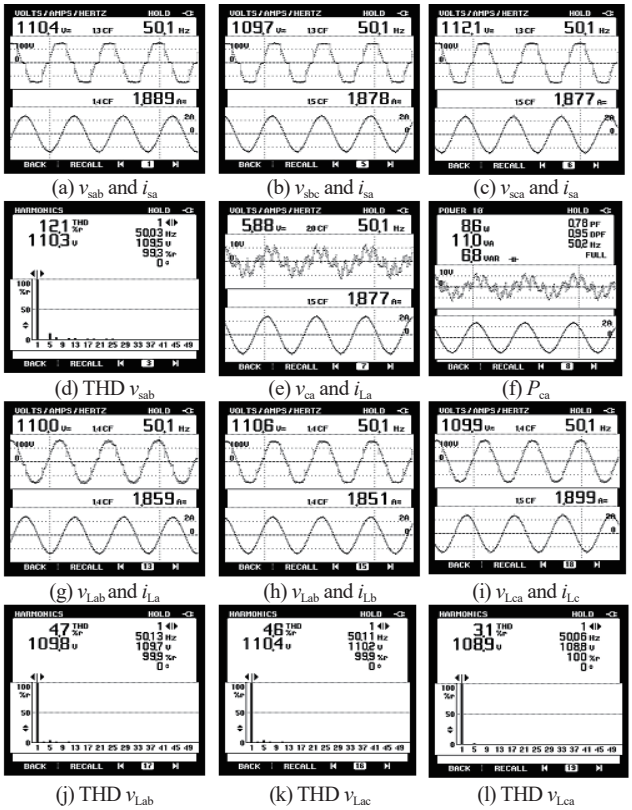

(a) v_{sab} and i_{sa} (b) v_{sbc} and i_{sa} (c) v_{sca} and i_{sa}

(d) THD v_{sab} (e) v_{ca} and i_{La} (f) P_{ca}

(g) v_{Lab} and i_{La} (h) v_{Lab} and i_{Lb} (i) v_{Lca} and i_{Lc}

(j) THD v_{Lab} (k) THD v_{Lac} (l) THD v_{Lca}

Fig. 11. Voltage THD spectrum of three-phase system using AZQLMS and optimized FOPID-based control in DVR.

The DVR's steady-state performance under supply-side voltage distortion is examined in Fig. 11. Fig. 11(a)–(d) demonstrates that the uncompensated source voltage waveforms (v_{sabc}) and source current (i_{sa}) are detailed, with phase values of 110.4, 109.7, and 112.1 V and a harmonic distortion level around 12.1%. Fig. 11(e) and (f) shows the compensation voltage (v_{ca}) and phase compensation power (p_{ca}), respectively. The load voltages (v_{Labc}) compensated values are 110.0, 110.6, and 109.9 V

TABLE III
COMPARATIVE STUDY OF VOLTAGE STABILIZATION OF DC LINK

Before compensation with 12.1% THD		After compensation	
Supply voltage	Values	Load voltage	Values
V_{sa}	110.4 V	V_{La}	110.0 V, 4.4%
V_{sb}	109.7 V	V_{Lb}	110.6 V, 4.6%
V_{sc}	112.1 V	V_{Lc}	109.9 V, 3.1%

as per Fig. 11 (g) and (i) with distortion levels reduced to 4.7%, 4.6%, and 3.1% as per Fig. 11 (j) and (l). Summarized statistical values for the voltage distortion before and after compensation with experimental results depicted in Table III The experimental results are all at 110 V supply voltage.

VI. CONCLUSION

In this work, DVR is developed with an AZQLMS and optimized fractional order proportional integral derivative (FOPID) based control to compensate the voltage power quality (PQ) problems. To perform compensation, AZQLMS and FOPID-FLO are observed superior over LMS-PI under transitory conditions in terms of ripple reduction of quick settle time, peak overshoot, and undershoot of 0.18 s, 5.7%, and 3.4%, respectively. Also, adaptive zero-attracting quaternion-based least mean square (AZQLMS) effectively computes the fundamental components of direct and quadrature under voltage perturbations in the DVR control circuit. The AZQLMS adaptively adjusts the step/learning rate based on the error rate. From the simulation results it is found that the load voltage THD is well maintained within the allowable limit of 3.78%. In addition, from the experimental results exhibit the AZQLMS and FOPID-FLO strategy that minimized the THD of the load voltage as per the standard IEEE 519. These percentages verify that the quality of the voltage is better if the AZQLMS and FOPID-FLO strategy is used.

For future research, we aim to explore the application of this hybrid metaheuristics algorithm to optimize the gain variables of FOPID for a wider range of optimization problems. Additionally, efforts will be directed towards the experimental implementation of this control strategy to assess its robustness under varying grid voltage conditions.

In summary, the conclusions drawn are as follows:

1. The AZQLMS and FOPID-FLO strategies effectively limit the experimental THD of load voltage to approximately 4.7%, 4.6%, and 3.1%, which is well below the IEEE 519 standard.

2. Among the evaluated methods, FOPID-FLO demonstrates superior convergence of the objective function compared to FOPID-MPA.

3. FOPID-FLO outperforms FOPID-MPA, making it a more effective choice for tuning the gain variables of FOPID.

APPENDIX

System simulation parameters:

Non-ideal supply ($v_{L\text{-}L}$) = 415 V, 50 Hz; load rating =16 kVA, 0.8 p.f; load current (i_L) = 21.98 A ; DVR transformer rating = 3 000 VA, 100/150 V; V_{DC} = 300 V; amplitude of terminal voltage V_t = 339 V; DC link capacitor (C_{DC}) = 4 700 μF; Filter inductor (L_f) = 1 mH; LPF cut of frequency = 8 Hz; Sampling time (t_s) = 20 μs. AQLSM controlling parameters: $\alpha = 0.08$ and $\mu = 5\times10^{-4}$.

Non-ideal grid voltage (v_{sabc}) 110 V, 50 Hz; load = 0.353 kVA with 0.66 p.f. (lag.); voltage of ac bus (V_t) = 90 V, voltage (V_{dc}) at DC link = 70 V; capacitor value of dc bus (C_{dc}) = 3 500 μF; rating of injection transformer 4 kVA, 35/35 V; series interfacing inductance (L_{se}) = 0.5 mH; filter component R_f =10 Ω, C_f =120 μF and switching frequency = 10 kHz.

REFERENCES

[1] M. P. Kazmierkowski, "Power theories for improved power quality (Pasko, M. and Benysek, G.; 2012) [Book News]," in *IEEE Industrial Electronics Magazine*, vol. 7, no. 1, pp. 68–69, 2013.

[2] A. Ghosh and G. Ledwich, in *Power Quality Enhancement Using Custom Power Devices*, New York, NY: USA, Springer Science and Business Media, 2012.

[3] A. K. Sadigh and K. M. Smedley, "Review of voltage compensation methods in dynamic voltage restorer (DVR)," in *Proceedings of IEEE Power and Energy Society General Meeting*, San Diego, CA, USA, 2012, pp. 1–8.

[4] A. M Kazemi and M. T. Haque, "A new control strategy for unified power quality conditioner (UPQC) in distribution systems, "in *Proceedings of International Conference on Power System Technology*, Chongqing, China,2006, pp. 1–5.

[5] Mahmoud A. El-Gammal, Amr Y. Abou-Ghazala, and Tarek I. El-Shennawy, "Dynamic voltage restorer (DVR) for voltage sag mitigation", *International Journal on Electrical Engineering and Informatics*, vol. 3, no. 1, pp. 1–11, 2011.

[6] P. Kanjiya, B. Singh, A. Chandra, and K. Al-Haddad, "SRF theory revisited to control self-supported dynamic voltage restorer (DVR) for unbalanced and nonlinear loads," in *IEEE Transactions on Industry Applications*, vol. 49, no. 5, pp. 2330–2340, Sept.-Oct. 2013.

[7] P. Kumar, S. R. Arya, K. D. Mistry, and B. C. Babu, "Performance evaluation of GRNN and ANFIS controlled DVR using machine learning in distribution network," in *Journal of Optimal Control Applications and Methods*, 2022.

[8] T. A. Naidu, A. Al-Durra, T. H. M. El-Fouly, and H. Zeineldin, "Optimization based variable learning factor least mean square algorithm to control DVR in infected grid systems," in *Proceedings of 2020 IEEE International Conference on Power Electronics, Drives and Energy Systems (PEDES)*, Jaipur, India, 2020, pp. 1–6.

[9] L. Shen, D. Jiang, and H. Zhu, "Control study for suppressing rotor vibration of the six-pole hybrid magnetic bearing system based on no-parameter variable-step-size least-mean-square algorithm," in *IEEE Transactions on Power Electronics*, vol. 40, no. 8, pp. 10672–10681, Aug. 2025.

[10] S. J. Lim and J. G. Harris, "Combined LMS/F algorithm," in *Electronic*

Letter, vol. 33, no. 6, pp. 467–468, Mar. 1997.

[11] S. R. Arya, K. D. Mistry, and P. Kumar, "Least mean mixed norm square/fourth adaptive algorithm with optimized FOPID gains for voltage power quality mitigation," in *IEEE Journal of Emerging and Selected Topics in Power Electronics*, vol. 11, 3, pp. 632–2640, Jun. 2023.

[12] L. Luo and W. Z. Zhu, "An optimized zero-attracting LMS algorithm for the identification of sparse system," in *IEEE/ACM Transactions on Audio, Speech, and Language Processing*, vol. 30, pp. 3060–3073, 2022.

[13] A. Kumar, N. Gupta, and V. Gupta, "Experimental prototype of a novel feed forward compensation for DC-link voltage stabilization in grid-tied PV system," in *International Transactions on Electrical Energy Systems*, vol. 30, no. 1, pp.1–26, 2020.

[14] P. Kumar, S. R. Arya, and K. D. Mistry, "Performance enhancement of DVR Using adaptive neural fuzzy and extreme learning machine-based control strategy," in *International Journal of Fuzzy Systems*, vol. 24, pp. 3416–3430, 2022.

[15] W. Budahab, M. Hamouda, and K. Al-Haddad, "A fuzzy logic based controller of DC-link voltage regulation of parallel inverters operation during unintended islanding mode," in *Proceedings of IECON 2017 - 43rd Annual Conference of the IEEE Industrial Electronics Society*, Beijing, China, 2017, pp. 7891–7896.

[16] I. A. Falahah, O. A. Baik, S. Alomari, G. Bektemyssova, S. Gochhait, I. Leonova, O. P. Malik, F. Werner, and M. Dehghani, "Frilled lizard optimization: A novel bio-inspired optimizer for solving engineering applications," in *Computers, Materials and Continua*, vol. 79, vol. 3, pp. 3631–3678, 2024.

[17] A.Nasir, I.Rasool, and D. Sibtain, "Adaptive fractional order PID controller based MPPT for PV connected grid system under changing weather conditions, " in *Journal of Electrical Engineering and Technology*, vol. 16, pp. 2599–2610, 2021.

Ganesh Kumar Budumuru received his B. Tech. degree from Avanthi Institute of Engineering and Technology, Visakhapatnam, and his M. Tech. degree from University College of Engineering, Kakinada. Currently, he is a Research Scholar in the Department of Electrical Engineering at Veer Surendra Sai University of Technology, Odisha, India. His research interests include power quality, renewable energy systems, and electric vehicles.

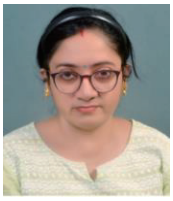

Papia Ray received her Bachelor of Engineering (Electrical Engineering) degree from Government Engineering College (Muzaffarpur Institute of Technology) at Muzaffarpur, Bihar, India, in 1998, the Master of Technology (Power Systems) from National Institute of Technology, Jamshedpur in 2002 and Ph.D. degree from Indian Institute of Technology, Delhi in 2013. She is presently serving as Professor in Electrical Engineering Department of National Institute of Technical Teachers' Training and Research, Kolkata-700106, India. She has more than 20 years of teaching experience. Her research interest includes power system protection, wide area measurement systems, power quality, renewable energy, forecasting, biomedical engineering etc.

Prashant Kumar received the Bachelor of Technology in electrical engineering from Hooghly Engineering and Technology College, Hooghly, India, in 2009 and M. Tech in power system from S.R.M University, Kattankulathur, India, in 2013. He is currently pursuing the Ph.D. degree in electrical engineering from Sardar Vallabhbai National Institute of Technology, Surat, India. His research area includes applications of machine learning and power quality and design of custom power devices.

Sabha Raj Arya received Bachelor of Engineering degree in electrical engineering from Government Engineering College Jabalpur, in 2002, Master of Technology in power electronics from Motilal National Institute of Technology, Allahabad, in 2004 and Ph.D. degree in electrical engineering from Indian Institute of Technology (I.I.T) Delhi, New Delhi, India, in 2014. He joined the Department of Electrical Engineering, Sardar Vallabhbhai National Institute of Technology, Surat, as Assistant Professor and became Associate Professor and Professor in 2019 and 2023 respectively in same institute. His areas of interest include power quality, power electronics, power filter design, design of dc/dc converters and distributed power generation.

A Family of Single-Phase Back-to-Back Three-Level Power Factor Correction Rectifiers

Hui MA, Guofang CHEN, Kun XIANG, Liping FAN, Lei XI, and Yuehua HUANG

***Abstract*—In this paper, a family of back-to-back three-level power factor correction (BT-PFC) converters is proposed. A bidirectional switch unit is cascaded or embedded in the midpoint between the bridge arm and the two capacitors of the back-to-back PFC to achieve three output voltage levels during the frequency period. The proposed topologies can effectively reduce the harmonic content and lower the equivalent switching frequency. Firstly, the derivation methods and circuit characteristics of the proposed topologies are analyzed and compared, and one of the topologies is chosen as an example to describe its operating principle. Furthermore, decoupling closed-loop control and modulation technology of the proposed BT-PFC converter are analyzed in detail. Finally, an experimental prototype with an input of 220 V/50 Hz and a rated output of 1 kW/400 V is designed based on the BT-PFC-VI circuit. The experimental results show that the proposed single-phase BT-PFC has higher efficiency and flexibility is verified.**

***Index Terms*—Back-to-back, power factor correction, three-level converter, voltage stress.**

I. Introduction

With the continuous expansion of DC application scenarios, multilevel rectifier circuits are widely used in LEDs, air conditioners and electric vehicle charging piles. Therefore, multilevel rectifiers have become a hot research topic for scholars at home and abroad [1]–[5]. However, the multilevel rectifier will cause serious harmonic pollution in the system and affect the operation of electrical equipment. Hence, power factor correction (PFC) technology is frequently employed as a viable solution in addressing this issue. The introduction of a multilevel PFC topology improves the circuit efficiency and harmonic quality, while also offering the advantages of simple control, low voltage stress and lower switching losses [6]–[9].

Compared with two-level circuit topology, three-level bridgeless PFC topology has obvious advantages in terms of reducing switching loss and improving power factor [10]–[12]. A variety of commonly used Boost PFC circuits are compared in [13]–[14], and the proposed topology is evaluated and compared through loss analysis and simulation verification, demonstrating the advantages of the bridgeless PFC topology. The diode clamp topology is combined with the traditional back-to-back topology in [15], and a three-level bridgeless boost PFC rectifier is proposed, where the switching is only subjected to half of the output DC voltage, leading to an improvement in circuit efficiency. The PFC topology proposed in [16] achieves high efficiency by diminishing losses through a reduction in the number of semiconductor devices within the current flow path.

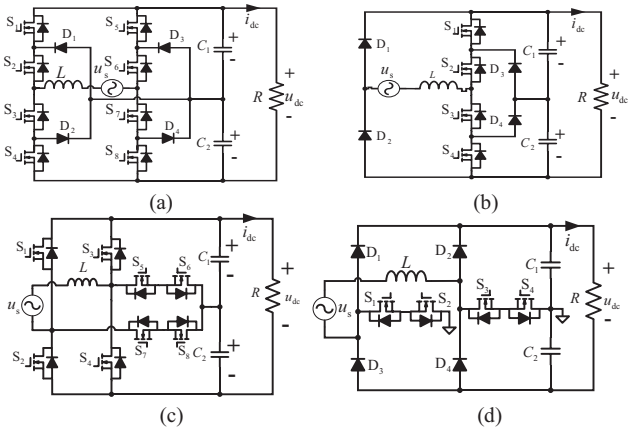

Fig. 1. Single-phase PFC rectifiers. (a) Bidirectional diode clamp type. (b) Unidirectional diode clamp type. (c) Bidirectional T-topology. (d) Unidirectional T-topology.

In the multilevel topology, the diode clamped and T-type structures are composed of diodes and fully controlled devices, which can achieve efficient energy conversion and transmission [17]–[21]. Back-to-back structures are widely used because of their low on-state loss, low common-mode interference and low control complexity [22]–[25]. The traditional diode clamp three-level topology is shown in Fig. 1(a), which is widely used in power transmission and distribution systems because of its bidirectional power flow [26]. However, the number of active switches is a significant disadvantage of this topology. As shown in Fig. 1(b), it is a unidirectional three-level power factor correction circuit, which reduces four active switches, and improve the efficiency compared to the bidirectional diode clamp type. Additionally, Fig. 1(c) shows the dual T-type three-level topology with bidirectional power

Manuscript received May 02, 2025; revised July 16, 2025; accepted August 15, 2025. Date of publication September 30, 2025; date of current version August 22, 2025. This work was supported in part by National Natural Science Foundation of China under the grant 52377191. (*Corresponding author: Hui Ma.*)

H. Ma, G. Chen, X. Li, and Y. Huang are with Department of College of Electrical Engineering & New Energy, China Three Gorges University, Yichang 443002, China (e-mail: mahui@ctgu.edu.cn; 202308580121014@ctgu.edu.cn; Xilei@ctgu.edu.cn; HuangYuehua@ctgu.edu.cn).

K. Xiang and L. Fan are with Department of State Gird Hubei Yichang Power Supply Co., Ltd., Yichang 443000, China (e-mail: Xiangkun@ctgu.edu.cn; FanLiping@ctgu.edu.cn).

Digital Object Identifier 10.24295/CPSSTPEA.2025.00028

flow. Compared with the diode clamped topology, the T-type topology reduces the number of clamped diodes and solves the problems of asymmetric circuit structure and uneven loss distribution. In order to further reduce the cost and the number of switches, the improved T-type three-level topology shown in Fig. 1(d) is obtained, in which the switches S_1 and S_2 are connected in reverse series to form a back-to-back structure. By cascading or embedding the back-to-back structure with diode clamp and T-type bridge arms, a family of three-level BT-PFC is proposed.

In order to facilitate the pulse distribution and reduce the switching losses of the topology, combining the switch bridge arm in Fig. 1(b) with the back-to-back structure in Fig. 1(d), the back-to-back three-level PFC converter in Fig. 2 is obtained. By replacing the switches S_3~S_6 in the back-to-back three-level PFC-I converter shown in Fig. 2(a) with diodes and forming the diode uncontrolled rectifier bridge arm, the back-to-back three-level BT-PFC-II shown in Fig. 2(b) can be obtained. Fig. 2(c) shows the back-to-back three-level BT-PFC-III, so as to achieve a smaller number of switches. Fig. 2(d)–(f) show bridgeless three-level rectifiers cascaded with different bidirectional switching units, where the topologies are shown in Fig. 2(d) for BT-PFC-IV, Fig. 2(e) for BT-PFC-V, and Fig. 2(f) for BT-PFC-VI.

The neutral point of the BT-PFC-I-III topology is connected to the AC side through an embedded bidirectional switch, forming a three-level structure. The embedded bidirectional switching device replaces the original bridge arm. The BT-PFC-IV-VI topology adds a cascade unit between the diode uncontrolled rectifier bridge arm and the split capacitor, which realizes bidirectional current flow. Both types of topologies connect reverse series back-to-back structure switches between the rectifier bridge arms.

The structure of this paper is as follows. In Section II, the voltage stress and device number of three-level PFC topologies based on embedded and cascaded structures are compared, and introduced the derivation process and operation principle of BT-PFC-VI topology. In Section III, a rigorous examination was conducted on the mathematical model of the circuit and topological losses. Section IV will introduce modulation techniques and control strategies for this specific topology family. Detailed experimental validation is presented in Section V, followed by a comprehensive summary of conclusions in Section VI.

II. Topology Comparison and Operation Principle

A. Topology Characteristics and Comparison

Based on the optimization and improvement of the three-level BT-PFC-I converter shown in Fig. 2(a), the voltage stress characteristics of each switch and diode in the proposed back-to-back three-level power correction circuit at the same power level are analyzed. The maximum voltage stress of each component in the five circuits of BT-PFC-II~VI is shown in Table I. It can be seen from Table I that the voltage stress of the switches in the proposed BT-PFC topology is half of the DC

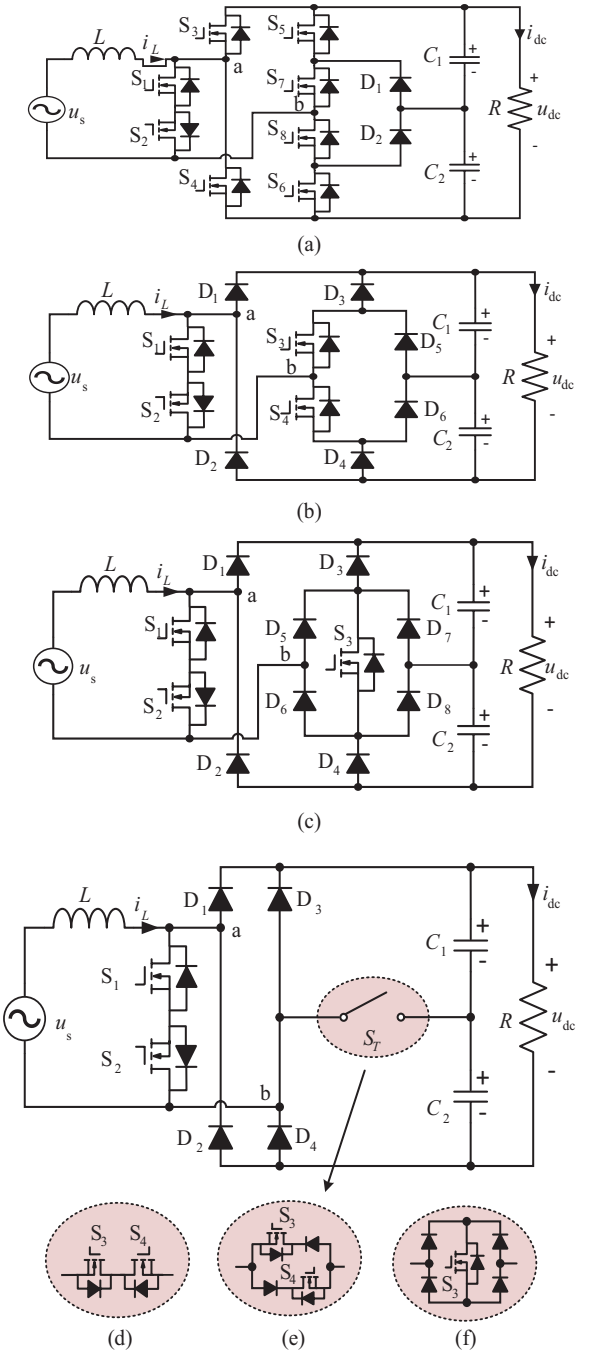

Fig. 2. Family of back-to-back three-level PFC converter. (a) BT-PFC-I. (b) BT-PFC-II. (c) BT-PFC-III. (d) BT-PFC-IV. (e) BT-PFC-V. (f) BT-PFC-VI

TABLE I
Voltage Stress of the Proposed Topologies Devices

Devices	BT-PFC-II	BT-PFC-III	BT-PFC-IV	BT-PFC-V	BT-PFC-VI
S_1~S_3	$u_{dc}/2$	$u_{dc}/2$	$u_{dc}/2$	$u_{dc}/2$	$u_{dc}/2$
S_4	$u_{dc}/2$	—	$u_{dc}/2$	$u_{dc}/2$	—
D_1~D_4	u_{dc}	u_{dc}	u_{dc}	u_{dc}	u_{dc}
D_5, D_6	$u_{dc}/2$	u_{dc}	—	$u_{dc}/2$	$u_{dc}/2$
D_7, D_8	—	$u_{dc}/2$	—	—	$u_{dc}/2$

TABLE II
NUMBER AND RATED VOLTAGE OF POWER DEVICES IN THE CURRENT PATH ACROSS VARIOUS VOLTAGE LEVELS

Levels	Device(Number×Rated voltage)					
	BT-PFC-I	BT-PFC-II	BT-PFC-III	BT-PFC-IV	BT-PFC-V	BT-PFC-VI
$+u_{dc}$	3×S6	3×D6	3×D6	2×D6	2×D6	2×D6
$-u_{dc}$	3×S6	3×D6	3×D6	2×D6	2×D6	2×D6
$+1/2u_{dc}$	1×D4,1×S4,2×S6	1×D6,1×D4,1×S4	2×D6,1×D4,1×S4	1×D6,2×S4	1×D6,1×D4,1×S4	1×D6,2×D4,1×S4
$-1/2u_{dc}$	1×D4,1×S4,2×S6	1×D6,1×D4,1×S4	2×D6,1×D4,1×S4	1×D6,2×S4	1×D6,1×D4,1×S4	1×D6,2×D4,1×S4
+0	2×S4	2×S4	2×S4	2×S4	2×S4	2×S4
−0	2×S4	2×S4	2×S4	2×S4	2×S4	2×S4
Total	2×D4,4×S4,4×S6	4×D6,2×D4,4×S4	6×D6,2×D4,3×S4	4×D6,4×S4	4×D6,2×D4,4×S4	4×D6,4×D4,3×S4

Note: 4 and 6 correspond to rated voltages of 400 V and 600 V for respective devices.

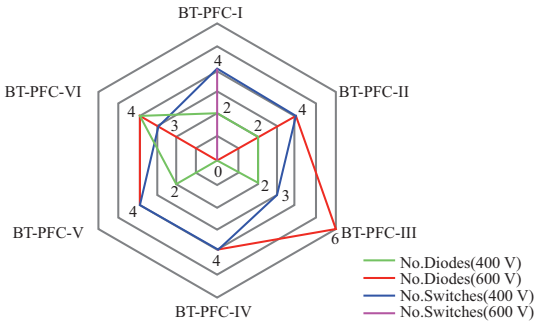

Fig. 3. Comparison of the number of devices with different rated voltage topologies.

side voltage, which reduces the circuit switching loss and is consistent with the theoretical analysis.

Table II shows the number of devices and rated voltage that pass through the corresponding current path of the topology proposed in this article at different output levels. From Table II, it can be seen that BT-PFC-I has a higher number of switching devices through which current flows compared to other topologies, resulting in increased circuit losses. When the voltage level is $\pm 1/2u_{dc}$, the topology BT-PFC-III has one more diode conducting in the current path than BT-PFC-II, resulting in slightly higher total switching losses.

Fig. 3 shows a comparison of the number of devices with different rated voltage topologies. It can be seen from Fig. 3 that BT-PFC-I has eight switches and six diodes, making it the most expensive topology compared to other topologies. BT-PFC-II uses two fewer diodes and one more switch than BT-PFC-III, so the cost difference is not significant. The BT-PFC-IV topology has only four diodes and four switches compared to other topologies, resulting in the lowest cost.

A back-to-back bridgeless three-level rectifier based on unidirectional diode clamp and T-type topology is proposed, which preserves the characteristics and performance of the circuit topology and achieves three-level by using fewer switching devices. Table III presents a comparison of the number of components between the family topology proposed in this article and other three-level topologies. Compared with references [6], [9], and [10], the topology BT-PFC-III and BT-PFC-VI proposed in this paper have a reduced number of switching devices, thus reducing the complexity of control. Although only two switches are used in [8], the increase in the number of inductors and capacitors resulted in increased costs and consideration of equipment heat dissipation issues. Topology BT-PFC-I and BT-PFC-IV use fewer diodes, resulting in reduced conduction losses in the circuit. Topology BT-PFC-II~IV can achieve unidirectional power flow and reduce electromagnetic interference generated in the system.

B. Operation Principle of the Proposed Topologies

The back-to-back three-level PFC rectifier (BT-PFC-VI), as shown in Fig. 2(f), is taken as an example to analyze the operation principle, the BT-PFC-VI topology is composed of a AC voltage source u_s, one inductor (L), two capacitors (C_1 and C_2), three switches (S_1, S_2 and S_3), and eight diodes (D_1–D_8). Fig. 4 illustrates the current paths of the six operation modes, and this circuit operates symmetrically during the positive and negative half-cycle. Additionally, the states of the switches are documented in Table IV, with "1" and "0" signifying the "ON" and "OFF" states of the power switches, respectively. Subsequently, a detailed analysis of the six operational modes of the BT-PFC-VI is conducted.

Mode 1: S_1 and S_2 are on. In this mode, the positive line current i_L is linearly increasing. Meanwhile, the input inductor L accumulates energy and the capacitors C_1 and C_2 provide power to the load R. The bridge arm voltage u_{ab}=0. The equivalent circuit of this mode is shown in Fig. 4(a).

$$\begin{cases} L\,\mathrm{d}i_L/\mathrm{d}t = u_s \\ C\mathrm{d}\left(u_{C1}+u_{C2}\right)/2\mathrm{d}t = -u_{dc}/R \end{cases} \tag{1}$$

Mode 2: S_3 are on. At this time, the capacitor C_1 is charged by the positive line current i_L, and the DC load current discharges the capacitor C_2. During this state, the voltage u_{ab}=+u_{C1}=+u_{dc}/2. The equivalent circuit of this mode is shown in Fig. 4(b).

$$\begin{cases} L\,\mathrm{d}i_L/\mathrm{d}t = u_s - u_{C1} \\ C_1\,\mathrm{d}u_{C1}/\mathrm{d}t = i_L - u_{dc}/R \end{cases} \tag{2}$$

Mode 3: When the voltage u_{ab} is "+u_{dc}", all the active switches are OFF. The inductor releases its stored energy to the output capacitors C_1, C_2 and the load resistor R through the bridge diodes D_1 and D_4. The equivalent circuit of this mode is shown in Fig. 4(c).

TABLE III
COMPARISON OF THE PROPOSED TOPOLOGY WITH OTHER THREE-LEVEL TOPOLOGIES

Parameter	Topology									
	BT-PFC-I	BT-PFC-II	BT-PFC-III	BT-PFC-IV	BT-PFC-V	BT-PFC-VI	In [6]	In [8]	In [9]	In [10]
No. of switches	8	4	3	4	4	3	4	2	6	4
No. of diodes	2	6	8	4	6	8	4	4	2	6
No. of inductors	1	1	1	1	1	1	1	2	2	2
No. of capacitors	2	2	2	2	2	2	2	3	2	2
No. of gate drivers	8	4	3	4	4	3	4	2	6	4
Power flow	BPF	UPF	UPF	UPF	UPF	UPF	UPF	UPF	UPF	UPF

Note: BPF and UPF indicate bidirectional and unidirectional power flow respectively.

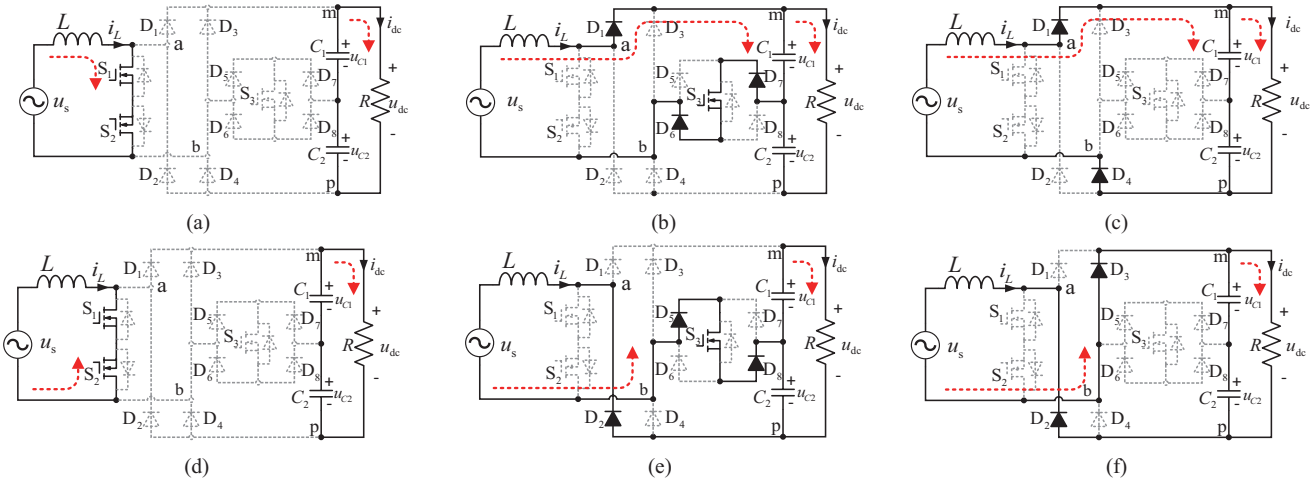

Fig. 4. Current flow path during different output voltage levels. (a) $u_{ab}=+0$. (b) $u_{ab}=+u_{dc}/2$. (c) $u_{ab}=+u_{dc}$. (d) $u_{ab}=-0$. (e) $u_{ab}=-u_{dc}/2$. (f) $u_{ab}=-u_{dc}$.

TABLE IV
SWITCHS STATUS TABLE OF BT-PFC-VI

Modes		Switching states			System parameters		
		S_1	S_2	S_3	C_1	C_2	u_{ab}
$i_L>0$	1	1	1	0	Discharge	Discharge	+0
	2	0	0	1	Charge	Discharge	u_{C1}
	3	0	0	0	Charge	Charge	$u_{C1}+u_{C2}$
$i_L<0$	4	1	1	0	Discharge	Discharge	−0
	5	0	0	1	Discharge	Charge	$-u_{C2}$
	6	0	0	0	Charge	Charge	$-(u_{C1}+u_{C2})$

$$\begin{cases} L\,\mathrm{d}i_L/\mathrm{d}t = u_s - u_{dc} \\ C\mathrm{d}\left(u_{C1}+u_{C2}\right)/2\mathrm{d}t = i_L - u_{dc}/R \end{cases} \tag{3}$$

For the negative half-line cycle, the corresponding operating modes for BT-PFC-VI are shown in Fig. 4(d), (e) and (f), which are similar with the positive half-line cycle.

From the above operation analysis, the proposed single-phase back-to-back three-level power factor correction converters are capable of generating three voltage levels, achieved through the appropriate PWM scheme for each switch. The key waveforms corresponding to the six operating modes are shown in Fig. 5.

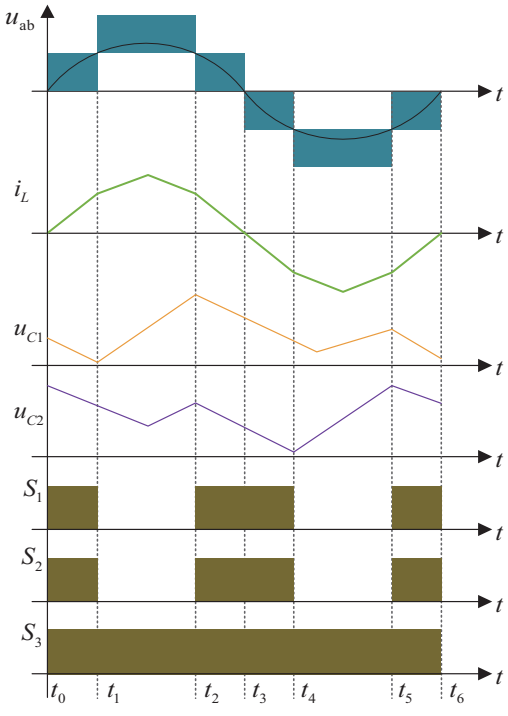

Fig. 5. Key waveform of BT-PFC-VI in a grid cycle.

III. Mathematical Model and Performance Analysis

A. Mathematical Model

Based on the analysis of the switching equivalent mathematical model of the BT-PFC-VI topology proposed, the symbolic function sgn (i_L), is defined as follows:

$$\mathrm{sgn}(i_L)=\begin{cases}1 & i_L>0\\ -1 & i_L<0\end{cases} \tag{4}$$

where sgn(i_L) = 1 indicates that inductive current at positive half cycle of the power supply (i_L >0). Furthermore, sgn(i_L) = −1 indicates that inductive current at negative half cycle of the power supply (i_L <0).

According to the current path under each mode in Fig. 4, the output bridge arm voltage u_{ab} can be derived as follows:

$$u_{ab}=u_{ap}-u_{bp}=(a-b)u_{C1}+(e-f)u_{C2} \tag{5}$$

the current on the DC side can be derived as follows:

$$\begin{cases}i_m=(a-b)i_L\\ i_o=(c-d)i_L\\ i_p=(-e-f)i_L\end{cases} \tag{6}$$

where the expression a to f are defined as follows:

$$\begin{cases}a=\overline{S_1}\overline{S_2}\dfrac{1+\mathrm{sgn}(i_L)}{2}\\ b=\overline{S_1}\overline{S_2}\overline{S_3}\dfrac{1-\mathrm{sgn}(i_L)}{2}\\ c=S_3\dfrac{1+\mathrm{sgn}(i_L)}{2}\\ d=S_3\dfrac{1-\mathrm{sgn}(i_L)}{2}\\ e=\overline{S_1}\overline{S_2}\overline{S_3}\dfrac{1+\mathrm{sgn}(i_L)}{2}\\ f=\overline{S_1}\overline{S_2}\dfrac{1-\mathrm{sgn}(i_L)}{2}\end{cases} \tag{7}$$

S_a(a=1,2,3,4) indicates the on-off status of each switch in the corresponding topology, is defined as follows:

$$\begin{cases}S_a=1\\ \overline{S_a}=0\end{cases}\quad a=1,2,3,4 \tag{8}$$

where"1"and"0"indicates the"ON"and"OFF"states of the power switches.

According to (5)–(8), the proposed circuit can be simplified into the equivalent circuit shown in Fig. 6.

B. Circuit Loss Analysis of Devices

Based on a family of single-phase back-to-back three-level power factor correction converters, the power device losses of BT-PFC-I~VI are mainly discussed. The losses of the MOSFET predominantly contain conduction losses and switching losses. Since the MOSFET possesses on-state resistance during conduction. There is an on-resistance voltage drop at both ends of the device and generates conduction losses $P_{\text{s-con}}$, which is:

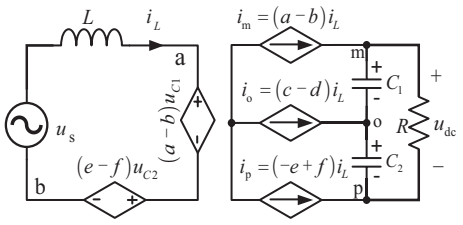

Fig. 6. Equivalent circuit diagram of the mathematic model.

$$P_{\text{s-con}}=\frac{r_{ds}}{T_L}\int_0^{T_L}I_S^2(t)\mathrm{d}t=r_{ds}I_{S,\text{rms}}^2 \tag{9}$$

where r_{ds} is the on-state resistance of MOSFET, $I_{S,\text{rms}}$ is the RMS value of the current flowing through the MOSFET and T_L is the stable working time of the device.

During the transition between the on-state and off-state of the device in a MOSFET, switching losses are generated, which is:

$$\begin{aligned}P_{\text{s-sw}}&=\frac{0.5V_{in}}{T}\int_0^{T}I_S(t)\,\mathrm{d}t\left(t_{on}+t_{off}\right)f_{sw}\\ &=0.5V_{in}I_{S,avg}\left(t_{on}+t_{off}\right)f_{sw}\end{aligned} \tag{10}$$

where V_{in} and $I_{S,avg}$ are the RMS value of the input voltage and the output current, t_{on} and t_{off} are the crossover time of drain current and voltage conversion in switching process respectively, and f_{sw} corresponds to the switching frequency.

Similarly, the power losses of the diode in a cycle consists mainly of static losses and dynamic losses. The turn-on loss of the diode is negligible, due to the fact that the forward recovery time t_f and reverse recovery time t_r are both extremely short. Diode on-state loss can be expressed as:

$$P_{\text{Son}}=V_f\int_0^{T}I(t)\,\mathrm{d}t/T=V_fI_{D,avg} \tag{11}$$

where V_f indicates the positive conduction voltage drop.

The turn-off losses of the diode is due to a certain reverse leakage current generated when the diode is turned off, which will lead to energy loss and increase the loss of the diode. The turn-off losses P_{Doff} can be expressed as:

$$P_{\text{Doff}}=K_fU_{rp}f_{sw}t_{rr}\int_0^{T}I(t)\,\mathrm{d}t/T=0.5U_{rp}I_{rp}f_{sw}t_{rr} \tag{12}$$

where U_{rp} and I_{rp} are the reverse peak voltage and current, t_{rr} is the diode reverse recovery time.

The components used in this paper are IRFP460 for MOSFETs and RHRP3060 for diodes. Table V shows the parameters for IRFP460 and RHRP3060 as the datasheets. The operat-

TABLE V
COMPONENT PARAMETERS

Components	Parameters	Values
IRFP460	r_{ds}	0.27 Ω
	t_{on}	18 ns
	t_{off}	110 ns
	t_r	59 ns
	t_f	58 ns
RHRP3060	U_f	1.7 V
	U_{rp}	600 V
	I_{rp}	250 μA
	t_b	18 ns

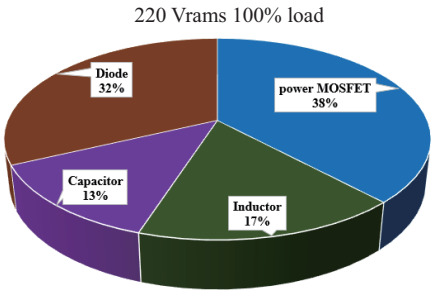

Fig. 7. Loss distribution diagrams at 220 Vrams under rated load.

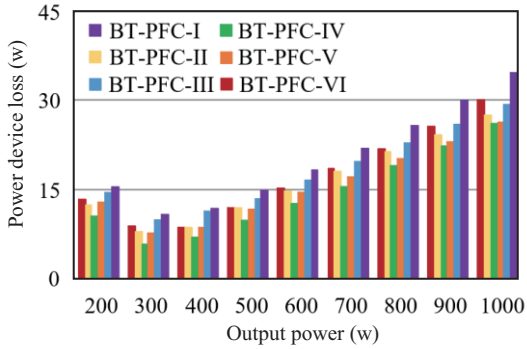

Fig. 8. Comparison of losses of six topological devices proposed under different output powers.

ing frequency is f_{sw}= 20 kHz.

According to (9)–(12), Fig. 7 give the detailed loss distribution diagrams at the rated load of 220 Vrams for the BT-PFC-I. And the comparison of losses among the six topological devices proposed under different output powers is shown in Fig. 8. From Fig. 8, it can be seen that when the output power is 300 W, the losses of each topology device are the lowest. BT-PFC-I has the lowest device loss at each output power, which is mainly related to the number of devices on the current path in each operating mode. Due to the largest number of devices, BT-PFC-I has the highest device loss at each output power.

Fig. 9 shows the efficiency diagrams of various topologies at different output power rates. As can be seen from the Fig. 9, the topology efficiency proposed in this paper is significantly better

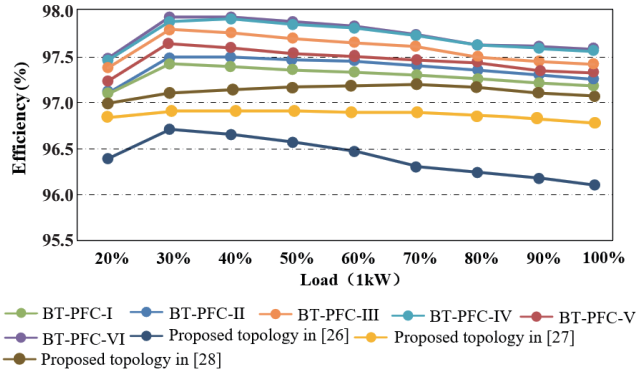

Fig. 9. Efficiency comparison curves at different load conditions.

than that of the traditional clamping topology and the newest three-level circuit [26]–[28], and the efficiency reaches the maximum between 40% and 50%. The optimal efficiency of BT-PFC-VI can reach 97.9%. For the other topologies proposed in this paper, the efficiency of each working condition is more than 97%, and the rated output efficiency is more than 97.3%, demonstrating the superior performance of the proposed topology.

IV. MODULATION SCHEME AND CONTROL STRATEGY

A. Modulation Scheme

The single-phase back-to-back three-level power factor correction converter uses the same-phase carrier wave superimposed SPWM modulation technology to achieve pulse signal distribution. Fig. 10 shows the principle of the SPWM modulation used in this paper. It can be seen from Fig. 10 that the two sets of triangular carriers of equal frequency and amplitude are generated at positive and negative half cycles in the logic selection waveform. The modulating waves in each of the four regions are compared with the triangular carriers in each layer to output three levels, where the modulating waves are divided into four intervals (−1, −1/2], (−1/2,0−], [0+,1/2), [1/2,1).

The expression for the reference signal V_{ref} is as follows:

$$V_{ref} = V_M \sin(2\pi f_M t + \theta) + 2V_C \tag{13}$$

where V_M is the peak value of the modulated and V_C is the peak value of the carrier wave.

The modulation coefficient can be defined as:

$$m = \frac{V_M}{2V_C} \tag{14}$$

The four carrier signals are represented as follows:

$$v_i = \begin{cases} v_1 \in [0.5,1] \\ v_2 \in [0,0.5] \\ v_3 \in [-0.5,0] \\ v_4 \in [-1,-0.5] \end{cases} (i = 1,2,3,4) \tag{15}$$

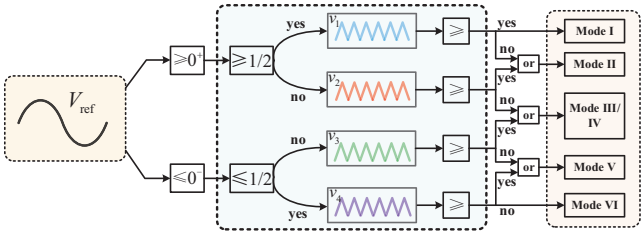

Fig. 10. SPWM modulation schematic.

TABLE VI
SWITCH STATE OF EACH MODULATION STAGE

V_{ref}	S_1	S_2	S_3
$0.5 \leqslant V_{ref} < 1$	OFF	OFF	ON if $V_{ref} < v_1$ OFF if $V_{ref} > v_1$
$0 \leqslant V_{ref} < 0.5$	ON if $V_{ref} < v_2$ OFF if $V_{ref} > v_2$	ON if $V_{ref} < v_2$ OFF if $V_{ref} > v_2$	ON if $V_{ref} > v_2$ OFF if $V_{ref} < v_2$
$-0.5 < V_{ref} \leqslant 0$	ON if $V_{ref} > v_3$ OFF if $V_{ref} < v_3$	ON if $V_{ref} > v_3$ OFF if $V_{ref} < v_3$	ON if $V_{ref} < v_3$ OFF if $V_{ref} > v_3$
$-1 < V_{ref} \leqslant 2$	OFF	OFF	ON if $V_{ref} > v_4$ OFF if $V_{ref} < v_4$

The modulation process of BT-PFC-VI topology can be divided into four stages, and the switching states of each stage are shown in Table VI. In the positive half-cycle, the modulation wave is compared with the dual-layer carrier waves v_1 and v_2 to output modes I, II, and III. When the modulated wave is in the interval [1/2,1), compared with the triangular carrier v_1, if it is greater than the triangular carrier, the mode I signal is output, if it is less than the mode II signal is output; when in the interval [0+, 1/2), compared with the triangular carrier v_2, if it is greater than the triangular carrier, the mode two signal is output, if it is less than the mode III signal is output. In the negative half cycle, the modulated wave is compared with the double-layer carriers v_3 and v_4 in the negative half cycle, and the modes IV, V and VI are output. When the modulated wave is in the interval (−1/2,0−], compared with the triangular carrier v_3, if it is greater than the triangular carrier, the mode IV signal is output, if it is less than the mode V signal is output; in the interval (−1, 2], compared with triangle carrier v_4, if it is greater than triangle carrier, mode V signal will be output, and if it is less than, mode VI signal will be output.

The pulse distribution of the BT-PFC-VI topology is shown in Fig. 11, and the mode selection can be distribution according to the corresponding switch state in Table IV to obtain the three-level waveform. The pulse simulation corresponding to BT-PFC-VI is shown in Fig. 12. It can be seen that the adopted PWM method demonstrates strong versatility and confirms the accuracy of the PWM strategy.

B. Control Strategy

The voltage-current dual closed-loop proportional-integral (PI) control strategy used in this paper is shown in Fig. 13. The voltage outer loop ensures the stability of the output voltage

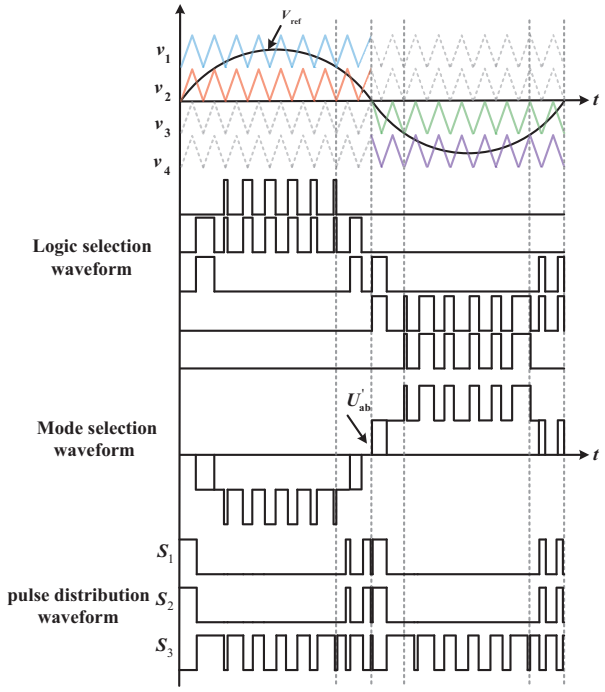

Fig. 11. Schematic diagram of switches pulse distribution.

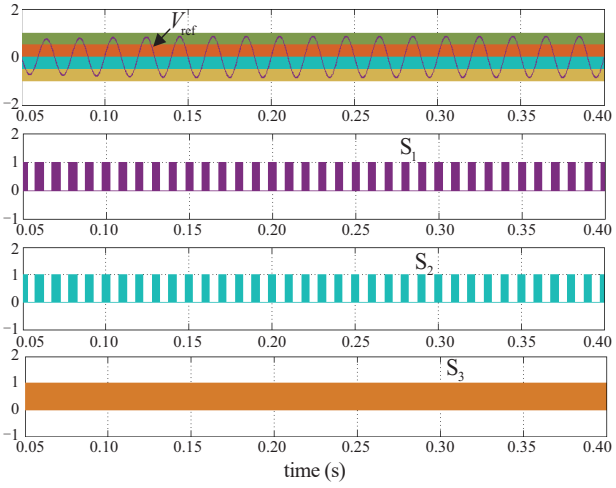

Fig. 12. The simulation diagram of switches pulse distribution.

u_{dc}, acting as the reference for the current inner loop. The difference between u_{dc} and reference value u_{dc}^* is input to the PI controller to create an error signal. This error signal is then adjusted by the phase information of the grid voltage U_s, resulting in the input reference signal i_L^* for the current inner loop. The reference current i_L^* along with the inductance current i_L from the AC side are input into the PI controller as modulation signals, which are compared and modulated alongside a triangular carrier wave to produce a pulse signal.

Considering the delay of sampling and the small signal characteristics of PWM control, Fig. 14 shows the block diagram of the current inner loop controller. $H_c(s)$ is the current inner loop controller, i_s^* is the system input, and u_s is the system disturbance. T_i is the sampling period of the current, k_{pwm} is the equivalent gain of the rectifier, and the time constant of the

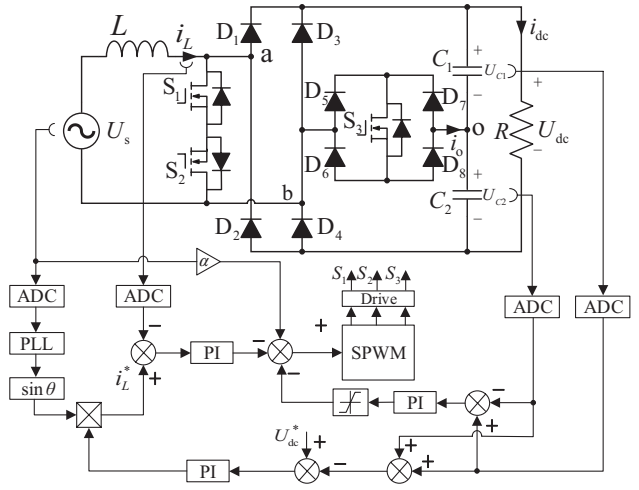

Fig. 13. Control system block diagram.

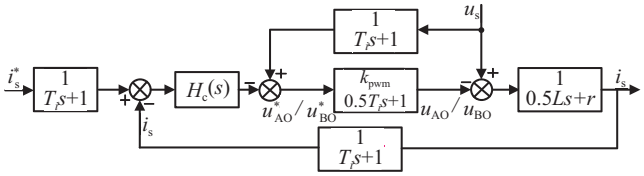

Fig. 14. Block diagram of current loop.

small inertia link caused by PWM modulation is $T_i/2$.

Ignoring the fluctuation of u_s, the transfer function of the PI controller can be written as a zero pole expression as follows:

$$H_c(s) = k_{iP} + \frac{k_{iI}}{s} = \frac{k_{iP}s + k_{iI}}{s} \tag{16}$$

where k_{iP} and k_{iI} are the proportional coefficient and integral coefficient of the current inner loop, respectively.

The open-loop transfer function H_{oi} (s) of the current inner loop is

$$H_{oi}(s) = \frac{k_{pwm}(k_{iP}s + k_{iI})}{s(1.5T_i s+1)(0.5Ls+r)} \tag{17}$$

Further obtaining the current closed-loop transfer function $H_{ci}(s)$ is

$$H_{ci}(s) = \frac{H_{oi}(s)}{1+H_{oi}(s)} = \frac{k_{pwm}k_{iP}s + k_{pwm}k_{iI}}{0.75LT_i s^3 + (1.5rT_i + 0.5L)s^2 + (r + k_{pwm}k_{iP})s + k_{pwm}k_{iI}} \tag{18}$$

The design of the current inner loop needs to consider the tracking speed of the current, adopt the control theory of zero pole cancellation, and ignore the sampling of the current signal. The closed-loop transfer function can be further simplified as

$$H_{ci}(s) = \frac{1}{1+\frac{0.5L}{k_{pwm}k_{iP}}s} \tag{19}$$

The structure of the dual closed-loop control system is shown in Fig. 15, where the voltage outer loop is used to maintain stable output of the DC side voltage, and a reference current in phase with the power supply voltage is obtained through a phase-locked loop as the input of the inner loop.

The expression for the PI controller H_v(s) of the voltage outer loop is as follows:

$$H_v(s) = \frac{k_{vP}s + k_{vI}}{s} \tag{20}$$

where k_{vP} and k_{vI} are the proportional coefficient and integral coefficient of the voltage outer loop, respectively.

The open-loop transfer function $H_{ov}(s)$ of the voltage outer loop control system is obtained as follows:

$$H_{ov}(s) = H_v(s)\cdot H_{ci}(s)\cdot\frac{0.5kR_L}{0.5R_L Cs+1} \tag{21}$$

Therefore, the closed-loop transfer function of the entire circuit topology control loop can be expressed as

$$H_{cv}(s) = \frac{H_{ov}(s)}{1+H_{ov}(s)} \tag{22}$$

The amplitude frequency characteristic curves of the current inner loop and voltage outer loop are shown in Fig. 16. The controller parameters are selected as follows: k_{iP}=9, k_{iI}=1, k_{vP}=0.2 and k_{vI}=3.8. Fig. 16(a) shows the amplitude frequency characteristic curve of the current loop. It can be seen that the open-loop system has a high gain of nearly 50 dB in the low frequency range, so the system can effectively resist external input disturbances. The cutoff frequency of the open-loop system is around 3500 Hz, with a corresponding phase margin of about 50°. The system ensures stability while also considering dynamic performance. The gain and phase of the system in the low-frequency range are both close to 0 dB, indicating that the system can follow the changes of the input reference signal without steady-state error. Fig. 16(b) shows the amplitude frequency characteristic curve of the voltage outer loop. It can be seen that the voltage outer loop system meets the steady-state requirements and has advantages such as large gain in the low frequency range, small static error, and fast system response. It demonstrates excellent dynamic performance and can achieve zero static error control for power frequency signals.

V. Experimental Verifications

In this section, the main experimental results obtained with the BT-PFC-VI are presented. The controller adopts DSP TMS320F28335. Fig. 17 shows the experimental circuit of the BT-PFC-VI, while Table VII details the parameters associated

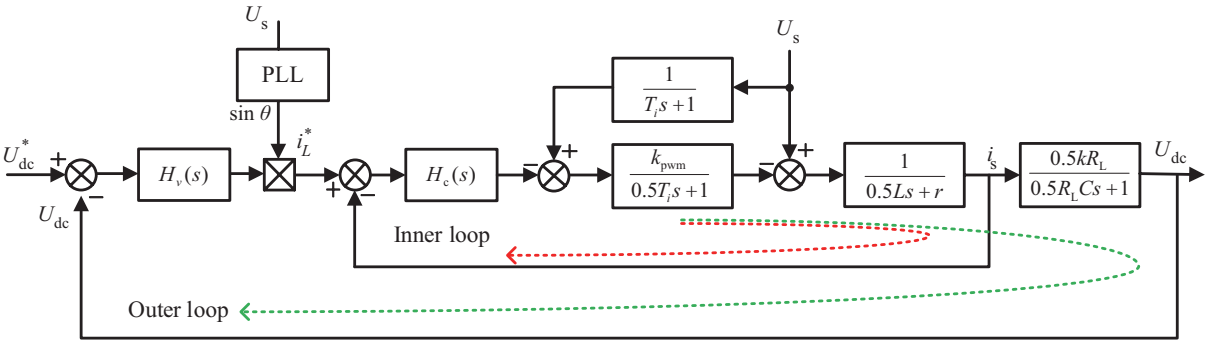

Fig. 15. Block diagram of double-control loop.

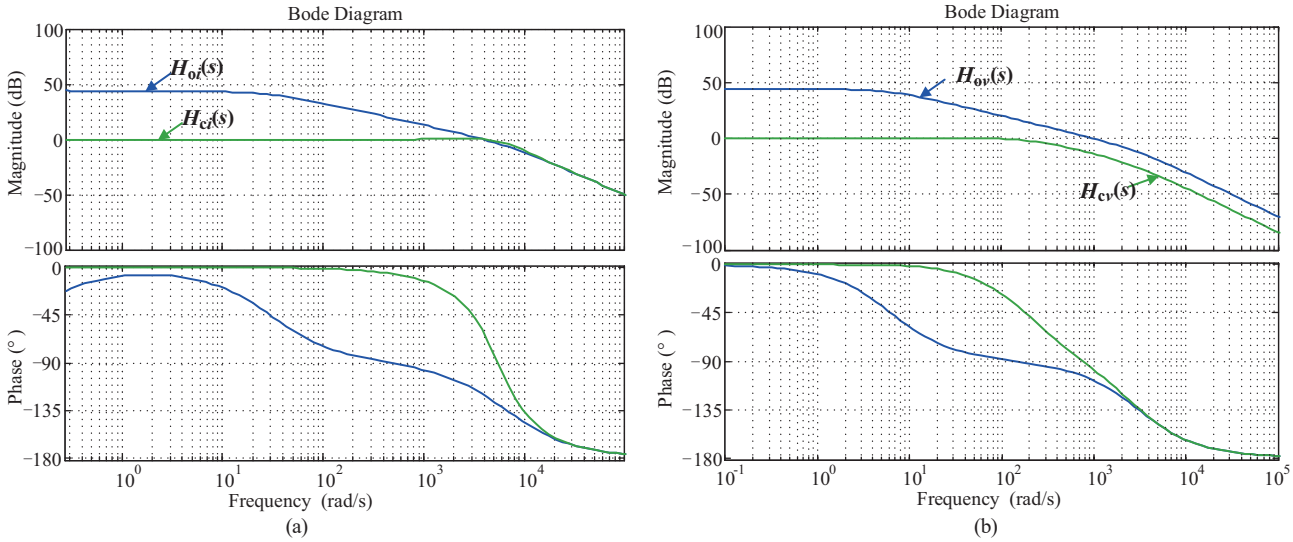

Fig. 16. Amplitude frequency characteristic curve of dual closed-loop controller. (a) Current inner loop. (b) Voltage outer loop.

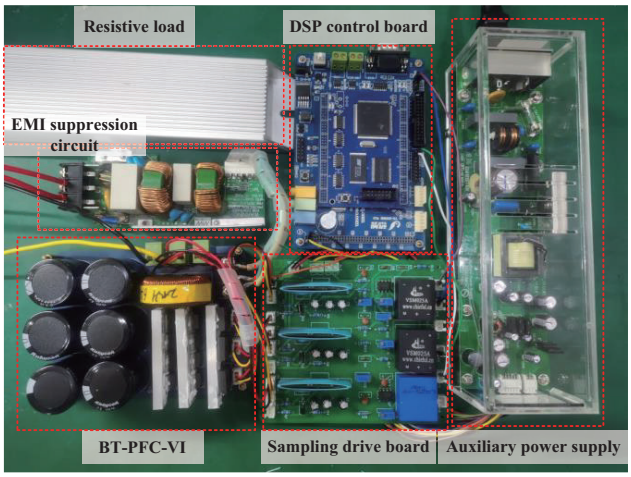

Fig. 17. Experimental prototype platform.

TABLE VII
PARAMETERS OF THE EXPERIMENTAL CIRCUIT

Parameters	Values
Input voltage V_g	200 V
Output voltage V_d	400 V
Grid frequency f_g	50 Hz
Inductor L	2 mH
Capacitors C_1 / C_2	990 μF
Switching frequency f_s	20 kHz
Rated power P_o	1 kW
Diode	RHRP3060
MOSFET	IRFP460
Controller chip	TMS320F28335

with the experimental circuit.

Fig. 18 shows the pulse distributions of switches S_1~S_3, which correspond to Table IV and Fig. 11 and are consistent with the theoretical analysis. The voltage and current experimental waveforms of the BT-PFC-VI topology under stable operation at a rated power of 1 kW are shown in Fig. 19. The grid side voltages and currents and the upper and lower capacitor voltages are shown in Fig. 19(a). It can be seen from Fig. 19(a) that the input voltage us in phase with the input current i_L and meets unity power factor. Fig. 19(b) shows the DC output voltage waveforms and the voltage u_{ab} between the bridge arms a and b. In Fig. 19(b), it can be seen that the voltage between

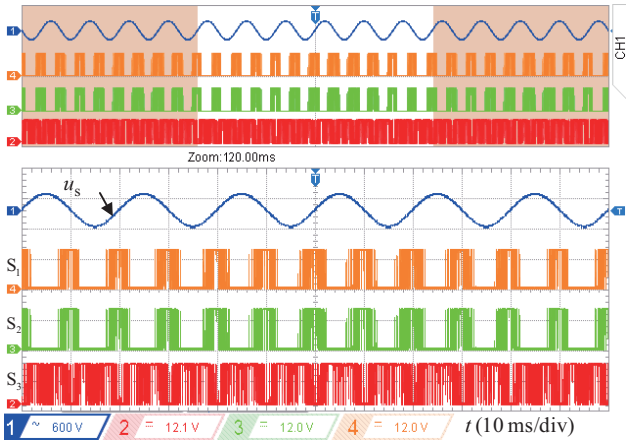

Fig. 18. Switch pulse distribution waveform of BT-PFC-VI.

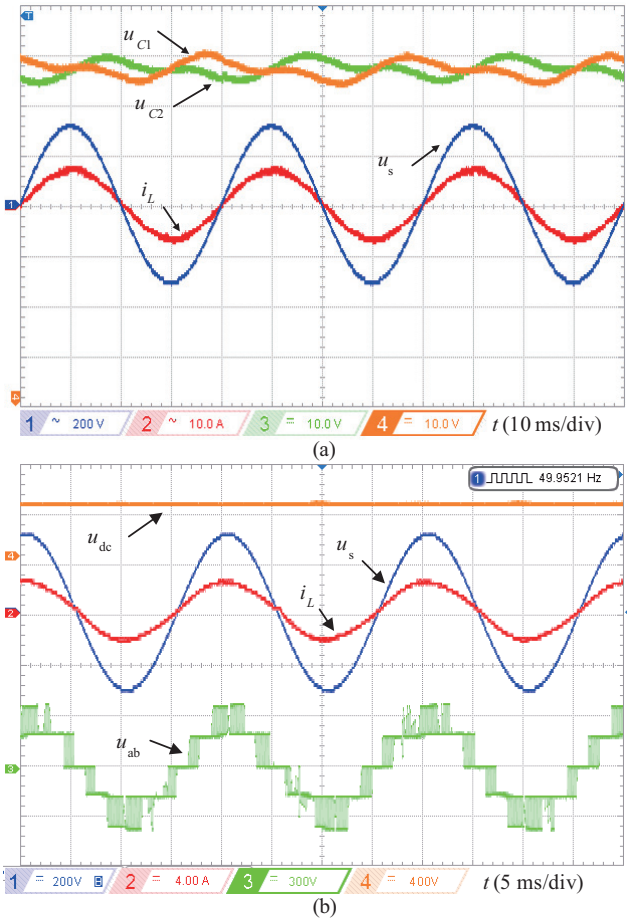

Fig. 19. Voltage and current waveform in steady state. (a) Grid-side voltage and current, and the capacitor voltage u_{C1} and u_{C2}. (b) Input bridge-arm voltage u_{ab}, the DC output voltage u_{dc}.

the two bridge arms conforms to the operating characteristics of the three-level circuit, which is consistent with the theoretical analysis. The DC output voltage u_{dc} is controlled stably at 400 V.

Fig. 20 shows the THD of the BT-PFC-VI topology operating at an output power of 1 kW. As shown in the Fig. 20, the experimental THD is 3.22%, which meets the IEC 6100-3-2 standard (less than 5%). The THD and volume comparison of

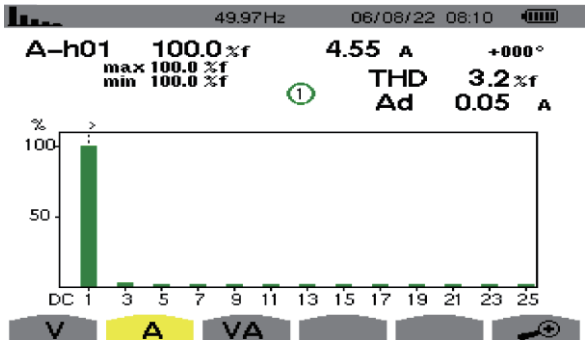

Fig. 20. THD analysis results of BT-PFC-VI circuit.

TABLE VIII
COMPARISON OF THD AND CAPACITY OF THE PROPOSED TOPOLOGY

Topology	THD	Volume
BT-PFC-I	3.40%	Big
BT-PFC-II	3.29%	Small
BT-PFC-III	3.35%	Medium
BT-PFC-IV	3.30%	Small
BT-PFC-V	3.26%	Medium
BT-PFC-VI	3.22%	Medium

six topologies are shown in Table VIII.

The dynamic response of supply current and voltage with switches controlled/uncontrolled is shown in Fig. 21. Fig. 21(a) shows the voltage and current waveforms of the BT-PFC-VI during the process from controllable to uncontrollable. It can be seen from Fig. 21(a) that the current is passed through the diode bridge arm, with serious distortion and high harmonic and the DC output voltage is stable at about 310 V. Fig. 21(b) shows the voltage and current waveforms of the BT-PFC-VI during the process from uncontrollable to controllable. In Fig. 21(b), it can be seen that the input current effectively follows the voltage and the DC side output voltage rises to recover to 400 V.

Fig. 22 shows the waveforms of DC output voltage, split capacitor voltage, and input current when the resistive load on the DC side jumps between 2 kW and the rated 1kW in a steady-state operation of the topology. In Fig. 22(a), it can be seen that the simulation depicts the overload condition where the load transitions from the rated 1 kW to 2 kW, resulting in a brief and small fluctuation in the system. The input current amplitude jumps from 3.4 A to 6.1 A, approximately twice the rated current of the inductor. The capacitor and input voltage remain smoothly transitioning to the rated state without any sudden changes, reaching a new stable state after 0.1 s. As shown in Fig. 22(b), the topology reaches the stable state of 1 kW within 0.1 s when the load decreases from 2 kW to the rated 1 kW, meeting the time requirements for load transitions in the system.

Fig. 23 shows the input and output voltage and current wave forms when the reference voltage on the dc side changes abruptly. As shown in Fig. 23(a), the AC side inductor current

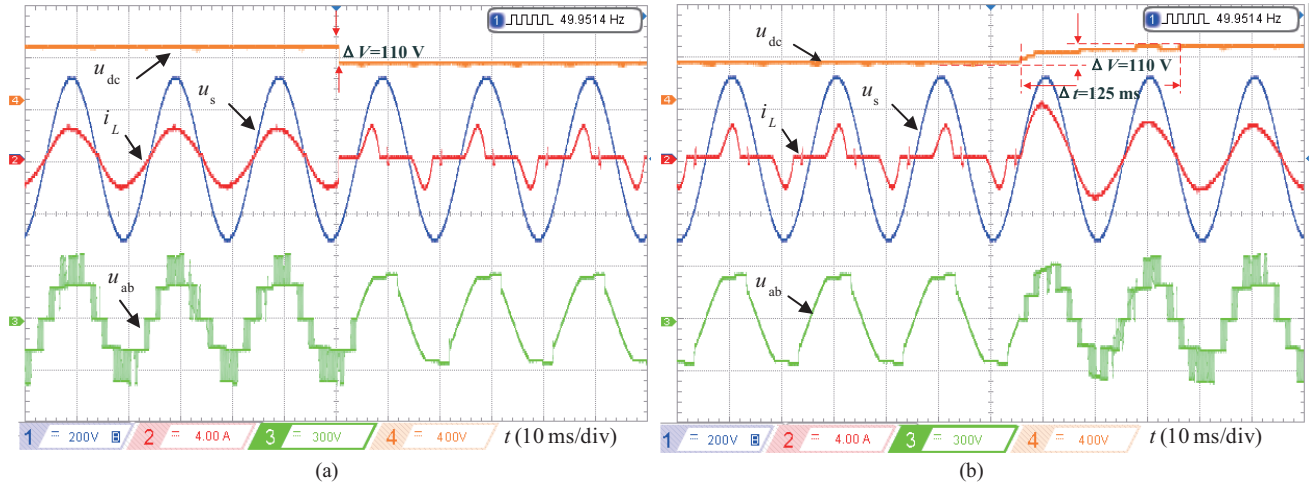

Fig. 21. Dynamic response of supply current and voltage with switches controlled/uncontrolled. (a) Controllable process jump to uncontrollable process. (b) Uncontrolled process jump to controllable process.

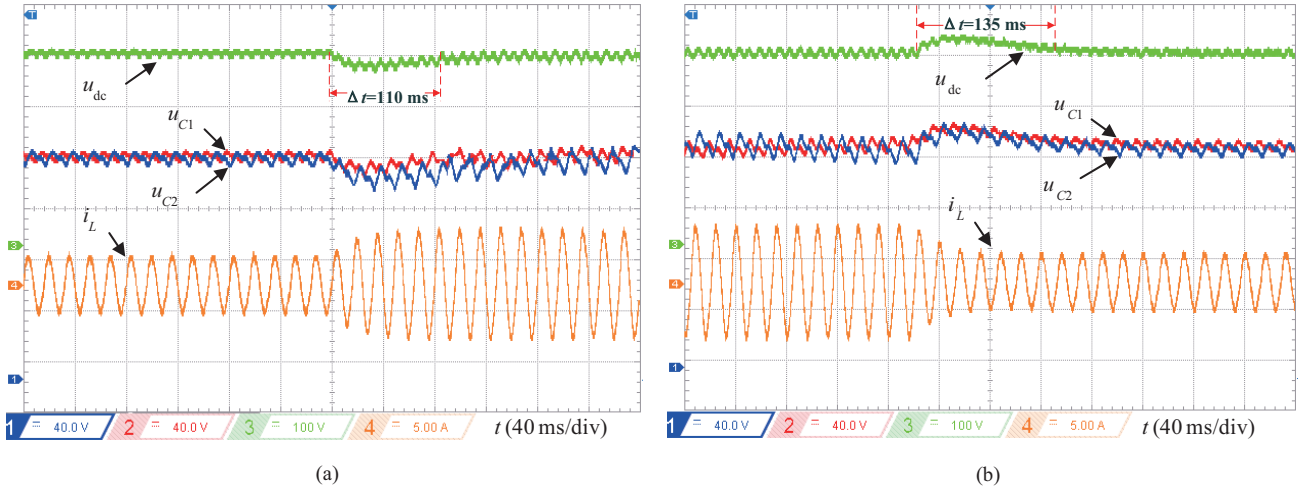

Fig. 22. The dynamic waveforms of load jumping. (a) Experimental results during load jumps from 1 kW to 2 kW. (b) Experimental results during load jumps from 2 kW to 1 kW.

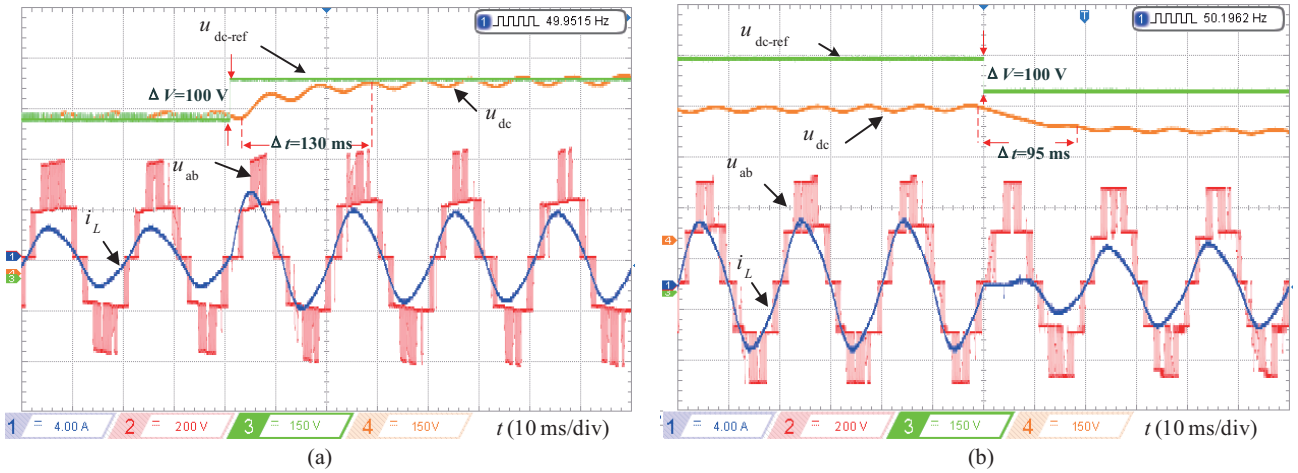

Fig.23 The dynamic waveforms of reference voltage. (a) Experimental results during the reference voltage increases from 400 V to 500 V. (b) Experimental results during the reference voltage increases from 500 V to 400 V.

waveform spikes once and then falls back to a steady state when the reference voltage jumps from 400 V to 500V. The inductor current still maintains a sinusoidal waveform, and the circuit realizes unit power factor correction. The output voltage u_{dc} on the DC side stabilizes at 500 V after a gentle transition of 40 ms. In Fig. 23(b), The input current i_L appears briefly distorted and then recovers the sinusoidal waveform when the DC-side reference voltage drops. The bridge arm voltage satisfies the three-level characteristics and the DC side voltage is stabilized after a 20 ms transition.

VI. Conclusion

A family of single-phase back-to-back three-level power factor correction converters is proposed based on the diode clamp and T-type three-level topology, which can reduce the voltage stress of switch devices. Take the single-phase back-to-back three-level converter(BT-PFC-VI) as an example to explain its circuit topology, operating mode, control and modulation. Finally, an experimental prototype with a rated output of 1 kW/400 V was built. The experimental results demonstrate the feasibility and superiority of the proposed PFC topology.

References

[1] J. Liu, D. Dong, and D. Zhang, "Hybrid modular multilevel rectifier: A new high-efficient high-performance rectifier topology for HVDC power delivery," in *IEEE Transactions on Power Electronics*, vol. 36, no. 8, pp. 8583–8587, Aug. 2021.

[2] H. Cheng, Z. Zhao, and C. Wang, "A novel unidirectional three-phase multilevel rectifier composed of star-connected three single-phase topology based on five-level flying capacitor DC-DC converter," in *IEEE Transactions on Industrial Electronics*, vol. 70, no. 6, pp. 5493–5503, Jun. 2023.

[3] C. Li, J. Hu, and M. Zhao, "Grid-voltages ensorless predictive current control of three-phase PWM rectifier with fast dynamic response and high accuracy," in *CPSS Transactions on Power Electronics and Applications*, vol. 8, no. 3, pp. 269–277, Sept. 2023.

[4] J. Liu, J. K. Motwani, D. Zhang, and D. Dong, "Unidirectional hybrid multilevel rectifier family for MV/HV applications: analysis and comparative evaluation," in *IEEE Transactions on Power Electronics*, vol. 39, no. 3, pp. 1–13, Nov. 2023.

[5] Z. He, H. Ding, Z. Zhang, Z. Chen, Z. Yao, F. Deng, Y. Jiang, and Y. Tang, "Optimized modulation method for three-level boost converter with ZVS under unbalanced-load operation," in *IEEE Transactions on Power Electronics*, vol. 38, no. 11, pp. 13811–13824, Nov. 2023.

[6] J.-S. Kim, S.-H. Lee, W.-J. Cha, and B.-H. Kwon, "High-efficiency bridgeless three-level power factor correction rectifier," in *IEEE Transactions on Industrial Electronics*, vol. 64, no. 2, pp. 1130–1136, Feb. 2017.

[7] K. K, P. K. Kesavan, N. Harischandrappa, and V. B., "Design and laboratory validation of a grid-interfaced totem-pole PFC converter with PR controller and isolated phase modulated converter for solar-powered next-gen EV charging system," in *CPSS Transactions on Power Electronics and Applications*, vol. 10, no. 1, pp. 32–43, Mar. 2025.

[8] M. Pourmahdi, H. Heydari-doostabad, R. Ghazi, and T. O'Donnell, "Buck-Boost common ground bridgeless PFC (CGBPFC) rectifies with positive/negative output," in *IEEE Transactions on Power Electronics*, vol. 37, no. 2, pp. 1272–1282, Feb. 2022.

[9] V. Monteiro, J. C. Ferreira, A. A. Nogueiras Meléndez, and J. L. Afonso, "Model predictive control applied to an improved five-level bidirectional converter," in *IEEE Transactions on Industrial Electronics*, vol. 63, no. 9, pp.5879–5890, Sept. 2016.

[10] H. Ma, K. Zheng, H. Jiang, and H. Yin, "A family of dual-boost bridgeless five-level rectifiers with common-core inductors," in *IEEE Transactions on Power Electronics*, vol. 36, no. 11, pp. 12565–12578, Nov. 2021.

[11] Y. He, H. Liu, J. Zhang, C. Shen, X. Xie, and L. Hang, "A compact single-phase cascaded three-level AC/DC converter with variable DC bus voltage and low CM noise," in *IEEE Transactions on Power Electronics*, vol. 39, no. 1, pp. 398–408, Jan. 2024.

[12] W. A. P. Castiblanco, A. Toebe, and C. Rech, "Five-level switched-capacitor unidirectional rectifier with reduced number of components," in *IEEE Transactions on Power Electronics*, vol. 38, no. 12, pp. 15045–15054, Dec. 2023.

[13] M. Park, J. Baek, Y. Jeong, and G. Moon, "An interleaved totem-pole bridgeless boost PFC converter with soft-switching capability adopting phase-shifting control," in *IEEE Transactions on Power Electronics*, vol. 34, no. 11, pp. 10610–10618, Nov. 2019.

[14] H. Vahedi, A. A. Shojaei, A. Chandra, and K. Al-Haddad, "Five-level reduced-switch-count Boost PFC rectifier with multicarrier PWM," in *IEEE Transactions on Industry Applications*, vol. 52, no. 5, pp. 4201–4207, Sept.-Oct. 2016.

[15] L. Huang, F. Chen, W. Yao, and Z. Lu, "Flexible mode bridgeless Boost PFC rectifier with high efficiency over a wide range of input voltage," in *IEEE Transactions on Power Electronics*, vol. 32, no. 5, pp. 3513–3524, May 2017.

[16] Q. W. Low and L. Siek, "A single-stage dual-output tri-mode ACDC regulator for inductively powered application," in *IEEE Transactions on Circuits and Systems I: Regular Papers*, vol. 66, no. 9, pp. 3620–3630, Sept. 2019.

[17] J. Zhou, J. O. Ojo, F. Tang, J. Haruna, and P. C. Loh, "A carrier-based discontinuous PWM for single and parallel three-level T-type converters with neutral-point potential balancing," in *IEEE Transactions on Industry Applications*, vol. 57, no. 5, pp. 5117–5127, Sept.-Oct. 2021.

[18] D. Wu, M. Sondharangalla, and R. Ayyanar, "Isolated bridgeless PFC converter based on active-clamped SEPIC," in *CPSS Transactions on Power Electronics and Applications*, vol. 7, no. 3, pp. 239–250, Sept. 2022.

[19] F. Guo, Z. Ma, F. Diao, Y. Zhao, P. Wheeler, and Y. Cao, "Hybrid active PWM strategy with dual-mode modulation waves of three-level T-type converter for aircraft turboelectric propulsion systems," in *IEEE Transactions on Industry Applications*, vol. 59, no. 6, pp. 7150–7162, Nov.-Dec. 2023.

[20] V. Dargahi, M. Abarzadeh, K. A. Corzine, J. H. Enslin, A. K. Sadigh, and J. Rodriguez, "Fundamental circuit topology of duo-active-neutral-point-clamped, duo-neutral-point-clamped, and duo-neutral-point-piloted multilevel converters," in *IEEE Journal of Emerging and Selected Topics in Power Electronics*, vol. 7, no. 2, pp. 1224–1242, Jun. 2019.

[21] B. Li, H. Tian, L. Ding, X. Wu, G. J. Kish, and Y. R. Li, "An improved three-level neutral point clamped converter system with full-voltage balancing capability for bipolar low-voltage DC grid," in *IEEE Transactions on Power Electronics*, vol. 38, no. 12, pp. 15792–15803, Dec. 2023.

[22] Z. Liu, Z. Xia, F. Li, G. Wang, and C. Li, "A capacitor voltage precharge method for back-to-back five-level active neutral-point-clamped converter," in *IEEE Transactions on Industrial Electronics*, vol. 68, no. 10, pp. 9277–9286, Oct. 2021.

[23] X. Xu, Z. Zheng, K. Wang, B. Yang, and Y. Li, "A comprehensive study of common mode voltage reduction and neutral point potential balance for a back-to-back three-level NPC converter," in *IEEE Transactions on Power Electronics*, vol. 35, no. 8, pp. 7910–7920, Aug. 2020.

[24] M. Tsai, M. Chao, and P. Cheng, "Control techniques for the back-to-back neutral-point clamped converter in asynchronous operation," in *IEEE Transactions on Power Electronics*, vol. 35, no. 3, pp. 2334–2341, Mar. 2020.

[25] X. Xu, Z. Zheng, K. Wang, B. Yang, and Y. Li, "A carrier-based common-mode voltage elimination method for back-to-back three-level NPC converters," in *IEEE Transactions on Power Electronics*, vol. 37, no. 3, pp. 3040–3052, Mar. 2022.

[26] X. Zhang, G. Tan, X. Wu, Q. Wang, W. Zhang, T. Xia, and T. Shi, "Single-phase three-level PWM rectifier predictive control with fixed switching frequency based on current convex optimization," in *IEEE Transactions on Power Electronics*, vol. 36, no. 10, pp. 12090–12101, Oct. 2021.

[27] H. Ma, Y. Pan, Y. Lu, X. Chen, and Y. Huang, "Research on single-phase three-level pseudo totem-pole rectifiers with a unified pulse-width modulation," in *IEEE Journal of Emerging and Selected Topics in Power*

Electronics, vol. 11, no. 5, pp. 5052–5061, Oct. 2023.

[28] Z. Chen, P. Davari, and H. Wang, "Single-phase bridgeless PFC topology derivation and performance benchmarking," in *IEEE Transactions on Power Electronics*, vol. 35, no. 9, pp. 9238–9250, Sept. 2020.

Hui Ma was born in Kaifeng, Henan Province, China in 1985. He received the Ph.D. degree in Power Electronics from the South China University of Technology, Guangzhou, China, in 2016. He is currently an Associate Professor in the College of Electrical Engineering & New Energy, China Three Gorges University, Yichang. His current research interests include the high-power density rectifiers, multilevel converters, and electric energy.

Guofang Chen was born in xiangyang, Hubei Province, China, in 2001. He received the B.S. degrees in electrical engineering from Yangtze University, Jingzhou, China, in 2023. He is currently pursuing the M.D. degree in the College of Electrical Engineering & New Energy, China Three Gorges University, Yichang, China. His research interest is multilevel converters.

Kun Xiang was born in 1984 and has a M.E. degree. He received the B.S. degree in the College of Electrical Engineering & New Energy, China Three Gorges University, Yichang, China. His main research interests include multilevel converters, grid-connected inverters and renewable energy systems.

Liping Fan was born in 1983. Master's degree in engineering. She received the B.S. degree in the College of Electrical Engineering & New Energy, China Three Gorges University, Yichang, China. Her main research interests include power electronic converters and integrated automation of power system relay protection.

Lei Xi received the M.S. degree in control theory and control engineering from the Harbin University of Science and Technology, and the Ph.D. degree from the School of Electric Power, South China University of Technology, China, in 2016. He is currently an Associate Professor with the College of Electrical Engineering and New Energy, China Three Gorges University. His research interests include load frequency control, artificial intelligence techniques, and automatic generation control.

Yuehua Huang was born in May 1972. He graduated from the Huazhong University of Science and Technology, majoring in electrical machinery and control, in 1994. He is currently a Professor with China Three Gorges University. His major research interests include intelligent control, detection, and automation equipment.

Dual-Layer Control Strategy for Wind-Storage Combined Frequency Regulation Based on Hybrid Energy Storage Lifetime Loss Optimization

Yunlu LI, Guotao SONG, Jinliang HUANG, and Zhouying LIU

Abstract—**With the increasing penetration of renewable energy, the inertia deficiency in power systems has become more severe. Existing wind-storage joint frequency regulation (FR) strategies exhibit significant limitations in coordinated control capability and energy storage system (ESS) lifetime management. To address these challenges, this paper proposes a hierarchical control strategy for coordinated optimization of wind farms (WF) and hybrid energy storage systems (HESS). First, a multi-constraint regulation mechanism is established to dynamically switch power operation curves by assessment of frequency and the operating states of wind turbine generators (WTG) and HESS. Second, a smooth transition algorithm is designed to suppress the frequency secondary drop (FSD) by controlling the dynamic trajectory of power curves. For HESS, a dual-layer optimization framework combining model predictive control (MPC) and fuzzy logic control (FLC) is employed: the upper layer performs rolling optimization of control objectives, while the lower layer utilizes FLC to allocate power between the supercapacitor and the battery, adjust the operation curve, and optimize the battery charging strategy based on the state of charge (SOC) and frequency feedback. Simulation results demonstrate that the proposed strategy reduces frequency deviation by 60%–80% and decreases battery lifetime loss by more than 20% under various operating conditions.**

Index Terms—**Coordinated control, energy storage life optimization, frequency secondary drop, hybrid energy storage, state of charge recovery.**

I. Introduction

UNDER the background of the "dual carbon" goals, efforts are dedicated to constructing a new-type power system dominated by renewable energy, characterized primarily by high-proportion renewable energy integration and power electronic devices (abbreviated as "dual-high") [1]. As the penetration of wind power continues to increase, the grid inertia gradually decreases, and the issue of insufficient FR resources becomes more prominent.

Manuscript received May 03, 2025; revised July 14, 2025; accepted August 06, 2025. Date of publication September 30, 2025; date of current version August 22, 2025. This work was supported in part by Higher Education Discipline Innovation Project under the grant D23005. (*Corresponding author: Yunlu Li.*)

All authors are with Shenyang University of Technology, Liaoning 110870 China (e-mail: liyunlu@sut.edu.cn; sgt@smail.sut.edu.cn; HJL@smail.sut.edu.cn; Lzy0619@smail.sut.edu.cn).

Digital Object Identifier 10.24295/CPSSTPEA.2025.00027

To address the issue of inertia decline, commonly used control methods include power reserve [2] and rotor kinetic energy utilization [3]. Compared to power reserves, utilizing rotor kinetic energy allows the WTG to operate in maximum power point tracking (MPPT) mode, thereby making more efficient use of wind energy. The adaptive adjustment of control parameters based on frequency deviation and rate of change of frequency aims to improve system stability [4], [5]. However, during the rotor speed recovery process, this method leads to insufficient active power, which in turn causes FSD [6]. The method of improving FSD by adjusting WTG output power enhances performance [7], but the fixed control coefficients introduce deviations when responding to different frequency variations. To effectively avoid FSD, a decreasing linear function is designed to control rotor speed recovery [8], [9]. However, the impact of the current rotor speed on the recovery process still needs to be considered.

In recent years, energy storage devices have experienced rapid development in renewable energy power stations. Utilizing the rapid response of supercapacitors and the high energy density of batteries, this progress provides novel approaches to address frequency-related issues [10], [11]. When the load disturbance exceeds the boundary, ESS expands the frequency stability domain [12]. However, due to poor coordination with WTG, the ESS activation speed is slow, resulting in an excessively low minimum frequency point. The coordination of wind-storage FR is enhanced by limiting torque in combination with a dual-layer MPC [13]. However, its performance is not optimal under large load disturbances. In [14], [15], optimized power allocation between wind turbines and ESS through MPC effectively improved wind-storage coordination, yet failed to consider ESS lifespan and economic performance.

During battery charging and discharging processes, SOC is closely related to lifetime loss. Maintaining SOC within the 60%–80% range typically helps extend battery longevity [16]. In [17], a coordinated control strategy for WTG and HESS was proposed, leveraging supercapacitors' rapid response characteristics to deliver low-latency, high-efficiency FR. However, this method neglected the influence of SOC on battery lifetime loss. The author uses a WF and ESS coordinated frequency support strategy based on a state machine algorithm [18], which keeps the SOC between 70% and 80%. Nevertheless, the strategy suppressed ESS frequency support capability due to excessive

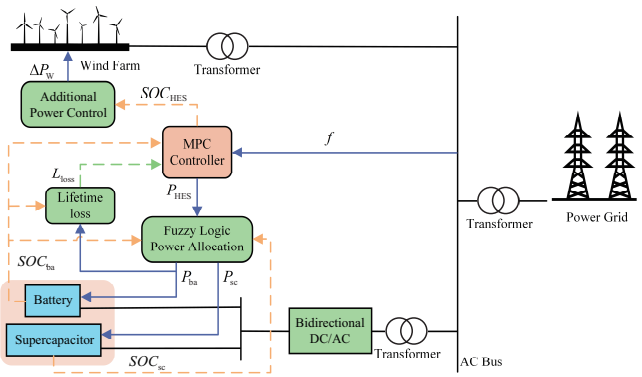

Fig. 1. Overall structure of the wind-storage joint system.

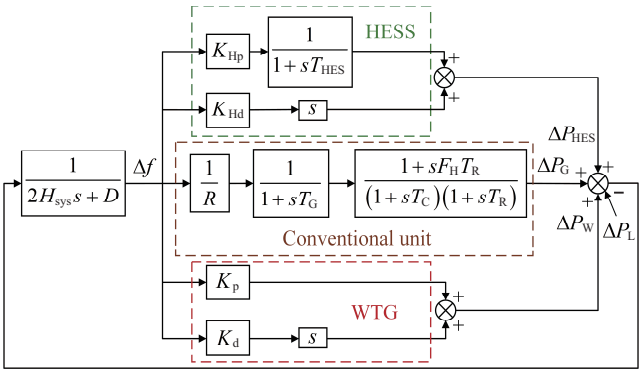

Fig. 2. Frequency response model.

adaptive feedback power. Furthermore, by using a droop control curve to set the exchange power for SOC recovery and maintaining SOC at a higher level, both SOC recovery and FR occur simultaneously, which interferes with the frequency response performance [19]. In [20], adaptive power is provided for SOC recovery to maintain SOC at specific levels between 50% and 80%. The author enhances the coordination between the WF and ESS through a dual-layer control strategy and optimizes the SOC recovery process to minimize power purchase costs [21]. However, maintaining the SOC at 50% overlooks the impact of this operating condition on battery lifespan degradation.

In summary, this paper proposes a novel coordinated FR strategy that integrates WF and HESS, addressing key challenges in inertia deficiency, battery lifespan degradation, and dynamic coordination. Different from traditional methods that treat frequency control and battery health separately, the proposed method achieves adaptive, closed-loop optimization across multiple control layers. The main contributions are as follows:

1) This paper, for the first time, introduces a dynamic switching mechanism of WTG power curves based on the SOC, overcoming the limitations of traditional fixed control curves. By adjusting power output according to real-time operating conditions, the proposed method effectively suppresses abrupt changes in electromagnetic power and mitigates the FSD, reducing frequency deviation by more than 60%.

2) A novel dual-layer FR control framework combining MPC and FLC is proposed. The upper-layer controller enables dynamic adjustment of multi-objective optimization, while the lower-layer controller achieves precise power allocation between the supercapacitor and the battery. This approach surpasses conventional single-layer or empirical rule-based control strategies, realizing a coordinated optimization of control performance and battery lifetime, with a reduction in lifetime degradation exceeding 20%.

3) A closed-loop SOC recovery mechanism is proposed that feeds back multi-cycle SOC deviation into a dedicated frequency domain, enabling the system to dynamically adjust charging commands and gradually restore SOC to its target range. This feedback mechanism enhances system sustainability across long-term FR operations, which is rarely addressed in existing literature.

The remainder of this paper is as follows. Section II introduces the frequency response characteristics. Section III improves the wind turbine's inertia control. Section IV introduces the HESS control strategy. Section V verifies the proposed strategy.

II. Frequency Response Characteristics

The overall structure of the wind-storage coordinated FR system is illustrated in Fig. 1. In this framework, ΔP_{W} denotes the additional active power of the WTG; f represents the grid frequency; L_{loss} is the battery lifetime loss coefficient. SOC_{HES}, SOC_{ba}, and SOC_{sc} denote the SOC of the HESS, battery, and supercapacitor, respectively, while P_{HES}, P_{ba}, and P_{sc} correspond to their respective power outputs. The MPC controller optimizes the power command based on the grid frequency and HESS status, and the output is distributed between the battery and supercapacitor through the FLC. The SOC is further fed back to the additional power control loop to dynamically adjust the output of the WTG.

To investigate the frequency response characteristics of wind-storage hybrid systems, a model is established, as shown in Fig. 2. $\Delta f(s)$, ΔP_{L}, ΔP_{G}, and ΔP_{HES} represent frequency deviations, load power fluctuations, traditional unit power fluctuations, and HESS power fluctuations, respectively; K_{d} and K_{p} denote the wind turbine inertia coefficient and droop coefficient; H_{sys} represents the grid equivalent inertia constant; D corresponds to the grid equivalent damping coefficient; K_{Hd} and K_{Hp} specify the HESS inertia coefficient and droop coefficient; $1/R$ signifies the unit regulation power coefficient of conventional units.

$G_1(s)$ represents the transfer function of the conventional unit:

$$G_1(s)=\frac{1}{1+sT_{\mathrm{G}}}\frac{1+sF_{\mathrm{H}}T_{\mathrm{R}}}{(1+sT_{\mathrm{C}})(1+sT_{\mathrm{R}})} \tag{1}$$

$$G_2(s)=\frac{1}{1+sT_{\mathrm{HES}}} \tag{2}$$

where T_{G}, F_{H}, T_{R}, T_{C}, and T_{HES} denote the time constant of the

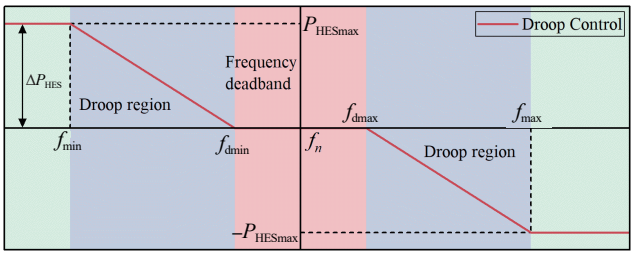

Fig. 3. Traditional control strategy of HESS.

thermal power unit, the reheater gain, the reheat time constant, the turbine time constant, and the HESS response time constant, respectively.

From Fig. 2, the frequency response analytical expression of the system is obtained as:

$$\Delta f(s)=\frac{-\Delta P_{\mathrm{L}}}{(2H_{\mathrm{sys}}+K_{\mathrm{d}}+K_{\mathrm{Hd}})s+D+K_{\mathrm{p}}+K_{\mathrm{Hp}}G_2+\dfrac{1}{R}G_{\mathrm{I}}} \tag{3}$$

It can be observed that increasing K_{d} and K_{Hd} are equivalent to increasing the equivalent inertia constant of the power grid, while increasing K_{p} and K_{Hp} corresponds to increasing the equivalent damping coefficient of the power grid in (3).

When a power imbalance ΔP_{L} occurs, the initial rate of change of frequency is determined by the system's inertia. Neglecting the initial influence of damping control, the rate of change of frequency can be expressed as:

$$\frac{\mathrm{d}\Delta f}{\mathrm{d}t}=-\frac{\Delta P_{\mathrm{L}}}{2H_{\mathrm{sys}}+K_{\mathrm{d}}+K_{\mathrm{Hd}}} \tag{4}$$

where $\mathrm{d}\Delta f/\mathrm{d}t$ is the rate of change of frequency.

By applying the final value theorem to analyze the power system under a load disturbance ΔP_{L}, the steady-state frequency deviation Δf can be expressed as:

$$\Delta f=\lim_{s\to 0}s\Delta f(s) \tag{5}$$

$$\Delta f=\frac{R}{1+(K_{\mathrm{p}}+K_{\mathrm{Hp}}+D)R}\Delta P_{\mathrm{L}} \tag{6}$$

According to (4)–(6), the rate of change of frequency and frequency deviation are directly proportional to the load disturbance and inversely proportional to the equivalent inertia coefficient and equivalent damping coefficient.

III. Inertial Response and Optimal Control of Wind-Storage Combined System

A. Inertia Response Phase

WTGs typically operate in MPPT control mode to capture as much mechanical power as possible. The mechanical power captured under this mode, denoted as P_{MPPT}, is expressed as:

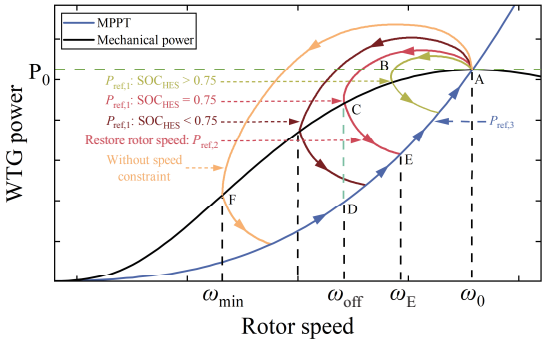

Fig. 4. Power variation curve of the wind turbine generator.

$$\begin{cases}P_{\mathrm{MPPT}}(\omega)=k_{\mathrm{opt}}\omega_{\mathrm{r}}^{\ 3}\\ k_{\mathrm{opt}}=0.5\rho\pi R^2C_{\mathrm{pmax}}\left(R/\lambda_{\mathrm{opt}}\right)^3\end{cases} \tag{7}$$

where P_{MPPT} is the mechanical power; k_{opt} is the maximum power coefficient; ω_{r} is the rotor speed; ρ is the air density; R is the rotor radius; C_{pmax} is the maximum wind energy utilization coefficient, and λ_{opt} is the optimal tip speed ratio.

Before the system experiences a disturbance, the WTG operates stably at point A (as shown in Fig. 4). When a disturbance occurs, the WTG begins to absorb or release rotor kinetic energy, exhibiting an equivalent inertia response. This dynamic process can be expressed as:

$$J\omega_{\mathrm{r}}\mathrm{d}\omega_{\mathrm{r}}/\mathrm{d}t=P_{\mathrm{MPPT}}-P_{\mathrm{e}} \tag{8}$$

where J is the moment of inertia, and P_{e} is the electromagnetic power.

As analyzed in the previous section, by adjusting the inertia and droop coefficients, the inertial response and damping characteristics of conventional synchronous generators can be emulated. At this time, the WTG output active power is:

$$P_{\mathrm{ref,1}}=P_{\mathrm{MPPT}}+\Delta P_{\mathrm{W}} \tag{9}$$

$$\Delta P_{\mathrm{W}}=K_{\mathrm{d}}\,\mathrm{d}\Delta f/\mathrm{d}t+K_{\mathrm{p}}\Delta f \tag{10}$$

The HESS typically employs an inertia-droop integrated control strategy (as shown in Fig. 3) to leverage its fast FR capability, where $[f_{\mathrm{dmin}},f_{\mathrm{dmax}}]$ represents the frequency deadband.

$$\Delta P_{\mathrm{HES}}=K_{\mathrm{Hd}}\,\mathrm{d}\Delta f/\mathrm{d}t+K_{\mathrm{Hp}}\Delta f \tag{11}$$

In the inertia response phase of conventional wind-storage coordinated systems, inertia and droop coefficients are typically tuned to reduce $\mathrm{d}\Delta f/\mathrm{d}t$ and Δf. However, this tuning process often neglects the operational safety of the WTG and the HESS. To address this, this paper incorporates WTG rotor speed and HESS SOC constraints into the coefficient tuning process, effectively preventing the rotor speed from dropping to the F-point and triggering generator tripping. Additionally, the power operation curve is dynamically adjusted based on the HESS state (as shown in Fig. 4), thereby enhancing the coordination and operational safety of the wind-storage system.

$$\begin{cases} K_{\mathrm{d}} = \dfrac{2}{0.04 + \mathrm{e}^{-m_1|\mathrm{d}\Delta f/\mathrm{d}t|}}(\omega^2 - \omega_{\min}^2)\eta \\ K_{\mathrm{p}} = (\dfrac{1}{\delta}\dfrac{1}{1+e^{-m_2|\Delta f|}}\dfrac{\omega_{\mathrm{r}}^2 - \omega_{\min}^2}{\omega_{\max}^2 - \omega_{\min}^2})\eta \end{cases} \tag{12}$$

where δ is the wind turbine adjustment coefficient; $\omega_{\min}$ and $\omega_{\max}$ are the minimum and maximum rotational speeds of the WTG; m_1 and m_2 are the adjustment coefficients.

The coefficient m_1 in (12) is determined based on the rotor time constant of the WTG to ensure the smoothness of the inertia response process and to avoid abrupt changes that exceed the mechanical system's response capability. The design of coefficient m_2 takes into account the filtering characteristics and actuator delays in the control system, thereby ensuring the accurate execution of control commands. The specific values of both coefficients are obtained through simulation tests under various disturbance scenarios, aiming to achieve an optimal balance between fast dynamic response and control stability.

η is the control coefficient determined based on the feedback SOC information:

$$\eta = 1 + \alpha\frac{SOC_{\mathrm{ref}} - SOC}{SOC_{\max} - SOC_{\min}} \tag{13}$$

where α is the adjustment coefficient, and SOC_{ref} is the target value.

The adjustment coefficient α in (13) regulates the active power output of the WTG by modulating the coefficient η, ensuring that the output power weight η undergoes significant changes when the SOC deviates from its target value. This enables effective regulation of the HESS state while avoiding excessive impact on system frequency stability. The value of α is determined based on the SOC-lifetime characteristic curve provided by the battery manufacturer, such that the system's frequency response capability appropriately decreases when the SOC approaches its boundary. Through simulation analyses under various disturbance scenarios for different α values, the optimal parameter is selected to ensure good control performance and robustness under multiple operating conditions.

B. Power Optimization During Rotor Speed Recovery Phase

According to (9), when the WTG exits FR, its output power instantly decreases by ΔP_{W} (corresponding to C-D in Fig. 4) and switches back to the MPPT mode, entering the rotor speed recovery phase. This results in a power deficit and induces the FSD phenomenon.

This paper improves the power curve during the rotor speed recovery process (C-E-A in Fig. 4). According to [22], the condition for speed recovery is:

$$|\omega_{\mathrm{r}}(t+T) - \omega_{\mathrm{r}}(t)| \leqslant 4 \times 10^{-7}\ \text{p.u.} \tag{14}$$

(14) describes the key characteristic point during the inertia response process of the WTG, where the rotor speed decreases to a minimum value and then begins to recover. At this moment, the rate of change of rotor speed $\mathrm{d}\omega_{\mathrm{r}}/\mathrm{d}t \approx 0$, indicating that the rotor speed tends to stabilize and reach its lowest point. This marks the end of the inertia release stage, and the system enters the rotor speed recovery phase. This criterion is consistent with the dynamic characteristics of the inertia response of the WTG.

If the rotor speed of the WTG satisfies (14), it can be determined that the system has entered the speed recovery phase. At this point, the reference power is given by:

$$P_{\mathrm{ref},2} = P_{\mathrm{ref},1}(t_{\mathrm{off}})\exp\left[-\left(\frac{\omega_{\mathrm{r}}\left(t - t_{\mathrm{off}}\right)}{\mu\omega_{\mathrm{off}}}\right)^2\right] \tag{15}$$

In (15), ω_{off} and t_{off} represent the rotor speed and time at the point of rotor speed convergence, respectively, and μ is the adjustment coefficient.

Finally, when the power curve reaches point E in Fig. 4, $P_{\mathrm{ref},2} = P_{\mathrm{MPPT}}(\omega_{\mathrm{E}})$. Subsequently, the WTG restores the rotor speed along the MPPT curve (E-A in Fig. 4). At this stage, the output reference power is:

$$P_{\mathrm{ref},3} = P_{\mathrm{MPPT}}(\omega) = k_{\mathrm{opt}}\omega_{\mathrm{r}}^3\omega_{\mathrm{r}} > \omega_{\mathrm{E}} \tag{16}$$

IV. Coordinated Optimization of Battery Lifetime and Frequency Regulation

A. Battery Lifetime Loss Model

The HESS studied in this paper mainly consists of batteries and supercapacitors, with supercapacitors having a longer lifespan compared to batteries. And its lifespan can be considered constant over a certain planning horizon [23].

The remaining lifespan of the battery is primarily reflected in its effective capacity. When the capacity degrades to 80% of its rated value, it is considered the end of its lifespan [24]. The calculation formula for the throughput method is:

$$E_{\mathrm{thr}} = \frac{2\sum_{i=1}^{n} E_{\mathrm{ba}} DOD_i N_i}{n} \tag{17}$$

where E_{thr} is the average total energy throughput; E_{ba} is the rated capacity of the battery; DOD_i is the depth of discharge for the i-th test; N_i is the total number of cycles for the i-th test; n is the total number of tests conducted.

The lifetime loss coefficient L_{loss} can be used to measure the degree of battery lifetime loss:

$$L_{\mathrm{loss}} = E_{\mathrm{loss}} / E_{\mathrm{thr}} \tag{18}$$

where E_{loss} is the energy throughput of the battery in cycle T.

In the actual charging and discharging process of the battery, operating at a low SOC increases its energy throughput. Therefore, the equivalent energy throughput of the battery can be expressed as [25]:

$$f\left[SOC(t)\right]=\begin{cases}1.3 & 0<SOC(t)<0.5\\ -1.5SOC(t)+2.05 & 0.5\leqslant SOC(t)\leqslant 1\end{cases} \tag{19}$$

$$E_{\text{loss}}=\int_0^T\left|P_{\text{ba}}(t)\right|f\left[SOC(t)\right]\mathrm{d}t \tag{20}$$

where $P_{\text{ba}}(t)$ is the charge and discharge power value of the battery at time t, and $f[SOC(t)]$ is the energy throughput weight factor associated with the SOC.

B. Upper-Layer MPC Frequency Regulation Strategy

The dynamic frequency model of the power grid is given by:

$$\dot{f}=\frac{\Delta P}{2H}f_0=\frac{-P_{\text{L}}+P_{\text{G}}+P_{\text{W}}}{2H}f_0 \tag{21}$$

where $\dot{f}$ is the actual frequency of the power grid; P_{G} is the active power of the traditional unit; P_{W} is the active power of the WTG, and f_0 is the rated frequency of the power grid.

By applying the Euler method, (21) can be discretized as:

$$f(k+1)=f(k)+\frac{T_{\text{S}}f_0}{2H}P_{\text{HES}}(k)+\frac{T_{\text{S}}f_0}{2H}\Delta P(k) \tag{22}$$

where T_{S} is the discrete-time constant; k represents the time step of control, and $P_{\text{HES}}(k)=P_{\text{ba}}(k)+P_{\text{sc}}(k)$.

Without considering the charging and discharging efficiency of batteries and supercapacitors and losses of converters, the discrete equation is:

$$\begin{cases}SOC_{\text{ba}}(k+1)=SOC_{\text{ba}}(k)-\dfrac{T_{\text{S}}P_{\text{ba}}(k)}{E_{\text{ba}}}\\ SOC_{\text{sc}}(k+1)=SOC_{\text{sc}}(k)-\dfrac{T_{\text{S}}P_{\text{sc}}(k)}{E_{\text{sc}}}\end{cases} \tag{23}$$

where E_{sc} is the rated capacity of the supercapacitor.

The HESS system is predominantly composed of high-capacity batteries; thus, the overall SOC of the HESS is primarily determined by the SOC of the battery. Consequently, (23) can be uniformly expressed as:

$$SOC_{\text{HES}}(k+1)=SOC_{\text{HES}}(k)-\frac{T_{\text{S}}P_{\text{HES}}(k)}{E_{\text{HES}}} \tag{24}$$

where E_{HES} is the total rated capacity of HESS, $E_{\text{HES}}=E_{\text{ba}}+E_{\text{sc}}$.

According to (18)–(20), the discrete equation for battery lifetime loss can be expressed as:

$$L_{\text{loss}}(k+1)=L_{\text{loss}}(k)+\frac{T_{\text{S}}f\left[SOC_{\text{HES}}(k)\right]\left|P_{\text{ba}}(k)\right|}{E_{\text{thr}}} \tag{25}$$

The HESS must satisfy the following constraints:

$$\begin{cases}SOC_{\text{HESmin}}\leqslant SOC_{\text{HES}}\leqslant SOC_{\text{HESmax}}\\ -P_{\text{HESmax}}\leqslant P_{\text{HES}}\leqslant P_{\text{HESmax}}\end{cases} \tag{26}$$

where SOC_{HESmin} and SOC_{HESmax} represent the minimum and maximum SOC of the HESS, respectively, and P_{HESmax} is the maximum power of the HESS.

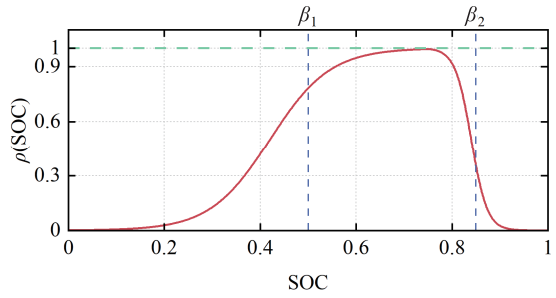

Fig. 5. Frequency regulation capability function.

During frequency fluctuation suppression, the SOC of the HESS directly affects its FR capability and lifespan. To ensure charging margin, the SOC target is set to 75% in this paper. Based on this, an FR capability function, $\rho(SOC)$, is proposed to describe the relationship between SOC and FR capability.

$$\rho(SOC)=\begin{cases}1-\dfrac{1}{1+e^{-r_1(\beta_1-SOC)}} & 0<SOC\leqslant 0.75\\ 1-\dfrac{1}{1+e^{-r_2(SOC-\beta_2)}} & 0.75<SOC\leqslant 1\end{cases} \tag{27}$$

where r_1 and r_2 represent the smoothing coefficients.

The selection of r_1 and r_2 is based on the transition slopes of the weighting function near β_1 and β_2, combined with simulation tuning. This design ensures that the weighting function rapidly decreases when the SOC approaches the boundaries, while maintaining continuity and smoothness, thereby avoiding severe fluctuations or numerical instability in the control system.

Fig. 5 shows that when the SOC is within the $[\beta_1, \beta_2]$ range, the HESS exhibits stronger FR ability. When SOC $<\beta_1$, discharging accelerates battery lifespan degradation, the WTG output should be increased; when SOC $>\beta_2$, insufficient charging headroom compromises the battery's health. Based on this, ρ(SOC) is incorporated into the MPC objective function as a weighting coefficient.

$$\begin{aligned}J=\min\Bigg[&\sum_{i=1}^{p}\left(1-\rho\left(SOC_{\text{HES}}(k)\right)\right)\left(SOC_{\text{HES}}(k+i)-SOC_{\text{ref}}\right)^2+\\ &\sum_{i=1}^{p}\rho\left(SOC_{\text{HES}}(k)\right)\left(f(k+i)-f_0\right)^2+\\ &\lambda\sum_{i=1}^{p}E_{\text{loss}}\left(k+i\right)^2+\gamma\sum_{i=1}^{p}\left(\frac{P_{\text{HES}}(k+i)}{P_{\text{HESrata}}}\right)^2\Bigg]\end{aligned} \tag{28}$$

where P_{HESrate} is the rated power of the HESS; λ and γ are the weighting coefficients, and p represents the prediction horizon.

C. Lower-Level Dynamic Power Allocation Optimization Strategy for HESS

In practical systems, to prolong the lifespan, the filter time constant is typically adjusted via SOC feedback to avoid over-

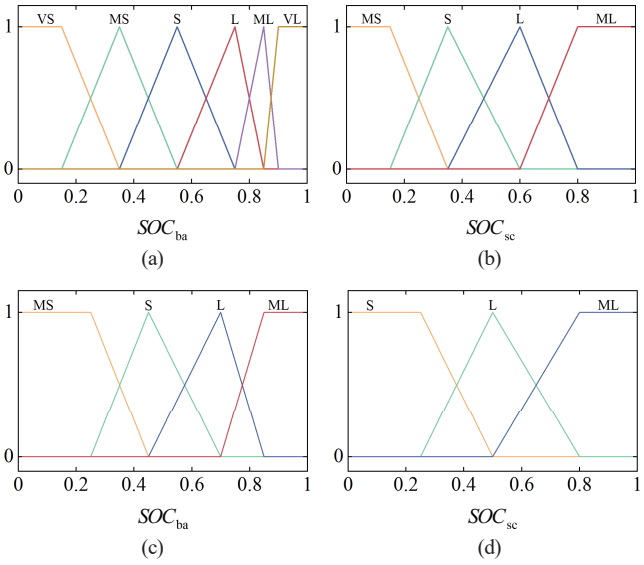

Fig. 6. Membership function of input. (a) SOC_{ba} during discharge. (b) SOC_{sc} during discharge. (c) SOC_{ba} during discharge. (d) SOC_{sc} during discharge.

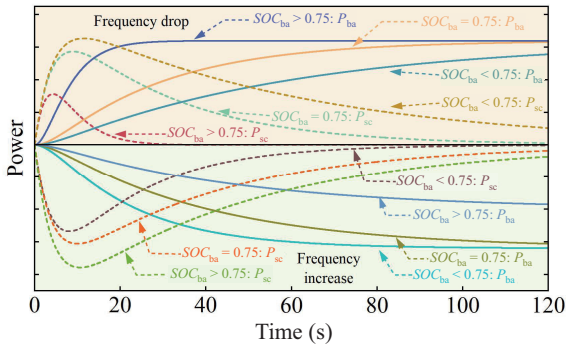

Fig. 7. HESS power operation curve.

charging and over-discharging [26]. The FLC can control the system by converting the SOC differences into corresponding control variables through preset logical rules [27]. Based on this approach, the membership functions of the fuzzy controller are established, as shown in Fig. 6.

The transfer function of the first-order high-pass is given by:

$$H_{high}(s) = s / (1+T_S) \tag{29}$$

where T is the filter time constant.

The cutoff frequency f_c is:

$$f_c = 1 / (2\pi T) \tag{30}$$

The system operates in two conditions based on grid frequency: discharge and charge. By adjusting the cutoff frequency, high-frequency power is allocated to the supercapacitor, while low-frequency power with a longer time scale is assigned to the battery. This enables real-time switching of the HESS operation curve, as illustrated in Fig. 7.

The FR control strategy process for the wind-storage hybrid system proposed in this paper is shown in Fig. 8.

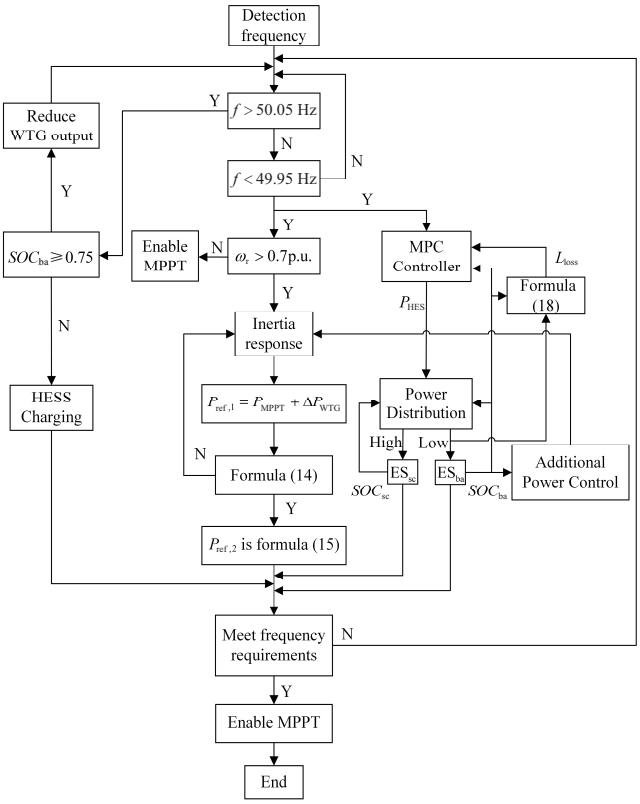

Fig. 8. FR flowchart of the wind-storage joint system.

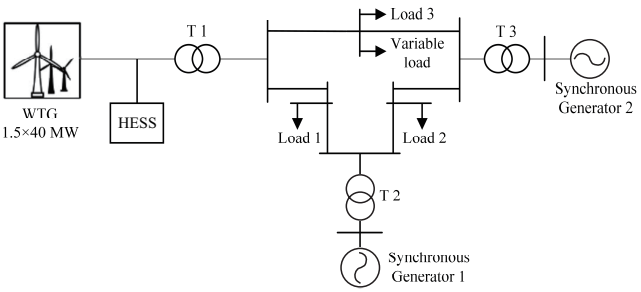

Fig. 9. The outline of the test system.

V. Case Analysis

In this study, a wind-storage hybrid system model, as shown in Fig. 9, was built in MATLAB/Simulink to verify the effectiveness of the proposed strategy. The model includes a wind turbine unit, two synchronous generator units, a HESS, a variable load, and three loads with a total capacity of 250 MW. Detailed parameters of the system are listed in Table I.

A. Effectiveness Analysis of the Improved Wind Turbine Frequency Regulation Strategy

To demonstrate the FR effect, this section compares four strategies under the conditions of a rated wind speed of 10 m/s and load disturbances of 0.1 p.u., 0.15 p.u., and 0.25 p.u. at 10 seconds: MPPT, traditional fixed coefficient control, adaptive coefficient control, and the proposed optimization power curve

TABLE I
SYSTEM PARAMETERS

	Parameter	Value	Unit
WTG	Quantity	40	unit
	Rated power	1.5	MW
	Inertia constant	5	s
Battery	Rated capacity	2	MWh
	Initial SOC	75	%
Supercapacitor	Rated capacity	0.5	MWh
	Initial SOC	75	%
Synchronous machine	Quantity	2	unit
	Rated power	100	MW

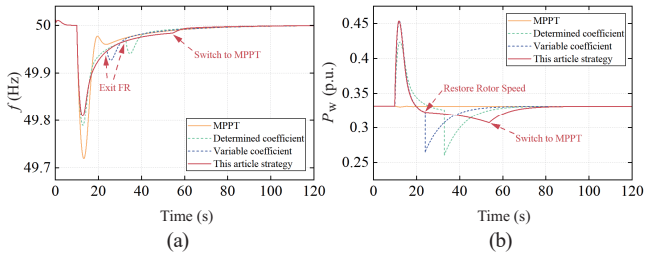

Fig. 10. Comparison results under 0.1 p.u. load disturbance. (a) Grid frequency. (b) WTG power.

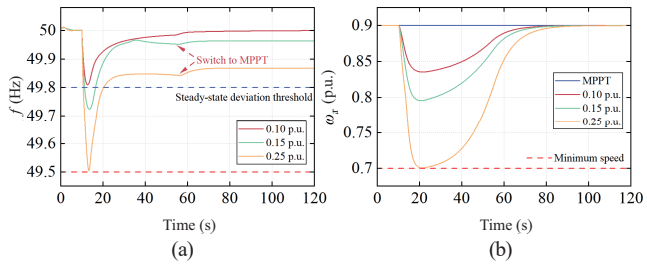

Fig. 11. Comparison results under 0.1–0.25 p.u. load disturbance. (a) Grid frequency. (b) WTG rotor speed.

control strategy for suppressing FSD.

Fig. 10 illustrates that under a 0.1 p.u. load disturbance, the proposed control strategy utilizes WTG's FR capability more effectively than other strategies, raising the minimum grid frequency to 49.81 Hz and increasing the peak WTG electromagnetic power to 0.45 p.u. Additionally, during the speed recovery process, it smooths the decline in WTG electromagnetic power, thereby preventing the FSD phenomenon and maintaining a minimum value of 0.3 p.u., which is more than 15.4% higher than that of other strategies.

As seen in Fig. 11, under a 0.25 p.u. load disturbance, the proposed control strategy can still effectively ensure that the system frequency remains within a safe threshold. However, after the wind turbine generator fully responds to the FR demand, the rotor speed drops to the minimum value (0.7 p.u.), indicating that the FR capability has reached its limit. When the load disturbance exceeds 0.25 p.u., the FR capability of

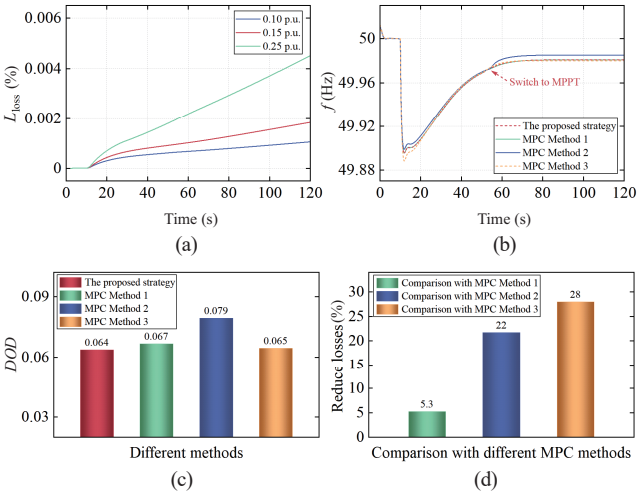

Fig. 12. Comparison results of system parameters. (a) Lifetime loss. (b) Grid frequency. (c) DOD. (d) Method comparison.

the wind turbine alone can no longer meet the system's FR requirements. In such cases, the fast response capability of the HESS is needed to provide additional frequency support when large load disturbances occur.

B. Coordinated Output Analysis of Wind-Storage System under HESS Lifespan Optimization

To verify the effectiveness of the HESS in optimizing lifespan and assisting wind turbine FR, this study compares four MPC strategies under a 0.15 p.u. step load disturbance:

MPC Method 1, a multi-objective optimization strategy without a power allocation mechanism; MPC Method 2, which optimizes for frequency stability at 50 Hz only; MPC Method 3, which implements the MPC control strategy from [28], maintaining the SOC at 50% while assisting the WTG in FR; The proposed strategy, an improved multi-objective optimization strategy that introduces a dynamic power allocation mechanism and adaptively adjusts weight coefficients.

The data in Fig. 12(a) show that as the load increases, the battery's lifetime loss gradually rises from 0.001% to 0.004%. Particularly under high-load disturbances, the battery undertakes more FR tasks, accelerating capacity degradation. Therefore, it is necessary to balance the battery's power during the FR process to reduce excessive battery usage.

At 10 s, a 0.15 p.u. step load disturbance occurs. Simulation results (as shown in Figs. 12(b) and 13) demonstrate that, compared to the baseline scenario without HESS configuration, all four MPC strategies can improve the system's lowest frequency point by over 60%, with a faster dynamic response. Compared to the proposed strategy, while the MPC Method 2 slightly improves the minimum frequency point, the peak discharge power of the battery reaches 0.57 p.u., an increase of 26.6%, which accelerates battery degradation. MPC Method 3, with ESS SOC maintained around 50%, leads to increased lifetime loss, with the loss curve rising to 0.0025%. In contrast, the proposed strategy reduces the growth of lifetime loss by

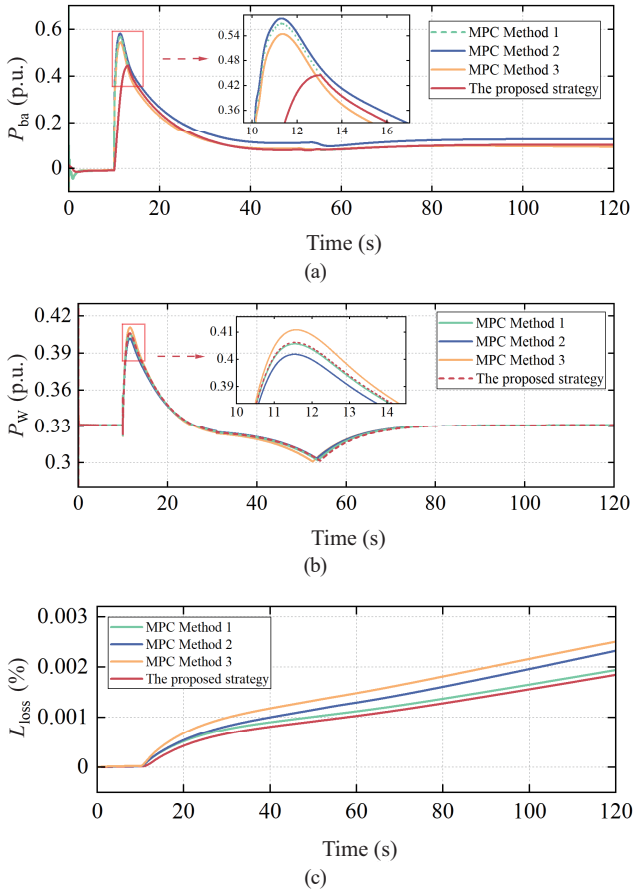

Fig. 13. Comparison of parameter variations. (a) Battery power. (b) WTG power. (c) Lifetime loss.

allocating high-frequency power to the supercapacitor, keeping the battery output peak below 0.45 p.u.

A comparison of the HESS DOD and lifetime loss across the four MPC strategies, as illustrated in Figs. 12(c) and (d) lead to the following conclusions: The proposed control strategy can reduce the battery's DOD to a maximum of 19% compared to the other three MPC methods. Compared to MPC Method 1, the proposed strategy can reduce battery lifetime loss by approximately 5.3%; compared to MPC Method 2, it can reduce it by approximately 22%; and compared to MPC Method 3, it can reduce it by approximately 28%.

C. Analysis of Frequency Response and Battery Lifespan Optimization under Different Scenarios

In practical operation, the SOC of the HESS will continuously fluctuate. If the optimization strategy proposed in this paper is not implemented, the SOC may rise to 90% or drop close to 20%, significantly weakening its FR capability. Therefore, it is essential to restore the SOC to the target range [21]. Given the stochastic nature of daily load fluctuations, this section sets up six simulation scenarios (as shown in Table II) to verify the effectiveness of HESS frequency response and lifespan optimization under different initial SOCs and random load fluctuations (as shown in Fig. 14).

TABLE II
SIMULATION SCENARIO

Scenario	Initial SOC	MPC Method	Load Disturbance/p.u.
1	20%	The proposed strategy	−0.15~0.25
2	20%	MPC method 2	−0.15~0.25
3	40%	The proposed strategy	−0.15~0.25
4	40%	MPC method 2	−0.15~0.25
5	75%	The proposed strategy	−0.15~0.25
6	90%	The proposed strategy	−0.15~0.25
7	90%	MPC method 2	−0.15~0.25
8	50%	MPC method 3	−0.15~0.25

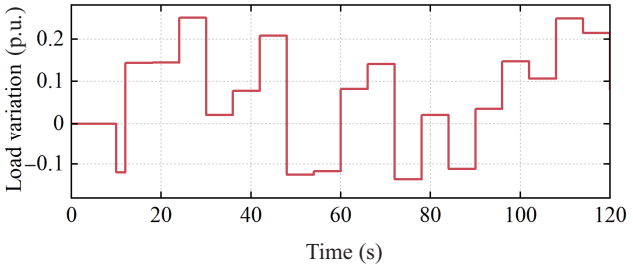

Fig. 14. Load variation.

As shown in Figs. 15(a) and 15(c)–(d), the frequency deviation in all six scenarios meets the grid requirements. The detailed analysis is as follows:

In Scenarios 1 and 2, the HESS operates under an extremely low SOC condition, with an initial value of 20%. When a sudden load increase occurs, the proposed multi-objective optimization strategy dynamically adjusts the power trajectories of both the WTG and HESS, thereby enhancing the utilization of the wind turbine's rotational kinetic energy. In contrast, MPC Method 2 does not modify the power curve, resulting in increased HESS output. During the load reduction phase, the control strategy in Scenario 1 maintains constant WTG output while prioritizing HESS charging, resulting in a lower frequency peak compared to Scenario 2.

Compared to Scenarios 3 and 4, the lower initial SOC in Scenario 1 leads to a more pronounced effect of the control strategy. In Scenario 6, the HESS starts with a higher SOC and is therefore capable of handling a larger share of the FR task, which reduces the need to extract kinetic energy from the WTG rotor. However, during the load shedding stage, as the SOC approaches saturation, the control strategy stabilizes the frequency by reducing the WTG output, resulting in a 60% increase in the frequency peak relative to Scenario 1. In Scenarios 4 and 7, due to the adoption of single-objective optimization in the MPC controller, the frequency response characteristics of both scenarios are nearly identical. In contrast, Scenarios 5 and 8 incorporate SOC-tracking constraints, enabling dynamic power allocation between the HESS and WTG. Nevertheless, due to a lower initial SOC in Scenario 8, its charging power is significantly higher than that in Scenario 5.

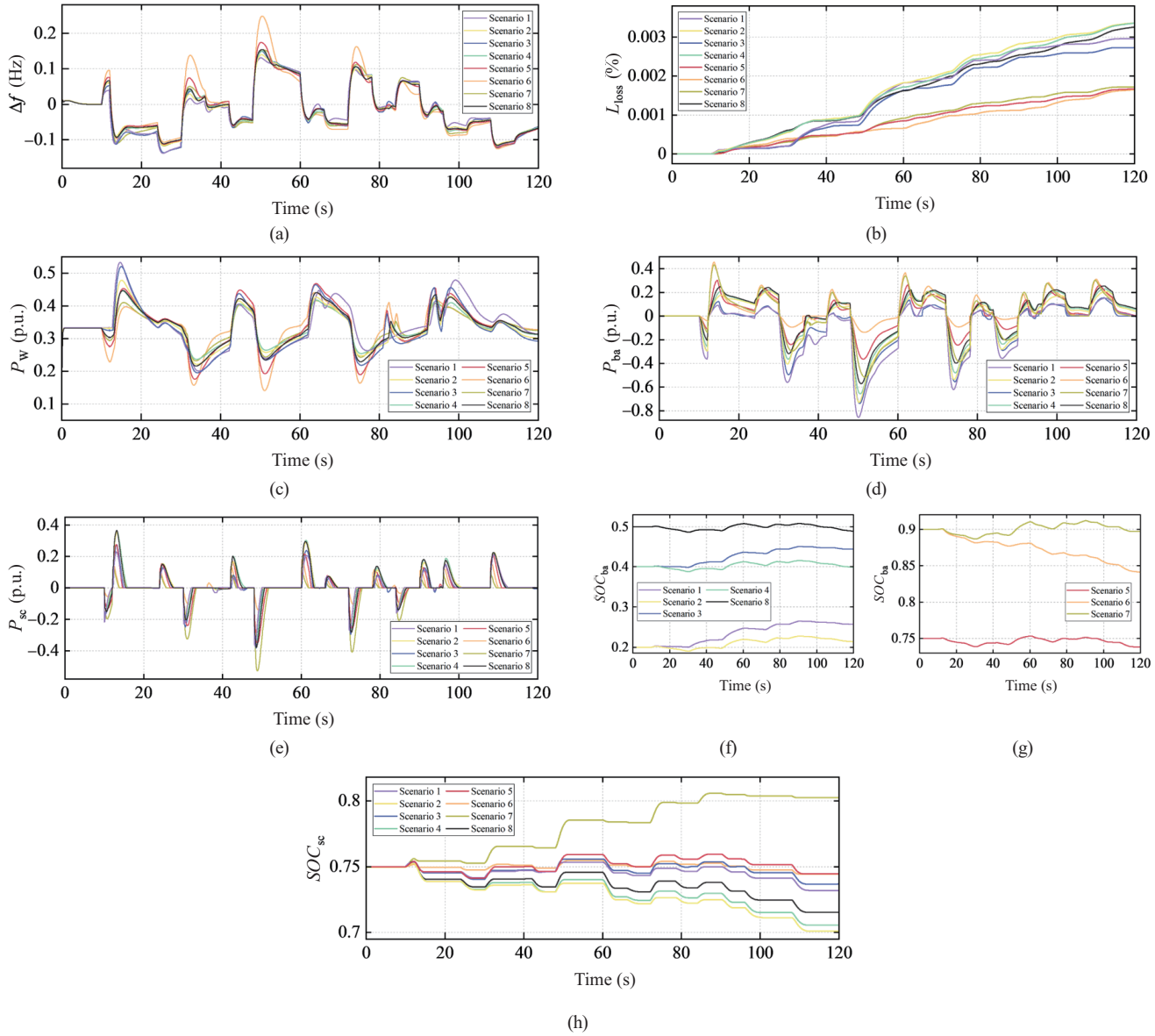

Fig. 15. Comparison results under different scenarios. (a) Frequency deviation. (b) Lifetime loss. (c) WTG power. (d) Battery power. (e) Supercapacitor power. (f) Battery SOC. (g) Battery SOC. (h) Supercapacitor SOC.

Figs. 15(b)–(e) present a detailed analysis of battery lifetime loss under six scenarios as follows:

Compared to Scenario 2, Scenario 1 reduces battery lifetime degradation by approximately 13% through switching the power trajectories between the HESS and WTG, and by dynamically adjusting the cutoff frequency based on the FLC, thereby enhancing the supercapacitor's ability to respond to high-frequency power components. Due to the higher initial SOC in Scenario 3, its lifetime loss is reduced by 8% and 20% compared to Scenarios 1 and 4, respectively. In Scenario 5, the HESS consistently operates in a high SOC range, resulting in an additional 33% reduction in lifetime loss compared to Scenario 3. Although Scenario 6 also maintains a high SOC level, it releases more power to reserve charging capacity, increasing the energy throughput.

During the frequency response process, Scenario 6 actively increases power output to restore SOC during frequency drops, whereas Scenario 7 fails to effectively reduce charging power during frequency rises, resulting in slightly higher lifetime loss than Scenario 6. Although Scenario 8 incorporates SOC constraints, it operates under a persistently low SOC range, leading to significant lifetime loss. In contrast, the optimized strategy adopted in Scenario 5 significantly improves the SOC operating range, reducing battery lifetime loss by up to 43%.

Figs. 15(c)–(h) illustrate that, compared to Scenario 2, Scenario 1 dynamically coordinates the power output between the HESS and WTG based on the SOC level, reducing the discharge power of the HESS while increasing its charging power. Meanwhile, the FLC optimizes power allocation according to the SOC difference between the battery and supercapacitor, enabling the SOC to be restored to the target level and thereby preparing the system for subsequent FR tasks. Compared to

Scenarios 3 and 4, Scenario 1 starts with a lower initial SOC and exhibits a faster recovery rate.

In the comparison between Scenarios 6 and 7, Scenario 6 adjusts the cutoff frequency during the frequency drop phase, allowing the battery to supply more power while the supercapacitor primarily suppresses high-frequency components. During the frequency rise phase, the WTG output is reduced, and the HESS halts charging, facilitating the restoration of SOC to its target level. Both Scenarios 5 and 8 adopt a dual-layer control strategy that maintains the SOC near the target value.

VI. Conclusions

Based on an in-depth analysis of the causes of FSD and the mechanisms of battery lifetime loss, this paper proposes a novel coordinated control strategy. The key conclusions are as follows:

1) A multi-state constraint-based mechanism is introduced to dynamically switch the WTG power curve in real time. The study reveals that FSD amplitude is not only affected by control parameters but is also closely related to rotor speed. By optimizing the power trajectory, the proposed method effectively suppresses FSD and reduces frequency deviation by 60%–80% compared with conventional methods.

2) A dual-layer FR control framework based on MPC and FLC is developed. The upper-layer MPC optimizes power commands by jointly considering frequency deviations and HESS states, while the lower-layer FLC allocates power between the battery and supercapacitor based on their SOC differences. This strategy leverages the complementary characteristics of the battery and supercapacitor, reducing battery lifetime degradation by over 20% and maintaining SOC within a healthy range.

3) To address the limitation of traditional methods where strict SOC constraints hinder subsequent FR tasks, a SOC recovery mechanism oriented toward multi-cycle FR is proposed. This approach feeds SOC deviations back into the control loop, gradually restoring the battery state to ensure that the HESS can continuously and reliably participate in FR tasks.

References

[1] X. Xie, J. He, H. Mao, and H. Li, "New issues and classification of power system stability with high shares of renewables and power electronics," in *Proceedings of the CSEE*, vol. 41, no. 2, pp. 461–475, Jan. 2021.

[2] A. Zertek, G. Verbic, and M. Pantos, "A novel strategy for variable-speed wind turbines' participation in primary frequency control," in *IEEE Transactions on Sustainable Energy*, vol. 3, no. 4, pp. 791–799, Oct. 2012.

[3] A. B. T. Attya and T. Hartkopf, "Control and quantification of kinetic energy released by wind farms during power system frequency drops," in *IET Renewable Power Generation*, vol. 7, no. 3, pp. 210–224, May 2013.

[4] Y. Zhou, D. Zhu, X. Zou, C. He, J. Hu, and Y. Kang, "Adaptive temporary frequency support for DFIG-based wind turbines," in *IEEE Transactions on Energy Conversion*, vol. 38, no. 3, pp. 1937–1949, Sept. 2023.

[5] H. Lao, L. Zhang, P. Song, T. Zhao, and L. Zou, "Wind power sustained frequency regulation strategy with dynamic optimized state recovery behavior," in *Power System Technology*, vol. 44, no. 12, pp. 4504–4512, Dec. 2020.

[6] Z. Zhang, P. Kou, Y. Zhang, and D. Liang, "Coordinated predictive control of offshore DC collection grid and wind turbines for frequency response: A scheme without secondary frequency drop," in *IEEE Transactions on Sustainable Energy*, vol. 14, no. 3, pp. 1488–1503, Jul. 2023.

[7] Y. Tang, P. Yang, and Y. Yang, "Frequency response control strategy of wind turbines considering frequency secondary drop," in *Automation of Electric Power Systems*, vol. 47, no. 9, pp. 166–174, May 2023.

[8] K. Liu, Y. Qu, H. -M. Kim, and H. Song, "Avoiding frequency second dip in power unreserved control during wind power rotational speed recovery," in *IEEE Transactions on Power Systems*, vol. 33, no. 3, pp. 3097–3106, May 2018.

[9] D. Yang, Y. Xu, H. Gao, T. Zheng, and E. Jin, "Self-adaptive frequency control scheme of a doubly-fed induction generator with smooth rotor speed recovery," in *Power System Protection and Control*, vol. 50, no. 6, pp. 172–179, Mar. 2022.

[10] C. Liang, P. Wang, X. Han, W. Qin, Y. Jia, and T. Yuan, "Battery energy storage selection based on a novel intermittent wind speed model for improving power system dynamic reliability," in *IEEE Transactions on Smart Grid*, vol. 9, no. 6, pp. 6084–6094, Nov. 2018.

[11] S. Chen, T. Zhang, H. B. Gooi, R. D. Masiello, and W. Katzenstein, "Penetration rate and effectiveness studies of aggregated BESS for frequency regulation," in *IEEE Transactions on Smart Grid*, vol. 7, no. 1, pp. 167–177, Jan. 2016.

[12] J. Liu, S. Zhu, P. Liu, and P. Wu, "Coordinated control strategy for wind turbine and energy storage equipment considering system frequency safety and stability constraints," in *Power System Protection and Control*, vol. 52, no. 1, pp. 73–84, Jan. 2024.

[13] Y. Zhu, Q. Shi, S. Cai, Z. Wei, and H. Zang, "Wind-storage joint frequency modulation and power optimization allocation based on two-dimensional dynamic load and two-layer MPC," in *Electric Power Automation Equipment*, vol. 44, no. 8, pp. 1–8, Aug. 2024.

[14] T. Dong, B. Zhai, X. Li, Q. Yang, Y. Lin, X. Chen, and J. Wen, "Optimal control strategy for combined wind-storage system to participate in frequency response," in *Power System Technology*, vol. 46, no. 10, pp. 3980–3989, Oct. 2022.

[15] L. Yu, P. Kou, Y. Feng, and H. Feng, "Model predictive control strategy for combined wind-storage system to participate in frequency response," in *Automation of Electric Power Systems*, vol. 43, no. 12, pp. 36–43, Jun. 2019.

[16] A. A. Adeyemo and O.T. Amusan, "Modelling and multi-objective optimization of hybrid energy storage solution for photovoltaic powered off-grid net zero energy building," in *Journal of Energy Storage*, vol. 55, no. Part. A, pp. 105273, Nov. 2022.

[17] T. Rahimi, L. Ding, M. Kheshti, R. Faraji, J. M. Guerrero, and G. D. A. Tinajero, "Inertia response coordination strategy of wind generators and hybrid energy storage and operation cost-based multi-objective optimizing of frequency control parameters," in *IEEE Access*, vol. 9, pp. 74684–74702, 2021.

[18] J. Tan and Y. Zhang, "Coordinated control strategy of a battery energy storage system to support a wind power plant providing multi-timescale frequency ancillary services," in *IEEE Transactions on Sustainable Energy*, vol. 8, no. 3, pp. 1140–1153, Jul. 2017.

[19] P. Iurilli, C. Brivio, and M. Merlo, "SoC management strategies in Battery Energy Storage System providing Primary Control Reserve," in *Sustainable Energy Grids & Networks*, vol. 19, pp. 100230, Sept. 2019.

[20] C. Jamroen and S. Sirisukprasert, "A voltage regulation strategy with state of charge management using battery energy storage optimized by a self-learning particle swarm optimization," in *Computers and Electrical Engineering*, vol. 101, pp. 108103, Jul. 2022.

[21] M. Pei, Q. Wang, L. Ye, Y. Luo, L. Sha, Z. Zhang, and X. Song, "Hierarchical control strategy of wind-storage frequency support for SOC recovery optimization and arbitrage revenue," in *Applied Energy*, vol. 365, pp. 123229, Jul. 2024.

[22] J. Zhao, M. Li, X. He, and R. Zhu, "Coordinated control strategy of wind power and energy storage in frequency regulation based on torque limit control," in *Transactions of China Electrotechnical Society*, vol. 34, no. 23, pp. 4982–4990, Dec. 2019.

[23] A. Berrueta, A. Ursúa, I. S. Martín, A. Eftekhari, and P. Sanchis, "Supercapacitors: electrical characteristics, modeling, applications, and future trends," in *IEEE Access*, vol. 7, pp. 50869–50896, 2019.
[24] J. Li, Z. Zhang, B. Shen, Z. Gao, D. Ma, P. Yue, and J. Pan, "The capacity allocation method of photovoltaic and energy storage hybrid system considering the whole life cycle," in *Journal of Cleaner Production*, vol. 275, pp. 122902, Dec. 2020.
[25] C. Liu, X. Wang, X. Wu, and J. Gou, "Economic scheduling model of microgrid considering the lifetime of batteries," in *IET Generation, Transmission & Distribution*, vol. 11, no. 3, pp. 759–767, Feb. 2017.
[26] J. Dang, J. Seuss, L. Suneja, and R. G. Harley, "SOC feedback control for wind and ESS hybrid power system frequency regulation," in *2012 IEEE Power Electronics and Machines in Wind Applications*, Denver, CO, USA, 2012. pp. 1–7.
[27] S. Zhang, Y. Mishra, and M. Shahidehpour, "Fuzzy-logic based frequency controller for wind farms augmented with energy storage systems," in *IEEE Transactions on Power Systems*, vol. 31, no. 2, pp. 1595–1603, Mar. 2016.
[28] D. Cirio, F. Conte, B. Gabriele, C. Gandolfi, S. Massucco, M. R. Rapizza, and F. Silvestro, "Fast frequency regulation from a wind farm-BESS unit by model predictive control: Method and hardware-in-the-loop validation," in *IEEE Transactions on Sustainable Energy*, vol. 14, no. 4, pp. 2049–2061, Oct. 2023.

Yunlu Li received the B.S. in electronic information engineering from Shenyang University of Technology in 2009, the M.S. degree in control engineering in 2011, and Ph.D degree in power electronics and drives from Northeastern University in 2017, Shenyang, China. He worked as a post-doc researcher in Shenyang University of Technology from 2017 to 2019. He worked as a guest researcher at the department of energy technology in Aalborg University, Denmark from 2018 to 2019. He is currently a associate professor in school of electrical engineering with Shenyang University of Technology, Shenyang, China.

His research interests include data-driven modeling of power system, renewable energy generation technology.

Guotao Song was born in 1999. He is currently studying Electrical Engineering at Shenyang University of Technology, pursuing the M.S. degree. His research direction is the optimization control of wind-storage combined frequency regulation.

Jinliang Huang was born in 1999. He is currently studying Electrical Engineering at Shenyang University of Technology, pursuing the M.S. degree. His research direction is microgrid modeling and renewable energy grid integration.

Zhouying Liu was born in 2001. She is currently studying Electrical Engineering at Shenyang University of Technology, pursuing the M.S. degree. Her research direction is the optimization control of load-side frequency regulation in power systems.

Electromechanical Coupling Resonance Analysis and Compensation Strategy of IPMSM Drive System Considering Current Measurement Offset Error

Xinglai GE, Yangjing LIU, Yun ZUO, and Huimin WANG

***Abstract*—The current measurement offset errors (CMOEs) raise concerns regarding the performance degradation of interior permanent-magnet synchronous motor (IPMSM) drive system. Considering this, a detailed analysis of the impact of CMOE is conducted in this paper, and a compensation strategy is proposed. Based on the established dual-inertia model of the IPMSM drive system, the effects of CMOE on electromechanical coupling resonance are analyzed. Furthermore, the CMOE compensation scheme based on an improved adaptive observer is designed to eliminate these adverse effects. In the proposed compensation scheme, adaptive gains are designed to ensure effective compensation performance at different speeds. In addition, the proposed compensation scheme is decoupled from vector control and has a relatively small impact on the control performance of the motor. Finally, extensive tests are conducted to validate the effectiveness of the proposed method.**

***Index Terms*—Adaptive current measurement offset error (CMOE) observer, CMOE, electro-mechanical coupling resonance, interior permanent-magnet synchronous motor (IPMSM) drive system.**

I. Introduction

INTERIOR permanent-magnet synchronous motors (IPMSMs) are widely used in subways, electric vehicles and other fields due to high reliability and good dynamic performance [1], [2]. Various control strategies for IPMSMs, such as vector control and direct torque control, have been extensively studied over the past few decades. To ensure high performance of these control methods, precise measurement of motor current is still a basic prerequisite [3].

However, due to factors such as prolonged operation, temperature drift and aging, the process of sampling motor phase currents inevitably introduces offset errors, even in well-constructed systems [4], [5]. These DC offsets in the measured phase currents can induce torque ripples in IPMSM drives which are typically interconnected with mechanical components. Meanwhile, torque ripples in the traction motor can trigger electromechanical coupling resonance, amplifying system vibrations significantly [6]-[8]. Prolonged exposure to such vibrations can accelerate mechanical shaft fatigue, shortening the lifespan of mechanical components [9], [10]. As such, it's essential to analyze the electromechanical coupling resonance induced by current measurement offset error (CMOE) and implement effective suppression strategies.

Many studies have analyzed the impact of CMOE on permanent-magnet synchronous motor (PMSM) drive systems [11]-[17]. As noted in [11] and [12], CMOE causes DC offsets in the measured phase currents of PMSMs. These DC offsets result in fundamental-frequency components in the *d*- and *q*-axis currents. Moreover, CMOE adversely impacts the motion performance of PMSM drive systems [13], [14]. Even with closed-loop motor control, CMOE can still induce motor torque ripples and undesirable fluctuations in rotational speed [15], [16]. Previous studies concentrate primarily on the electrical aspects of PMSM drive systems, including motor current, torque, and rotational speed [17]. However, these studies have not considered the resonance problem caused by the coupling of electrical and mechanical components. This issue requires further analysis to fully understand and mitigate the impact of CMOE on the IPMSM drive system.

To mitigate the influence of CMOE, various error calibration methods for current sensors have been proposed. They can be divided into two main categories: one mitigates the effects induced by CMOE, while the other directly estimates and compensates for CMOE itself. The first category focuses on mitigating the effects without directly estimating CMOE through resonant controllers [18], harmonic elimination algorithms [19], [20], and iterative self-learning controllers [21]. In addition to extensive computational requirements and complex structural design, these methods cannot directly compensate for the CMOE itself. The second category aims at estimating and directly compensating for CMOE itself [22]-[27]. The simplest attempt is to update and correct the offset error during motor shutdown or initial operation [14], but this approach cannot compensate for the offset error that results from temperature after long-term operation. In [22], a calibration

Manuscript received May 18, 2025; revised June 28, 2025; accepted July 28, 2025. Date of publication September 30, 2025; date of current version August 22, 2025. This work was supported in part by National Natural Science Foundation of China under the grant 52177060 and Fundamental Research Funds for the Central Universities under the grants 2682024CX015 and 2682025GH033. (*Corresponding author: Yangjing Liu.*)

All authors are with the Ministry of Education Key Laboratory of Magnetic Suspension Technology and Maglev Vehicle, Southwest Jiaotong University, Chengdu 610031, China (e-mail: xlge@swjtu.edu.cn; yangjingliu@my.swjtu.edu.cn; zuoyun@my.swjtu.edu.cn; wanghuimin@my. swjtu.edu.cn).

Digital Object Identifier 10.24295/CPSSTPEA.2025.00025

strategy based on the detection voltage injection method was introduced, which is simple to implement. However, sampling noise can cause deviations in error parameter estimation and compensation, resulting in poor dynamic performance. In [23], the estimated CMOE value was obtained from the reference voltage provided by the current controller, leading to concerns about dynamic performance. A new method for decoupling the interference from the outer loop speed controller in CMOE correction was proposed in [24], but it encounters current controller saturation issues. Furthermore, both methods are coupled with vector control, limiting their flexibility in application. In [25], a fast CMOE calibration method with high reliability was proposed, which is not limited by vector control methods. However, this method is only applicable to dual PMSMs, and the motor inductance cannot be too small. In [26] and [27], a PI-type observer designed in the stationary reference frame for CMOE compensation was proposed, which is decoupled from the vector control and flexible to apply. However, it is susceptible to disturbances from varying-frequency AC components. Further research is required to address the issue of interference caused by the AC components.

Based on the aforementioned issues, this paper establishes a dual-inertia model of the IPMSM drive system and analyzes the influence of CMOE on the IPMSM drives. Subsequently, an improved adaptive observer is proposed to compensate for CMOE. The proposed method can mitigate the interference from variable-frequency AC components, and has a minimal impact on motor control performance. The effectiveness of the proposed method is verified on both a 3kW IPMSM experimental platform and a hardware-in-the-loop (HIL) platform.

This paper is organized as follows: Section II analyzes electromechanical coupling resonance in the IPMSM drive system induced by CMOE. In Section III, the limitations of the conventional PI-type CMOE observer are pointed out, and an improved CMOE compensation method is proposed. Subsequently, experimental tests are conducted to validate the proposed method, and the results are presented in Section IV. Finally, Section V presents the conclusions of this study.

II. Electromechanical Coupling Resonance Caused by CMOE

Based on the established dual-inertia IPMSM drive model, the effects of CMOE on electromagnetic harmonic torque and its potential to cause electromechanical resonance are analyzed in this section.

A. Effects of CMOE

The electromagnetic torque of IPMSMs can be expressed as (1), where n_p is the number of pole pairs, ψ_f is the permanent magnetic flux linkage, L_d and L_q are the d- and q-axis inductances, i_{sd} and i_{sq} are the value of the d- and q-axis stator currents, respectively.

$$T_e = 1.5 n_p \left[\psi_f i_{sq} + i_{sq} i_{sd} (L_d - L_q) \right] \tag{1}$$

It can be observed that the torque is directly influenced by i_{sd} and i_{sq}. Therefore, the impact of CMOE on i_{sd} and i_{sq} needs to be explored. Since the sum of three-phase currents is 0, two current sensors are usually installed to measure the phase currents of IPMSM. i_{sa_m}, i_{sb_m}, Δi_{sa_off}, and Δi_{sb_off} are the measured values and the CMOEs of a- and b-phase stator currents. The vector-controlled IPMSM drive system under the influence of CMOEs is shown in Fig. 1.

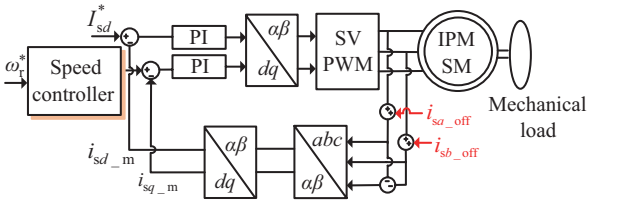

Fig. 1. Vector-controlled IPMSM drive system considering current measurement offset errors.

The relationship between the actual phase current i_{sa} and i_{sb} and the measured values can be expressed as

$$\begin{cases} i_{sa\_m} = i_{sa} + \Delta i_{sa\_off} \\ i_{sb\_m} = i_{sb} + \Delta i_{sb\_off} \\ i_{sc\_m} = -(i_{sa\_m} + i_{sb\_m}) \end{cases} \tag{2}$$

With (2), the stator currents measured in the α-β reference frame as

$$\begin{cases} i_{s\alpha\_m} = i_{s\alpha} + \Delta i_{s\alpha\_off} \\ i_{s\beta\_m} = i_{s\beta} + \Delta i_{s\beta\_off} \\ \Delta i_{s\alpha\_off} = \Delta i_{sa\_off} \\ \Delta i_{s\beta\_off} = \sqrt{3}(\Delta i_{sa\_off} + 2\Delta i_{sb\_off})/3 \end{cases} \tag{3}$$

where $i_{s\alpha\_m}$, $i_{s\beta\_m}$, $i_{s\alpha}$, $i_{s\beta}$, $\Delta i_{s\alpha\_off}$, and $\Delta i_{s\beta\_off}$ are the measured values, the actual values of the α- and β-axis stator currents, and the DC offset errors in the α- and β-axis stator currents, respectively.

It can be further derived that

$$\begin{cases} i_{sd\_m} = i_{sd} + \Delta i_{sd\_off} \\ i_{sq\_m} = i_{sq} + \Delta i_{sq\_off} \\ \Delta i_{sd\_off} = I_{dc} \sin(\omega_r t + \varphi) \\ \Delta i_{sq\_off} = I_{dc} \cos(\omega_r t + \varphi) \end{cases} \tag{4}$$

$$\begin{cases} I_{dc} = \sqrt{\Delta i^2_{sa\_off} + \dfrac{1}{3}(\Delta i_{sa\_off} + 2\Delta i_{sb\_off})^2} \\ \varphi = \tan^{-1}\left[\sqrt{3}\Delta i_{sa\_off} \big/ (\Delta i_{sa\_off} + 2\Delta i_{sb\_off}) \right] \end{cases} \tag{5}$$

where i_{sd_m}, i_{sq_m}, i_{sd}, i_{sq}, Δi_{sd_off}, and Δi_{sq_off} represent the measured values, the actual values, and the offset errors of the d- and q-axis stator currents. ω_r is the electrical angular speed in the stationary reference frame. I_{dc} and φ represent the amplitude and initial phase of the CMOEs on the d- and q-axis offset errors, respectively.

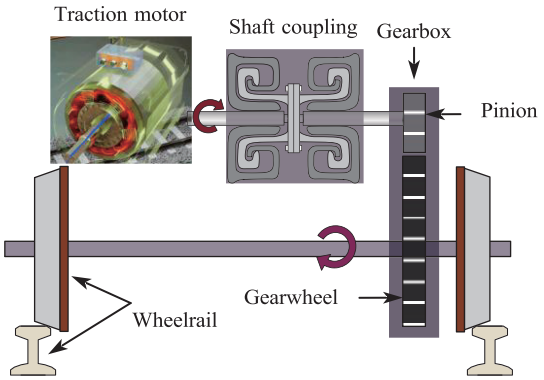

Fig. 2. The basic power unit structure of the IPMSM mechanical drive.

Based on the above derivation, the effect of CMOE on electromagnetic torque can be expressed as

$$\begin{aligned} T_{\mathrm{e}} &= \frac{3}{2} n_{\mathrm{p}} [i_{sq} + I_{\mathrm{dc}} \cos(\omega_{\mathrm{r}} t + \varphi)] \times \\ &\quad \{\psi_f + (L_d - L_q)[i_{sd} + I_{\mathrm{dc}} \sin(\omega_{\mathrm{r}} t + \varphi)]\} \\ &= \frac{3}{2} n_{\mathrm{p}} \begin{pmatrix} \psi_f i_{sq} + (L_d - L_q) i_{sd} i_{sq} \\ + (L_d - L_q) I_{\mathrm{dc}} i_{sq} \sin(\omega_{\mathrm{r}} t + \varphi) \\ + \psi_f I_{\mathrm{dc}} \cos(\omega_{\mathrm{r}} t + \varphi) \\ + (L_d - L_q) I_{\mathrm{dc}} i_{sd} \cos(\omega_{\mathrm{r}} t + \varphi) \\ + \frac{1}{2} (L_d - L_q) I_{\mathrm{dc}}^2 \sin(2\omega_{\mathrm{r}} t + 2\varphi) \end{pmatrix} \end{aligned} \tag{6}$$

Since the difference between L_d and L_q in an IPMSM is relatively small, (6) can be rewritten as

$$T_{\mathrm{e}} = T_{\mathrm{e0}} + T_{\mathrm{2e0}} \cos(\omega_{\mathrm{r}} t + \varphi_1) \tag{7}$$

where T_{e0} is the actual electromagnetic torque, T_{2e0} and φ_1 represent the amplitude and initial phase of the disturbance torque caused by CMOE. As shown in (7), CMOE introduces harmonics at the fundamental stator electrical frequency into the electromagnetic torque of the IPMSM.

Applying the Laplace transform on (7) and neglecting φ_1 to simplify the analysis, we can obtain

$$T_{\mathrm{e}}(s) = \frac{T_{\mathrm{e0}}}{s} + \frac{s T_{\mathrm{2e0}}}{s^2 + \omega_{\mathrm{r}}^2} \tag{8}$$

B. Electromechanical Coupling Resonance Analysis

The structure of IPMSM drive system is complex. The mechanical drive device and the electrical system together constitute an electromechanical coupling system. Taking the train traction drive system based on IPMSM as an example, the basic mechanical driveline, as depicted in Fig. 2, comprises a traction motor, a shaft coupling, a gearbox, and the wheel-rail interface.

To analyze the electromechanical coupling resonance caused by CMOE, the IPMSM mechanical drive is equivalently simplified into the dual-inertia model. Fig. 3 shows the dual-inertia model of IPMSM drives. T_{e}, T_{w} and T_{l} are the motor electromagnetic torque, the shaft torque, and the load torque, respectively. D, K, J_{m} and J_{l} are the damping coefficient, stiffness of the transmission shaft, the rotational inertias of the IPMSM and the mechanical load, respectively. θ_{m}, θ_{l}, ω_{m} and ω_{l} are the rotational angles of the motor shaft, the mechanical load shaft, the angular velocities of the motor shaft and the mechanical load shaft, respectively.

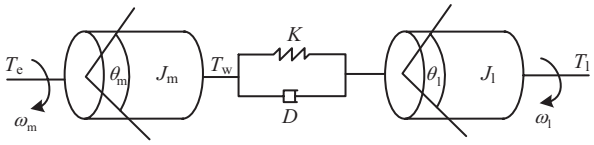

Fig. 3. Dual-inertia model of the IPMSM mechanical drive.

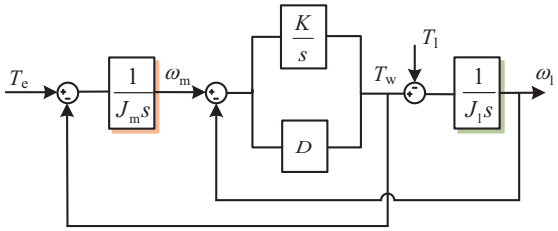

Fig. 4. Block diagram of LTI model of the dual-inertia system.

According to Newton second law, the dynamic differential equations governing the drive system can be expressed as

$$\begin{cases} J_{\mathrm{m}} \ddot{\theta}_{\mathrm{m}} + T_{\mathrm{w}} = T_{\mathrm{e}} \\ J_{\mathrm{l}} \ddot{\theta}_{\mathrm{l}} - T_{\mathrm{w}} = -T_{\mathrm{l}} \\ T_{\mathrm{w}} = D(\dot{\theta}_{\mathrm{m}} - \dot{\theta}_{\mathrm{l}}) + K(\theta_{\mathrm{m}} - \theta_{\mathrm{l}}) \end{cases} \tag{9}$$

With the Laplace transform, it can be further derived as

$$\begin{cases} J_{\mathrm{m}} \theta_{\mathrm{m}} s^2 + D(\theta_{\mathrm{m}} - \theta_{\mathrm{l}}) s + K(\theta_{\mathrm{m}} - \theta_{\mathrm{l}}) = T_{\mathrm{e}} \\ J_{\mathrm{l}} \theta_{\mathrm{l}} s^2 - D(\theta_{\mathrm{m}} - \theta_{\mathrm{l}}) s - K(\theta_{\mathrm{m}} - \theta_{\mathrm{l}}) = -T_{\mathrm{l}} \\ \omega_{\mathrm{m}} = \theta_{\mathrm{m}} s \\ \omega_{\mathrm{l}} = \theta_{\mathrm{l}} s \end{cases} \tag{10}$$

The LTI model of the dual-inertia system is shown in Fig. 4. Since the damping coefficient D is generally very small, it can be omitted in the subsequent analysis. The transfer function can be obtained as [28]

$$\begin{aligned} G_{\mathrm{l}}(s) &= \frac{\omega_{\mathrm{m}}(s)}{T_{\mathrm{e}}(s)} = \frac{J_{\mathrm{l}} s^2 + K}{J_{\mathrm{m}} J_{\mathrm{l}} s^3 + (J_{\mathrm{m}} + J_{\mathrm{l}}) K s} \\ &= \frac{1}{(J_{\mathrm{m}} + J_{\mathrm{l}})} \frac{\frac{J_{\mathrm{l}} s^2}{K} \omega_{\mathrm{NTF}}^2 + \omega_{\mathrm{NTF}}^2}{s^3 + s\omega_{\mathrm{NTF}}^2} \end{aligned} \tag{11}$$

$$G_2(s)=\frac{\omega_{\mathrm{m}}(s)}{T_{\mathrm{l}}(s)}=\frac{-K}{J_{\mathrm{m}}J_{\mathrm{l}}s^3+(J_{\mathrm{m}}+J_{\mathrm{l}})Ks}=\frac{-1}{(J_{\mathrm{m}}+J_{\mathrm{l}})}\frac{\omega_{\mathrm{NTF}}^2}{s^3+s\omega_{\mathrm{NTF}}^2} \tag{12}$$

where

$$\omega_{\mathrm{NTF}}=\sqrt{\frac{K(J_{\mathrm{m}}+J_{\mathrm{l}})}{J_{\mathrm{m}}J_{\mathrm{l}}}} \tag{13}$$

In (13), ω_{NTF} is the natural vibration frequency. Resonance occurs when the oscillation frequency induced by excitation approaches the natural vibration frequency of the mechanical transmission device [29].

Combining (11) and (12), the unit step response of ω_{m} can be obtained as

$$\omega_{\mathrm{m}}(s)=G_{\mathrm{l}}(s)T_{\mathrm{e}}(s)+G_2(s)T_{\mathrm{l}}(s)=G_a+G_b \tag{14}$$

then

$$\begin{aligned}G_a&=(\frac{T_{\mathrm{e0}}}{s}+\frac{sT_{2\mathrm{e0}}}{s^2+\omega_{\mathrm{r}}^2})G_{\mathrm{l}}(s)\\&=\frac{(\frac{J_{\mathrm{l}}s^2}{K}+1)\omega_{\mathrm{NTF}}^2}{(J_{\mathrm{m}}+J_{\mathrm{l}})(s^2+\omega_{\mathrm{NTF}}^2)}\left[\frac{T_{\mathrm{e0}}}{s^2}+\frac{T_{2\mathrm{e0}}}{(s^2+\omega_{\mathrm{r}}^2)}\right]\\&=\frac{1}{(J_{\mathrm{m}}+J_{\mathrm{l}})}\left(\begin{array}{l}\dfrac{\frac{J_{\mathrm{l}}}{K}\omega_{\mathrm{NTF}}^2-1}{s^2+\omega_{\mathrm{NTF}}^2}T_{\mathrm{e0}}+\dfrac{1}{s^2}T_{\mathrm{e0}}\\+\dfrac{\frac{1-\frac{J_{\mathrm{l}}}{K}\omega_{\mathrm{NTF}}^2}{(\omega_{\mathrm{r}}^2-\omega_{\mathrm{NTF}}^2)}\omega_{\mathrm{NTF}}^2}{s^2+\omega_{\mathrm{NTF}}^2}T_{2\mathrm{e0}}\\+\dfrac{\frac{(1-\omega_{\mathrm{r}}^2\frac{J_{\mathrm{l}}}{K})\omega_{\mathrm{NTF}}^2}{(\omega_{\mathrm{NTF}}^2-\omega_{\mathrm{r}}^2)}}{s^2+\omega_{\mathrm{r}}^2}T_{2\mathrm{e0}}\end{array}\right)\end{aligned} \tag{15}$$

$$\begin{aligned}\mathrm{G}_b&=\frac{-1}{(J_{\mathrm{m}}+J_{\mathrm{l}})}\frac{\omega_{\mathrm{NTF}}^2}{s^3+s\omega_{\mathrm{NTF}}^2}T_{\mathrm{l}}(s)\\&=\frac{-1}{(J_{\mathrm{m}}+J_{\mathrm{l}})}\frac{\omega_{\mathrm{NTF}}^2}{s^3+s\omega_{\mathrm{NTF}}^2}\frac{T_{\mathrm{l}}}{s}\\&=\frac{1}{(J_{\mathrm{m}}+J_{\mathrm{l}})}(\frac{1}{s^2+\omega_{\mathrm{NTF}}^2}T_{\mathrm{l}}-\frac{1}{s^2}T_{\mathrm{l}})\end{aligned} \tag{16}$$

With the inverse Laplace transform, (14) be further derived that

$$\omega_{\mathrm{m}}(t)=\frac{1}{(J_{\mathrm{m}}+J_{\mathrm{l}})}\left(\begin{array}{l}(T_{\mathrm{e0}}-T_{\mathrm{l}})t\\+\dfrac{\left(\frac{J_{\mathrm{l}}}{K}\omega_{\mathrm{NTF}}^2-1\right)T_{\mathrm{e0}}+T_{\mathrm{l}}}{\omega_{\mathrm{NTF}}}\sin(\omega_{\mathrm{NTF}}t)\\+\dfrac{\left(1-\frac{J_{\mathrm{l}}}{K}\omega_{\mathrm{NTF}}^2\right)\omega_{\mathrm{NTF}}}{(\omega_{\mathrm{r}}^2-\omega_{\mathrm{NTF}}^2)}T_{2\mathrm{e0}}\sin(\omega_{\mathrm{NTF}}t)\\+\dfrac{\left(1-\omega_{\mathrm{r}}^2\frac{J_{\mathrm{l}}}{K}\right)\omega_{\mathrm{NTF}}^2}{\omega_{\mathrm{r}}(\omega_{\mathrm{NTF}}^2-\omega_{\mathrm{r}}^2)}T_{2\mathrm{e0}}\sin(\omega_{\mathrm{r}}t)\end{array}\right) \tag{17}$$

From the aforementioned analysis, CMOE introduces harmonic torque at the fundamental stator electrical frequency ω_{r}. As shown in (17), when ω_{r} approaches the system natural frequency ω_{NIF}, the frequency difference (ω_{r} - ω_{NIF}) approaches zero. This leads to energy build-up at the natural frequency, thereby triggering the electromechanical coupling resonance. In addition, the amplitude of the input excitation caused by CMOE directly amplifies the resonance response magnitude.

III. Proposed CMOE Compensation Method

To mitigate CMOE-induced electromechanical coupling resonance in IPMSM drives, the limitations of the conventional PI-type observer are discussed and the improved adaptive CMOE observer for IPMSM drives is constructed in this section.

A. Conventional PI-Type Observer

The voltage equations of IPMSM are given by

$$\begin{cases}u_{s\alpha}=R_{\mathrm{s}}i_{s\alpha}+pL_{\mathrm{q}}i_{s\alpha}+E_\alpha\\u_{s\beta}=R_{\mathrm{s}}i_{s\beta}+pL_{\mathrm{q}}i_{s\beta}+E_\beta\end{cases} \tag{18}$$

where R_{s} is the stator resistance, p is the differential operator, $u_{s\alpha}$, $u_{s\beta}$ are the stator voltage components. E_α, E_β are the back electromotive force (EMF), which can be expressed as [30], [31]

$$\begin{cases}E_\alpha=\left[(L_d-L_q)\omega_{\mathrm{r}}i_{sd}+\omega_{\mathrm{r}}\psi_f\right](-\sin\theta_{\mathrm{r}})\\E_\beta=\left[(L_d-L_q)\omega_{\mathrm{r}}i_{sd}+\omega_{\mathrm{r}}\psi_f\right](\cos\theta_{\mathrm{r}})\end{cases} \tag{19}$$

where θ_{r} is the rotor position.

Considering the effect of CMOE, (18) can be further derived as

$$\begin{cases}\dot{i}_{s\alpha\_\mathrm{m}}=\dfrac{u_{s\alpha}-R_{\mathrm{s}}i_{s\alpha\_\mathrm{m}}-E_\alpha}{L_q}+\mathrm{Z}_\alpha\\\dot{i}_{s\beta\_\mathrm{m}}=\dfrac{u_{s\beta}-R_{\mathrm{s}}i_{s\beta\_\mathrm{m}}-E_\beta}{L_q}+\mathrm{Z}_\beta\end{cases} \tag{20}$$

with

$$\begin{cases}Z_\alpha=\dfrac{R_{\mathrm{s}}}{L_q}\Delta i_{s\alpha\_\mathrm{off}}+\Delta\dot{i}_{s\alpha\_\mathrm{off}}\approx\dfrac{R_{\mathrm{s}}}{L_q}\Delta i_{s\alpha\_\mathrm{off}}\\Z_\beta=\dfrac{R_{\mathrm{s}}}{L_q}\Delta i_{s\beta\_\mathrm{off}}+\Delta\dot{i}_{s\beta\_\mathrm{off}}\approx\dfrac{R_{\mathrm{s}}}{L_q}\Delta i_{s\beta\_\mathrm{off}}\end{cases} \tag{21}$$

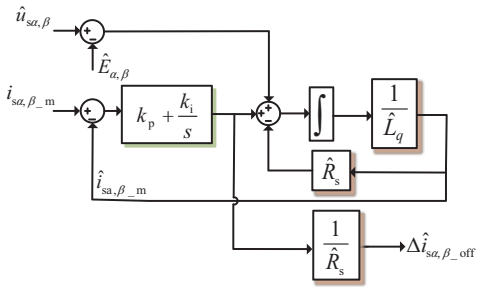

Fig. 5. Block diagram of the conventional PI-type observer.

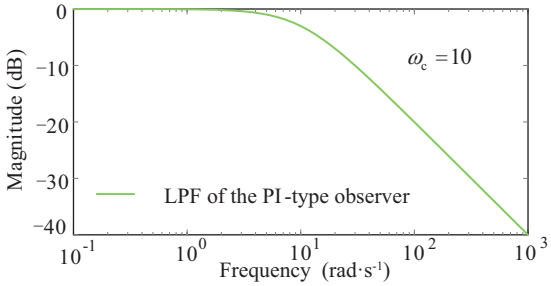

Fig. 6. Amplitude-frequency characteristics of the PI-type observer.

where Z_α and Z_β are the disturbances. CMOEs are DC components in the stationary reference frame, and the differential term in (21) can be neglected.

With (21), the PI-type observer is designed as [26].

$$\Delta\hat{i}_{s\alpha,\beta\_off} = \frac{1}{\hat{R}_s}(k_p + \frac{k_i}{s})(i_{s\alpha,\beta\_m} - \hat{i}_{s\alpha,\beta\_m}) \tag{22}$$

where k_p and k_i represent the gains of the PI-type observer, and the superscript "^" defines the estimated variable.

The estimated currents can be derived as

$$\hat{i}_{s\alpha,\beta\_m} = \frac{\hat{u}_{s\alpha,\beta} - \hat{E}_{\alpha,\beta} + \hat{R}_s\Delta\hat{i}_{s\alpha,\beta\_off}}{\hat{L}_q s + \hat{R}_s} \tag{23}$$

Fig. 5 shows the conventional PI-type observer for IPMSM drives. The input is defined as the difference between the measured α- and β-axis stator currents and the estimated α- and β-axis currents. The output is the CMOE in the α- and β-axis stator currents. By substituting (23) into (22), the following equation can be derived as

$$\Delta\hat{i}_{s\alpha,\beta\_off} = \frac{\hat{L}_q s + \hat{R}_s}{\hat{L}_q s^2 + (k_p + \hat{R}_s)s + k_i} \times \frac{k_p s + k_i}{\hat{R}_s} \times \left(\frac{R_s}{L_s s + R_s}\Delta i_{s\alpha,\beta\_off} + \frac{u_{s\alpha,\beta} - E_{\alpha,\beta}}{L_s s + R_s} - \frac{\hat{u}_{s\alpha,\beta} - \hat{E}_{\alpha,\beta}}{\hat{L}_s s + \hat{R}_s} \right) \tag{24}$$

Without considering motor parameter mismatches and signal calculation errors, a second-order low-pass filter (LPF) is obtained as

$$\Delta\hat{i}_{s\alpha,\beta\_off} = \frac{k_p s + k_i}{\hat{L}_q s^2 + (k_p + \hat{R}_s)s + k_i}\Delta i_{s\alpha,\beta\_off} \tag{25}$$

To achieve pole-zero cancellation, the gains of the PI-type observer are set as

$$\begin{cases} k_p = \hat{L}_q\omega_c \\ k_i = \hat{R}_s\omega_c \end{cases} \tag{26}$$

With (26), (25) can be simplified as

$$\frac{\Delta\hat{i}_{s\alpha,\beta\_off}}{\Delta i_{s\alpha,\beta\_off}} = \frac{\omega_c}{s + \omega_c} \tag{27}$$

where ω_c determines the filtering bandwidth of the PI-type observer.

In practice, the voltage is typically reconstructed using the DC bus voltage and the state of switching device states, while the back-EMF in IPMSMs is generally estimated based on the flux constant. Therefore, deviations in these estimates can arise due to motor parameter variations. It is difficult to achieve accurate values for voltage and back-EMF signals, and the errors are denoted as $\Delta u_{s\alpha,\beta}$ *and* $\Delta E_{\alpha,\beta}$. Considering this, the following equation can be obtained as

$$\Delta\hat{i}_{s\alpha,\beta\_off} = \frac{k_p s + k_i}{\hat{L}_q s^2 + (k_p + \hat{R}_s)s + k_i}\Delta i_{s\alpha,\beta\_off} + \frac{1}{\hat{R}_s}\frac{k_p s + k_i}{\hat{L}_q s^2 + (k_p + \hat{R}_s)s + k_i}\begin{bmatrix} u_{s\alpha,\beta} - \hat{u}_{s\alpha,\beta} \\ \hat{E}_{\alpha,\beta} - E_{\alpha,\beta} \end{bmatrix} \tag{28}$$

With (26), (28) can be further derived as

$$\Delta\hat{i}_{s\alpha,\beta\_off}(s) = \frac{\omega_c}{s + \omega_c} i_{s\alpha,\beta\_off}(s) + \frac{\omega_c}{s + \omega_c}\frac{1}{\hat{R}_s}\left[\Delta E_{\alpha,\beta}(s) - \Delta u_{s\alpha,\beta}(s)\right] \tag{29}$$

In (29), $i_{s\alpha,\beta\_off}(s)$ denotes the DC component, while $\Delta u_{s\alpha,\beta}$ and $\Delta E_{\alpha,\beta}$ represent AC disturbance components whose frequency is proportional to the motor speed in the IPMSM drive system. For IPMSM drives, the observer should sufficiently attenuate speed-dependent disturbances across the full operating speed range, thereby constraining estimation error during dynamic operation of IPMSMs.

The amplitude-frequency characteristic of the PI-type observer is depicted in Fig. 6, which implies that the observer has low-pass filter performance. However, the fixed gains in the PI-type observer result in a constant filter bandwidth, rendering it ineffective against low-frequency AC disturbances. Furthermore, the amplitude of these AC disturbance components increases at lower motor speed, so the estimation accuracy

of the conventional PI-type observer will be further deteriorated.

B. Construction of the Improved Adaptive CMOE Observer

The conventional PI-type observer cannot mitigate the interference from variable-frequency AC components caused by the motor parameter mismatch. To address this problem, an improved adaptive observer is designed in this paper.

The magnitude characteristic of (27) is given by

$$\left|\frac{\Delta\hat{i}_{s\alpha,\beta\_\mathrm{off}}(j\omega_\mathrm{r})}{\Delta i_{s\alpha,\beta\_\mathrm{off}}(j\omega_\mathrm{r})}\right| = \frac{\omega_\mathrm{c}}{\sqrt{\omega_\mathrm{c}^2+\omega_\mathrm{r}^2}} \tag{30}$$

As illustrated in (30), the bandwidth of the adaptive CMOE observer can be designed as

$$\begin{cases} \omega_\mathrm{c} = \mu\omega_\mathrm{r} \\ \omega_{\mathrm{c}\min} \leqslant \omega_\mathrm{c} \leqslant \omega_{\mathrm{c}\max} \end{cases} \tag{31}$$

where μ is the attenuation gain that determines the amplitude reduction, while ω_{cmin} and ω_{cmax} are the minimum and the maximum bandwidth of the adaptive observer. The adaptive observer adjusts exclusively the bandwidth magnitude while maintaining fixed parameterization, so ω_c is always positive and will not affect the stability of the observer.

Substituting (31) into (30) yields

$$\frac{\omega_\mathrm{c}}{\sqrt{\omega_\mathrm{c}^2+\omega_\mathrm{r}^2}} = \frac{\mu\omega_\mathrm{r}}{\sqrt{\mu^2\omega_\mathrm{r}^2+\omega_\mathrm{r}^2}} = \frac{1}{\sqrt{1+\dfrac{1}{\mu^2}}} \tag{32}$$

It can be seen that when μ is appropriately selected to be less than 1, the proposed adaptive gains can ensure effective amplitude attenuation for variable-frequency AC components.

Consequently, the gains of the improved CMOE observer are set as follows

$$\begin{cases} k_\mathrm{p} = \mu\hat{L}_q\omega_\mathrm{r} \\ k_\mathrm{i} = \mu\hat{R}_\mathrm{s}\omega_\mathrm{r} \end{cases} \tag{33}$$

At this point, the block diagram of the improved CMOE observer is shown in Fig. 7. Substituting (33) into (25), the improved adaptive observer can finally be derived as

$$\Delta\hat{i}_{s\alpha,\beta\_\mathrm{off}} = \frac{\mu\omega_\mathrm{r}}{s+\mu\omega_\mathrm{r}}\Delta i_{s\alpha,\beta\_\mathrm{off}} \tag{34}$$

Based on the above analysis, the improved observer can eliminate the error in the equivalent back-EMF. For simplicity, the back-EMF calculation of the improved CMOE observation can be simplified to

$$\begin{cases} \hat{E}_\alpha = -\omega_\mathrm{r}\psi_f \sin\theta_\mathrm{r} \\ \hat{E}_\beta = \omega_\mathrm{r}\psi_f \cos\theta_\mathrm{r} \end{cases} \tag{35}$$

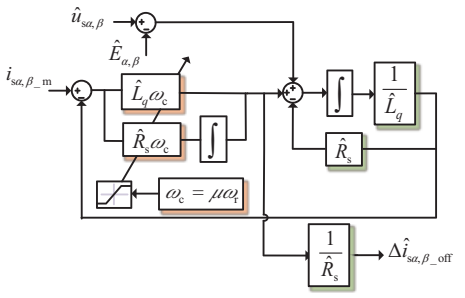

Fig. 7. Block diagram of the improved CMOE observer.

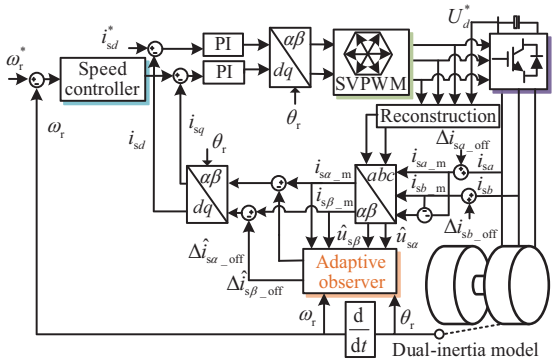

Fig. 8. Vector-controlled IPMSM drive system with the proposed CMOE compensation method.

Integrating the improved CMOE observer into the IPMSM drive system, the block diagram of the CMOE compensation control is shown in Fig. 8. It can be observed that the proposed method compensates for CMOE based on observation in the α-β stationary reference frame. Therefore, whether the system employs two-phase or three-phase sampling, it does not affect the performance of the proposed compensation method.

C. Robustness Analysis of the Adaptive Observer

The performance of conventional PI-type observer is affected by motor parameter errors, so additional filter and integrator regulator are typically required [27]. Considering motor parameter mismatches and signal calculation errors, that is

$$\begin{cases} \hat{R}_\mathrm{s} = R_\mathrm{s} + \Delta R_\mathrm{s} \\ \hat{L}_q = L_q + \Delta L_q \\ \hat{u}_{s\alpha,\beta} = u_{s\alpha,\beta} + \Delta u_{s\alpha,\beta} \\ \hat{E}_{\alpha,\beta} = E_{\alpha,\beta} + \Delta E_{\alpha,\beta} \end{cases} \tag{36}$$

where ΔR_s is the stator resistance error and ΔL_q is the q-axis inductance error.

Combining (24) and (33) yields,

$$\begin{aligned} \Delta\hat{i}_{s\alpha,\beta\_\mathrm{off}} = & \frac{\mu\omega_\mathrm{r}}{s+\mu\omega_\mathrm{r}}\frac{s\hat{L}_q+\hat{R}_\mathrm{s}}{\hat{R}_\mathrm{s}} \\ & \times\left(\frac{R_\mathrm{s}\Delta i_{\alpha,\beta\_\mathrm{off}}}{sL_q+R_\mathrm{s}} + \frac{u_{s\alpha,\beta}-E_{\alpha,\beta}}{sL_q+R_\mathrm{s}} - \frac{\hat{u}_{s\alpha,\beta}-\hat{E}_{\alpha,\beta}}{s\hat{L}_q+\hat{R}_\mathrm{s}}\right) \end{aligned} \tag{37}$$

In view of motor parameter variations and signal calculation inaccuracies, substituting (36) into (37) yields:

$$\Delta\hat{i}_{s\alpha,\beta\_\text{off}}=\frac{\mu\omega_\text{r}}{s+\mu\omega_\text{r}}\frac{1}{\hat{R}_\text{s}}\times\left\{\begin{aligned}&R_\text{s}\Delta i_{s\alpha,\beta\_\text{off}}(s)+\Delta E_{\alpha,\beta}(s)-\Delta u_{s\alpha,\beta}(s)\\&+(s\Delta L_q+\Delta R_\text{s})\left[\frac{R_\text{s}}{sL_q+R_\text{s}}\Delta i_{s\alpha,\beta\_\text{off}}(s)+i_{s\alpha,\beta}(s)\right]\end{aligned}\right\}\tag{38}$$

In (38), adaptive gains of the proposed scheme can attenuate the AC error components of $\Delta u_{s\alpha,\beta}$ and $\Delta E_{\alpha,\beta}$. Meanwhile, by setting s to zero, the estimated DC error components can be obtained

$$\Delta\hat{i}_{s\alpha,\beta\_\text{off}}(0)=\frac{1}{\hat{R}_\text{s}}\left[\begin{aligned}&R_\text{s}\Delta i_{s\alpha,\beta\_\text{off}}(0)+\Delta R_\text{s}\Delta i_{s\alpha,\beta\_\text{off}}(0)\\&+\Delta R_\text{s}i_{s\alpha,\beta}(0)\end{aligned}\right]\tag{39}$$

Then,

$$\Delta\hat{i}_{s\alpha,\beta\_\text{off}}(0)=\frac{R_\text{s}}{\hat{R}_\text{s}}\Delta i_{s\alpha,\beta\_\text{off}}(0)+\frac{\Delta R_\text{s}}{\hat{R}_\text{s}}i_{s\alpha,\beta\_\text{m}}(0)\tag{40}$$

Assuming the feedback current value is close to reference value, i_{sd_m} and i_{sq_m} can be regarded as DC values in steady state [26]. As a result, $i_{s\alpha,\beta\_\text{m}}$ in the second term of (40) is an AC component, and $i_{s\alpha,\beta\_\text{m}}(0)$ will be zero. The CMOE estimation error introduced by the first term in (40) is proportional to deviations in stator resistance. By incorporating the estimated CMOE into the motor closed-loop control, the effect of stator resistance mismatch on the performance of the adaptive observer is almost mitigated. This will be validated through experiments in Section IV.

IV. Experimental Tests

The experiment platform in Fig. 9 is constructed for verification of the proposed compensation method, and the experimental setup consists of a 3 kW IPMSM, two inverters, and an induction motor that applies load torque. The compensation method is implemented on an IPMSM experimental platform, with motor parameters listed in Table I. The method is implemented by a DSP TMS320F28335 controller. In the experiments, DC offset is introduced into the *a*- and *b*-phase stator currents to emulate CMOE. The different injection conditions of DC offset errors are detailed in Table II.

Due to the high natural vibration frequency of the existing permanent-magnet motor test platform, the stator frequency of the IPMSM cannot reach the natural vibration frequency of its mechanical components. Therefore, to effectively validate the effectiveness of the proposed CMOE compensation method, the experiments are conducted in two parts. Comparative experiments with the conventional method are conducted on the aforementioned experimental platform, and the performance of the improved compensation method is validated. Moreover, additional experiments will be conducted on an HIL platform to verify that CMOEs cause electromechanical coupling resonance and that the proposed method suppresses this resonance in the IPMSM system.

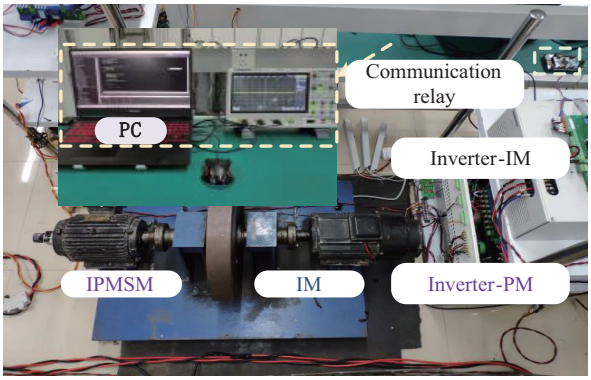

Fig. 9. Experimental platform.

TABLE I
Parameters of the Experimental IPMSM

Parameters	Value	Parameters	Value
Rated power	3 kW	Inertia	3.13 kg·m^2
Rated voltage	380 V	Rated speed	1500 rpm
Rated current	6.5 A	Permanent magnetic flux linkage	0.72 Wb
Stator resistance	1.8 Ω	*q*-axis inductance	142 mH
Sampling frequency	5 kHz	*d*-axis inductance	38 mH

TABLE II
Different Injection Conditions of DC Offset Error

Test case	Test conditions
Case 1	$\Delta i_{s\alpha\_\text{off}}=0.5$ A, $\Delta i_{s\beta\_\text{off}}=-0.5$ A Accordingly, $\Delta i_{s\alpha\_\text{off}}=0.5$ A, $\Delta i_{s\beta\_\text{off}}=-0.29$ A
Case 2	$\Delta i_{s\alpha\_\text{off}}=0.8$ A, $\Delta i_{s\beta\_\text{off}}=-0.5$ A Accordingly, $\Delta i_{s\alpha\_\text{off}}=0.8$ A, $\Delta i_{s\beta\_\text{off}}=-0.12$ A
Case 3	$\Delta i_{s\alpha\_\text{off}}=0.3$ A, $\Delta i_{s\beta\_\text{off}}=-0.2$ A Accordingly, $\Delta i_{s\alpha\_\text{off}}=0.3$ A, $\Delta i_{s\beta\_\text{off}}=-0.06$ A
Case 4	$\Delta i_{s\alpha\_\text{off}}=2$ A, $\Delta i_{s\beta\_\text{off}}=0$ A Accordingly, $\Delta i_{s\alpha\_\text{off}}=2$ A, $\Delta i_{s\beta\_\text{off}}=1.2$ A

A. CMOE Compensation Experimental Verification

As a first step, the performance of the proposed scheme is compared with the conventional scheme under low-speed and speed variation conditions of the motor. The bandwidth ω_c of the conventional observer is set to 1, while the attenuation coefficient μ for the improved observer is set to 0.005. As shown in Fig. 10(a), the DC offset of the Case 1 is injected in IPMSM drive system and the motor speed is set to 100 r/min. When the motor speed is varied from 600 r/min to 200 r/min, the estimation performance of the conventional observer decreases markedly as shown in Fig. 10(b). Furthermore,

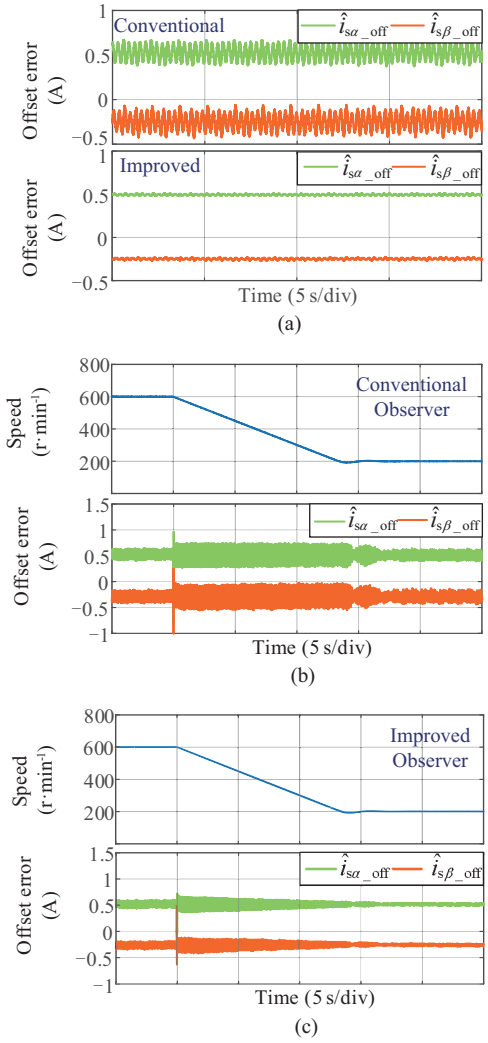

Fig. 10. Comparison of conventional observer and improved observer: (a) At low motor speed 100 r/min; (b) Output of the conventional observer when speed changes; (c) Output of the improved observer when speed changes.

the estimation value of the conventional observer contains a higher-amplitude AC component when the motor speed decreases. In contrast, as shown in Fig. 10(c), due to the designed adaptive gains, the improved observer has better estimation performance under motor speed variations.

To provide a clearer comparison of the performance between the two schemes. Table III presents the experimental results of both. It can be seen that the improved observer provides higher estimation accuracy at low motor speed and speed variations.

The performance of the IPMSM drive system with the proposed method is tested. As shown in the Fig. 11, a DC offset error of Case 1 is injected in the system, causing a DC offset in the three-phase currents. After applying the proposed compensation method, the three-phase currents return to the normal value. When CMOE is injected in Case 2, fluctuations in motor speed and actual *d*- and *q*-axis currents similarly occur, as seen from Fig. 12. However, when the proposed method is applied, these fluctuations in both motor speed and currents are significantly mitigated. Even with variations in the

TABLE III
PERFORMANCE COMPARISON BETWEEN THE IMPROVED SCHEME AND CONVENTIONAL SCHEME

Scheme	Low-speed		Speed variation	
	Max (A)	Min (A)	Max (A)	Min (A)
The conventional observer	0.18	−0.17	0.5	−1
The improved observer	0.03	−0.02	0.2	−0.3

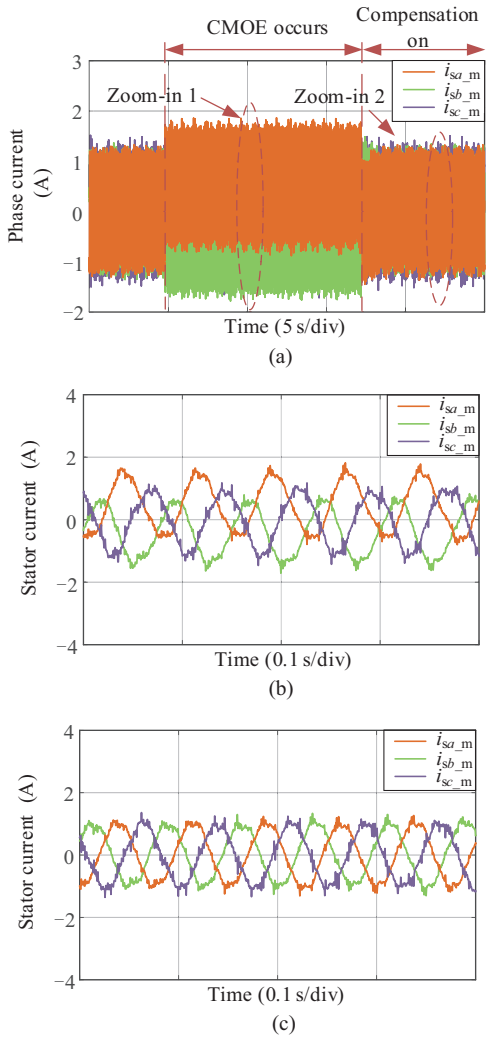

Fig. 11. Phase current estimation performance of the proposed method: (a) The whole estimation performance. (b) The zoom-in 1. (c) The zoom-in 2.

magnitude of injected CMOEs, the motor speed and the actual *d*- and *q*-axis currents remain stable, which can be attributed to the proposed compensation method.

Additionally, FFT analysis of the motor speed and currents are performed, focusing on the *q*-axis current due to its stable fluctuation frequency. As seen from Fig. 12(b) and (c), when CMOE is applied, the motor speed and the *q*-axis current exhibit fluctuations at the motor fundamental frequency. When the proposed method is applied, ripples in motor speed and

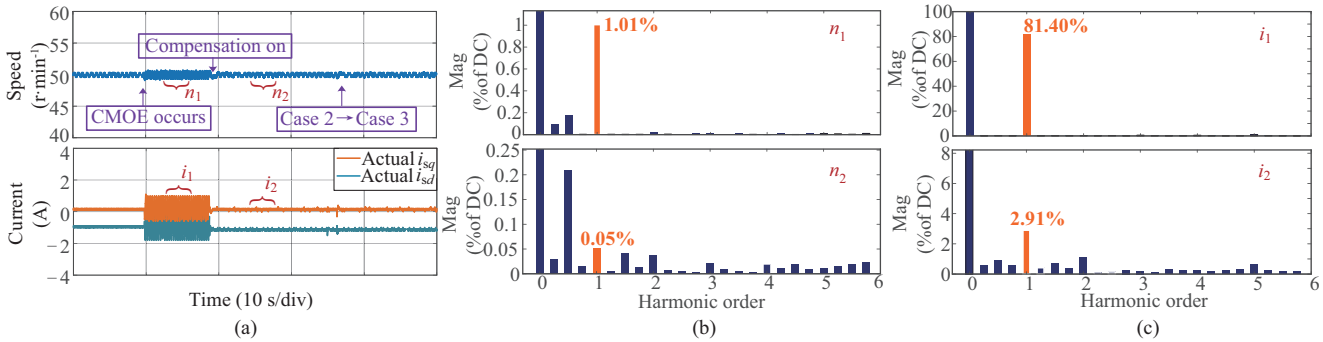

Fig. 12. Performance of the IPMSM drive with the proposed method: (a) The motor speed and current performance. (b) FFT analysis of the motor speed. (c) FFT analysis of the motor current.

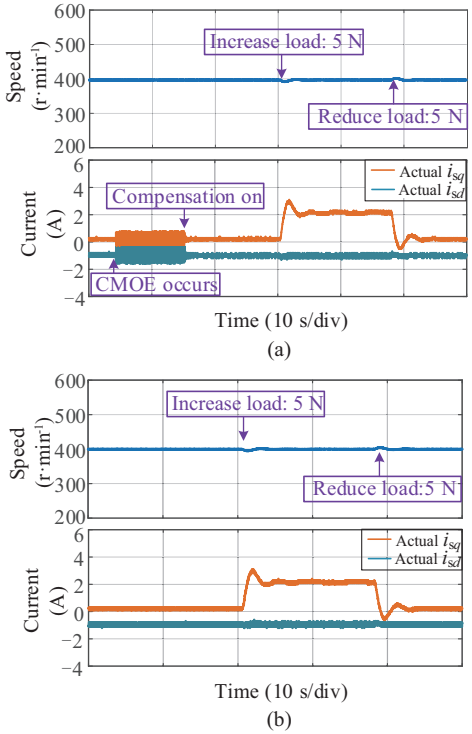

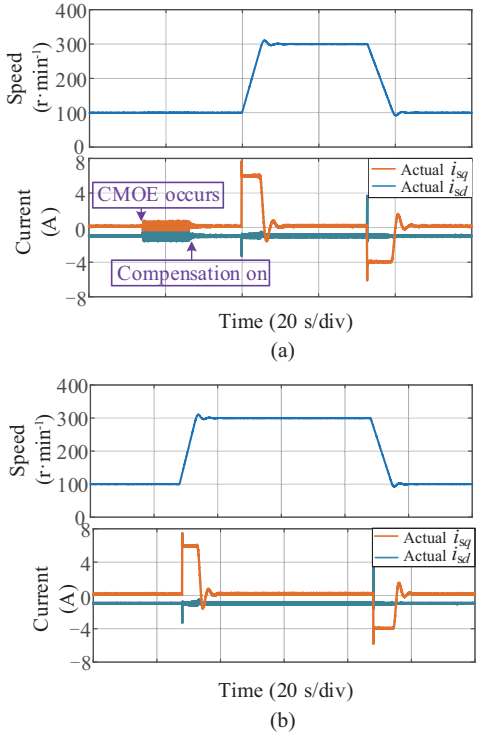

Fig. 13. Dynamic performance of the proposed method under load variations: (a) With the proposed compensation method. (b) In the normal state for comparison.

Fig. 14. Dynamic performance of the proposed method under motor speed variations: (a) With the proposed compensation method. (b) In the normal state for comparison.

current induced by CMOEs are suppressed. The proposed method effectively mitigates speed fluctuations and current ripples at the fundamental frequency of the motor.

The dynamic performance of the IPMSM drive system with the proposed method is also tested. As shown in Fig. 13, the IPMSM drive system undergoes loading and unloading during CMOE of the Case 1 is injected into the IPMSM drive. It can be seen that the motor speed and the *d*- and *q*-axis currents demonstrate good dynamics. For comparison, Fig. 13(b) shows the IPMSM drive performance without the injection of CMOE or the proposed compensation method. It can be found that the dynamic performance of the IPMSM drive with the proposed method is similar to that observed in normal state. Therefore, the proposed method has a minimal impact on the motor performance under load variations.

Moreover, the motor speed is varied from 100 r/min to 300 r/min and then back to 100 r/min, as shown in Fig. 14. The proposed compensation method is applied, and the IPMSM system also exhibits good performance under speed variations. Fig. 14(b) shows a comparison that the dynamic performance of the motor with the proposed method closely resembles the normal state. Thus, the implementation of the compensation method exhibits negligible influence on the dynamic performance of the IPMSM drive system.

To further demonstrate the performance of the proposed method, Fig. 15 illustrates the estimation performance of the CMOE observer under motor parameter mismatches. In tests, the stator resistance is reduced to 80% of its original value and then restored. When the estimated value of the CMOE observer

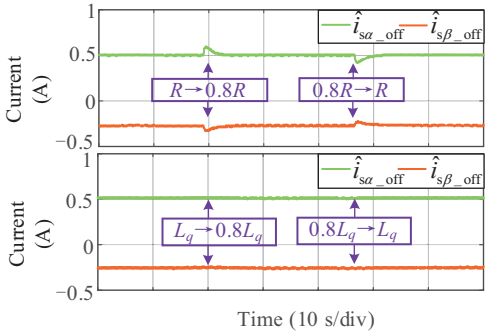

Fig. 15. Performance of the proposed method under motor parameter mismatches.

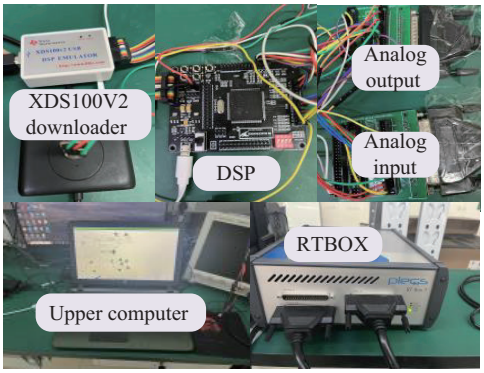

Fig. 16. HIL simulation experiment platform.

is incorporated into the motor closed-loop control, the estimated value of the proposed CMOE observer rapidly returns to its normal level. Furthermore, the q-axis inductance is adjusted from 100% of its original value to 80% and subsequently restored. As shown in Fig. 15, the estimation accuracy of the CMOE observer is unaffected. Consequently, the proposed improved compensation method demonstrates high robustness against motor parameter mismatches.

B. Electromechanical Coupling Resonance HIL Test Verification

An HIL platform has been established for demonstrating that the proposed method can suppress electromechanical coupling resonance induced by CMOE in the IPMSM system. As shown in Fig. 16, the HIL testing platform consists of a host computer, RTBOX simulator, TMS320F28335 controller, and IO board. The parameters of the dual-inertia model of IPMSM drives in this test are shown in Table IV.

The mechanical natural vibration frequency of the IPMSM mechanical drive in the HIL experiment platform as shown in Fig.17, which presents the bode plot of $G_l(s)$ and $G_m(s)$. $G_m(s)$ is the transfer functions of motor speed relative to the electromagnetic torque. $G_l(s)$ is the transfer functions of load speed relative to the electromagnetic torque. It can be seen that the gains of $G_l(s)$ and $G_m(s)$ increase sharply at the natural vibration frequency ω_{NTF}, which is 30 Hz approximately.

The relationship between the motor speed and the motor stator frequency as

TABLE IV
PARAMETERS OF MECHANICAL TRANSMISSION SYSTEM

Parameters	Value
Motor rotational inertia J_m	3.13 kg·m^2
Load rotational inertia J_l	17.5 kg·m^2
Torsional stiffness K	97954 N·m/rad
Damping coefficient D	2.4 N·m/(rad/s)

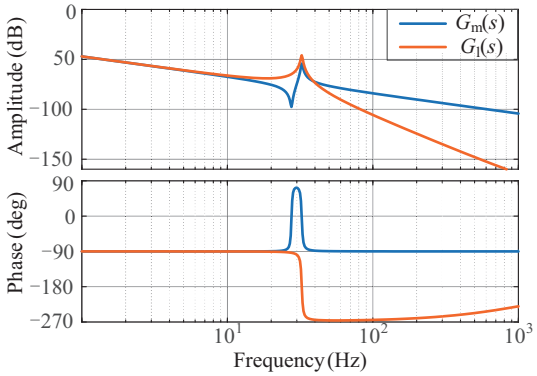

Fig. 17. Bode diagram of the dual-inertia model of the IPMSM drive system.

$$n = \frac{60 f_s}{n_p} \tag{41}$$

where f_s is the stator frequency of the motor, n is the motor speed, n_p is the number of pole pairs (set to 4). When electromechanical coupling resonance occurs, the stator frequency of the motor approaches the natural vibration frequency of the mechanical transmission device. Therefore, the stator frequency f_s in this test is set to 30 Hz, and it follows that the motor speed is set to 450 r/min.

Fig. 18 shows the electromechanical coupling resonance in IPMSM drive system and the suppression performance of the proposed method. When the IPMSM drive system runs stably without CMOEs, the electromagnetic excitation torque remains steady. The acceleration of the mechanical load side stays at zero indicating no vibration on the mechanical load side. However, when CMOE occurs (Case 4 is injected), significant first-order ripple components (i.e., corresponding to the motor fundamental frequency) are observed in the motor torque. Clearly, CMOE induces an excitation torque of 30 Hz in the IPMSM system, as shown in Fig. 18(b). Under the influence of this excitation torque, the load acceleration on the mechanical side exhibits significant vibration. As seen from Fig. 18(c), the acceleration of the mechanical load undergoes significant variations at its natural vibration frequency. Consequently, when the excitation torque frequency induced by CMOE approaches the natural vibration frequency of IPMSM drives, electromechanical coupling resonance occurs in the IPMSM drive system. This test confirms the argument presented in this paper.

When the proposed suppression scheme is applied, the electromagnetic excitation torque is restored to stability and

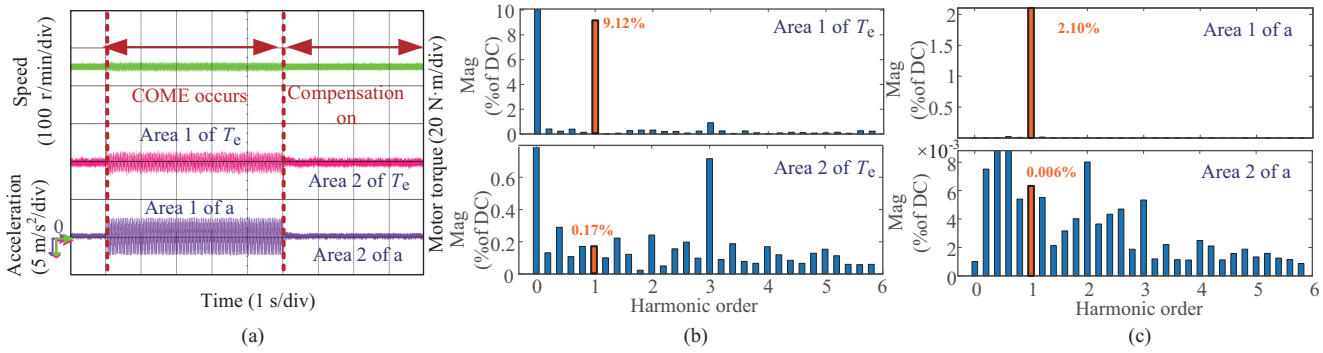

Fig. 18. Electromechanical coupling resonance HIL test: (a) Experimental test results. (b) FFT analysis of the motor torque. (c) FFT analysis of the mechanical load acceleration.

the acceleration of the mechanical load returns to normal. Such resonance of the mechanical components in the IPMSM drive system is eliminated. Combining the FFT analysis results from Fig. 18(b) and (c), it can be seen that the excitation torque content is significantly reduced from 9.12% to 0.17% after applying the suppression scheme. The vibration amplitude of the load acceleration on the mechanical side is significantly reduced from 2.10% to 0.006%, so the coupling resonance problem is effectively suppressed. Therefore, the proposed compensation scheme effectively suppresses the electromechanical coupling resonance induced by CMOE in IPMSM drive systems.

V. Conclusions

The presence of CMOE negatively impacts the performance of IPMSM drive systems. Research on CMOE in IPMSMs has mainly focused on electrical aspects while neglecting the resonant effects of electromechanical coupling. This paper pointed out that CMOE can induce electromechanical coupling resonance of IPMSM drive systems when the stator frequency of IPMSMs approaches the natural vibration frequency of the mechanical transmission device. To eliminate the adverse effects of CMOE, a PI-type observer was developed as an attempt. However, its performance was affected by motor parameter mismatches and speed variations. Based on this, an improved CMOE observer with adaptive gains was proposed for the IPMSM drive system, and the proposed compensation scheme significantly enhanced accuracy and stability. A series of experimental results indicated that the proposed scheme is promising in alleviating the influence of CMOE on electromechanical coupling resonance in IPMSM drives.

References

[1] Y. Zuo, H. Wang, X. Ge, Y. Zuo, A. T. Woldegiorgis, X. Feng, and C. H. T. Lee, "A novel current measurement offset error compensation method based on the adaptive observer for IPMSM drives," in *IEEE Transactions on Industrial Electronics*, vol. 71, no. 4, pp. 3371–3382, Apr. 2024.

[2] G. Wang, M. Valla, and J. Solsona, "Position sensorless permanent magnet synchronous machine drives—A review," in *IEEE Transactions on Industrial Electronics*, vol. 67, no. 7, pp. 5830–5842, Jul. 2020.

[3] Y. Zuo, X. Ge, Y. Chang, Y. Chen, D. Xie, H. Wang, and A. T. Woldegiorgis, "Current sensor fault-tolerant control for speedsensorless induction motor drives based on the SEPLL current reconstruction scheme," in *IEEE Transactions on Industry Applications*, vol. 59, no. 1, pp. 845–856, Jan./Feb. 2023.

[4] X. Feng, B. Wang, Z. Wang, and W. Hua, "Investigation and diagnosis of current sensor fault in permanent magnet machine drives," in *IEEE Transactions on Industrial Electronics*, vol. 72, no. 2, pp. 1261–1270, Feb. 2025.

[5] Y. Kang and D. D. Reigosa, "Dq-transformed error and current sensing error effects on self-sensing control," in *IEEE Journal of Emerging and Selected Topics in Power Electronics*, vol. 10, no. 2, pp. 1935–1945, Apr. 2022.

[6] Q. Wang, K. Rajashekara, Y. Jia, and J. Sun, "A real-time vibration suppression strategy in electric vehicles," in *IEEE Transactions on Vehicular Technology*, vol. 66, no. 9, pp. 7722–7729, Sept. 2017.

[7] J. Song-Manguelle, S. Schröder, T. Geyer, G. Ekemb, and J. -M. Nyobe-Yome, "Prediction of mechanical shaft failures due to pulsating torques of variable-frequency drives," in *IEEE Transactions on Industry Applications*, vol. 46, no. 5, pp. 1979–1988, Sept.-Oct. 2010.

[8] Q. Li, S. Liu, W. Fang, X. Li, and Z. Tse, "Sideband vibration suppression of interior permanent magnet synchronous motors for electric vehicles under multiple operating conditions," in *IEEE Transactions on Transportation Electrification*, vol. 9, no. 1, pp. 322–335, Mar. 2023.

[9] S. Zhu, W. Zhao, J. Ji, G. Liu, and C. H. T. Lee, "Generation mechanism and suppression measure of electromagnetic vibration in permanent magnet synchronous machine: A review," in *IEEE Transactions on Transportation Electrification,* vol. 10, no. 4, pp. 9513–9528, Dec. 2024.

[10] T. H. Pham, P. F. Wendling, S. J. Salon, and H. Acikgoz, "Transient finite element analysis for an induction motor with external circuit connections and electromechanical coupling," in *IEEE Transactions on Energy Conversion*, vol. 14, no. 4, pp. 1407–1412, Dec. 1999.

[11] Q. Zhang, H. Guo, Y. Liu, C. Guo, F. Zhang, Z. Zhang, and G. Li., "A novel error-injected solution for compensation of current measurement errors in PMSM drive," in *IEEE Transactions on Industrial Electronics*, vol. 70, no. 5, pp. 4608–4619, May 2023.

[12] Dae-Woong Chung and S. -K. Sul, "Analysis and compensation of current measurement error in vector-controlled AC motor drives," in *IEEE Transactions on Industry Applications*, vol. 34, no. 2, pp. 340–345, Mar.-Apr. 1998.

[13] A. Wireko-Brobby, Y. Hu, G. Wang, C. Gong, W. Lang, and Z. Zhang, "Analysis of the sources of error within PMSM-based electric powertrains—a review," in *IEEE Transactions on Transportation Electrification*, vol. 10, no. 3, pp. 6370–6406, Sept. 2024.

[14] C. Attaianese, M. D'Arpino, M. D. Monaco, and L. P. D. Noia, "Model based detection and estimation of DC offset of phase current sensors for field oriented PMSM drives," in *IEEE Transactions on Industrial Electronics*, vol. 70, no. 6, pp. 6316–6325, Jun. 2023.

[15] L. Yan, Z. Q. Zhu, and B. Shao, "Current measurement gain compensa-

tion using high-frequency signal injection in dual threephase PMSM systems," in *IEEE Transactions on Industrial Electronics*, vol. 71, no. 4, pp. 3472–3482, Apr. 2024.

[16] X. Yu, X. Wu, T. Wu, D. Yang, Z. Lei, and S. Huang, "An FTSMObased current measurement offset error compensation method in SPMSM drives," in *IEEE Transactions on Industrial Electronics*, vol. 72, no. 7, pp. 6840– 6851, Jul. 2025.

[17] Y. Zuo, H. Wang, X. Ge, Y. Liu, S. Zhu, and C. H. T. Lee, "A simple current measurement scaling error compensation method for PMSM drives," in *IEEE Transactions on Power Electronics*, vol. 39, no. 11, pp. 14122–14128, Nov. 2024.

[18] Z. Zhou, C. Xia, Y. Yan, Z. Wang, and T. Shi, "Disturbances attenuation of permanent magnet synchronous motor drives using cascaded predictive-integral-resonant controllers," in *IEEE Transactions on Power Electronics*, vol. 33, no. 2, pp. 1514–1527, Feb. 2018.

[19] Y. Bai, B. Li, Q. Wang, D. Ding, G. Zhang, G. Wang, and D. Xu, "An adaptive-frequency harmonic suppression strategy based on vector reconstruction for current measurement error of PMSM drives," in *IEEE Transactions on Power Electronics*, vol. 38, no. 1, pp. 34–40, Jan. 2023.

[20] K. Zhang, M. Fan, Y. Yang, Z. Zhu, C. Garcia, and J. Rodriguez, "An improved adaptive selected harmonic elimination algorithm for current measurement error correction of PMSMs," in *IEEE Transactions on Power Electronics*, vol. 36, no. 11, pp. 13128–13138, Nov. 2021.

[21] W. Qian, S. K. Panda, and J. X. Xu, "Speed ripple minimization in PM synchronous motor using iterative learning control," in *IEEE Transactions on Energy Conversion*, vol. 20, no. 1, pp. 53–61, Mar. 2005.

[22] J. Lu, Y. Hu, G. Chen, Z. Wang, and J. Liu, "Mutual calibration of multiple current sensors with accuracy uncertainties in IPMSM drives for electric vehicles," in *IEEE Transactions on Industrial Electronics*, vol. 67, no. 1, pp. 69–79, Jan. 2020.

[23] M. Kim, S. -K. Sul, and J. Lee, "Compensation of current measurement error for current-controlled PMSM drives," in *IEEE Transactions on Industry Applications*, vol. 50, no. 5, pp. 3365–3373, Sept./Oct. 2014.

[24] K. -W. Lee and S. -I. Kim, "Dynamic performance improvement of a current offset error compensator in current vector-controlled SPMSM drives," in *IEEE Transactions on Industrial Electronics*, vol. 66, no. 9, pp. 6727–6736, Sept. 2019.

[25] Y. Song, J. Lu, Y. Hu, X. Wu, and G. Wang, "Fast calibration with raw data verification for current measurement of dual-PMSM drives," in *IEEE Transactions on Industrial Electronics*, vol. 71, no. 7, pp. 6875–6885, Jul. 2024.

[26] S. Lee, H. Kim, and K. Lee, "Current measurement offset error compensation in vector-controlled SPMSM drive systems," in *IEEE Journal of Emerging and Selected Topics in Power Electronics*, vol. 10, no. 2, pp. 2619–2628, Apr. 2022.

[27] S. Lee and K. Lee, "Current measurement offset error compensation for IFOC induction motor drives," in *IEEE Transactions on Industry Applications*, vol. 59, no. 4, pp. 4130–4139, Jul./Aug. 2023.

[28] I. X. Bogiatzidis, A. N. Safacas, E. D. Mitronikas, and G. A. Christopoulos, "A novel control strategy applicable for a dual AC drive with common mechanical load," in *IEEE Transactions on Industry Applications*, vol. 48, no. 6, pp. 2022–2036, Nov./Dec. 2012.

[29] S. -M. Yang and S. -C. Wang, "The detection of resonance frequency in motion control systems," in *IEEE Transactions on Industry Applications*, vol.50, no. 5, pp. 3423–3427, Sept./Oct. 2014.

[30] G. Zhang, G. Wang, D. Xu, R. Ni, and C. Jia, "Multiple-AVF crossfeedback-network-based position error harmonic fluctuation elimination for sensorless IPMSM drives," in *IEEE Transactions on Industrial Electronics*, vol.63, no. 2, pp. 821–831, Feb. 2016.

[31] Y. Zhang, Z. Yin, C. Bai, G. Wang, and J. Liu, "A rotor position and speed estimation method using an improved linear extended state observer for IPMSM sensorless drives," in *IEEE Transactions on Power Electronics*, vol. 36, no. 12, pp. 14062–14073, Dec. 2021.

Xinglai Ge received the B.S., M.S., and Ph.D. degrees in electrical engineering from Southwest Jiaotong University (SWJTU), Chengdu, China, in 2001, 2004, and 2010, respectively. He is currently a Full Professor with the School of Electrical Engineering, Southwest Jiaotong University and a Vice Director of Department of Power Electronics and Power Drive. From October 2013 to October 2014, he was a visiting scholar at the School of Electrical and Computer Engineering, Georgia Institute of Technology, Atlanta, GA, USA. He is the author and co-author of more than 70 technical papers. His research interests include stability analysis and control of electrical traction system, fault diagnosis and reliability evaluation of traction converter and motor drive system.

Yangjing Liu received the B.Eng. degree in electrical engineering and automation from Hunan University of Technology in Zhuzhou, China, in 2023. She is currently working toward the M.Eng. degree in electrical engineering with Southwest Jiaotong University, Chengdu, China.

Her current research focuses on suppressing electromechanical coupling resonance in permanent magnet synchronous motor drive systems.

Yun Zuo received the B.Eng. degree in electrical engineering and automation from Dalian Jiaotong University, Dalian, China, in 2019. He is currently working toward the Ph.D. degree in electrical engineering with Southwest Jiaotong University, Chengdu, China.

His research interests include ac motor drive systems and its sensor fault tolerance and sensorless control.

Huimin Wang received the B.Eng. and Ph.D. degrees from Southwest Jiaotong University (SWJTU), Chengdu, China, in 2016 and 2021, respectively, both in electrical engineering.

From October 2019 to October 2020, he has been a Visiting Ph.D. Student with the Department of Energy Technology, Aalborg University, Denmark. He is currently an Assistant Professor with SWJTU. His research interests include ac motor drive system and its speed-sensorless control, synchronization techniques in grid-connected system, and reliability evaluation in traction drives.

Dr. Wang was a recipient of one ESI Highly Cited Paper on *IEEE Journal of Emerging and Selected Topics in Power Electronics*, and a recipient of the Best Paper Award of IEEE Transportation Electrification Conference and EXPO Asia-Pacific (ITEC Asia-Pacific) in 2019.

State and Disturbance Estimator Based Feedback Controller Synthesis for Hybrid Electric Vehicle

Sangeeta SINGH and Bhanu PRATAP

***Abstract*—The development of an output feedback controller (OFC) for a hybrid electric vehicle (HEV) is presented in this paper. The light-weighted DC motor-driven model of HEV is considered which includes a high degree of nonlinearity as uncertainty. The nonlinearity, uncertainty, and non-assessable states of the HEV plant model are estimated using a state and uncertainty estimator (SUE). The proposed controller is designed for speed control of the motor for optimal operation of HEV to meet the model range specifications based on SUE and output feedback. A suitable reference trajectory has been obtained for a smooth tracking response of motor speed. The uncertainty considered in this paper is significantly large and does not require satisfying the constraints (bounded/finite derivative to be 0, etc.). The estimator-based OFC is synthesized for the attenuation of the effect of nonlinearity and uncertainty to stabilize the HEV. For the analysis of stability, sufficient conditions for the synthesis of OFC have been obtained using the Lyapunov theory and linear matrix inequality approach. The simulation study has been done to show the efficacy of the proposed OFC control scheme. The performance of the proposed scheme has been analyzed by a comparative evaluation with the existing control schemes in terms of tracking performance, lesser tracking error, bounded control input under actuator limit, attenuation of the effect of nonlinearity and uncertainty, etc. Finally, it is concluded that the HEV performance using the proposed control scheme has been enhanced in comparison with existing schemes.**

***Index Terms*—Hybrid electric vehicle, linear matrix inequality, nonlinear system, output feedback controller, state and uncertainty estimator.**

Nomenclature

Symbol	Description
g	Acceleration constant
C_d	Aerodynamic drag coefficient
ρ	Air density
ω_H	Angular speed of motor
i_H	Armature current (field current)
L_a	Armature inductance
R_a	Armature resistance
u_H	Control input of HEV plant
V_H	Control input voltage
$\boldsymbol{R}$	Control weighting matrix
v_H	Driving velocity of vehicle
ω_{fd}	External disturbance/uncertainty
$\tilde{x}_H$	Estimation error
T_L	External torque for motor drive
$\boldsymbol{D}_H$	Feed-forward matrix (disturbance matrix)
R_f	Field winding resistance
A	Frontal area of vehicle
$\boldsymbol{K}_{LQR}$	Gain of LQR controller
G	Gearing ratio
ϕ_H	Hill climbing angle
L_f	Inductance of field winding
J	Inertia of motor
$\boldsymbol{B}_H$	Input matrix
m	Mass of vehicle
L_{af}	Mutual inductance between armature and field winding
$\boldsymbol{K}_H$, $\boldsymbol{\Gamma}_H$	Output feedback controller gains
y_H	Output of the vehicle
$\boldsymbol{C}_H$	Output matrix
r	Radius of tyre
μ_{rr}	Rolling resistance coefficient
$\boldsymbol{F}_H$, $\boldsymbol{N}_H$, $\boldsymbol{L}_H$, $\boldsymbol{E}_H$, $\boldsymbol{O}_H$, $\boldsymbol{G}_H$	State and uncertainty estimator gains
$\boldsymbol{A}_H$	State matrix of HEV plant
$\boldsymbol{z}_H$	State vector of estimator model
$\boldsymbol{x}_H$	State vector of HEV plant
$\boldsymbol{Q}$	State weighting matrix
F_H	Total traction force of vehicle
$\tilde{\omega}_{fd}$	Uncertainty estimation error
B	Viscous coefficient

Manuscript received May 29, 2025; revised July 05, 2025; accepted August 02, 2025. Date of publication September 30, 2025; date of current version August 22, 2025. No funding was received to assist with the preparation of this manuscript. (*Corresponding author: Sangeeta Singh*.)

All authors are with the Department of Electrical Engineering, NIT Kurukshetra, Haryana 136119, India (e-mail: Sangeetasingh.nitk@gmail.com; bhanu@nitkkr.ac.in).

Digital Object Identifier 10.24295/CPSSTPEA.2025.00026

I. Introduction

HYBRID electric vehicles (HEVs) possess one of the most cost-effective and virtuous energy attributes among the recent applications (Fig. 1). The HEVs have widely taken into the interest of many researchers because of having an alternate fuel operation technique; and thus, allowing less dependency on limited environmental energy concerns [1]−[2]. With this development of alternate fuel energy-powered vehicles, the efficiency of the vehicle has improved. The conversion and the

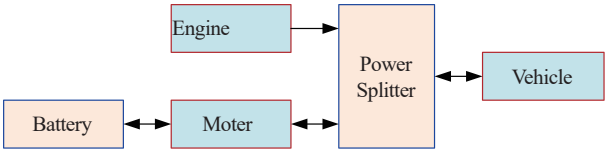

Fig. 1. Hybrid electric vehicle system [4].

storage of energy are possible with the available heat energy while applying the vehicle brakes in the form of kinetic energy. Also, HEVs with various advancements such as reliability, low-cost emission with a wide range of driveability, optimal fuel economy, etc. The HEVs are designed with the combination of both the internal combustion engine and the electric batteries and provide the cause for propulsion of the vehicle [3]–[4]. Thus, HEVs are further classified in different categories based on their working and utilization of the energy source in the vehicle likeseries HEV, parallel HEV, series-parallel HEV, and plug-in HEV as per the access of their propulsion scheme [5].

Almost all the industrial systems and vehicular technologies exhibit uncertainties and disturbances which causes adverse effects on the stability and the performance of the respective control system. In case of HEVs closed-loop [6] model, the inner feedback/feed-forward loop are composed for uncertainty/state estimator and further responsible for the attenuation and rejections of other external disturbances or unknown states with a nominal approximation of HEV plant [7]. As in the start of the input position, the disturbance observer estimates the external disturbance which will restrain the plant's uncertainties, while establishing lumped behavior of external disturbance and uncertain terms. Since uncertainties and disturbance are lumped concerning each other for any control system. However, this corresponds to the robust behavior of the controller connected for the outer loop of the respective HEV modeling and achieves stability in case of various model uncertainties [8].

The HEV models are designed with different nonlinear characteristics [9] and thus, there is a need for control schemes and monitoring for their optimal working conditions and better adaptability in practical applications. Also, the dynamic modeling of HEV involves various unmeasured variables such as vehicle speed, battery and motor currents, and battery and motor voltages which have been determined by developing control strategies based on the feedback observations. Most of the contributions are made for the linear control applications of the HEVs have been reported in the literature [10]–[14]. The linear control approaches such as proportional-integral-derivative (PID) controller, linear quadratic regulator (LQR), H-∞ controller, linear quadratic Gaussian (LQG) controller, and model predictive control (MPC), etc. are effectively incorporated to control the HEV system. A fuzzy-based PID controller [15] has been investigated in [10] where an extended Kalman filter is used for the training and optimization of the suspension system. A robust control technique based on gain scheduled LQR has been applied on HEV for the yaw moment control [11]. An H-∞ controller with LQR has been presented for an integrated motor-transmission powertrain system [16] in discrete time to track the reference speed signals for the drivetrain and attenuate the effect of motor lags [12]. For frequency stabilization of interconnected plug-in HEV, an optimal controller using a LQG [17] control scheme with an integral action has been developed [13]. A model predictive control-based nonlinear strategy has been studied to stabilize an electric vehicle with experimental results [14].

Traditionally disturbance observers are designed in sequence of nonlinear system dynamics. As discussed, observer-based control with the estimation of states of systems is also modeled for the stability of the system process. Thus, synthesizing an observer for any system with exogenous disturbances will estimate both states and the disturbance of the system. Where the gains of the observer can be formulated using linear matrix inequality (LMI) equations to achieve asymptotic stability of the system [18]. Modeling of HEV systems emerges with various uncertainties such as tracking the vehicular speed, battery performance and regulations, stability context, the robustness of vehicle transmission, disturbance effects, and other dynamical constraints. These factors are responsible for the designing of the system based on observer approximations.

The well-known problems of HEV operation are identified as the uncertain and nonlinear dynamics with the external disturbances and frictions. This paper presents a state and uncertainty estimator (SUE) based output feedback control (OFC) scheme to improve the HEV performance considering the above-said problems. The system uncertainty, nonlinearity, disturbance, and friction are generally considered as unknown and sometimes difficult to evaluate. Therefore, the proposed control scheme has been developed for a light-weight HEV model to observe the response of state estimation, uncertainty estimation, and output tracking, etc. The simulation exercises have been done to present the efficacy of the proposed control scheme. The performance of HEV operation has been improved as compared to the performance using the existing control scheme [19]. The results obtained with the proposed scheme are resulted in good convergence of states in terms of estimation and regulation, bounded control input under the consideration of a wide range of uncertainty. The sufficient conditions for the controller life span are usually expressed in terms of LMI or bilinear matrix inequalities (BMI). A dynamic control agent of a T-S fuzzy system with time varying time delay is observed by using Lyapunov function method [20]. Based on the LMI, the second order Lyapunov function can control the results obtained with improved and low maintenance output feedback and relax the limitations in the existing results [21].

In addition, a modified time fuzzy control strategy can be obtained to solve the completely different and uncertain spoofing attacksand the size of the combination of state variables can be changed. It is guaranteed to be bounded in the case of spoofing attacks. And adjust the size of the state variable convergence area [22]–[23]. The main contributions and novelties of this paper are summarized as follows:

• A novel OFC is developed for a highly nonlinear, uncertain light-weight HEV system, where full state measurements are not available.

• A robust SUE is proposed to jointly estimate the unmeasur-

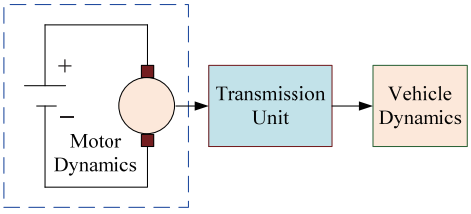

Fig. 2. HEV system [14].

able states and the unknown uncertainties/disturbances of the HEV plant, enabling efficient control even under high degrees of nonlinearity and external perturbations.

• Unlike existing works which assume bounded or slowly varying uncertainties, the proposed controller operates effectively under large, fast-varying, and unstructured uncertainties without requiring restrictive assumptions (e.g., zero derivative or bounded rates).

• The control synthesis is rigorously formulated using LMI techniques in the Lyapunov framework, ensuring guaranteed stability and robustness.

• A comparative simulation study demonstrates the superiority of the proposed SUE-based OFC over conventional controllers (e.g., PID, LQR, H-∞) in terms of tracking performance, uncertainty attenuation, and actuator constraint satisfaction. These contributions collectively offer a practically viable and theoretically sound solution for high-performance control of HEVs under uncertain and nonlinear dynamics.

The rest of the paper is categorized as follows. In Section II, the dynamical modeling of the HEV system is introduced. The problem formulation with control objectives is described in Section III. In Section IV, an SUE for the HEV system is designed. The proposed SUE-based OFC is designed for HEV and presented in Section V. In Section VI, the simulation study is carried out in MATLAB and the results obtained are compared with the existing control scheme. Finally, the simulation results have been concluded in Section VII.

II. Modelling of Hybrid Electric Vehicle (HEV)

The mechanical model of a light weighted HEV (Fig. 2.) has been considered to have two sub-models such as vehicle dynamics model (VDM) and motor dynamics model (MDM) [24]. The major factors considered for the VDM are aerodynamic drag, conditions of road, acceleration, and hill climbing, etc. A transmission unitconsisting of the gearing system is used to connect the MDM with the VDM. HEVs operation on the basis of speed may vary from zero to full speed. For HEVs applications, the control signal to the propulsion control module is given by the driver in the form of acceleration or deceleration by applying accelerator or break pedal [25]. The propulsion control system of HEV is used the DC motor for propulsion. The control system design for the speed of DC motor is required to control the HEV system [26].

Vehicle dynamic model (VDM): Considering the factors affecting the dynamics of HEV, the dynamical equation of VDM model of HEV is given by [27],

$$F_{\mathrm{H}}=\mu_{\mathrm{rr}}mg+1/2\,\rho AC_{\mathrm{d}}v_{\mathrm{H}}^{2}+mg\sin\phi_{\mathrm{H}}+m\,\mathrm{d}v_{\mathrm{H}}/\mathrm{d}t \tag{1}$$

Considering the dynamics of HEV in (1), the terms used are as follows.

(i) $\mu_{\mathrm{rr}}mg$ represents the force of rolling resistance,

(ii) $1/2\,\rho AC_{\mathrm{d}}v_{\mathrm{H}}^{2}$ represents the force of aerodynamic drag,

(iii) $mg\sin\phi_{\mathrm{H}}$ represents the force of hill climbing,

(iv) $m\,\mathrm{d}v_{\mathrm{h}}/\mathrm{d}t$ represents the force of acceleration.

A counter-productive torque is generated by the traction force to the driving motor given by

$$T_{\mathrm{L}}=F_{\mathrm{H}}\,r/G \tag{2}$$

Motor dynamic model (MDM): The dynamical equation of MDM model of HEV driven by DC motoris given by [28],

$$J\,\mathrm{d}\omega_{\mathrm{H}}/\mathrm{d}t=L_{\mathrm{af}}i_{\mathrm{H}}^{2}-B\omega_{\mathrm{H}}-T_{\mathrm{L}} \tag{3a}$$

$$\left(L_{\mathrm{a}}+L_{\mathrm{f}}\right)\mathrm{d}i_{\mathrm{H}}/\mathrm{d}t=\bar{V}_{\mathrm{H}}-\left(R_{\mathrm{a}}+R_{\mathrm{f}}\right)i_{\mathrm{H}}-L_{\mathrm{af}}i_{\mathrm{H}}\omega_{\mathrm{H}} \tag{3b}$$

The dynamics of HEV system (1)–(3) can be expressed in the form of differential equations as

$$\{J+m\,[r/G]^{2}\}\,\mathrm{d}\omega_{\mathrm{H}}/\mathrm{d}t=L_{\mathrm{af}}i_{\mathrm{H}}^{2}-B\omega_{\mathrm{H}}-r/G\,[\mu_{\mathrm{rr}}mg+1/2\,\rho AC_{\mathrm{d}}v_{\mathrm{H}}^{2}+mg\sin\,\phi_{\mathrm{H}}] \tag{4a}$$

$$\left(L_{\mathrm{a}}+L_{\mathrm{f}}\right)\mathrm{d}i_{\mathrm{H}}/\mathrm{d}t=\bar{V}_{\mathrm{H}}-\left(R_{\mathrm{a}}+R_{\mathrm{f}}\right)i_{\mathrm{H}}-L_{\mathrm{af}}i_{\mathrm{H}}\omega_{\mathrm{H}} \tag{4b}$$

The HEV driving velocity may vary with the change in angular speed of motor [29] according to the following equation given as,

$$v_{\mathrm{H}}=G/r\,\omega_{\mathrm{H}} \tag{5}$$

State space modelling of hEV: The dynamical model of HEV (1)–(5) can be rewritten in the form given by,

$$\begin{aligned}\dot{x}_{\mathrm{H}}&=\bar{f}_{\mathrm{H}}\left(\boldsymbol{x}_{\mathrm{H}}\right)+\bar{g}_{\mathrm{H}}\left(\boldsymbol{x}_{\mathrm{H}}\right)u_{\mathrm{H}}\\ y_{\mathrm{H}}&=\bar{h}_{\mathrm{H}}\left(\boldsymbol{x}_{\mathrm{H}}\right)\end{aligned} \tag{6}$$

where $\boldsymbol{x}_{\mathrm{H}}=[\omega_{\mathrm{H}}\;\; i_{\mathrm{H}}]^{\mathrm{T}}$, $u_{\mathrm{H}}=\bar{V}_{\mathrm{H}}$, and $y_{\mathrm{H}}=\omega_{\mathrm{H}}$ represents the state vector, control input, and output of the HEV. The nonlinear functions [30] $\bar{f}_{\mathrm{H}}\left(\boldsymbol{x}_{\mathrm{H}}\right)$, $\bar{g}_{\mathrm{H}}\left(\boldsymbol{x}_{\mathrm{H}}\right)$, and $\bar{h}_{\mathrm{H}}\left(\boldsymbol{x}_{\mathrm{H}}\right)$ are as follow,

$$\bar{f}_{\mathrm{H}}(\boldsymbol{x}_{\mathrm{H}})=\begin{bmatrix}A_1x_1+A_2x_1^{2}+A_3x_2^{2}+A_4\\ A_5x_2+A_6x_1x_2\end{bmatrix}\equiv\begin{bmatrix}\bar{f}_{1\mathrm{H}}(\boldsymbol{x}_{\mathrm{H}})\\ \bar{f}_{2\mathrm{H}}(\boldsymbol{x}_{\mathrm{H}})\end{bmatrix},$$

$$\bar{g}_{\mathrm{H}}(\boldsymbol{x}_{\mathrm{H}})=\begin{bmatrix}0\\ B_2\end{bmatrix}\equiv\begin{bmatrix}\bar{g}_{1\mathrm{H}}(\boldsymbol{x}_{\mathrm{H}})\\ \bar{g}_{2\mathrm{H}}(\boldsymbol{x}_{\mathrm{H}})\end{bmatrix},\;\bar{h}_{\mathrm{H}}\left(\boldsymbol{x}_{\mathrm{H}}\right)=\boldsymbol{x}_1$$

where

$$A_1=-B/\left\{J+m\left(\frac{r}{G}\right)^{2}\right\},\quad A_2=-\left\{\frac{r\rho AC_{\mathrm{d}}}{2G}\right\}/\left\{J+m\left(\frac{r}{G}\right)^{2}\right\},$$

$$A_3=L_{\mathrm{af}}/\left\{J+m\left(\frac{r}{G}\right)^{2}\right\},\quad A_4=-\left\{\frac{r\mu_{\mathrm{rr}}mg}{G}\right\}/\left\{J+m\left(\frac{r}{G}\right)^{2}\right\},$$

$A_5 = -(R_a+R_f)/(L_a+L_f)$, $A_6 = -(L_{af}x_1x_2)/(L_a+L_f)$, and $B_2 = 1/(L_a+L_f)$. The angle of hill climbing ϕ_H is considered to be 0.

Linearized model of HEV: The nonlinear model [16] of HEV (6) can be linearized about the non-origin with the help of Taylor's series method. The linearized model of the considered model of HEV (6) is obtained as

$$\begin{aligned} \dot{x}_H &= \boldsymbol{A}_H \boldsymbol{x}_H + \boldsymbol{B}_H u_H \\ y_H &= \boldsymbol{C}_H \boldsymbol{x}_H \end{aligned} \tag{7}$$

The above nominal plant model of HEV is controllable which will be used for the development of proposed SUE based controller.

III. Problem Formulation

A problem of designing an output feedback controller [34] for smooth operation of a light weighted HEV (Fig. 2) has been considered in this proposed work for the demonstration of performance enhancement.

The HEV model (7) including the effect of uncertainty and disturbance can be rewritten as

$$\begin{aligned} \dot{x}_H &= \underbrace{\boldsymbol{A}_H \boldsymbol{x}_H + \boldsymbol{B}_H u_H}_{\text{nominal model}} + \underbrace{\boldsymbol{D}_H \omega_{fd}}_{\text{uncertain model}} \\ y_H &= \boldsymbol{C}_H \boldsymbol{x}_H \end{aligned} \tag{8}$$

The first term of the above dynamical equation HEV represents the nominal plant model whereas, the second term represents the parametric uncertainty and external disturbance. The second term is assumed usually to be unknown and is estimated with the help of SUE for the design of proposed controller.

Control objectives: The objective of this paper is to develop a state and uncertainty estimator based output feedback controller for a light weighted HEV system with the following properties.

(i) The plant output (measured speed of DC motor) converges to the specified reference trajectory,

(ii) The reference tracking error of the plant output and trajectory approach to zero,

(iii) The tracking performance must satisfy the constraint on the input voltage,

(iv) The optimal performance of HEV is need to be achieved with the effect of uncertainty and disturbance.

The proposed SUE based feedback controller has been developed in the next sections.

IV. Design of State and Uncertainty Estimator (SUE)

In this section, an SUE for HEV system (8) is designed. An assumption has been stated for the development of SUE.

Assumption 1: Considering the output matrix $\boldsymbol{C}_H$ and disturbance matrix $\boldsymbol{D}_H$ of full rank where the matrix $\boldsymbol{C}_H\boldsymbol{D}_H$ has the same rank as $\boldsymbol{D}_H$.

The state and uncertainty estimator for the HEV uncertain model (8) is given by,

$$\dot{z}_H = \boldsymbol{N}_H \boldsymbol{z}_H + \boldsymbol{G}_H u_H + \boldsymbol{L}_H y_H \tag{9a}$$

$$\hat{x}_H = \boldsymbol{z}_H - \boldsymbol{F}_H y_H \tag{9b}$$

$$\hat{\omega}_{fd} = \left(\boldsymbol{C}_H \boldsymbol{D}_H\right)^{-1} \dot{y}_H - \boldsymbol{E}_H \hat{\boldsymbol{x}}_H - \boldsymbol{O}_H u_H \tag{9c}$$

Theorem 1: Considering the HEV system (8) with the SUE (9) satisfying Assumption 1. If there exist the matrices $\boldsymbol{N}_H \in \Re^{2\times2}$, $\boldsymbol{G}_H \in \Re^{2\times1}$, $\boldsymbol{L}_H \in \Re^{2\times1}$, $\boldsymbol{F}_H \in \Re^{2\times1}$, $\boldsymbol{E}_H \in \Re^{1\times2}$, $\boldsymbol{O}_H \in \Re^{1\times1}$, and $\boldsymbol{P}_H \in \Re^{2\times2}$, such that the states and uncertainty converges asymptotically and the following conditions are fulfilled [32].

$$\boldsymbol{N}_H\boldsymbol{M}_H - \boldsymbol{M}_H\boldsymbol{A}_H + \boldsymbol{L}_H\boldsymbol{C}_H = 0 \tag{10}$$

$$\boldsymbol{G}_H = \boldsymbol{M}_H\boldsymbol{B}_H \tag{11}$$

$$\boldsymbol{M}_H\boldsymbol{D}_H = 0 \tag{12}$$

$$\boldsymbol{M}_H = \boldsymbol{I}_H + \boldsymbol{F}_H\boldsymbol{C}_H \tag{13}$$

$$(\boldsymbol{C}_H\boldsymbol{D}_H) + \boldsymbol{C}_H\boldsymbol{A}_H - \boldsymbol{E}_H = 0 \tag{14}$$

$$(\boldsymbol{C}_H\boldsymbol{D}_H) + \boldsymbol{C}_H\boldsymbol{B}_H - \boldsymbol{O}_H = 0 \tag{15}$$

$$\boldsymbol{N}_H^T\boldsymbol{P}_H + \boldsymbol{P}_H\boldsymbol{N}_H < 0 \tag{16}$$

Proof: The state estimation error is defined as,

$$\tilde{\boldsymbol{x}}_H = \hat{\boldsymbol{x}}_H - \boldsymbol{x}_H \tag{17}$$

Using (8), (9b), and (13), the expression (17) becomes

$$\tilde{\boldsymbol{x}}_H = \boldsymbol{z}_H - \boldsymbol{M}_H\boldsymbol{x}_H \tag{18}$$

Substituting (8) and (9a) in the derivative of (18), the error dynamic becomes

$$\begin{aligned} \dot{\tilde{\boldsymbol{x}}}_H = \boldsymbol{N}_H\tilde{\boldsymbol{x}}_H + (\boldsymbol{N}_H\boldsymbol{M}_H - \boldsymbol{M}_H\boldsymbol{A}_H + \boldsymbol{L}_H\boldsymbol{C}_H)\boldsymbol{x}_H + \\ (\boldsymbol{G}_H - \boldsymbol{M}_H\boldsymbol{B}_H)u_H - \boldsymbol{M}_H\boldsymbol{D}_H\omega_{fd} \end{aligned} \tag{19}$$

The error dynamic (19) can be rewritten, if the conditions (10)–(12) hold as,

$$\dot{\tilde{\boldsymbol{x}}}_H = \boldsymbol{N}_H + \tilde{\boldsymbol{x}}_H \tag{20}$$

Choose a Lyapunov function,

$$V_{\tilde{x}} = \tilde{\boldsymbol{x}}_H^T\boldsymbol{P}_{oH}\tilde{\boldsymbol{x}}_H \tag{21}$$

Substituting (20) in the derivative of (21) gives,

$$\dot{V}_{\tilde{x}} = \tilde{\boldsymbol{x}}_H^T\left[\boldsymbol{N}_H^T\boldsymbol{P}_H + \boldsymbol{P}_H\boldsymbol{N}_H\right]\tilde{\boldsymbol{x}}_H \tag{22}$$

The expression (22) becomes negative definite, if holds the condition (16). Hence, Theorem 1 is proved.

Now, the uncertainty estimation error is defined as,

$$\tilde{\omega}_{fd} = \hat{\omega}_{fd} - \omega_{fd} \tag{23}$$

Using (9c), the expression (23) can be written as,

$$\begin{aligned} \tilde{\omega}_{fd} &= \left(\boldsymbol{C}_H\boldsymbol{D}_H\right)^{-1}\boldsymbol{C}_H\left(\boldsymbol{A}_H\boldsymbol{x}_H + \boldsymbol{B}_H u_H + \boldsymbol{D}_H\omega_{fd}\right) - \boldsymbol{E}_H\hat{\boldsymbol{x}}_H - \boldsymbol{O}_H u_H - \omega_{fd} \\ \tilde{\omega}_{fd} &= \left\{\left(\boldsymbol{C}_H\boldsymbol{D}_H\right)^{-1}\boldsymbol{C}_H\boldsymbol{A}_H - \boldsymbol{E}_H\right\}\boldsymbol{x}_H + \left\{\left(\boldsymbol{C}_H\boldsymbol{D}_H\right)^{-1}\boldsymbol{C}_H\boldsymbol{B}_H - \boldsymbol{O}_H\right\}u_H - \boldsymbol{E}_H\tilde{\boldsymbol{x}}_H \end{aligned} \tag{24}$$

The error dynamic (24) can be rewritten, if the conditions (14), (15) hold as,

$$\tilde{\omega}_{\text{fd}} = -\boldsymbol{E}_{\text{H}}\tilde{\boldsymbol{x}}_{\text{H}} \tag{25}$$

From (25), it can be observed that if, $\tilde{\boldsymbol{x}}_{\text{H}} \to 0$, then $\tilde{\omega}_{\text{fd}} \to 0$.

The expression (16) is a BMI equation and difficult to obtain the solution. Thus, Theorem 2 has been defined to transform into the LMI expression.

Theorem 2: Considering the HEV system (8) with the SUE (9), and the state estimation error (17) and uncertainty estimator error (23) asymptotically converge to zero, if there exist the matrices $\boldsymbol{N}_{\text{H}} \in \Re^{2\times 2}$, $\boldsymbol{G}_{\text{H}} \in \Re^{2\times 1}$, $\boldsymbol{L}_{\text{H}} \in \Re^{2\times 1}$, $\boldsymbol{F}_{\text{H}} \in \Re^{2\times 1}$, $\boldsymbol{E}_{\text{H}} \in \Re^{1\times 2}$, $\boldsymbol{O}_{\text{H}} \in \Re^{1\times 1}$, and $\boldsymbol{P}_{\text{H}} \in \Re^{2\times 2}$, such that the following conditions are fulfilled [32].

$$\begin{aligned}&[(\boldsymbol{I}_{2\times 2} + \boldsymbol{U}_{\text{H}}\boldsymbol{C}_{\text{H}})\boldsymbol{A}_{\text{H}}]^{\text{T}}\boldsymbol{P}_{\text{H}} + \boldsymbol{P}_{\text{H}}[(\boldsymbol{I}_{2\times 2} + \boldsymbol{U}_{\text{H}}\boldsymbol{C}_{\text{H}})\boldsymbol{A}_{\text{H}}] - \boldsymbol{C}_{\text{H}}^{\text{T}}\bar{\boldsymbol{H}}_{\text{H}}^{\text{T}} - \bar{\boldsymbol{H}}_{\text{H}}\boldsymbol{C}_{\text{H}} \\ &+ (\boldsymbol{V}_{\text{H}}\boldsymbol{C}_{\text{H}}\boldsymbol{A}_{\text{H}})^{\text{T}}\boldsymbol{Q}_{\text{H}}^{\text{T}} + \boldsymbol{Q}_{\text{H}}(\boldsymbol{V}_{\text{H}}\boldsymbol{C}_{\text{H}}\boldsymbol{A}_{\text{H}}) < 0\end{aligned} \tag{26}$$

where

$$\boldsymbol{U}_{\text{H}} = -\boldsymbol{D}_{\text{H}}(\boldsymbol{C}_{\text{H}}\boldsymbol{D}_{\text{H}})^{-1} \tag{27}$$

$$\boldsymbol{V}_{\text{H}} = \boldsymbol{I} - \boldsymbol{C}_{\text{H}}\boldsymbol{D}_{\text{H}}(\boldsymbol{C}_{\text{H}}\boldsymbol{D}_{\text{H}})^{-1} \tag{28}$$

$$\boldsymbol{Q}_{\text{H}} = \boldsymbol{P}_{\text{H}}\boldsymbol{Y}_{\text{H}} \tag{29a}$$

$$\bar{\boldsymbol{H}}_{\text{H}} = \boldsymbol{P}_{\text{H}}\boldsymbol{H}_{\text{H}} \tag{29b}$$

Proof: Using the conditions given in (12) and (13), we have

$$\boldsymbol{F}_{\text{H}}(\boldsymbol{C}_{\text{H}}\boldsymbol{D}_{\text{H}}) = -\boldsymbol{D}_{\text{H}} \tag{30}$$

The solution of (30) can be written as [33],

$$\boldsymbol{F}_{\text{H}} = -\boldsymbol{D}_{\text{H}}(\boldsymbol{C}_{\text{H}}\boldsymbol{D}_{\text{H}})^{-1} + \boldsymbol{Y}_{\text{H}}[\boldsymbol{I} - (\boldsymbol{C}_{\text{H}}\boldsymbol{D}_{\text{H}})(\boldsymbol{C}_{\text{H}}\boldsymbol{D}_{\text{H}})^{-1}] = \boldsymbol{U}_{\text{H}} + \boldsymbol{Y}_{\text{H}}\boldsymbol{V}_{\text{H}} \tag{31}$$

Define a new expression,

$$\boldsymbol{H}_{\text{H}} = \boldsymbol{L}_{\text{H}} + \boldsymbol{N}_{\text{H}}\boldsymbol{F}_{\text{H}} \tag{32}$$

Using (10), (13), and (32), following equation can be obtained as,

$$\boldsymbol{N}_{\text{H}} = \boldsymbol{M}_{\text{H}}\boldsymbol{A}_{\text{H}} - \boldsymbol{H}_{\text{H}}\boldsymbol{C}_{\text{H}} \tag{33}$$

Using (32) and (33), the observer gain matrix $\boldsymbol{L}_{\text{H}}$ can be written by

$$\boldsymbol{L}_{\text{H}} = \boldsymbol{H}_{\text{H}}(\boldsymbol{I} + \boldsymbol{C}_{\text{H}}\boldsymbol{F}_{\text{H}}) - \boldsymbol{M}_{\text{H}}\boldsymbol{A}_{\text{H}}\boldsymbol{F}_{\text{H}} \tag{34}$$

The inequality (16) will be modified using (13), (30), and (33) as,

$$\begin{aligned}&[(\boldsymbol{I}_{2\times 2} + \boldsymbol{U}_{\text{H}}\boldsymbol{C}_{\text{H}})\boldsymbol{A}_{\text{H}}]^{\text{T}}\boldsymbol{P}_{\text{H}} + \boldsymbol{P}_{\text{H}}[(\boldsymbol{I}_{2\times 2} + \boldsymbol{U}_{\text{H}}\boldsymbol{C}_{\text{H}})\boldsymbol{A}_{\text{H}}] - \boldsymbol{C}_{\text{H}}^{\text{T}}\boldsymbol{H}_{\text{H}}^{\text{T}}\boldsymbol{P}_{\text{H}} - \\ &\boldsymbol{P}_{\text{H}}\boldsymbol{H}_{\text{H}}\boldsymbol{C}_{\text{H}} + (\boldsymbol{V}_{\text{H}}\boldsymbol{C}_{\text{H}}\boldsymbol{A}_{\text{H}})^{\text{T}}\boldsymbol{Y}_{\text{H}}^{\text{T}}\boldsymbol{P}_{\text{H}} + \boldsymbol{P}_{\text{H}}\boldsymbol{Y}_{\text{H}}(\boldsymbol{V}_{\text{H}}\boldsymbol{C}_{\text{H}}\boldsymbol{A}_{\text{H}}) < 0\end{aligned} \tag{35}$$

Suppose that, $\boldsymbol{Q}_{\text{H}} = \boldsymbol{P}_{\text{H}}\boldsymbol{Y}_{\text{H}}$ and $= \bar{\boldsymbol{H}}_{\text{H}}\boldsymbol{P}_{\text{H}}\boldsymbol{H}_{\text{H}}$. The expression (35) can be rewritten as,

$$\begin{aligned}&[(\boldsymbol{I}_{2\times 2} + \boldsymbol{U}_{\text{H}}\boldsymbol{C}_{\text{H}})\boldsymbol{A}_{\text{H}}]^{\text{T}}\boldsymbol{P}_{\text{H}} + \boldsymbol{P}_{\text{H}}[(\boldsymbol{I}_{2\times 2} + \boldsymbol{U}_{\text{H}}\boldsymbol{C}_{\text{H}})\boldsymbol{A}_{\text{H}}] - \boldsymbol{C}_{\text{H}}^{\text{T}}\bar{\boldsymbol{H}}_{\text{H}}^{\text{T}} - \bar{\boldsymbol{H}}_{\text{H}}\boldsymbol{C}_{\text{H}} \\ &+ (\boldsymbol{V}_{\text{H}}\boldsymbol{C}_{\text{H}}\boldsymbol{A}_{\text{H}})^{\text{T}}\boldsymbol{Q}_{\text{H}}^{\text{T}} + \boldsymbol{Q}_{\text{H}}(\boldsymbol{V}_{\text{H}}\boldsymbol{C}_{\text{H}}\boldsymbol{A}_{\text{H}}) < 0\end{aligned} \tag{36}$$

The expression of BMI (16) has been transformed into LMI (36). Hence the Theorem 2 is proved.

Finally, the SUE gains are calculated by solving the LMI (36) and computing $\boldsymbol{E}_{\text{H}} = (\boldsymbol{C}_{\text{H}}\boldsymbol{D}_{\text{H}})^{-1}\boldsymbol{C}_{\text{H}}\boldsymbol{A}_{\text{H}}$ and $\boldsymbol{O}_{\text{H}} = (\boldsymbol{C}_{\text{H}}\boldsymbol{D}_{\text{H}})^{-1}\boldsymbol{C}_{\text{H}}\boldsymbol{B}_{\text{H}}$. The proposed SUE based feedback controller has been developed in the next section.

V. Design of SUE Based Output Feedback Controller (OFC)

In this section, an SUE based OFC for HEV system (8) is designed. An assumption has been stated for the development of OFC.

Assumption 2: Considering the input matrix $\boldsymbol{B}_{\text{H}}$ and disturbance matrix $\boldsymbol{D}_{\text{H}}$ of full rank where the matrix $\boldsymbol{B}_{\text{H}}\boldsymbol{D}_{\text{H}}$ has the same rank as $\boldsymbol{B}_{\text{H}}$.

The SUE based output feedback controller for the HEV uncertain model (8) is given by,

$$u_{\text{H}} = -\boldsymbol{K}_{\text{H}}\hat{\boldsymbol{x}}_{\text{H}} - \boldsymbol{\Gamma}_{\text{H}}\hat{\omega}_{\text{fd}} \tag{37}$$

Theorem 3: Considering the HEV system (8) with the SUE (9) and OFC (37) satisfying Assumption 2. If there exist the matrices $\boldsymbol{N}_{\text{H}} \in \Re^{2\times 2}$, $\boldsymbol{G}_{\text{H}} \in \Re^{2\times 1}$, $\boldsymbol{L}_{\text{H}} \in \Re^{2\times 1}$, $\boldsymbol{F}_{\text{H}} \in \Re^{2\times 1}$, $\boldsymbol{E}_{\text{H}} \in \Re^{1\times 2}$, $\boldsymbol{O}_{\text{H}} \in \Re^{1\times 1}$, $\boldsymbol{K}_{\text{H}} \in \Re^{1\times 2}$, $\boldsymbol{\Gamma}_{\text{H}} \in \Re^{1\times 1}$, $\boldsymbol{P}_{\text{oH}} \in \Re^{2\times 2}$, and $\boldsymbol{P}_{\text{cH}} \in \Re^{2\times 2}$, such that the states and uncertainty converges asymptotically and the conditions (10)–(15) along with the following two conditions are fulfilled [32].

$$\boldsymbol{D}_{\text{H}} - \boldsymbol{B}_{\text{H}}\boldsymbol{\Gamma}_{\text{H}} = 0 \tag{38}$$

$$\boldsymbol{\Psi}_{\text{H}}^{\text{T}}\bar{\boldsymbol{P}}_{\text{H}} + \bar{\boldsymbol{P}}_{\text{H}}\boldsymbol{\Psi}_{\text{H}} < 0 \tag{39}$$

where, $\bar{\boldsymbol{P}}_{\text{H}} = \begin{bmatrix} \boldsymbol{P}_{\text{cH}}^{-1} & 0 \\ 0 & \boldsymbol{P}_{\text{cH}} \end{bmatrix}$ and, $\boldsymbol{\Psi}_{\text{H}} = \begin{bmatrix} (\boldsymbol{A}_{\text{H}} - \boldsymbol{B}_{\text{H}}\boldsymbol{K}_{\text{H}}) & (-\boldsymbol{B}_{\text{H}}\boldsymbol{K}_{\text{H}} + \boldsymbol{D}_{\text{H}}\boldsymbol{E}_{\text{H}}) \\ 0 & \boldsymbol{N}_{\text{H}} \end{bmatrix}$.

Substituting the control law (37) in the HEV system model (8), gives

$$\dot{\boldsymbol{x}}_{\text{H}} = (\boldsymbol{A}_{\text{H}} - \boldsymbol{B}_{\text{H}}\boldsymbol{K}_{\text{H}})\boldsymbol{x}_{\text{H}} - \boldsymbol{B}_{\text{H}}\boldsymbol{K}_{\text{H}}\tilde{\boldsymbol{x}}_{\text{H}} + (\boldsymbol{D}_{\text{H}} - \boldsymbol{B}_{\text{H}}\boldsymbol{\Gamma}_{\text{H}})\hat{\omega}_{\text{fd}} - \boldsymbol{D}_{\text{H}}\tilde{\omega}_{\text{fd}} \tag{40}$$

Using (38), (40) can be rewritten as,

$$\dot{\boldsymbol{x}}_{\text{H}} = (\boldsymbol{A}_{\text{H}} - \boldsymbol{B}_{\text{H}}\boldsymbol{K}_{\text{H}})\boldsymbol{x}_{\text{H}} + (\boldsymbol{D}_{\text{H}}\boldsymbol{E}_{\text{H}} - \boldsymbol{B}_{\text{H}}\boldsymbol{K}_{\text{H}})\tilde{\boldsymbol{x}}_{\text{H}} \tag{41}$$

Therefore, from (20) and (42), we can have following form of state and uncertainty estimation errors,

$$\underbrace{\begin{bmatrix} \dot{\boldsymbol{x}}_{\text{H}} \\ \dot{\tilde{\boldsymbol{x}}}_{\text{H}} \end{bmatrix}}_{\dot{\bar{\boldsymbol{x}}}_{\text{H}}} = \underbrace{\begin{bmatrix} (\boldsymbol{A}_{\text{H}} - \boldsymbol{B}_{\text{H}}\boldsymbol{K}_{\text{H}}) & (\boldsymbol{D}_{\text{H}}\boldsymbol{E}_{\text{H}} - \boldsymbol{B}_{\text{H}}\boldsymbol{K}_{\text{H}}) \\ 0 & \boldsymbol{N}_{\text{H}} \end{bmatrix}}_{\boldsymbol{\Psi}_{\text{H}}} \underbrace{\begin{bmatrix} \boldsymbol{x}_{\text{H}} \\ \tilde{\boldsymbol{x}}_{\text{H}} \end{bmatrix}}_{\bar{\boldsymbol{x}}_{\text{H}}} \tag{42}$$

Thus,

$$\dot{\bar{\boldsymbol{x}}}_{\text{H}} = \boldsymbol{\Psi}_{\text{H}}\bar{\boldsymbol{x}}_{\text{H}} \tag{43}$$

Choose a Lyapunov function,

$$V_{\bar{x}} = \bar{\boldsymbol{x}}_{\text{H}}^{\text{T}}\bar{\boldsymbol{P}}_{\text{H}}\bar{\boldsymbol{x}}_{\text{H}} \tag{44}$$

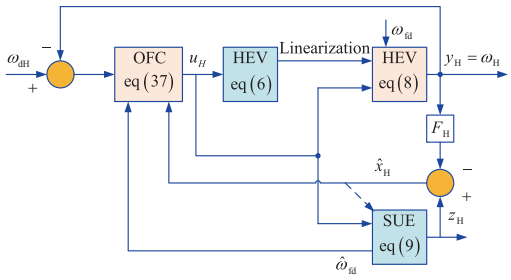

Fig. 3. Block diagram of proposed SUE (9) based OFC (37) for HEV model (6) and (8).

Substituting (43) in the derivative of (44) gives a following expression,

$$\dot{V}_{\bar{x}} = \bar{\boldsymbol{x}}_H^{\mathrm{T}}\left[\boldsymbol{\Psi}_H^{\mathrm{T}}\bar{\boldsymbol{P}}_H + \bar{\boldsymbol{P}}_H\boldsymbol{\Psi}_H\right]\bar{\boldsymbol{x}}_H \tag{45}$$

The expression (45) becomes negative definite, if holds the condition (39). Hence, Theorem 3 is proved.

The expression (39) is a bilinear equation and difficult to obtain the solution. Thus, Theorem 4 has been defined to transform into the LMI expression.

Theorem 4: Considering the HEV system (8) with the SUE (37) and controller (38) can be stabilized while satisfying Assumptions 1 and 2. If there exist the matrices $\boldsymbol{N}_H \in \Re^{2\times 2}$, $\boldsymbol{G}_H \in \Re^{2\times 1}$, $\boldsymbol{L}_H \in \Re^{2\times 1}$, $\boldsymbol{F}_H \in \Re^{2\times 1}$, $\boldsymbol{E}_H \in \Re^{1\times 2}$, $\boldsymbol{O}_H \in \Re^{1\times 1}$, $\boldsymbol{K}_H \in \Re^{2\times 2}$, $\boldsymbol{\Gamma}_H \in \Re^{1\times 1}$, $\boldsymbol{P}_{oH} \in \Re^{2\times 2}$, and $\boldsymbol{P}_{cH} \in \Re^{2\times 2}$, such that the following conditions are fulfilled [32],

$$\boldsymbol{A}_H\boldsymbol{P}_{cH} + \boldsymbol{A}_H^{\mathrm{T}}\boldsymbol{P}_{cH} - \boldsymbol{B}_H\boldsymbol{R}_H - \boldsymbol{R}_H^{\mathrm{T}}\boldsymbol{B}_H^{\mathrm{T}} < 0 \tag{46}$$

where,

$$\boldsymbol{\Gamma}_H = \boldsymbol{B}_H^{+}\boldsymbol{D}_H \tag{47}$$

$$\boldsymbol{K}_H = \boldsymbol{R}_H\boldsymbol{P}_{cH}^{-1} \tag{48}$$

Proof: The expression (39) can be expanded using (42) as,

$$\begin{bmatrix}(\boldsymbol{A}_H - \boldsymbol{B}_H\boldsymbol{K}_H) & (\boldsymbol{D}_H\boldsymbol{E}_H - \boldsymbol{B}_H\boldsymbol{K}_H)\\ 0 & \boldsymbol{N}_H\end{bmatrix}^{\mathrm{T}}\begin{bmatrix}\boldsymbol{P}_{cH}^{-1} & 0\\ 0 & \boldsymbol{P}_{cH}\end{bmatrix} + \begin{bmatrix}\boldsymbol{P}_{cH}^{-1} & 0\\ 0 & \boldsymbol{P}_{cH}\end{bmatrix}\begin{bmatrix}(\boldsymbol{A}_H - \boldsymbol{B}_H\boldsymbol{K}_H) & (\boldsymbol{D}_H\boldsymbol{E}_H - \boldsymbol{B}_H\boldsymbol{K}_H)\\ 0 & \boldsymbol{N}_H\end{bmatrix} < 0 \tag{49}$$

$$\begin{bmatrix}\left(\boldsymbol{P}_{cH}^{-1}\boldsymbol{A}_H + \boldsymbol{A}_H^{\mathrm{T}}\boldsymbol{P}_{cH}^{-1} - \boldsymbol{P}_{cH}^{-1}\boldsymbol{B}_H\boldsymbol{K}_H - \boldsymbol{K}_H^{\mathrm{T}}\boldsymbol{B}_H^{\mathrm{T}}\boldsymbol{P}_{cH}^{-1}\right) & \left(\boldsymbol{P}_{cH}^{-1}\boldsymbol{D}_H\boldsymbol{E}_H - \boldsymbol{P}_{cH}^{-1}\boldsymbol{B}_H\boldsymbol{K}_H\right)\\ \left(\boldsymbol{P}_{cH}^{-1}\boldsymbol{D}_H\boldsymbol{E}_H - \boldsymbol{P}_{cH}^{-1}\boldsymbol{B}_H\boldsymbol{K}_H\right)^{\mathrm{T}} & \left(\boldsymbol{P}_{cH}\boldsymbol{N}_H + \boldsymbol{N}_H^{\mathrm{T}}\boldsymbol{P}_{cH}\right)\end{bmatrix} < 0 \tag{50}$$

The expression (50) can be transformed into the following form using Schur complement [34],

$$\begin{aligned}&(\boldsymbol{P}_{cH}^{-1}\boldsymbol{A}_H + \boldsymbol{A}_H^{\mathrm{T}}\boldsymbol{P}_{cH}^{-1} - \boldsymbol{P}_{cH}^{-1}\boldsymbol{B}_H\boldsymbol{K}_H - \boldsymbol{K}_H^{\mathrm{T}}\boldsymbol{B}_H^{\mathrm{T}}\boldsymbol{P}_{cH}^{-1}) -\\ &(\boldsymbol{P}_{cH}^{-1}\boldsymbol{D}_H\boldsymbol{E}_H - \boldsymbol{P}_{cH}^{-1}\boldsymbol{B}_H\boldsymbol{K}_H)(\boldsymbol{P}_{oH}\boldsymbol{N}_H + \boldsymbol{N}_H^{\mathrm{T}}\boldsymbol{P}_{oH})^{-1}\cdot\\ &(\boldsymbol{P}_{cH}^{-1}\boldsymbol{D}_H\boldsymbol{E}_H - \boldsymbol{P}_{cH}^{-1}\boldsymbol{B}_H\boldsymbol{K}_H)^{\mathrm{T}} < 0\end{aligned} \tag{51}$$

$$\boldsymbol{P}_{oH}\boldsymbol{N}_H + \boldsymbol{N}_H^{\mathrm{T}}\boldsymbol{P}_{oH} < 0 \tag{52}$$

Due to (52), expression (51) will be

$$\begin{aligned}&(\boldsymbol{P}_{cH}^{-1}\boldsymbol{D}_H\boldsymbol{E}_H + \boldsymbol{P}_{cH}^{-1}\boldsymbol{B}_H\boldsymbol{K}_H)(\boldsymbol{P}_{oH}\boldsymbol{N}_H + \boldsymbol{N}_H^{\mathrm{T}}\boldsymbol{P}_{oH})^{-1}\cdot\\ &(\boldsymbol{P}_{cH}^{-1}\boldsymbol{D}_H\boldsymbol{E}_H - \boldsymbol{P}_{cH}^{-1}\boldsymbol{B}_H\boldsymbol{K}_H)^{\mathrm{T}} \leqslant 0\end{aligned} \tag{53}$$

Thus,

$$\begin{aligned}&(\boldsymbol{P}_{cH}^{-1}\boldsymbol{A}_H + \boldsymbol{A}_H^{\mathrm{T}}\boldsymbol{P}_{cH}^{-1} - \boldsymbol{P}_{cH}^{-1}\boldsymbol{B}_H\boldsymbol{K}_H - \boldsymbol{K}_H^{\mathrm{T}}\boldsymbol{B}_H^{\mathrm{T}}\boldsymbol{P}_{cH}^{-1}) <\\ &(\boldsymbol{P}_{cH}^{-1}\boldsymbol{D}_H\boldsymbol{E}_H - \boldsymbol{P}_{cH}^{-1}\boldsymbol{B}_H\boldsymbol{K}_H)(\boldsymbol{P}_{oH}\boldsymbol{N}_H + \boldsymbol{N}_H^{\mathrm{T}}\boldsymbol{P}_{oH})^{-1}\cdot\\ &(\boldsymbol{P}_{cH}^{-1}\boldsymbol{D}_H\boldsymbol{E}_H - \boldsymbol{P}_{cH}^{-1}\boldsymbol{B}_H\boldsymbol{K}_H)^{\mathrm{T}} \leqslant 0\end{aligned} \tag{54}$$

Therefore, (50) is equivalent to

$$\boldsymbol{P}_{cH}^{-1}\boldsymbol{A}_H + \boldsymbol{A}_H^{\mathrm{T}}\boldsymbol{P}_{cH}^{-1} - \boldsymbol{P}_{cH}^{-1}\boldsymbol{B}_H\boldsymbol{K}_H - \boldsymbol{K}_H^{\mathrm{T}}\boldsymbol{B}_H^{\mathrm{T}}\boldsymbol{P}_{cH}^{-1} < 0 \tag{55}$$

$$\boldsymbol{P}_{oH}\boldsymbol{N}_H + \boldsymbol{N}_H^{\mathrm{T}}\boldsymbol{P}_{oH} < 0 \tag{56}$$

Now, the BMI expression has been transformed to the LMI by multiplying $\boldsymbol{P}_{cH}$ pre and post to (55), results

$$\boldsymbol{A}_H\boldsymbol{P}_{cH} + \boldsymbol{P}_{cH}\boldsymbol{A}_H^{\mathrm{T}} - \boldsymbol{B}_H\boldsymbol{K}_H\boldsymbol{P}_{cH} - \boldsymbol{P}_{cH}\boldsymbol{K}_H^{\mathrm{T}}\boldsymbol{B}_H^{\mathrm{T}} < 0 \tag{57}$$

Suppose that, $\boldsymbol{\Gamma}_H = \boldsymbol{B}_H^{+}\boldsymbol{D}_H$ and $\boldsymbol{K}_H = \boldsymbol{R}_H\boldsymbol{P}_{cH}^{-1}$. The expression (57) can be rewritten as,

$$\boldsymbol{A}_H\boldsymbol{P}_{cH} + \boldsymbol{P}_{cH}\boldsymbol{A}_H^{\mathrm{T}} - \boldsymbol{B}_H\boldsymbol{R}_H - \boldsymbol{R}_H^{\mathrm{T}}\boldsymbol{B}_H^{\mathrm{T}} < 0 \tag{58}$$

The expression of BMI (39) has been transformed into LMI (58). Hence the Theorem 4 is proved.

Finally, the OFC gains are calculated by solving the LMI (58). The response proposed SUE based OFC has been simulated for performance analysis in the next section.

The proposed SUE (9) based OFC (37) design scheme for HEV model (6) and (8) can be expressed by a block diagram (Fig. 3).

VI. Simulation Results and Discussions

In this section, simulation studies have been presented to obtain the performance of the proposed control scheme. The simulations are performed using HEV system parameter given in Appendix.

Response of SUE (9) on linearized uncertain model of HEV (8): The considered model of HEV (8) in open-loop is operated with the control signal given by $u = 0.5\sin t$. The initial conditions for the HEV plant (8) and SUE (9) are considered as $\boldsymbol{x}_{0H} = [0.1 \;\; 0.1]^{\mathrm{T}}$ and $\boldsymbol{z}_{0H} = [0.05 \;\; 0.05]^{\mathrm{T}}$ respectively. Solving the LMI (26) as stated in Theorem 2 in Section IV, the gains of SUE (9) are obtained by $\boldsymbol{F}_H = [-1 \; -1]^{\mathrm{T}}$, $\boldsymbol{N}_H = \begin{bmatrix}-0.5 & 0\\ 0 & -20.1242\end{bmatrix}$, $\boldsymbol{L}_H = [0 \;\; -20.2707]^{\mathrm{T}}$, $\boldsymbol{G}_H = [0 \;\; 166.447]^{\mathrm{T}}$, $\boldsymbol{E}_H = [-0.0004 \;\; 0.0038]$, and $\boldsymbol{O}_H = 0$.

The simulation study has been done to reveal the SUE per-

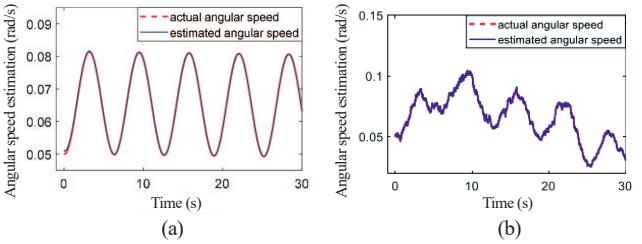

Fig. 4. Estimation of angular speed of motor. (a) without uncertainty, (b) with uncertainty.

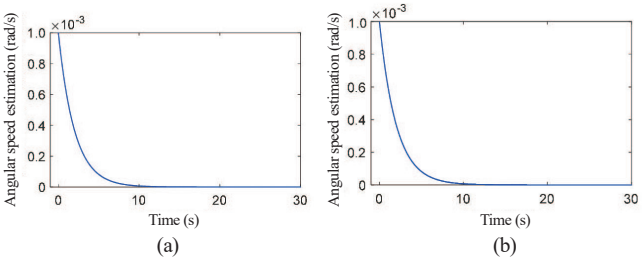

Fig. 5. Estimation error of angular speed of motor. (a) without uncertainty, (b) with uncertainty.

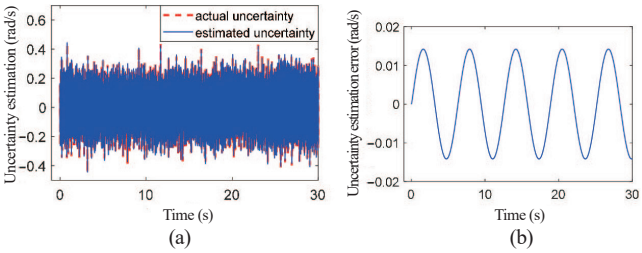

Fig. 6. Uncertainty. (a) estimation, (b) estimation error.

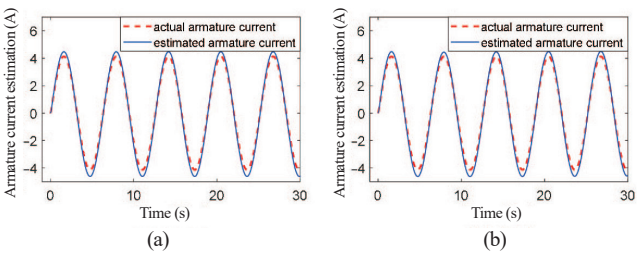

Fig. 7. Estimation of armature current of motor. (a) without uncertainty, (b) with uncertainty.

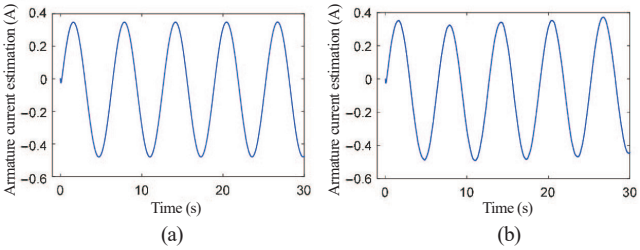

Fig. 8. Estimation error of armature current of motor. (a) without uncertainty, (b) with uncertainty.

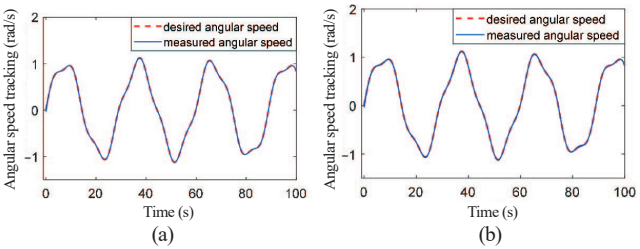

Fig. 9. Tracking of angular speed of motor. (a) without uncertainty, (b) with uncertainty.

formance in terms of converges of estimated states and uncertainty with the actual plant states and uncertainty (Fig. 4). The error of motor angular speed estimation is less and converges to zero (Fig. 5). The uncertainty effect in the HEV plant is estimated and depicted in Fig. 6.

The estimation response of other state (field/armature current of motor which is unmeasurable) is obtained and is plotted in Figs. 7 and 8.

Response of SUE based OFC (37) on linearized uncertain model of HEV (8): The considered model of HEV (8) in closed-loop [35] is operated with the SUE based control signal (37). The initial conditions for the HEV plant (8) and SUE (9) are considered as $\boldsymbol{x}_{0\mathrm{H}} = [0.1 \;\; 0.1]^{\mathrm{T}}$ and $\boldsymbol{z}_{0\mathrm{H}} = [0.05 \;\; 0.05]^{\mathrm{T}}$ respectively. Solving the LMIs (26) and (46) as stated in Theorem 2 and Theorem 4 given in Section IV and Section V respectively, and the gains of SUE based OFC (37) are obtained by $\boldsymbol{K}_{\mathrm{H}} = [0.0002 \;\; -0.01178]$ and $\boldsymbol{\Gamma}_{\mathrm{H}} = 0.006$. A robustification term has also been included to the control law (37) to for the attenuation of effect of uncertainty and disturbances. The design parameters of SUE remain same as stated in previous subsection.

The simulation study has been carried out to demonstrate the performance of SUE based OFC in terms of tracking of actual and estimated states (Fig. 9). The tracking error of motor angular speed actual and estimated is tends to zero (Fig. 10). The control input response is obtained which is bounded and under the limit of actuator of HEV (Fig. 11).

Response of SUE (9) and SUE based OFC (37) on nonlinear model of HEV (6): The performance response of linearized uncertain model of HEV (8) has been obtained above. However, the proposed control scheme has also been applied on the nonlinear model of HEV (6) to show its effectiveness. The response obtained from the nonlinear model with proposed SUE (9) and SUE based OFC (37) are shown in Figs. 12 and 13.

It is observed from the Table I that the performance of SUE remains stable with or without the presence of uncertainty as well as disturbance.

Performance comparative analysis with existing LQR control scheme: The proposed scheme has been compared with an LQR schemefor significant performance evaluation comparatively. The LQR control law gain has been calculated $\boldsymbol{K}_{\mathrm{LQR}} = [22.3496 \;\; 0.0350]$ from the standard Riccatti equation by assuming the design parameter $\boldsymbol{Q} = \mathrm{diag}\,[1000 \;\; 0]$ as state weighting matrix and $\boldsymbol{R} = 2$ as control weighting matrix.

Comparing the linearized/nonlinear model of HEV with the proposed control scheme and LQR scheme we have the shown

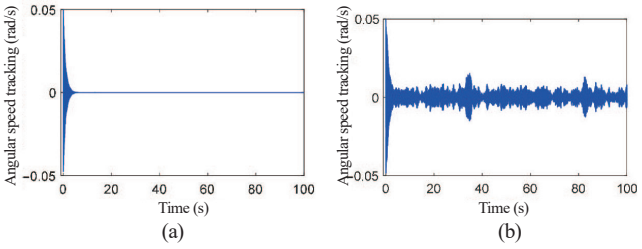

Fig. 10. Tracking error of angular speed of motor. (a) without uncertainty, (b) with uncertainty.

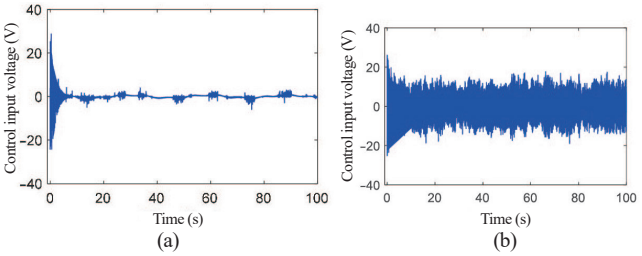

Fig. 11. Control input voltage. (a) without uncertainty, (b) with uncertainty.

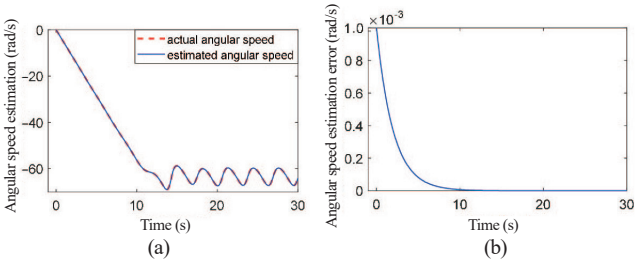

Fig. 12. Angular speed of motor. (a) estimation, (b) estimation error.

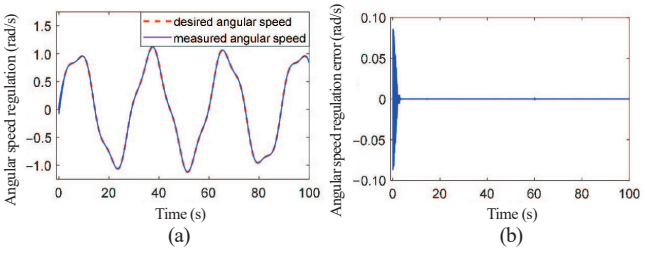

Fig. 13. Angular speed of motor. (a) tracking, (b) tracking error.

the observations in Figs. 14–17.

It is observed from the Table II that the performance of SUE based OFC remains stable with or without the presence of uncertainty as well as disturbance.

Comparing the above plots (Fig. 14 to Fig. 17) obtained for the linearized/nonlinear model of HEV with the proposed control scheme and LQR scheme, it can be observed that the optimal response has been achieved using LMI (26) and (46) using proposed scheme. The performance of controller is satisfactory for both the models of HEV with less error and stable response in the presence of parametric uncertainty (2% to 5%) and disturbance.

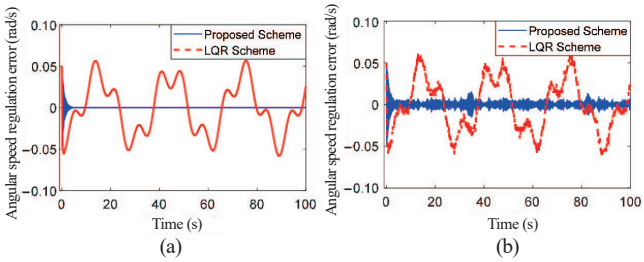

Fig. 14. Tracking error of angular speed of motor. (a) without uncertainty, (b) with uncertainty.

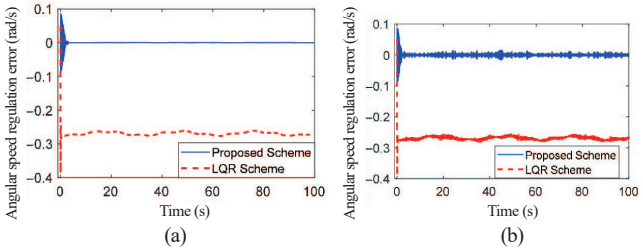

Fig. 15. Tracking error of angular speed of motor. (a) without uncertainty, (b) with uncertainty.

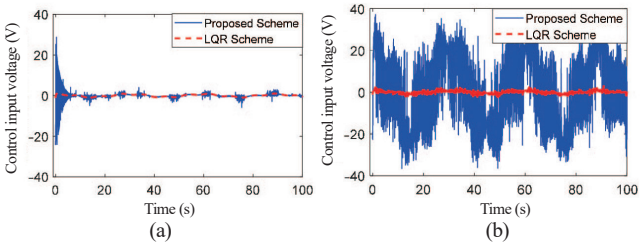

Fig. 16. Control input voltage. (a) without uncertainty, (b) with uncertainty.

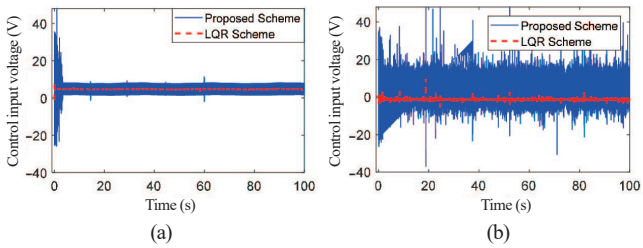

Fig. 17. Control input voltage. (a) without uncertainty, (b) with uncertainty.

VII. Conclusions

The performance of HEV in the application of electric vehicles has a significant role and its control is also decisive. A performance evaluation of SUE-based OFC for linearized as well as the nonlinear model of HEV has been proposed. The highlights of the work presented in this paper are (i) considering the linearized/nonlinear model of HEV, (ii) development of SUE for the estimation of unmeasurable state and uncertainty presenting the HEV plant, (iii) design of SUE based OFC controller for HEV considering the effect of parametric uncertainty and disturbance, (iv) detailed stability analysis using LMI and

TABLE I
ERROR RESPONSE ANALYSIS OF SUE

Response	HEV models	Without disturbance and uncertainty	With disturbance	With uncertainty	With disturbance and uncertainty
Angular speed estimation error	Linearized model	0.000241	0.000195	0.000271	0.001420
	Nonlinear model	0.000275	0.000434	0.000308	0.001617
Armature current estimation error	Linearized model	0.293600	0.289000	0.329844	0.517160

TABLE II
ERROR RESPONSE ANALYSIS OF SUE BASED OFC

Angular speed regulation error	HEV models	Without disturbance and uncertainty	With disturbance	With uncertainty	With disturbance and uncertainty
Proposed Scheme	Linearized model	0.0013	0.0035	0.0015	0.0023
	Nonlinear model	0.0051	0.0064	0.0057	0.0090
Existing LQR Scheme [19]	Linearized model	0.0290	0.0323	0.0326	0.0511
	Nonlinear model	0.2689	0.2699	0.3021	0.4737

Lyapunov theory for obtaining the optimal gains of estimator/controller, (v) simulation study for performance outcome as well as comparative evaluation for both linearized/nonlinear model. The results obtained with the proposed scheme are resulted in good convergence of states in terms of estimation and regulation, bounded control input under the consideration of a wide range of uncertainty. The proposed work in this paper can further extended for the tracking problem by considering the standard NEDC drive cycle test with nonlinear control schemes. This addition emphasizes our intent to validate the proposed control scheme under practical conditions in future work. However, the current study is limited to simulation-based validation. No experimental or hardware-in-the-loop testing has been conducted. Future work will focus on real-time implementation and experimental validation using an HEV test platform to assess practical feasibility and controller robustness under real-world conditions.

Appendix

All the physical parameters of the HEV system are defined in Table 3 with their physical values.

REFERENCES

[1] M. Ehsani, K. V. Singh, H. O. Bansal, M. A. Khan, M. U. Qureshi, and J. M. Miller, "State of the art and trends in electric and hybrid electric vehicles," in *Proceedings of the IEEE*, vol. 109, pp. 967–984, Jul. 2021.

[2] F. Donatantonio, A. Ferrara, P. Polverino, I. Arsie, and C. Pianese, "Novel approaches for energy management strategies of hybrid electric vehicles and comparison with conventional solutions," in *Energies*, vol. 15, no. 6, pp. 1975, Mar. 2022.

[3] Q. Luo, A. T. Nguyen, J. Fleming, and J. M. Dolan, "Unknown input observer based approach for distributed tube-based model predictive control of heterogeneous vehicle platoons," in *IEEE Transactions on Vehicular Technology*, vol. 70, pp. 2930–2944, Apr. 2021.

[4] S. Mahapatra, T. Egel, R. Hassan, R. Shenoy, and M. Carone, "Model-based design for hybrid electric vehicle systems," in *SAE Technical Paper Series*, art. no. 2008-01-0085, 2008.

[5] J. J. Jui, M. A. Ahmad, M.M. I. Molla, and M. I. M. Rashid, "Optimal energy management strategies for hybrid electric vehicles: A recent survey of machine learning approaches," in *Journal of Engineering Research*, vol. 12, no. 3, pp. 454–467, Sept. 2024.

[6] Y. Bi, T. Wang, J. Qiu, M. Li, C. Wei, and L. Yuan, "Adaptive decentralized finite-time fuzzy secure control for uncertain nonlinear CPSs under deception attacks," in *IEEE Transactions on Fuzzy Systems*, vol. 31, no. 8, pp. 2568–2580, 2023.

[7] V. Vu and W. Wang, "State/disturbance observer and controller synthesis for the T-S fuzzy system with an enlarged class of disturbances," in *IEEE Transactions on Fuzzy Systems*, vol. 26, pp. 3645–3659, Dec. 2018.

[8] X. Mao, P. Li, Z. Weng, and J. Zhao, "Distributed tube model predictive control for string stability of heterogeneous vehicle platoons," in *Proceedings of the Institution of Mechanical Engineers, Part I: Journal of Systems and Control Engineering*, vol. 237, no. 7, pp. 1015–1026, Jul. 2023.

[9] M. H. Khooban, T. Niknam, F. Blaabjerg, and M. Shasadeghi, "Free chattering hybrid sliding mode control for a class of non-linear systems: electric vehicles as a case study," in *IET Science, Measurement & Technology*, vol. 10, no. 7, pp. 776–785, 2016.

[10] N. A. Mohseni, N. Bayati, and T. Ebel, "Energy management strategies of hybrid electric vehicles: A comparative review," in *IET Smart Grid*, vol. 7, no. 3, pp. 191–220, Sept. 2023.

[11] Y. Lu, R. Zhen, Y. Liu, J. Zhong, C. Sun, Y. Huang, and A. Khajepour, "Practical solution for attenuating industrial heavy vehicle vibration: A new gain-adaptive coordinated suspension control system," in *Control Engineering Practice*, vol. 154, pp. 106125, Jan. 2025.

[12] A. Nikou and D. V. Dimarogonas, "Decentralized tube-based model predictive control of uncertain nonlinear multi-agent systems," in *arXiv preprint*, art. no. arXiv:1808.05408, Aug. 2018.

[13] A. Tuffaha, "The stochastic linear quadratic optimal control problem on Hilbert spaces: The case of non-analytic systems," in *Applied Mathematics & Optimization*, vol. 87, no. 3, pp. 58, Apr. 2023.

[14] S. Arora, A. Shukla, and M. Kumar, "Impact of electric vehicles on environment and grid: A comprehensive review," in *IEEE Transactions on Transportation Electrification*, vol. 10, no. 1, pp. 324–336, 2024.

[15] M. H. Khooban, M. Shasadeghi, T. Niknam, and F. Blaabjerg, "Analysis, control and design of speed control of electric vehicles delayed model: Multi-objective fuzzy fractional-order controller," in *IET Science, Measurement & Technology*, vol. 11, no. 3, pp. 249–261, 2017.

[16] M. Sharma and V. Verma, "Integrated fuzzy logic and neural network for hybrid electric vehicle powertrain control," in *IEEE Transactions on Control Systems Technology*, vol. 30, no. 5, pp. 1807–1818, May 2022.

[17] A. Pakniyat and P. E. Caines, "A class of linear quadratic Gaussian hybrid

TABLE III
HEV System Parameters [28]

Parameters	Symbols	Values	Parameters	Symbols	Values
Mass of the vehicle	m	800 kg	The inertia of motor	J	0.05 kg·m^2
Rolling resistance coefficient	μ_{rr}	0.015	Angular speed of motor	ω	2800 rad/min
Air density	ρ	1.25 kg/m^3	Winding inductance	L_{field}	$L_{field}+L_a$ = 6.008 mH
Drag coefficient	C_d	0.3	Armature inductance	L_a	
Frontal area of vehicle	A	1.8 m^2	Armature/field current	i	78 A
Driving velocity of vehicle	v	25 km/h	Armature resistance	R_a	$R_a + R_f$ = 0.12 Ω
Gravity acceleration	g	9.8 m/s^2	Field winding resistance	R_f	
Hill climbing angle	ϕ	0	Viscous coefficient	B	0.0002 N/(m/s)
Tyre radius	r	0.25 m	Mutual inductance bet^n armature & field winding	L_{af}	1.766 mH
Gearing ratio	G	11	Control input voltage	V	0 V – 48 V

optimal control problems with realization-independent Riccati equations," in *IFAC-PapersOnLine*, vol. 50, no. 1, pp. 2205–2210, 2017.

[18] E. Muhammad, A. Vali, A. Kashaninia, and V. Bahnamgol, "Stability enhancement of hybrid electric vehicles using optimal fuzzy logic," in *International Journal of Dynamics and Control*, vol. 12, no. 4, pp. 1130–1145, Jul. 2023.

[19] S. Singh and B. Pratap, "Continuous sliding mode controller design for light weighted hybrid electric vehicle," in *2018 IEEE 8th Power India International Conference (PIICON)*, Kurukshetra, India, 2018, pp. 1–6.

[20] P. Mei, H. R. Karimi, S. Yang, B. Xu, and C. Huang, "An adaptive fuzzy sliding-mode control for regenerative braking system of electric vehicles," in *International Journal of Adaptive Control and Signal Processing*, vol. 36, no. 2, pp. 391–410, Feb. 2022.

[21] K. Rajan, M. Gupta, and S. Misra, "Trends in powertrain architecture of plug-in and hybrid electric vehicles," in *IEEE Transactions on Intelligent Transportation Systems*, vol. 25, no. 3, pp. 2680–2694, 2024.

[22] H. Taghavifar, "EKF estimation based PID Type-2 fuzzy control of electric cars," in *Measurement*, vol. 173, pp. 108557, Mar. 2021.

[23] Z. Wang, U. Montanaro, S. Fallah, and D. O. Cabrera, "A gain scheduled robust linear quadratic regulator for vehicle direct yaw moment control," in *Mechatronics*, vol. 51, pp. 31–45, 2021.

[24] Q. Huang, Z. Huang, and H. Zhou, "Nonlinear optimal and robust speed control for a light-weighted all-electric vehicle," in *IET Control Theory & Applications*, vol. 3, no. 4, pp. 437–444, Apr. 2009.

[25] V. Sharma and S. Purwar, "Nonlinear controllers for a light-weighted all-electric vehicle using Chebyshev neural network," in *International Journal of Vehicular Technology*, vol. 2014, pp. 1–14, 2014.

[26] L. Yuan, H. Zhao, H. Chen, and B. Ren, "Model predictive controller-based optimal slip ratio control for electric vehicles," in *International Journal of Vehicle Autonomous Systems*, vol. 2020, pp. 8086590, 2020.

[27] F. Ahmad, A. A. A. El-Fergany, and A. Iqbal, "Nonlinear control in electric vehicles: challenges and recent developments," in *IEEE Transactions on Control Systems Technology*, vol. 32, no. 1, pp. 412–423, 2024.

[28] M. Razi, N. Murgovski, T. McKelvey, and B. Egardt, "Design and comparative analyses of optimal feedback controllers for hybrid electric vehicles," in *IEEE Transactions on Vehicular Technology*, vol. 70, pp. 2979–2993, Apr. 2021.

[29] M. Veysi, J. Aghaei, M. Shasadeghi, and S. Fallah, "Energy-efficient speed control of electric vehicles: linear matrix inequality approach," in *IEEE Transactions on Vehicular Technology*, vol. 69, no. 10, pp. 10469–10483, 2020.

[30] C. S. Choi, J. K. Park, and B. H. Lee, "Integrated modeling and simulation of hybrid electric vehicle powertrain with nonlinear control," in *IEEE Transactions on Transportation Electrification*, vol. 9, no. 4, pp. 7645–7658, 2023.

[31] J. Qiu, W. Ji, and H.-K. Lam, "A new design of fuzzy affine model-based output feedback control for discrete-time nonlinear systems," in *IEEE Transactions on Fuzzy Systems*, vol. 31, no. 5, pp. 1434–1444, 2023.

[32] B. Sakhdari and N. L. Azad, "Adaptive tube-based nonlinear MPC for ecological autonomous cruise control of plug-in hybrid electric vehicles," in *IEEE Transactions on Vehicular Technology*, vol 67, no. 12, pp. 11390–11401, Mar. 2018.

[33] L. Kamyabi, T. T. Lie, S. Madanian, and S. Marshall, "A Comprehensive review of hybrid state estimation in power systems: challenges, opportunities and prospects," in *Energies*, vol. 17, no. 19, pp. 4806, Sept. 2024.

[34] A. Parra, D. Tavernini, P. Gruber, and A. Bemporad, "On nonlinear model predictive control for energy-efficient torque-vectoring," in *IEEE Transactions on Vehicular Technology*, vol. 70, pp. 173–188, Jan. 2021.

[35] S. Song, J. H. Park, B. Zhang, and X. Song, "Event-based adaptive fuzzy fixed-time secure control for nonlinear CPSs against unknown false data injection and backlash-like hysteresis," in *IEEE Transactions on Fuzzy Systems*, vol. 31, no. 6, pp. 1939–1951, Apr. 2021.

Sangeeta Singh received the graduation degree in Electrical and Electronics Engineering from Uttar Pradesh Technical University, Lucknow, India, in 2009, the M.Tech. degree in Control and Instrumentation the Aligarh Muslim University, Aligarh, India in 2011. She is currently an Assistant Professor in the department of Electrical Engineering with JSS Academy of Technical Education, India. Her research interests include nonlinear control systems, hybrid electric vehicle, and intelligent control techniques.

Bhanu Pratap received the graduation degree in Electrical Engineering from Uttar Pradesh Technical University, Lucknow, India, in 2007, the M.Tech. degree in Control and Instrumentation, and the Ph.D. degree in Electrical Engineering from the Motilal Nehru National Institute of Technology, Allahabad, India, in 2009 and 2013, respectively. He is currently an Assistant Professor in the department of Electrical Engineering with National Institute of Technology, Kurukshetra, India. His research interests include intelligent control of nonlinear systems, robust and adaptive control, control of renewable energy systems, and control of hybrid electric vehicles.

CHINA POWER SUPPLY SOCIETY

China Power Supply Society (CPSS) founded in 1983 is a nonprofit, non-governmental academic and professional organization of scientists and engineers in the power supply & power electronics fields. CPSS is dedicated to achieving scientific and technological progress of power supply and the advancement of the power supply industry. CPSS website is www.cpss.org.cn.

ADMINISTRATIVE OFFICE

Add: 10th Floor, Datong Building, No.467 Huanghe Road, Nankai District, Tianjin, 300110, China

Tel: +86-22-27680796 Fax: +86-22-27687886

E-mail: cpss@cpss.org.cn Website: www.cpss.org.cn

CPSS TRANSACTIONS ON POWER ELECTRONICS AND APPLICATIONS

(Quarterly, Started in 2016)

Vol. 10 No. 3 Sept. 30, 2025

Sponsored by: China Power Supply Society (CPSS)

Technically Co-Sponsored by: IEEE Power Electronics Society (IEEE PELS)

Supported by: Sungrow Power Supply Co., Ltd.
Xiamen Kehua Hengsheng Co., Ltd.
Shenzhen Inovance Technology Co., Ltd.
StarPower Semiconductor Ltd.

Editor-in-Chief: Jinjun Liu

Published by: Editorial Office of CPSS TPEA

Address: 10th Floor, Datong Building, No. 467 Huanghe Road,
Nankai Dist., Tianjin, 300110, China

Tel: +86-22-27680796-18#

Fax: +86-22-27687886

E-mail: tpea@cpss.org.cn

Website: tpea.cpss.org.cn